Title

Measurement of jets produced in top quark events using the emu final state with 2 b-tagged jets in pp collisions at 8 TeV with the ATLAS detector

Author
Brosamer, Jacquelyn Kay

Publication Date
2016

Peer reviewed|Thesis/dissertation

Measurement of jets produced in top quark events using the $e\mu$ final state with 2 b-tagged jets in pp collisions at $\sqrt{s} = 8$ TeV with the ATLAS detector

by

Jacquelyn Kay Brosamer

A dissertation submitted in partial satisfaction of the

requirements for the degree of

Doctor of Philosophy

in

Physics

in the

Graduate Division

of the

University of California, Berkeley

Committee in charge:

Professor Marjorie Shapiro, Chair
Professor Leo Blitz
Professor Barbara Jacak

Spring 2016

Measurement of jets produced in top quark events using the $e\mu$ final state with 2 b-tagged jets in pp collisions at $\sqrt{s} = 8$ TeV with the ATLAS detector

Abstract

Measurement of jets produced in top quark events using the $e\mu$ final state with 2 b-tagged jets in pp collisions at $\sqrt{s} = 8$ TeV with the ATLAS detector

by

Jacquelyn Kay Brosamer

Doctor of Philosophy in Physics

University of California, Berkeley

Professor Marjorie Shapiro, Chair

The transverse momentum (p_{T}) and multiplicity of jets produced in top quark events are measured using 20.3 fb^{-1}of pp collision data at a center-of-mass energy of $\sqrt{s}$ =8 TeV. Jets are selected from top events requiring an opposite-charge $e\mu$ pair and two b-tagged jets in the final state. The data are corrected to obtain the particle-level fiducial cross section $\frac{1}{\sigma}\frac{d\sigma_{\mathrm{jet}}}{dp_T}$for additional jets with rank 1-4, where rank=1 is the leading additional jet. These distributions are used to obtain the extra jet multiplicity as a function of minimum jet p_{T} threshold. The results are compared with several next to leading order Monte Carlo generators. The resulting measurements can be used to tune Monte Carlo QCD modelling and may also reduce associated modelling uncertainties for LHC top quark physics measurements.

Contents

Contents **i**

List of Figures **v**

List of Tables **xvii**

1 Introduction **1**

2 Theory **3**
2.1 The Standard Model . . . 3
2.1.1 Particles of the SM . . . 3
2.1.2 Quantum chromodynamics . . . 4
2.1.2.1 Running of the coupling . . . 6
2.1.2.2 Parton distribution functions . . . 6
2.1.2.3 Factorization . . . 8
2.2 Top quark physics . . . 9
2.2.1 Top quark production at the LHC . . . 9
2.2.2 Top quark decays . . . 12
2.3 Beyond the SM . . . 14

3 Phenomenology at the LHC **16**
3.1 Simulation of hadron collisions . . . 16
3.2 Monte Carlo generators . . . 18
3.3 Jets . . . 20

4 The ATLAS detector and the LHC **23**
4.1 The Large Hadron Collider . . . 23
4.1.1 Accelerator Complex . . . 24
4.2 Beam conditions . . . 25
4.3 Overview of the ATLAS detector . . . 27
4.3.1 Coordinate system . . . 29
4.4 Inner detector . . . 30
4.4.1 Pixel detector . . . 30

4.4.2 SemiConductor Tracker . . . 32
4.4.3 Transition Radiation Tracker . . . 32
4.5 Calorimeters . . . 33
4.5.1 Electromagnetic calorimeter . . . 33
4.5.2 Hadronic calorimeter . . . 34
4.5.3 Clustering . . . 35
4.6 Muon System . . . 35
4.7 The trigger system . . . 36
4.7.1 Single electron trigger . . . 38
4.7.2 Single muon trigger . . . 39

5 Analysis strategy **40**

6 Object reconstruction **44**
6.1 Track reconstruction . . . 44
6.2 Primary vertex reconstruction . . . 45
6.3 Muons . . . 45
6.4 Electrons . . . 47
6.5 Jets . . . 47
6.6 b-tagged Jets . . . 50

7 Event selection **52**
7.1 Data samples . . . 52
7.1.1 Collision data . . . 52
7.1.2 Simulated Samples . . . 52
7.1.2.1 $t\bar{t}$ samples . . . 53
7.1.2.2 Single top samples . . . 53
7.1.2.3 Background samples . . . 53
7.1.3 Pileup jet samples . . . 54
7.2 Object definitions . . . 54
7.2.1 Reconstructed objects . . . 54
7.2.2 Truth objects . . . 56
7.2.3 Truth matching . . . 57
7.3 Event selection . . . 57
7.3.1 Cleaning cuts . . . 58
7.3.2 Event yields . . . 58
7.3.3 Reconstructed distributions . . . 58

8 Reconstruction of extra jets **62**
8.1 Matching criteria . . . 62
8.2 Background contributions to extra jets . . . 62
8.2.1 Pileup jets . . . 63

8.2.2 False jets . . . 64
8.3 Reconstruction level distributions . . . 66

9 Correction to particle-level **72**
9.1 Introduction to unfolding . . . 72
9.2 Procedure . . . 72
9.2.1 Binning . . . 73
9.2.2 Unfolding procedure . . . 75
9.2.3 Bias in extra jet distributions due to event selection requirements . . . 76
9.2.3.1 Reconstructed events that fail truth event selection . . . 77
9.2.3.2 Truth events that fail reconstructed event selection . . . 78
9.2.3.3 Event selection correction factors . . . 78
9.3 Validation . . . 84
9.3.1 Closure test . . . 84
9.3.2 Stress test . . . 85

10 Sources of uncertainty **88**
10.1 Detector modeling . . . 88
10.1.1 Nuisance parameters . . . 88
10.1.2 Computation of uncertainty . . . 89
10.2 Single top rate . . . 89
10.3 Pileup and false jet background . . . 91
10.4 Input extra jet spectrum . . . 91
10.5 Statistical uncertainty on migration matrix . . . 92
10.6 PDF modeling uncertainty . . . 92
10.7 Combined uncertainty . . . 92

11 Results **98**
11.1 Fully corrected distributions . . . 98
11.2 χ^2 comparisons and discussion . . . 103

12 Conclusions **105**

A Extra jets **106**
A.1 Truth distributions . . . 106
A.1.1 Kinematic distributions for b- and extra jets at truth level . . . 106
A.1.2 Jet distributions for $t\bar{t}$ events . . . 106
A.2 Unfolding validation . . . 110
A.2.1 Closure test . . . 110
A.3 Optimization of number of iterations for unfolding . . . 114
A.4 Detector level systematics . . . 136
A.4.1 Event counts for nuisance parameters . . . 136

A.5 Truth matching correction 139
A.6 Single top rate 141
A.7 Estimated double parton scattering as a function of minimum jet p_{T} 142

B Generator studies **143**
B.1 Introduction 143
B.2 Monte Carlo Samples 144
B.3 Heavy Flavor Hadron Production Fractions 145
B.4 Heavy Flavor Fragmentation 147
B.5 Heavy Flavor Hadron Decays 156
B.6 Summary 156

Bibliography **166**

List of Figures

2.1 Summary of measurements of α_S as a function of the respective energy scale, Q, from Ref. [4]. The respective degree of QCD perturbation theory used in the extraction of α_S is indicated in brackets (NLO: next-to-leading order; NNLO: next-to-next-to leading order; res. NNLO: NNLO matched with resummed next-to-leading logs; N3LO: next-to-NNLO). 7

2.2 MSTW 2008 NLO PDFs at $Q^2 = 10\text{GeV}^2$ and $Q^2 = 10^4\text{GeV}^2$ [10]. 8

2.3 Diagram from Ref. [8] illustrating the structure of a generic hard scattering process of two incoming partons A and B with PDFs $f_{a/A}$ and $f_{b/B}$. 10

2.4 Summary of the ATLAS direct m_{top} measurements. The results are compared with the ATLAS, Tevatron and Tevatron+LHC m_{top} combinations. For each measurement, the statistical uncertainty, the sum of the remaining uncertainties are reported separately. 11

2.5 Feynman diagrams for $t\bar{t}$ production at leading order QCD 11

2.6 Summary of LHC and Tevatron measurements of the top-pair production cross-section as a function of the centre-of-mass energy compared to the NNLO QCD calculation complemented with NNLL resummation (top++2.0). The theory band represents uncertainties due to renormalisation and factorisation scale, parton density functions and the strong coupling. The measurements and the theory calculation is quoted at m_{top}=172.5 GeV. Measurements made at the same centre-of-mass energy are slightly offset for clarity. 12

2.7 Summary of ATLAS measurements of the single top production cross-sections in various channels as a function of the center of mass energy compared to a theoretical calculation based on NLO QCD complemented with NNLL resummation. For the s-channel only an upper limit is shown. 13

2.8 Feynman diagrams for single top quark production at leading order QCD. From left to right: t-channel production as flavor excitation; t-channel production as W-gluon fusion; s-channel production; Wt-channel production. 13

2.9 Feynman diagrams for top quark decay. On the left, the top quark is shown decaying hadronically. On the right, the top quark is shown decaying leptonically. 14

3.1 Visualization of a top pair event from the SHERPA event generator. The hard scatter is shown in red, the parton shower in blue, the hadronzation in green, the underlying event in purple, and the QED final state radiation in yellow [20]. . . 17
3.2 The input constituents clustered both the k_T(left) and the anti-k_T(right) algorithms [35]. 22

4.1 The location of the four main LHC experiments: ALICE, ATLAS, CMS and LHCb. The LHC tunnel is 27 km in circumference, situated underneath the border of France and Switzerland, near the city of Geneva, as shown [42]. 24
4.2 The LHC accelerator complex boosts particles to increasingly higher energies before reaching the LHC. The particle beams are accelerated successively by Linac 2, the Proton Synchrotron Booster (PSB), the Proton Synchrotron (PS), the Super Proton Synchrotron (SPS) and then finally enter the LHC rings [37]. . 25
4.3 Cumulative luminosity versus time delivered to (green), recorded by ATLAS (yellow), and certified to be good quality data (blue) during stable beams and for pp collisions at 8 TeV center-of-mass energy in 2012. Luminosity can be lost due to data acquisition inefficiency or other effects. 26
4.4 Luminosity-weight distribution of the mean number of interactions per bunch crossing. Both the full data from the 2011 and 2012 *pp* runs at the LHC are shown. 27
4.5 Computer generated illustration of the whole ATLAS detector detector, with various subdetectors highlighted[46]. 28
4.6 A computer-generated image representing how the ATLAS detector functions. The transverse paths of different types of particles are shown interacting with different elements of the detector[47]. 29
4.7 Illustration of the ATLAS coordinate system[48]. 30
4.8 Schematic view of the Inner Detector: an $r-z$ slice of the cylindrical barrel, disc endcaps with support tubes, and the solenoid magnet. Lines of constant η are drawn [39]. 31
4.9 A diagram of the barrel of the Inner Detector: the three layers in the Pixels, the four layers in the SCT, and the many layers of the TRT [39]. 31
4.10 Cut-away view of the ATLAS calorimeter system [39]. 34
4.11 Diagram of an electromagnetic calorimeter barrel module[39]. 35
4.12 Diagram of a hadronic tile module[39]. 35
4.13 Diagram of the muon system[39]. 37
4.14 Schematic view of the calorimeter granularity available at the L1 trigger [51]. . . 38

5.1 Comparison of the truth level extra jet multiplicity and p_{T} distributions in generated $t\bar{t}$ events with an opposite-sign $e\mu$ pair and at least 2 b-jets. Jets are reconstructed using the anti-k_t algorithm with the distance parameter $R = 0.4$. Each simulation is normalized by the number of events passing the truth-level selection. The ratio plots compare each generator to the predictions of the baseline POWHEG+PYTHIA sample with the hdamp parameter set to ∞. 41

6.1 Display of a 2012 event with 25 reconstructed vertices [60]. 45
6.2 Reconstruction and identification efficiency for the muons as a function of p_{T} [62]. 46
6.3 Reconstruction and identification efficiency for the electrons as a function of E_T [62]. 48
6.4 Combined efficiency of the 24 GeV and 60 GeV electron triggers. [52]. 48
6.5 The relative Jet Energy Scale (JES) uncertainty for jets in the region [64]. . . . 49
6.6 Light-jet rejection (left) and c-jet rejection (right) as a function of the b-tag efficiency for the b-tagging algorithms discussed based on simulated $t\bar{t}$ events. [66]. 51

7.1 Distributions of the transverse momentum and η of the electron and muon in events with an opposite sign $e\mu$ pair and at least 2 b-jets in data and simulation. The distributions in data are compared to simulation normalized to data yields (see scale factors in Table 7.2). The ratio of different MC samples to data is shown with error bars corresponding to the MC statistical uncertainty and a shaded band corresponding to the data statistical uncertainty. 60
7.2 Distributions of the transverse momentum and η of the b-jets in events with an opposite sign $e\mu$ pair and at least 2 b-jets in the 2012 data. The distributions in data are compared to simulation, normalized to the same number of events as in the data (see scale factors in Table 7.2).. In events where more than two b-jets are reconstructed, the two highest p_{T} b-jets are selected and the remaining b-jet is classified as an extra jet (see Chapter 8). The ratio of different MC samples to data are shown with error bars corresponding to the MC statistical uncertainty and a shaded band corresponding to the data statistical uncertainty. Systematic uncertainties are not shown. 61

8.1 The η distribution of extra jets in simulation and data. 65
8.2 Mean number of reconstructed jets as a function of $< \mu >$ for jets in the p_T range $25 < p_T < 30$ GeV for (a) central and (b) forward jets in data events passing the e-μ selection before and after correction for pileup. Jets passing the 70% MV1 b-tagging selection are removed. The pileup rate is estimated using the ZeroBiasOverlay data stream. The blue markers show the pileup subtracted rate before correcting for the $< \mu >$-dependent efficiency of the JVF cut. The green points show the results after correction. 66
8.3 Distributions of minimum reconstructed ΔR betweeen extra jets in simulation and data for the the first, second, third and fourth extra jet. 67
8.4 Distributions of ΔR betweeen reconstructed extra jets and the nearest truth jet for the first, second, third and fourth extra jet. 68
8.5 Dependence of the unmatched extra jet rate on μ for the baseline simulation. . . 69

8.6 Distributions of the reconstructed extra jet multiplicity as a function of p_{T} threshold in simulation and data. The distributions in data are compared to $t\bar{t}$ simulation normalized to the same number of events as in the data. Extra jets from pileup are excluded in simulation by requiring a match to truth. Extra pileup jets are subtracted from the data. The ratio of different MC samples to data is shown with error bars corresponding to the MC statistical uncertainty and a shaded band corresponding to the data statistical uncertainty. Systematic uncertainities are not shown. 70
8.7 Distributions of reconstructed extra jet p_{T} in simulation and data. The distributions in data are compared to $t\bar{t}$ simulation normalized to the same number of events as in the data. Backgrounds from single top and extra pileup jets are included as background to $t\bar{t}$. The ratio of different MC samples to data is shown with error bars corresponding to the MC statistical uncertainty and a shaded band corresponding to the data statistical uncertainty. Systematic uncertainities are not shown. 71

9.1 Fraction of reconstructed extra jets with truth matches inside the fiducial region (a) and ratio of alternate generators to the baseline (b). This factor is used to correct the data for p_{T} smearing across the fiducial boundary. 76
9.2 Migration matrix between the truth and reconstructed number of extra jets in each bin (a) and distribution of 'missed' truth jets not matched to reco jets (b). Jets are binned according to both p_{T} value and rank. The matrix is filled from events passing both reconstructed and truth $e\mu$+2-b jet events in the baseline $t\bar{t}$ simulation. 'Missed' jets are handled by the RooUnfold framework. 77
9.3 Distributions of the (a) e p_{T}, (b) b-jet p_{T}, (c) b-jet MV1 weight and (d) extra jet multiplicity. Each distribution is normalized by the number of events falling in that category. Events were simulated with PowHeg+Pythia hdamp=∞ $t\bar{t}$. . 80
9.4 Distributions of the truth (a) $b-$jet p_{T}, (b) extra jet multiplicity, (c) leading extra jet p_{T} and (d) subleading extra jet p_{T}. Each distribution is normalized by the number of events falling in that category. Events were simulated with PowHeg+Pythia hdamp=∞ $t\bar{t}$ and required to pass the fiducial truth $e\mu$+2 b-jet selection. 81
9.5 Distributions of the truth (a) extra jet multiplicity, (b) leading extra jet p_{T}, (c) subleading extra jet p_{T} and (d) subsubleading extra jet p_{T} in bins of the average of the p_{T} of the two truth b-jets used to select the event. Each distribution is normalized by the number of events falling in that bin. Events were simulated with PowHeg+Pythia hdamp=∞ $t\bar{t}$ and required to pass the fiducial truth $e\mu$+2 b-jet selection. 82

9.6 (a) Ratio of unfolded extra jets to truth extra jets different $t\bar{t}$ generators (including a 2.9% contribution from single top). (b) Fractional difference of the correction factorfrom baseline for different generators. Extra jets in events passing reconstructed and truth selection for each generator are added to single top and used to fill a response matrix. Then each generator is unfolded against itself, using all selected reconstructed events. Extra jet truth distributions are made without any reconstruction requirements. Finally, the unfolded distribution is divided by the truth distribution to obtain a correction factor for each bin. . . 83

9.7 (a) Pull distribution and (b) fractional bias for the extra jets from the baseline $t\bar{t}$ simulation unfolded against a matrix filled with the baseline $t\bar{t}$ simulation with all correction factors. The Bayesian unfolding method with 2 iterations is used. One thousand pseudoexperiments, each the size of the events in data, are randomly selected from the sample and unfolded. Each bin of the pull distribution over the pseudoexperiments is fit with a gaussian. The black points show the fitted mean of each bin. A fitted mean of zero shows the unfolding is not signifigantly biased. The blue band shows the fitted σ of each bin. A fitted σ of one shows the unfolding correctly estimates the errors. 86

9.8 Fractional bias distributions for pseudoexperiments from alternative generators unfolded against a matrix filled with the baseline simulation. The truth spectrum of the baseline sample is reweighted to match jet p_{T} and multiplicity spectra of (a) PowHeg+Herwig(b) MadGraph+Pythia,
(c) PowHeg+Pythia hdamp=m_t, and (d) MC@NLO+ Herwig simulation. One thousand pseudoexperiments, each the size of the events in data, are constructed for each generator and unfolded. The Bayesian unfolding method with 2 iterations is used. Each bin of the distribution over the pseudoexperiments is fit with a gaussian. The black points show the fitted mean of each bin and the blue band shows the fitted sigma. 87

10.1 Ratio of reconstructed extra jets spectrum obtained from systematic variations of the 15 JES eigenstate nuisance parameters with respect to that obtained using the nominal parameters. The band shows the uncertainty obtained from the samples with gaussian variation of all nuisance parameters. The upper and lower lines shows uncertainty from the quadratic sum of the independent variations of each nuisance parameter by $\pm 1\sigma$. The distribution of samples values has fitted $\mu = 1$ and σ consistent with the $\pm 1\sigma$ method. 90

10.2 (a) bias and (b) fractional bias distributions PDF variations of MC@NLO+ Herwigunfolded with the nominal MC@NLO+ Herwigmigration matrix. Each bin of the distribution over the pseudoexperiments is fit with a gaussian. The outer product of the bias is used to compute the uncertainty due to the PDF. 93

10.3 Fractional bias distributions for pseudoexperiments from MadGraph+Pythia radiation samples unfolded against a matrix filled with nominal MadGraph+Pythia. The truth spectrum of the baseline sample is reweighted to match jet p_{T} and multiplicity spectra of (a) MadGraph+Pythia RadLo (b) MadGraph+Pythia RadHi simulation. One thousand pseudoexperiments, each the size of the events in data, are constructed for each generator and unfolded. The Bayesian unfolding method with 2 iterations is used. Each bin of the distribution over the pseudoexperiments is fit with a gaussian. The black points show the fitted mean of each bin and the blue band shows the fitted sigma. . . . 94
10.4 Unmatched jets in the baseline $t\bar{t}$ simulation and the hybrid sample. The difference between the two is used to estimate the uncertainty. 95
10.5 Sum of systematic uncertainties due to detector modeling. The ratio of the simulated extra jets reconstructed with each systematic variation is taken with respect to the nominal. The band shows the data statistical uncertainty for reference. . 96
10.6 (a) The covariance matrix associated with the statistical uncertainty of the input spectrum returned from `RooUnfold`. (b) The covariance matrix from all sources of uncertainty, obtained by adding the covariance matrices from all sources of systematic uncertainty to (a). This matrix is used to determine the χ^2 agreement between generators and the fully corrected data. 97

11.1 Distributions of the unfolded p_{T} of extra jets in data and simulation. Each sample is unfolded against a response matrix filled with baseline $t\bar{t}$ +single top simulation. The gray band on the ratio shows the sum of statistical and systematic uncertainties. 99
11.2 Distributions of the number of unfolded extra jets with p_{T} ¿ (a) 25, (b) 30, (c) 40 and (d) 50 GeV in data and simulation. Each sample is unfolded against a response matrix filled with baseline $t\bar{t}$ +single top simulation. The gray band on the ratio shows the sum of statistical and systematic uncertainties. 100
11.3 Distributions of the unfolded p_{T} of extra jets in data and simulation. Each sample is unfolded against a response matrix filled with baseline $t\bar{t}$ +single top simulation. The gray band on the ratio shows the sum of statistical and systematic uncertainties. 101
11.4 Distributions of the unfolded p_{T} of extra jets in data and simulation. Each sample is unfolded against a response matrix filled with baseline $t\bar{t}$ +single top simulation. The gray band on the ratio shows the sum of statistical and systematic uncertainties. 102
11.5 Visual representation of the χ^2 distributions for (a) PowHeg+Pythia hdamp=∞ (b) PowHeg+Pythia8 (c) MadGraph+Pythia and (d) PowHeg+Pythia hdamp=m_t. Each element ij of the matrix is given by $M_{ij} = (N^i_{mc} - N^i_{data})\sigma^{-1}_{ij}(N^j_{mc} - N^j_{data})^j$ where N^i_{mc} is the number of jets predicted in bin i, N^i_{data} is the number of jets in bin i in data, and σ^{-1} is the inverse of the covariance matrix. 104

A.1 Distributions of the truth b-jet (a) p_{T}, (b) b-jet η, (c) extra jet p_{T}, and (d) extra jet η in $t\bar{t}$ simulation.Several alternate physics models are compared to the baseline, each normalized by the number of selected truth events. 107
A.2 Distributions of the number of extra truth jets with $p_{\mathrm{T}} >$ (a) 25, (b) 30, (c) 40 and (d) 50 GeVin $t\bar{t}$ simulation. Several alternate physics models are compared to the baseline, each normalized by the number of selected truth events. 108
A.3 Distributions of the extra truth jet p_{T} in $t\bar{t}$ simulation for jet ranks 1-5 (a-e). Several alternate physics models are compared to the baseline, each normalized by the number of selected truth events. 109
A.4 Pull distributions for the extra jets from the baseline $t\bar{t}$ +Wt simulation unfolded against a matrix filled with the baseline $t\bar{t}$ +Wt simulation . The Bayesian unfolding method 4 iterations is used. One thousand pseudoexperiments, each the size of the events in data, are randomly selected from the sample and unfolded. A Gaussian is fit to the distributions of biases over the pseudoexperiments . . . 111
A.5 Pull distributions for the extra jets from the baseline $t\bar{t}$ +Wt simulation unfolded against a matrix filled with the baseline $t\bar{t}$ +Wt simulation . The Bayesian unfolding method 4 iterations is used. One thousand pseudoexperiments, each the size of the events in data, are randomly selected from the sample and unfolded. A Gaussian is fit to the distributions of biases over the pseudoexperiments. . . . 112
A.6 Pull distributions for the extra jets from the baseline $t\bar{t}$ +Wt simulation unfolded against a matrix filled with the baseline $t\bar{t}$ +Wt simulation . The Bayesian unfolding method 4 iterations is used. One thousand pseudoexperiments, each the size of the events in data, are randomly selected from the sample and unfolded. A Gaussian is fit to the distributions of biases over the pseudoexperiments . . . 113
A.7 Bias distribution for pseudoexperiments constructed from PowHeg+Herwig simulation unfolded against a matrix filled with the baseline simulation. One thousand pseudoexperiments, each the size of the events in data, are selected from the sample and unfolded. The Bayesian unfolding method with various numbers of iterations is used. Each bin of the distribution over the pseudoexperiments is fit with a gaussian. The black points show the fitted mean of each bin and the blue band shows the fitted sigma. 116
A.8 Bias distribution for pseudoexperiments constructed from PowHeg+Pythia hdamp=m_t simulation unfolded against a matrix filled with the baseline simulation. One thousand pseudoexperiments, each the size of the events in data, are selected from the sample and unfolded. The Bayesian unfolding method with various numbers of iterations is used. Each bin of the distribution over the pseudoexperiments is fit with a gaussian. The black points show the fitted mean of each bin and the blue band shows the fitted sigma. 117

A.9 Bias distribution for pseudoexperiments constructed from MadGraph+Pythia simulation unfolded against a matrix filled with the baseline simulation. One thousand pseudoexperiments, each the size of the events in data, are selected from the sample and unfolded. The Bayesian unfolding method with various numbers of iterations is used. Each bin of the distribution over the pseudoexperiments is fit with a gaussian. The black points show the fitted mean of each bin and the blue band shows the fitted sigma. 118
A.10 Bias distribution for pseudoexperiments constructed from PowHeg+Pythia hdamp=∞ fullsim simulation unfolded against a matrix filled with the baseline simulation. One thousand pseudoexperiments, each the size of the events in data, are selected from the sample and unfolded. The Bayesian unfolding method with various numbers of iterations is used. Each bin of the distribution over the pseudoexperiments is fit with a gaussian. The black points show the fitted mean of each bin and the blue band shows the fitted sigma. . . . 119
A.11 Bias distribution for pseudoexperiments constructed from MC@NLO+ Herwig simulation unfolded against a matrix filled with the baseline simulation. One thousand pseudoexperiments, each the size of the events in data, are selected from the sample and unfolded. The Bayesian unfolding method with various numbers of iterations is used. Each bin of the distribution over the pseudoexperiments is fit with a gaussian. The black points show the fitted mean of each bin and the blue band shows the fitted sigma. 120
A.12 Fractional bias distribution for pseudoexperiments constructed from PowHeg+Herwig simulation unfolded against a matrix filled with the baseline simulation. One thousand pseudoexperiments, each the size of the events in data, are selected from the sample and unfolded. The Bayesian unfolding method with various numbers of iterations is used. Each bin of the distribution over the pseudoexperiments is fit with a gaussian. The black points show the fitted mean of each bin and the blue band shows the fitted sigma. 121
A.13 Fractional bias distribution for pseudoexperiments constructed from PowHeg+Pythia hdamp=m_t simulation unfolded against a matrix filled with the baseline simulation. One thousand pseudoexperiments, each the size of the events in data, are selected from the sample and unfolded. The Bayesian unfolding method with various numbers of iterations is used. Each bin of the distribution over the pseudoexperiments is fit with a gaussian. The black points show the fitted mean of each bin and the blue band shows the fitted sigma. 122
A.14 Fractional bias distribution for pseudoexperiments constructed from MadGraph+Pythia simulation unfolded against a matrix filled with the baseline simulation. One thousand pseudoexperiments, each the size of the events in data, are selected from the sample and unfolded. The Bayesian unfolding method with various numbers of iterations is used. Each bin of the distribution over the pseudoexperiments is fit with a gaussian. The black points show the fitted mean of each bin and the blue band shows the fitted sigma. 123

A.15 Fractional bias distribution for pseudoexperiments constructed from PowHeg+Pythia hdamp=∞ fullsim simulation unfolded against a matrix filled with the baseline simulation. One thousand pseudoexperiments, each the size of the events in data, are selected from the sample and unfolded. The Bayesian unfolding method with various numbers of iterations is used. Each bin of the distribution over the pseudoexperiments is fit with a gaussian. The black points show the fitted mean of each bin and the blue band shows the fitted sigma. . . . 124
A.16 Fractional bias distribution for pseudoexperiments constructed from MC@NLO+ Herwig simulation unfolded against a matrix filled with the baseline simulation. One thousand pseudoexperiments, each the size of the events in data, are selected from the sample and unfolded. The Bayesian unfolding method with various numbers of iterations is used. Each bin of the distribution over the pseudoexperiments is fit with a gaussian. The black points show the fitted mean of each bin and the blue band shows the fitted sigma. 125
A.17 Pull distribution for pseudoexperiments constructed from PowHeg+Herwig simulation unfolded against a matrix filled with the baseline simulation. One thousand pseudoexperiments, each the size of the events in data, are selected from the sample and unfolded. The Bayesian unfolding method with various numbers of iterations is used. Each bin of the distribution over the pseudoexperiments is fit with a gaussian. The black points show the fitted mean of each bin and the blue band shows the fitted sigma. 126
A.18 Pull distribution for pseudoexperiments constructed from PowHeg+Pythia hdamp=m_t simulation unfolded against a matrix filled with the baseline simulation. One thousand pseudoexperiments, each the size of the events in data, are selected from the sample and unfolded. The Bayesian unfolding method with various numbers of iterations is used. Each bin of the distribution over the pseudoexperiments is fit with a gaussian. The black points show the fitted mean of each bin and the blue band shows the fitted sigma. 127
A.19 Pull distribution for pseudoexperiments constructed from PowHeg+Pythia8 simulation unfolded against a matrix filled with the baseline simulation. One thousand pseudoexperiments, each the size of the events in data, are selected from the sample and unfolded. The Bayesian unfolding method with various numbers of iterations is used. Each bin of the distribution over the pseudoexperiments is fit with a gaussian. The black points show the fitted mean of each bin and the blue band shows the fitted sigma. 128

A.20 Pull distribution for pseudoexperiments constructed from PowHeg+Pythia hdamp=∞ fullsim simulation unfolded against a matrix filled with the baseline simulation. One thousand pseudoexperiments, each the size of the events in data, are selected from the sample and unfolded. The Bayesian unfolding method with various numbers of iterations is used. Each bin of the distribution over the pseudoexperiments is fit with a gaussian. The black points show the fitted mean of each bin and the blue band shows the fitted sigma. 129
A.21 Bias distribution for pseudoexperiments constructed from MC@NLO+ Herwig simulation unfolded against a matrix filled with the baseline simulation. One thousand pseudoexperiments, each the size of the events in data, are selected from the sample and unfolded. The Bayesian unfolding method with various numbers of iterations is used. Each bin of the distribution over the pseudoexperiments is fit with a gaussian. The black points show the fitted mean of each bin and the blue band shows the fitted sigma. 130
A.22 The χ^2 of extra jets from the each $t\bar{t}$ simulation unfolded against a matrix filled with the same baseline $t\bar{t}$ simulation (PowHeg+Pythia hdamp=∞). All samples are atlfast. The same 3% contribution from Wt is included in both the migration matrix and the unfolding. The Bayesian unfolding method is used with iterations ranging from 1 to 10. One thousand pseudoexperiments, each the size of the events in data, are randomly selected from the sample and unfolded. The $\chi^2$is calculated according to Equation 9.6. The χ^2 in compares the fully corrected reco jets to truth jets in truth events. 135
A.23 The systematic uncertainty on the unfolded spectrum due uncertainties in the Wt atio of N^{unfolded} over N^{true} jets per GeVfor events from $t\bar{t}$ +single top simulation. The response matrix is filled with the 97.1% $t\bar{t}$ events and nominal 2.9% single top events. The rate of single top is then varied and unfolded against the nominal matrix. 141

B.1 Comparison of the production fractions for various weakly decaying (a) bottom and (b) charm hadrons in Pythia8, Pythia6, Herwig++ and Herwig. The Σ_b should not decay weakly, but some weak decays of the Σ_b are observed in Herwig. 147
B.2 The b-quark fragmentation function obtained with Pythia8, Pythia6, Herwig++ and Herwig for (a) $\sqrt{s} = 91.2$ GeV and (b) $\sqrt{s} = 200$ GeV $e + e-$ collisions. DELPHI and SLD data in (a) are taken from References [128] and [129] respectively and are plotted without error bars. 150
B.3 The c-quark fragmentation function obtained with Pythia8, Pythia6, Herwig++ and Herwig for $\sqrt{s} = 10.53$ GeV for $e + e-$ collisions for (a) D^+ and (b) D^0 mesons. CLEO and Belle data are taken from References [131] and [130] respectively and are plotted without error bars. 151
B.4 The fragmentation function for for the parton shower, hadronization and underlying event modeling. 151

B.5 The jet width for (a) b-jets and (b) c-jets in POWHEG $t\bar{t}$ samples where Pythia8, PYTHIA6, Herwig++ and HERWIG have been used for the parton shower, hadronization and underlying event modeling. 152
B.6 The differential jet shape $\rho(r)$ distribution for (a) b-jets and (b) c-jets in POWHEG $t\bar{t}$ samples where Pythia8, PYTHIA6, Herwig++ and HERWIG have been used for the parton shower, hadronization and underlying event modeling. 152
B.7 The integral jet shape $\Psi(r, R = 0.4) \equiv \Sigma p_T(0, r) \sum p_T(0, R)$ distribution for (a) b-jets and (b) c-jets in POWHEG $t\bar{t}$ samples where Pythia8, PYTHIA6, Herwig++ and HERWIG have been used for the parton shower, hadronization and underlying event modeling. The legend includes the value and error of the mean of each distribution. 153
B.8 The p_T^{jet} distribution for (a) b-jets and (b) c-jets in POWHEG $t\bar{t}$ samples where Pythia8, PYTHIA6, Herwig++ and HERWIG have been used for the parton shower, hadronization and underlying event modeling. 153
B.9 The p_T^{hadron} distribution for (a) b-jets and (b) c-jets in POWHEG $t\bar{t}$ samples where Pythia8, PYTHIA6, Herwig++ and HERWIG have been used for the parton shower, hadronization and underlying event modeling. 154
B.10 The fragmentation function for (a) b-jets and (b) c-jets in the high p_{T} jet sample and for the subset of (c) b-jets and (d) c-jets containing exactly one heavy flavor hadron. 154
B.11 Comparison of lifetimes of the weakly decaying bottom hadrons (a) B^0, (b) B^+, (c) B_s^0 and (d) Λ_b for four different generators, PYTHIA6 version 427.2, Pythia8 version 175, Herwig++ version 2.6.3 and HERWIG version 6.520.2, both with and without EvtGen. EvtGen version 2.0 is used with the particle properties table provided with EvtGen and with its standard inclusive decay table DECAY_2010.DEC. The value of the B_s^0 lifetime in this default EvtGen particle properties table differs from the world average listed by the PDG [111]. 158
B.12 Comparison of lifetimes of the weakly decaying charm hadrons (a) D^0, (b) D^+, (c) D_s and (d) Λ_c in four different generators, PYTHIA6 version 427.2, Pythia8 version 175, Herwig++ version 2.6.3 and HERWIG version 6.520.2, both with and without EvtGen. EvtGen version 2.0 is used with the particle properties table provided with EvtGen and with its standard inclusive decay table DECAY_2010.DEC. 159

B.13 Comparison of semileptonic branching fraction $B \to e^-\overline{\nu_e}X$ of the weakly decaying bottom hadrons (a) B^0, (b) B^+, (c) B_s^0 and (d) Λ_b in four different generators, PYTHIA6 version 427.2, Pythia8 version 175, Herwig++ version 2.6.3 and HERWIG version 6.520.2, both with and without EvtGen. EvtGen version 2.0 is used with the particle properties table provided with EvtGen and with its standard inclusive decay table DECAY_2010.DEC, as well as a custom decay table with developed for ATLAS with the most up to date semileptonic fractions from the PDG. Only decays where the electron is the direct decay product of the bottom hadron are included here (e.g. electrons coming from charm or τ decays are excluded). The band shown for the world average branching fractions correspond to the measured decay fraction for $B \to e\nu X_c$ listed by the PDG[111]. The values of the B^0, B^+ and Λ_b^0 semileptonic fractions in the default EvtGen particle properties table have been tuned to the observed inclusive $B \to D\ell\nu +$ anything branching fraction, which has a larger uncertainty. 160
B.14 Comparison of semileptonic branching fraction $D \to e^-\overline{\nu_e}X$ of the weakly decaying charm hadrons (a) D^0, (b) D^+, (c) D_s and (d) Λ_c in four different generators, PYTHIA6 version 427.2, Pythia8 version 175, Herwig++ version 2.6.3 and HERWIG version 6.520.2, both with and without EvtGen. EvtGen version 2.0 is used with the particle properties table provided with EvtGen and with its standard inclusive decay table DECAY_2010.DEC, as well as a custom decay table with developed for ATLAS with the most up to date semileptonic fractions from the PDG. Only decays where the electron is the direct decay product of the charm are included. The values of the D^0, D^+, D_s^+ and Λ_c^+ semileptonic fractions in this default EvtGen particle properties table differ from the world averages listed by the PDG [111]. 161
B.15 Comparison of the multiplicity of charged, stable decay products for the weakly decaying bottom hadrons (a) B_0, (b) B^+, (c) B_s^0 and (d) Λ_b in Pythia8 PYTHIA6 Herwig++ HERWIG and EvtGen. A stable particle is defined as a particle with a proper lifetime $c\tau_0 > 10$ mm. 162
B.16 Comparison of multiplicity of charged, stable decay products for the weakly decaying charm hadrons (a) D^0, (b) D^+, (c) D_s and (d) Λ_c in Pythia8 PYTHIA6 Herwig++ HERWIG and EvtGen. A stable particle is defined as a particle with a proper lifetime $c\tau_0 > 10$ mm. 163
B.17 Comparison of the multiplicity of stable decay products for the weakly decaying bottom hadrons (a) B^0, (b) B^+, (c) B_s^0 and (d) Λ_b in Pythia8 PYTHIA6 Herwig++ HERWIG and EvtGen. A stable particle is defined as a particle with a proper lifetime $c\tau_0 > 10$ mm. 164
B.18 Comparison of the multiplicity of stable decay products for the weakly decaying charm hadrons (a) D^0, (b) D^+, (c) D_s and (d) Λ_c in Pythia8 PYTHIA6 Herwig++ HERWIG and EvtGen. A stable particle is defined as a particle with a proper lifetime $c\tau_0 > 10$ mm. 165

List of Tables

2.1 Spin and charge of particles in the SM. 4
2.2 Mass of particles in the SM, taken from Ref. [4]. 5

7.1 Number of events with opposite sign $e\mu$ and at least 2 b-jets in the data compared to that from Monte Carlo, broken down into contributions from $t\bar{t}$, Wt single top, Z+jets and dibosons. Only central values are shown here; systematic uncertainties are discussed in Chapter 10. 59
7.2 Number of events with an opposite sign $e\mu$ and at least 2 b-jets for different $t\bar{t}$ generators. The last column gives scale factor to normalize the sum of the $t\bar{t}$ simulatation and single top yields ($N_{\text{single top}} = 361.4$) to the data yield (12332). 59

9.1 Binning for unfolding of extra jets. Jets are binned simultaneously in both rank (p_{T} order) and p_{T}. For each jet rank, variable sized p_{T} bins are chosen so that at least 10 data events fall in each bin. The first bin in p_{T} for each rank is treated as underflow bins. These bins are not reported as part of the measurement. . . . 74
9.2 Number of events passing different combinations of truth and reconstructed selection requirements. 79
9.3 Number of selected reconstructed events that fail truth selection categorized by reason they have failed. The selections are applied sequentially in the order listed in the table. 79
9.4 Number of truth events that fail reconstruction selection categorized by reason they have failed. The selections are applied sequentially in the order listed in the table. 79

11.1 χ^2 between extra jet p_{T} spectra in fully corrected data and different generators. The first column represents the agreement including only (diagonal) statistical uncertainties. The second column also includes the covariance due to systematic uncertainties (primarily JES). 103

A.1 Comparison of the average bias per bin for stress tests with several different ttbar generators and unfolding methods. All samples are atlfast. For each generator, the measured jets from one thousand pseudoexperiments are unfolded against the baseline PowHeg+Pythia hdamp=∞ atlfast response matrix and compared to the input truth spectrum. 131
A.2 Comparison of the average bias squared per bin for stress tests with several different ttbar generators and unfolding methods. All samples are atlfast. For each generator, the measured jets from one thousand pseudoexperiments are unfolded against the baseline PowHeg+Pythia hdamp=∞ atlfast response matrix and compared to the input truth spectrum. 132
A.3 Comparison of the average returned bin error for stress tests with several different ttbar generators and unfolding methods. All samples are atlfast. For each generator, the measured jets from one thousand pseudoexperiments are unfolded against the baseline PowHeg+Pythia hdamp=∞ atlfast response matrix and compared to the input truth spectrum. 133
A.4 The χ^2 of extra jets from the each $t\bar{t}$ simulation unfolded against a matrix filled with the same baseline $t\bar{t}$ simulation (PowHeg+Pythia hdamp=∞). All samples are atlfast. The same 3% contribution from Wt is included in both the migration matrix and the unfolding. The Bayesian unfolding method is used with iterations ranging from 1 to 10. One thousand pseudoexperiments, each the size of the events in data, are randomly selected from the sample and unfolded. The $\chi^2$is calculated according to Equation 9.6. The χ^2 in compares the fully corrected reco jets to truth jets in truth events. 134
A.5 Number of selected events for various detector-modeling nuisance parameters. Events are siumlated with PowHeg+Pythia$t\bar{t}$ hdamp= ∞ simulation and compared to the nominal number, including scale factor event weights. 136
A.6 Bin-by-bin correction factors applied to the unfolded extra jet p_{T} distribution . . 139

B.1 Percentage probability that a bottom quark decays to a bottom hadron of a given species for Pythia8, Pythia6, Herwig++, Herwig and for the world average from Reference [111]. 146
B.2 Percentage probability that a charm quark fragments to a charmed hadron of a given species for Pythia8, Pythia6, Herwig++, Herwig and for the world average from Reference [127]. 147
B.3 The mean b-quark fragmentation function obtained with Pythia8, Pythia6, Herwig++ and Herwig for $\sqrt{s}$ = 91.2 GeV in $e + e-$ collisions. DELPHI and SLD data in (a) are taken from References [128] and [129] respectively. 150
B.4 The mean c-quark fragmentation function obtained with Pythia8, Pythia6, Herwig++ and Herwig for $\sqrt{s}$ = 10.53 GeV for $e + e-$ collisions for (a) D^+ and (b) D^0 mesons. CLEO and Belle data are taken from References [131] and [130] respectively. 150

B.5 The mean fragmentation function for b-jets and c-jets in POWHEG $t\bar{t}$ samples where Pythia8, PYTHIA6, Herwig++ and HERWIG have been used for the parton shower, hadronization and underlying event modeling. 152
B.6 The mean fragmentation function for (a) b-jets and c-jets in the high p_{T} jet sample and for the subset of (b) b-jets and c-jets satisfying the additional requirement that there be no other weakly decaying heavy flavor hadron with $p_{\mathrm{T}} > 5.0$ GeV within a cone $\Delta R = 1$ of the jet. 153
B.7 Mean number of charged, stable decay products for the weakly decaying bottom and charm hadrons species in Pythia8 PYTHIA6 Herwig++ HERWIG and EvtGen. A stable particle is defined as a particle with a proper lifetime $c\tau_0 > 10$ mm. 157
B.8 Mean number of stable decay products for the weakly decaying bottom and charm hadrons species in Pythia8 PYTHIA6 Herwig++ HERWIG and EvtGen. A stable particle is defined as a particle with a proper lifetime $c\tau_0 > 10$ mm. 157

Acknowledgments

This thesis would not have been possible without the support of a great many people.

Marjorie Shapiro is the best advisor I could have had. Not only is she a formidable scientist, but also one of the kindest and most empathetic people I've met. Her generosity and support made graduate school a great experience for me.

The ATLAS LBNL group was a great place to do my graduate work. The postdocs and other graduate students were great sources of knowledge throughout my research.

My amazing friends provided years of support through my journey. You know who you are and what you did. I certainly couldn't have made it without you.

Thanks to Pam Seifert for giving me my beautiful goat, Yoko. I hope to grow up to be half the woman that she is.

Finally, it goes without saying that I wouldn't be here without my family.

Chapter 1

Introduction

The Standard Model (SM) of particle physics has been very successful at describing the interactions of fundamental particles. With the discovery of the Higgs boson, the SM is complete and may be the correct theory up to the energy scale of gravity. The Large Hadron Collider (LHC) was built in order to probe the SM and look for solutions to some of the unknown issues in particle physics that may involve physics beyond the SM.

Despite the overwhelming success of the SM, some uncertainty remains in predictions in the Quantum Chromodynamics (QCD) sector. Due to its non-pertubative nature, QCD has not been as precisely measured as other parts of the SM. In particular, since the top quark was only discovered in the late 1990s, its decays and properties have not been as studied as thoroughly.

The top quark plays a special role in the SM and in searches for physics beyond the SM . Its large mass means its coupling to the Higgs Boson is large. This high mass, together with the presence of charged leptons, missing energy and b-jets as top decay products, make the top a primary source of background in many searches for new physics. For these reasons, accurate modeling of the properties of top quark events is an important part of the LHC program.

The inclusive top quark pair cross-section was measured using the exact same events as this thesis in Ref. [1]. This thesis builds upon this work by studying the production of jets in these events, which provides additional information about the production of QCD radiation in association with top quarks. The data are fully corrected to allow for direct comparisons to predictions by theoretical models. This will allow for improved agreement of future QCD predictions with LHC data.

This thesis is structured as follows. Chapter 2 reviews the SM and theoretical predictions for top quarks. Chapter 3 outlines simulation techniques and jet algorithms necessary for modeling of hadron collisions. Chapter 4 gives an overview of the ATLAS experiment. Chapter 5 describes the motivation and overall strategy for the thesis. Chapter 6 explains the procedures used to reconstruct physics objects. Chapter 7 outlines the data samples used and gives the requirements for selecting events. Chapter 8 describes the definition for extra jets and compares the simulation predictions to the data. Chapter 9 gives the unfolding

procedure used to correct the data for experimental biases. Chapter 10 outlines the sources and evaluation of systematic uncertainty. Chapter 11 presents the fully corrected results with comparisons between simulation and data.

Chapter 2

Theory

This chapter reviews some of the theoretical concepts relevant to the subsequent physics thesis. Aspects of the SM relevant to this analysis are introduced. The importance of the top quark within the SM is then discussed. Then, predictions for the production properties of top quarks at the LHC are reviewed.

2.1 The Standard Model

The SM of particle physics is one of the most precisely tested and successful theories in the history of physics [2]. The theory represents the best current understanding of the fundamental behavior of subatomic particles and provides the framework for particle physics predictions. Most predictions of the SM have been verified and found to be self-consistent up to the Planck scale (10^{15-19} GeV). A thorough treatment of the theoretical framework can be found in textbooks such as Refs. [2, 3, 4].

The SM uses the mathematical framework of Quantum Field Theory (QFT) to describe two kinds of particles, fermions and bosons. Fundamental interactions between these particles can be derived from the conservation of a symmetry called gauge invariance. This general principle maps conserved quantities to the invariance of the Lagrangian under some transformation, an example of Noether's theorem. The SM provides a unified description of the strong, weak and electromagnetic forces, but does not (yet) include gravity. The symmetry group of the SM is $SU(3) \times SU(2) \times U(1)$.

2.1.1 Particles of the SM

Tables 2.1-2.2 summarize the properties of the fundamental particles of the SM described below.

Fermions are spin-$\frac{1}{2}$ point-like particles that form ordinary matter. The two types of fermions are known as leptons and quarks. The three lepton generations, each with a charged lepton and a neutrino, interact via the electroweak force. The three quark generations, each

	particles			spin	electric charge
Quarks	$(u,d)_L$	$(c,s)_L$	$(t,b)_L$	$(\frac{1}{2},\frac{1}{2})$	$(+\frac{2}{3},-\frac{1}{3})$
	u_R	c_R	t_R	$\frac{1}{2}$	$+\frac{2}{3}$
	d_R	s_R	b_R	$\frac{1}{2}$	$-\frac{1}{3}$
Leptons	$(\nu_e,e^-)_L$	$(\nu_\mu,\mu^-)_L$	$(\nu_\tau,\tau^-)_L$	$(\frac{1}{2},\frac{1}{2})$	(0,-1)
	e^-_R	μ^-_R	τ^-_R	$\frac{1}{2}$	-1
Gauge bosons	g			1	0
	$W^\pm$ and Z			1	±1 and 0
	γ			1	0
Scalar boson	H			0	0

Table 2.1: Spin and charge of particles in the SM.

with an up-type and down-type quark, interact via both the electroweak force and the strong force. The strong force combines quarks into composite particles. Three such quarks form a baryon, while two quarks form a meson. Each fermionic generation is identical to the first, except for mass.

Bosons are fundamental particles with integer spin that mediate interactions between particles. Observed elementary bosons are all gauge bosons, except for the Higgs.

Electromagnetic (EM) force mediated by the massless and chargeless photon (γ). Since the photon is massless, the range of the EM force is infinite. The EM force is responsible for many common interactions, such as radiation of photons from excited atoms.

Weak force mediated by the $W^\pm$ and Z^0 bosons and is responsible for nuclear reactions such as beta decay .

Strong force mediated by gluons (g) is responsible for the formation of protons and neutrons. The strong force mediates interactions between quarks and hadrons.

Discovered in 2012 [6], the Higgs boson is the final particle in the SM. The Higgs field interacts with the electroweak gauge bosons to provide masses while preserving the local gauge invariance of the SM. At low energy, the EM and weak forces appear distinct. Above the unification energy ($\sim$ 100GeV), the EM and weak forces are unified into a single interaction known as the electroweak interaction.

2.1.2 Quantum chromodynamics

Quantum chromodynamics (QCD) is a gauge theory describing interactions of quarks and gluons via the strong force. The six flavors of quarks are u, d, s, c, b and t. Quarks and gluons carry a conserved quantum number called color, which is analogous to electric charge

	Particle	Mass
Leptons	e	0.511 MeV
	μ	105 MeV
	τ	1777 MeV
Gauge bosons	$W^{\pm}$	80.2 GeV
	Z	91.19 GeV
	H	126 GeV
Quarks	up (u)	1.7-3.3 MeV
	down (d)	4.1-5.8 MeV
	charm (c)	1.18-1.34 GeV
	strange (s)	70-120 MeV
	top (t)	173.34 ± 0.76 GeV[5]
	bottom (b)	4.18 ± 0.03 GeV
Hadrons	p	938 MeV
	n	939 MeV
	$\pi^{\pm}$	139.6 MeV
	π^0	135.0 MeV

Table 2.2: Mass of particles in the SM, taken from Ref. [4].

in QED. Neither quarks nor gluons can exist as free particles. Instead, color-neutral combinations of quarks, anti-quarks and gluons called hadrons are observed. The quark and gluon constituents of a hadron are traditionally called partons.

The QCD Lagrangian for the interaction between two quarks i and j can be written as [4]:

$$\mathcal{L}_{QCD} = \bar{\psi}_i(i\gamma^\mu \partial_\mu \delta_{ij} - g_s \gamma^\mu t^C_{ij} \mathcal{A}^C_\mu - m\delta_{ij})\psi_j - \frac{1}{4} G^A_{\mu\nu} G^{\mu\nu}_A, \tag{2.1}$$

$$\text{where } G^A_{\mu\nu} \equiv \partial_\mu \mathcal{A}^A_\nu - \partial_\nu \mathcal{A}^A_\mu - g_s f_{ABC} \mathcal{A}^B_\mu \mathcal{A}^C_\nu, \tag{2.2}$$

where repeated indices are summed over, γ^μ are the Dirac γ matrices. ψ_i is the quark-field spinor, where the color index i can correspond to one of three (N_C) quark flavors. $\mathcal{A}^B_\mu$ represents the gluon fields, where C runs from 1 to $N_C^2 - 1 = 8$, corresponding to eight types of gluons. The eight 3×3 generating matrices of $SU(3)$ are labeled as t^A and f_{ABC} the group structure constants of $SU(3)$. The fundamental parameters are the coupling g_s and the quark masses m.

The structure of the Lagrangian predicts three types of vertices: a quark-antiquark-gluon ($q\bar{q}g$) vertex proportional to g_s, a three gluon vertex proportional to g_s, and a four gluon vertex proportional to g_s^2. Since gluons carry color charge, they can directly couple to other gluons.

2.1.2.1 Running of the coupling

In the context of perturbative QCD, *order* refers to the degree of α_S used in the calulation: leading order (LO), next-to-leading order (NLO)next-to-next-to leading order (NNLO), etc. Pertubative QCD calculations at NLO and beyond necessarily involve these divergent quark and gluon loops. These divergences must be removed in order to obtain a physical result. In order to remove the divergences, the strong coupling constant must be "renormalized" and expressed as a function of an (unphysical) renormalization scale μ_R. If a calculation could be carried out to full order, there would be no μ_R dependence, so the the μ_R dependence indicates uncertainty from higher order corrections. Pertubative QCD predictions change depending on the scale of the probe. This is sometimes referred to as the "running" of the coupling constant. Predictions for a given process are evaluated with μ_R as close to the momentum transfer Q as possible, so that $\alpha_s(\mu_R \simeq Q)$ gives the effective strength of the strong force in that particular process.

The strong coupling constant $\alpha_S \equiv g_s^2/4\pi$ is related the renormalization scale μ_R by the renormalization group equation (RGE):

$$\mu_R^2 \frac{\alpha_S}{\mu_R^2} = \beta\left(\alpha_S\right) = -\left(b_0\alpha_S^2 + b_1\alpha_S^3 + b_2\alpha_S^4 + \cdots\right) \tag{2.3}$$

where the coefficients b are called the beta-function coefficients and depend on the number of quark colors. The values of the beta coefficients up to b_3 can be found in Ref. [7].

Figure 2.1 shows the NLO QCD prediction for α_S as a function of Q, as well as several experimentally measured values of α_S for discrete energy scales. While the value of α_S cannot be predicted, its dependence on Q can. Experimental measurement of the scale dependence agrees well with the theoretical predictions. The negative sign on the right side of Eqn.2.3 means that the strong coupling becomes weaker as the scale increases: $\alpha_S \sim 0.1$ for momentum transfers 100 GeV $\lesssim Q \lesssim$ 1 TeV. This running is the origin of *asymptomic freedom*, which allows partons to be considered approximately free at high energy. The divergence of the coupling constant at low energy results in the formation of stable hadrons and is called *confinement.*

2.1.2.2 Parton distribution functions

In high energy scattering, the proton cannot be modeled as three free non-interacting quarks in a bag; the internal partonic structure of the proton must be considered [4, 8]. The three *valence* quarks exist in a sea of virtual quark-antiquark pairs that arise from the gluons holding the quarks together. All of these partons contribute to the internal structure of the proton. The proton can be modeled as a collection of these partons that are each carrying a fraction x of the proton's momentum. The *Parton Distribution Function* (PDF) describes the internal proton structure via normalized momentum distribution functions of the constituent partons

Since the PDFs deal with the non-perturbative regime of QCD, PDFs must be determined by global fits to experimental measurements of deep inelastic and other hard-scattering

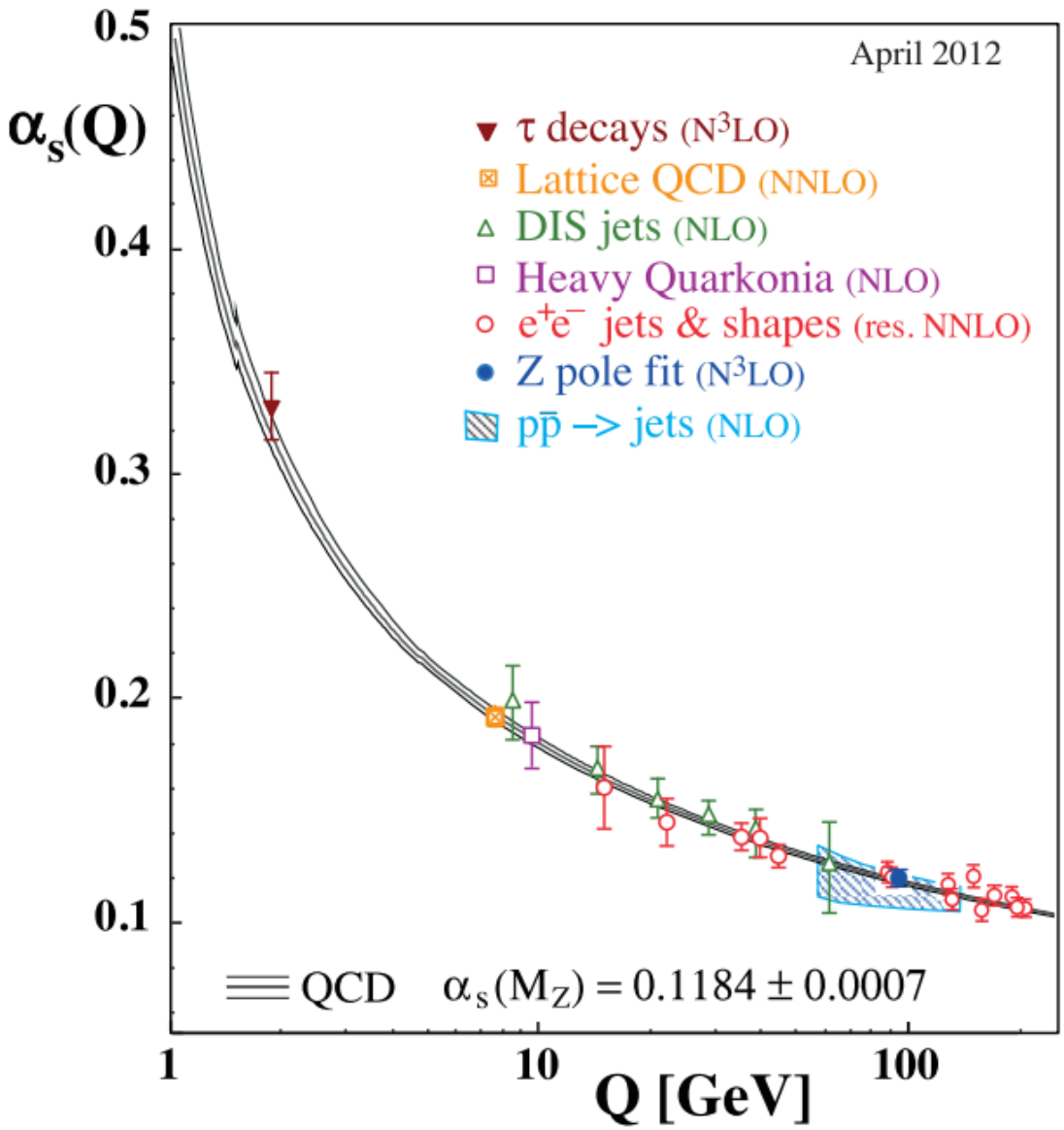

Figure 2.1: Summary of measurements of α_S as a function of the respective energy scale, Q, from Ref. [4]. The respective degree of QCD perturbation theory used in the extraction of α_S is indicated in brackets (NLO: next-to-leading order; NNLO: next-to-next-to leading order; res. NNLO: NNLO matched with resummed next-to-leading logs; N3LO: next-to-NNLO).

processes. PDFs derived from measurements of one process can be used for predictions in a different process. For example, positron-proton scattering data from the HERA experiment can be used to make predictions for proton-proton collision at the LHC. One common PDF set used at the LHC, called MSTW, is shown in Figure 2.2.

PDF measurements depend on the scale of the hard probe, so theoretical calculations

are needed to evolve the PDFs between experimental data points. The differential equations governing the μ^2 dependence of the PDFs are called the DGLAP equations and are derived in Ref. [9]. Much like the RGE introduces an arbitrary μ_R, the DGLAP equations introduce a factorization scale μ_F to absorb the divergences from soft parton emissions. To avoid unnaturally large logarithms in the pertubative expansion, μ_F and μ_R are usually assumed to be equal and of the order of the typical momentum scales of the hard scattering process. The theoretical uncertainty from the arbitrary choice of μ_F and μ_R is usually evaluated by repeating the calculation with the scale doubled and halved.

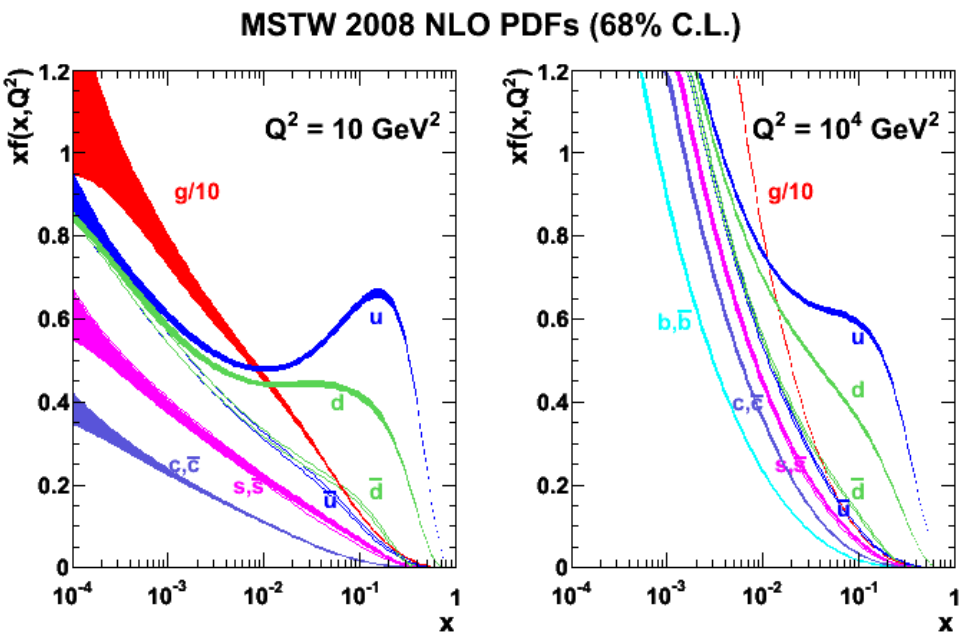

Figure 2.2: MSTW 2008 NLO PDFs at $Q^2 = 10$ GeV^2 and $Q^2 = 10^4$ GeV^2 [10].

2.1.2.3 Factorization

Because of the scale dependence of QCD, interactions can be separated into two regimes, with the transition around the QCD confinement scale, $\Lambda_{QCD} \sim 200$ MeV, the energy at which QCD because non-perturbative. At low energy, α_S is of order unity, so perturbative expansion is not possible. The quarks are bound together by soft gluon exchange into a hadron. At scales far above the QCD confinement scale, the partons can be considered free objects and can be treated with perturbative expansion.

The hard scatter interaction with momentum transfer Q occurs on a time scale that goes as $\tau \sim 1/Q$ which is much smaller than the time scale of interactions between protons $\tau \sim 1/\Lambda_{QCD}$. This fact allows high energy proton collisions to be *factorized* into two independent processes: the PDF, which a phenomelogical description of the momentum distribution

among the partons inside the proton which depends only on the momentum scale, and the partonic cross section $\hat{\sigma}$, which uses perturbative QCD to determine the calculates the scatter of the hard probe from one of the free partons inside the proton.

Specifically, the hadronic cross-section for a particular process can be written the weighting of the subprocess cross section with the PDFs $f_{q/A}(x)$ extracted from deep inelastic scattering experiments[8]:

$$\begin{aligned}\sigma(AB \to X) &= \int dx_a dx_b\, f_{a/A}(x_a, \mu_F^2) f_{b/B}(x_b, \mu_F^2) \hat{\sigma}_{ab\to X} \\ &= \int dx_a dx_b\, f_{a/A}(x_a, \mu_F^2) f_{b/B}(x_b, \mu_F^2) \times [\sigma_0 + \alpha_S(\mu_R^2)\sigma_1 + ...] \end{aligned} \quad (2.4)$$

which is diagramatically represented in Figure 2.3. The partonic cross-section can be pertubatively expanded in powers of the strong coupling constant α_S for some renormalization scale μ_R. The PDF $f_{a/A}(x_a, \mu_F^2)$ gives the probability that a proton with momentum p_A contains a parton a with momentum p_a. This function depends only on the fraction of the proton momentum distributed to parton a, $x_a \equiv p_a/p_A$, and the factorization scale μ_F.

2.2 Top quark physics

The top quark was first discovered at Fermilab in 1995 [11][12]. As the heaviest known fundamental particle, the top quark is an important probe of the SM and extensions of the SM. Before the LHC, the Tevatron provided the only experimental observation of the top. The LHC produces a top quark every few seconds, about a hundred times more frequently than the Tevatron. This signifigant increase in statistics allows precision measurements of the top at the LHC, which is sometimes called a "Top Factory."

Because of its large mass, the top quark plays a special role in the SM. The top mass is about the same as a gold atom nucleus, 40 times larger than the next heaviest quark and 10^5 times heavier than the lightest quark. The mass of the top quark has been precisely measured in different decay channels at both the LHC and the Tevatron. Figure 2.4 shows a recent summary of these measurements, which can be combined to give a world average of 173.34 ± 0.76 for the top quark mass.

The top has a very short lifetime ($\sim 5 \times 10^{-25}$ s), so it is the only quark that decays before it can form a hadron with other quarks. This unique property means that the top is the only "bare" quark that can be accessed experimentally.

2.2.1 Top quark production at the LHC

In pp collisions at the LHC, top quarks are mainly produced in pairs through the QCD processes $gg \to t\bar{t}$ and $q\bar{q} \to t\bar{t}$. The Feynman diagrams for these processes are shown in Figure 2.5. At Tevatron with $p\bar{p}$ collisions, $t\bar{t}$ production was dominated by quark annihilation ($\sim 85\%$). At the LHC, the higher collision energy and lack of valence anti-quarks in the

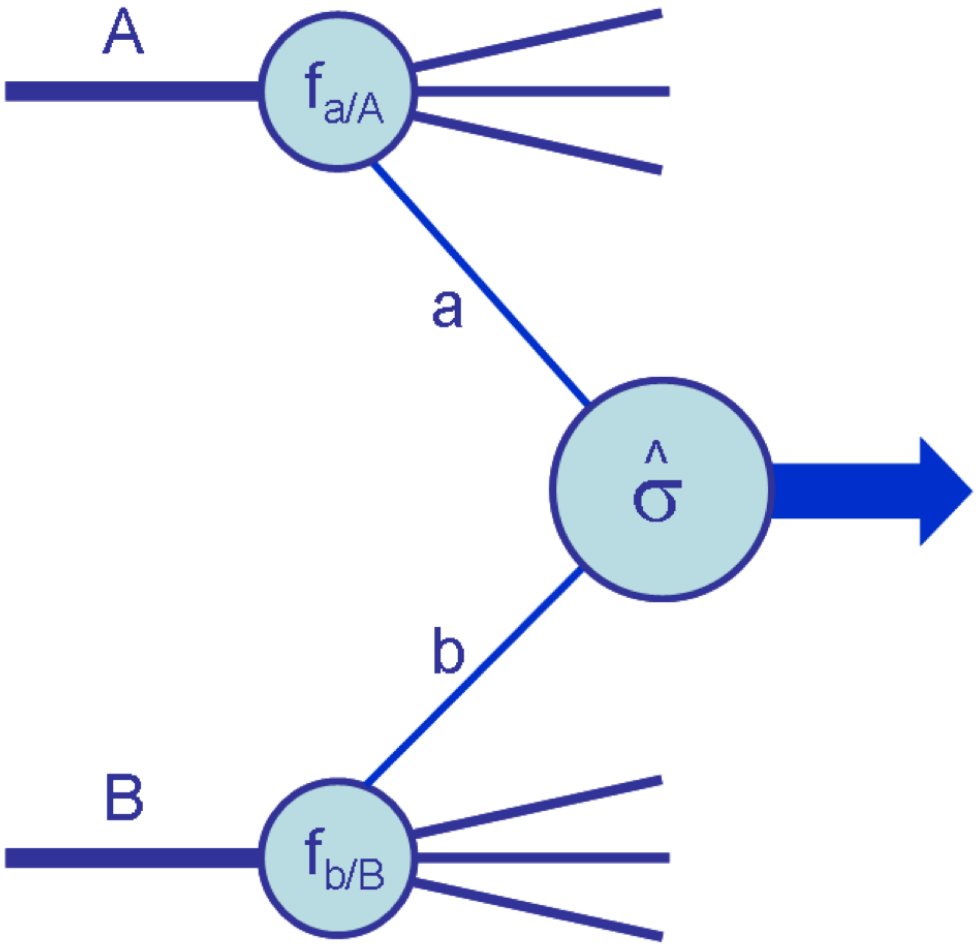

Figure 2.3: Diagram from Ref. [8] illustrating the structure of a generic hard scattering process of two incoming partons A and B with PDFs $f_{a/A}$ and $f_{b/B}$.

proton result in gluon-fusion dominated $t\bar{t}$ production ($\sim 85\%$) [4]. The total $t\bar{t}$ cross-section has been computed at next-to-next-to leading order (NNLO) with next-to-next-to-leading-log soft gluon resummation (NNLL) in Ref. [13] with a final theoretical uncertainty of $\sim 3\%$ and found to agree with experimental measurements. Figure 2.6 compares this calculation with measurements made at both in the LHC and Tevatron in various decay channels.

Top quarks can also be produced singly via electroweak processes. Because the weak coupling is much smaller than the strong coupling, fewer top quarks are produced singly than in pairs. The Feynman diagrams for single top production are shown in Figure 2.8. Single

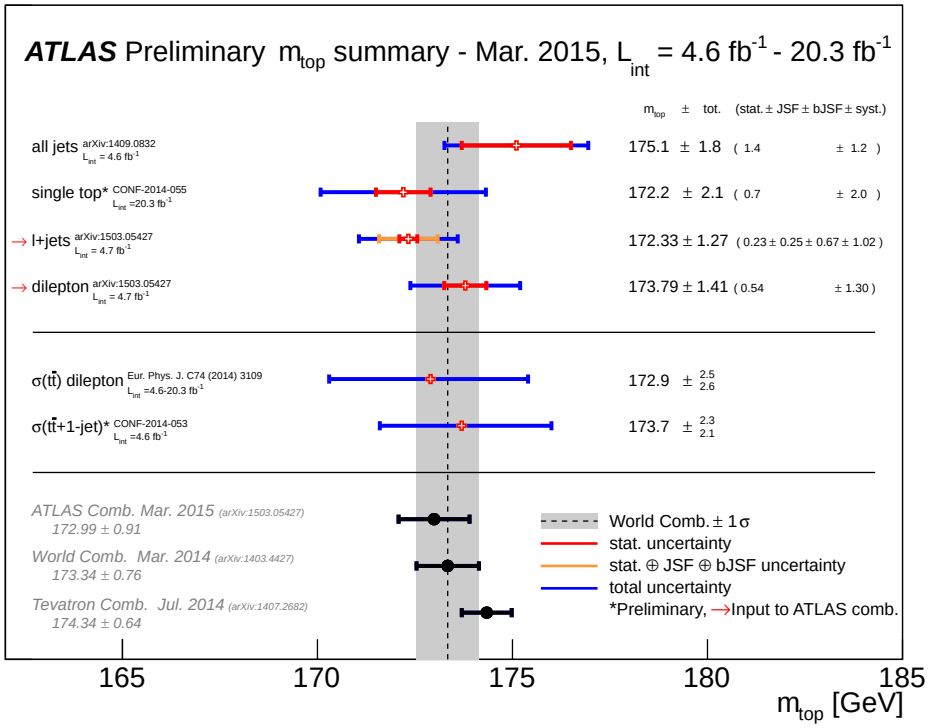

Figure 2.4: Summary of the ATLAS direct m_{top} measurements. The results are compared with the ATLAS, Tevatron and Tevatron+LHC m_{top} combinations. For each measurement, the statistical uncertainty, the sum of the remaining uncertainties are reported separately.

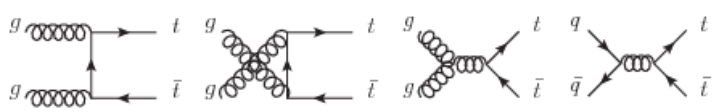

Figure 2.5: Feynman diagrams for $t\bar{t}$ production at leading order QCD

production can mediated by virtual s-channel and t-channel W-bosons. These production channels provide sensitivity to physics beyond the SM. Single tops are also produced in association with a W-boson (Wt-associated production). While negligible at the Tevatron, at the LHC, Wt-associated production provide a sizeable contribution to single top production. The inclusive cross-section for s-channel, t-channel and Wt-associated single top production has been computed to NNLO. This calculation is compared with the ATLAS experimental measurements of each channel in Figure 2.7.

The calculation of Wt at NLO is non-trivial since the NLO Wt production process interferes with the LO $t\bar{t}$ production[14]. Because of this interference, NLO Wt is not well-defined and a prescription must be adopted to deal with the interference to calculate Wt production beyond LO. The two most common prescriptions are *diagram removal* (DR) and *diagram subtraction* (DS). In the DS method, the resonant $t\bar{t}$ effects are removed at the cross-

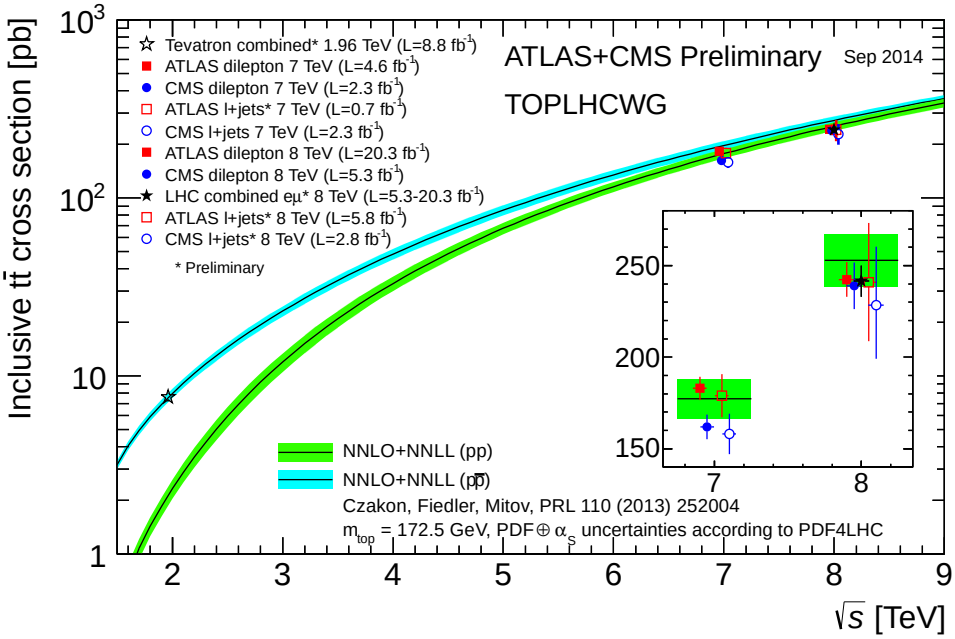

Figure 2.6: Summary of LHC and Tevatron measurements of the top-pair production cross-section as a function of the centre-of-mass energy compared to the NNLO QCD calculation complemented with NNLL resummation (top++2.0). The theory band represents uncertainties due to renormalisation and factorisation scale, parton density functions and the strong coupling. The measurements and the theory calculation is quoted at m_{top}=172.5 GeV. Measurements made at the same centre-of-mass energy are slightly offset for clarity.

section level. In the DR method, the resonant $t\bar{t}$ effects are removed from Wt at amplitude level. The difference between these two methods essentially corresponds to the interference between $t\bar{t}$ and Wt production. Due to this complication, the Wt is treated as part of the signal, rather than subtracted as background, in this thesis. This procedure is discussed in later chapters.

2.2.2 Top quark decays

In the SM, the top quark decays to a W boson and a down-type quark: $t \to qW$ where $q = b, s, d$. The rate of each of these decays is proportional to the square of the Cabibbo-Kobayashi-Masakawa (CKM) matrix, $|V_{tq}|^2$ [4]. Measured from experiment, the CKM matrix governs quark mixing in flavor-changing weak decays.

Weak hadron decays and the unitiary of the CKM matrix constrain the value of $0.9990 < |V_{tb}| < 0.9992$ at the 95% C.L [15]. Top quarks nearly always decay with $t \to Wb$. Figure 2.9 shows the decay of a top quark, both hadronically and leptonically.

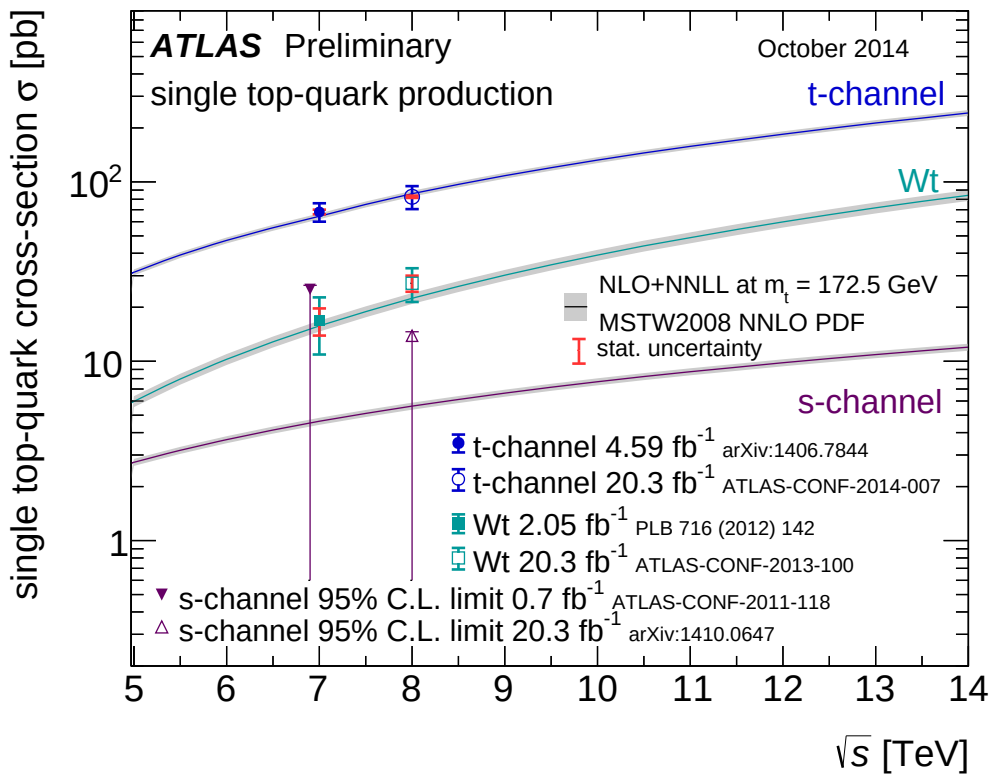

Figure 2.7: Summary of ATLAS measurements of the single top production cross-sections in various channels as a function of the center of mass energy compared to a theoretical calculation based on NLO QCD complemented with NNLL resummation. For the s-channel only an upper limit is shown.

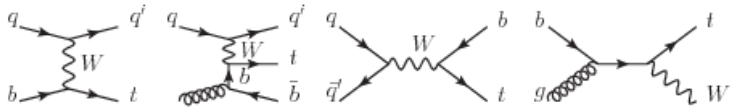

Figure 2.8: Feynman diagrams for single top quark production at leading order QCD. From left to right: t-channel production as flavor excitation; t-channel production as W-gluon fusion; s-channel production; Wt-channel production.

Experimentally, the decay modes of $t\bar{t}$ are distinguished by the decay of the two W-bosons:

All hadronic Both W bosons decay to quark pairs: $t\bar{t} \to WbWb \to bbqqqq$. Because there are 6 quarks in the final state, this channel has a large multi-jet background, which can be difficult to subtract.

Semi-leptonic One W boson decays to a quark pair and the other decays to a lepton and neutrino: $t\bar{t} \to WbWb \to bbqq\ell\nu$. This channel can be further categorized by lepton

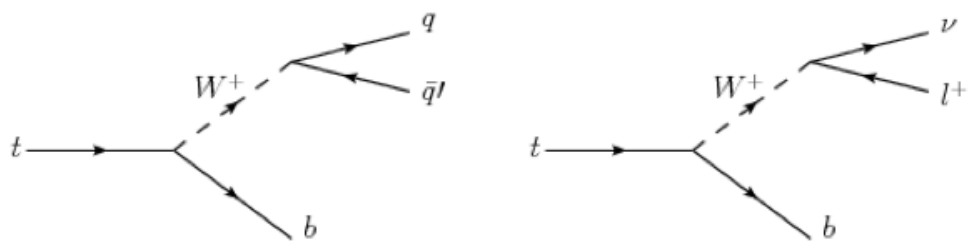

Figure 2.9: Feynman diagrams for top quark decay. On the left, the top quark is shown decaying hadronically. On the right, the top quark is shown decaying leptonically.

flavor.

Dileptonic Both W bosons decay to leptons: $t\bar{t} \to WbWb \to bb\ell\nu\ell\nu$. Though the dilepton channel has the fewest events, it often provides least background.

This thesis uses $t\bar{t}$ events from the dilepton $e\mu$ channel. The minimal background allows more robust generator comparisons.

2.3 Beyond the SM

In addition to providing a test of the SM, the top quark may also provide a window to physics at higher energy scales beyond the SM.

The top quark is important in aesthetic problem with the Higgs mass known as the hierarchy problem or fine tuning. The Higgs mechanism provides an explanation for electroweak symmetry breaking and acquisition of mass by other SM particles. As a scalar particle, the Higgs receives higher-order corrections to its physical (measured) mass from interactions with fermions, gauge bosons and itself. These corrections are on the order of the Planck scale, $\mathcal{O}(\Lambda^2 \approx 10^{30-38}$ GeV), while the observed mass is close to the electroweak scale, $\mathcal{O}(100$ GeV). Thus, in order to obtain the observed mass without introducing new physics, there must be an unnatural cancellation.

In addition to the hierarchy problem, there are several other open questions which cannot be explained by the SM. The SM does not account for the 85% of our universe made up of *dark matter* particles, or provide an explanation for the observed asymmetry between matter and anti-matter. The SM also does not account for the observed non-zero mass of neutrinos or have a way to incorporate gravitational interactions.

Theorists have formulated many extensions to the SM that address these puzzles. Perhaps the most widespread, Supersymmetry (SUSY) [16] proposes an additional superpartner for every particle in the SM. SUSY is especially popular because it naturally contains a light, stable, neutral dark matter candidate and solves the hierarchy problem. Diagrams from superpartners remove the need to fine tune the Higgs mass. Since SUSY has not been observed, the superpartners of SM particles must have different masses, and SUSY has to

be a broken symmetry. However, in order to satisfactorily solve the hierarchy problem, the superpartners with the largest contributions to the Higgs mass must be $\mathcal{O}$(TeV). This means that they should be discoverable at the LHC.

Another popular SM extension, called the Randall-Sundrum model [17], posits an extra dimension in which gravity would propagate. This model includes a new particle, a Kaluza-Klein gluon, that propagates into the extra dimension and decays into a top quark pair.

Many of the signals for new physics are dominated by the top quark since heavier particles are more sensitive to higher energy scales. The top pair production analyzed in this thesis is important as a background for $t\bar{t}$ resonances [18] and other searches [19].

Chapter 3

Phenomenology at the LHC

Events at hadron colliders are very messy, potentially producing hundreds of particles through many types of physics processes. To illustrate the complexity of such events, a schematic of a proton-proton collision event is shown in Figure 3.1. Two incoming protons collide to create the *hard scatter* shown in red. In this case, two gluons produce a pair of top quarks. The left top decays hadronically and the right decays leptonically. Partons produce radiation as they travel. The hard scatter plus parton radiation is collectively known as the *underlying event*, shown in purple. Partons are recombined into hadrons (shown as green blobs), a process called *hadronization*. The hadrons can both emit QED radiation (shown in yellow) and then decay further. The following chapter discusses concepts relevant to analyzing events at hadron colliders. First, terms and concepts in simulating events are introduced. Then, Monte Carlo event generators are discussed. Finally, jet algorithms and concepts are outlined.

3.1 Simulation of hadron collisions

In order to analyze complicated processes at huge machines like the LHC, software that virtually reproduces the physics experiment is necessary. In order to account for stochastic effects, Monte Carlo (MC) methods are used to simulate a large number of random events. In the actual experiment, ATLAS detects collisions produced by the LHC and stores these *events* using a data acquisition system. In the virtual simulation, event generators such as Herwig [21] and Pythia[22] produce final state particles. These particles are then processed through a detector simulation of ATLAS built with Geant 4[23]. The simulated and actual detector signals can then share the same event reconstruction framework and analysis. This allows a clear understanding of how the input physics is distorted step-by-step as it goes through the detector and reconstruction.

The distortions resulting from detector imperfections and reconstruction are particularly important to this thesis, so the following chapters will employ specific terms to refer to different aspects of the simulation process. *Generator-level* or *truth* particles refer to those

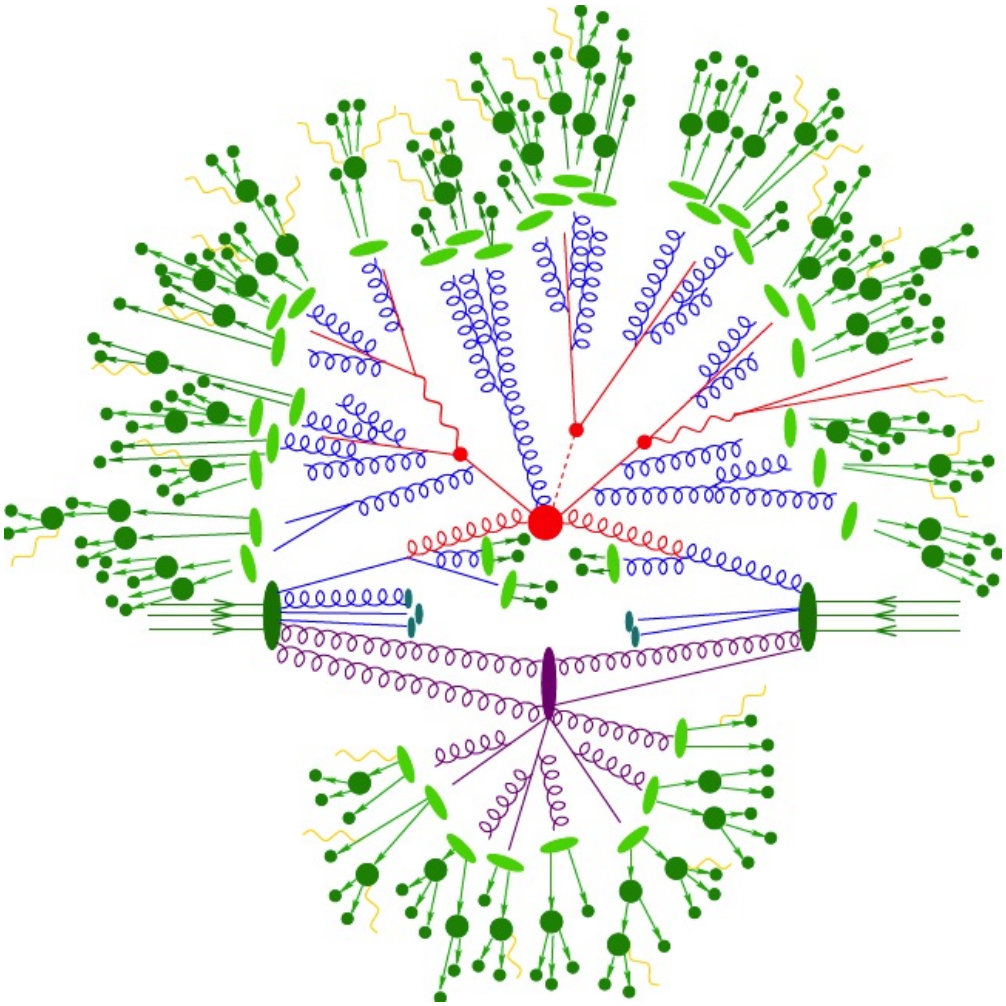

Figure 3.1: Visualization of a top pair event from the SHERPA event generator. The hard scatter is shown in red, the parton shower in blue, the hadronzation in green, the underlying event in purple, and the QED final state radiation in yellow [20].

produced by the MC generator before any detector interactions. *Detector-level* or *reconstructed* particles refer to those that have gone through the detector simulation and been reconstructed.

To go backwards from the (distorted) reconstructed to truth particles, the distortions introduced by the detector must be reversed. This correction process is referred to as *unfolding* and is further discussed in Chapter 9. Unfolding is necessary to compare actual data measured with the detector to theoretical predictions produced by generators.

3.2 Monte Carlo generators

In MC event generators, events are produced step-by-step, with random numbers pulled from quantum mechanical probability distributions at various stages[4, 24]. Averaging over a large number of events gives the expected final distribution of events. The goal is to start with a QFT matrix element in a form similar to Equation 2.4 and produce *final state*, stable particles that can be measured with a detector. The method outlined below uses a set of rules at each step to allow the iterative construction of an increasingly complex final state, resulting in hundreds of particles traveling in different directions. Since each particle has many degrees of freedom (mass, momentum, lifetime, flavor, etc.), each event involves thousands of choices. The result of the simulation must accurately describe the average final state particles as well as fluctuations around the average.

The steps to generate an event at the LHC can be summarized as follows:

- Two initial incoming protons are considered as a bag of partons with momentum distributed according to the proton PDFs and specified center of mass energy (in the case of this thesis, 8 TeV).

- Two partons, one from each proton, are collided to give the *hard process* of interest: $ug \to ug, u\bar{d} \to W^+$, etc. If unstable particles such as top quark or W/Z boson are produced, their decay is treated as part of the hard process in order to properly transfer properties such as spin correlations.

- Just as electromagnetic charges can emit bremsstrahlung, color charges (i.e. partons) can emit QCD radiation. These emissions are collectively called the *parton shower* (PS). Radiation emitted by partons before the collision is called Initial State Radiation (ISR). Radiation emitted by partons after the collision is called Final State Radiation (FSR) [1].

- Because the proton is made up of many partons, further parton pairs may collide within a single proton-proton collision. This process is called multiparton interactions (MPI).

[1] A true QCD calculation involves matrix elements that can interfere and hence no unique distinction between ISR and FSR is possible. The distinction between ISR and FSR makes sense in the context of MC generators because generators use a probabilistic approach that ignores such interference.

Each of these further collisions may have ISR or FSR. As calculated in Appendix A.7, MPI is found to be negligible for events selected by this thesis. MPI is different from pileup events, when several protons collide within a single bunch crossing. Pileup is further discussed in Chapter 4.

- After the parton collision, most of the energy remains in the beam remnants, which continue to travel in the original direction and carry color. As the partons from the collision recede, confinement forces come to dominate. These fields cannot be sufficiently described from first principles, so a model must be introduced to describe the evolution of partons into primary hadrons, a process known as *hadronization*. For example, PYTHIA uses a *string* method, where the confinement field is modeled as a string stretched between each color and its anti-color. Strings are then stretched until they break and creates a new pair. This process is repeated until the string energy is sufficiently low-energy and the quarks from adjacent breaks produce primary hadrons. The *cluster* model used by HERWIG groups quark pairs into colorless clusters. These clusters then decay into other colorless clusters or SM hadrons until only SM hadrons remain.

- Many of these primary hadrons are unstable and decay at different timescales. Some of these decays take place within the detector volume. For ATLAS, particles with $c\tau > 10$ mm are considered *final state* particles. Particles below this threshold are decayed by the event generator.

- At this point, the final state particles can be passed on to the detector simulation framework. Experimental information can be used to reconstuct what happened at the core of the process.

Using the above steps, the cross section for the range of final states produced a hard process of physics interest can be represented schematically as:

$$\sigma_{\text{final state}} = \sigma_{\text{hard process}} \times \mathcal{P}_{\text{tot, hard process} \rightarrow \text{final state}} \tag{3.1}$$

This equation must be properly integrated over phase-space as well as summed over all possible decay paths that lead to a given final state. The hard process $\sigma_{\text{hard process}}$ can be calculated as in Equation 2.4. The steps to reach the final state from the hard process are treated probabilistically.

Some of the available event generators provide software for each of the steps listed above, while others can only handle some of the steps. General-purpose generators such as PYTHIA, HERWIG, and SHERPA can handle the entire process, from matrix element to PS and hadronization. Other generators such as MC@NLO[25, 26] and POWHEG[27, 28, 29, 30] only generate a fixed order calculation of the hard process and must be interfaced to another generator, e.g. PYTHIA or HERWIG, for the PS.

Merging the hard process calculation with a PS program can be tricky. Both may produce wide angle radiation, so care must be taken not to double count partons. For NLO+PS,

double counting can happen because PS programs attempt to emulate effects of a true NLO calculation. Two different methods are used in MC@NLO and PowHeg to avoid double-counting. MC@NLO[25] uses an analytic computation to identify what parts of the NLO calculation is already present in the PS and then subtracting this portion from the shower before combining. This method requires a new calculation for each PS program since each PS uses different NLO approximations. For PowHeg[27, 28], the probability of each iterative spread of the shower is modified for the first emission such that exact NLO accuracy is reached. Then, any PS program can be used to shower the rest of the event with a p_{T} veto to ensure that the PS program doesn't produce any emissions harder than those from the NLO.

Finally, "afterburner" programs can be used to more accurately redecay special particles, such as Tauola for taus[31] or EvtGen for heavy flavor hadrons[32]. Studies of the effect of EvtGen on the modeling of heavy flavor decays and hadronization are presented in Appendix B.

Predictions from generators can be *tuned* by changing parameters of the showering and hadronization to match experimental data[33]. Each generator has many relatively free parameters, most used to model the non-perturbative hadronization process but also some for the perturbative hard interaction. All of these parameters have a physical motivation, but are usually only known via rough scale approximations. Some parameters like α_S can be measured experimentally but still must be adjusted since generators use them in a fixed-order scheme, unlike nature. These parameters can be grouped into sets such as flavor, fragmentation, hard process, etc. Most of the hard process parameters are tunes to Tevatron and LHC data, while most of the hadronization parameters come from LEP. The measurement of this thesis is important for future tuning of PS parameters since additional jets are sensitive to ISR/FSR.

3.3 Jets

Partons cannot be directly observed at the LHC since QCD confinement prevents partons from existing as free particles. Instead, narrow cones of hadrons and other particles from the hadronization of a parton are experimentally studied to determine the properties of the original parton. These cones are identified as experimentally observable objects called jets. Ideally, each jet would match with a parton shower initiated by a single hard parton. However, a jet may contain parts of showers from multiple partons and ISR/FSR.

Since a jet is not a fundamental physics object, a suitable definition must be adopted to analyze them. A *jet algorithm* used to build jets from final state particles in the generator record, partons in a QCD calculation, reconstructed charged particle tracks or energy deposits in the calorimeter. A good jet algorithm must be [34]

- Simple to implement for experimental analysis;
- Simple to implement for theoretical calculation;

- Defined at any order of perturbation theory;
- Yield finite cross sections at any order of perturbation theory;
- Yield cross sections relatively insensitive to hadronization model
- Infared and collinear (IRC) safe, e.g. jets should be stable under modification of final state particles via soft emissions or collinear splitting to avoid infinite results in calculations due to infrared divergences

Modern jet algorithm specifies the way the 4-vectors of the input constituents are combined with a distance metric. The standard algorithm used by both ATLAS, CMS and ALICE is the anti-$k_T$jet algorithm[35, 36], which fulfills the above criteria exceedingly well. The k_T algorithm is a closely related algorithm used in special cases with irregular jets.

The anti-k_T algorithm begins by defining the distances between two constituents i and j and between constituents i and the beam as:

$$d_{ij} = \min(p_{T,i}^{2k}, p_{T,j}^{2k}) \left(\frac{\Delta R_{ij}}{R_0}\right)^2 \tag{3.2}$$

$$d_{iB} = p_{T,i}^{2k} \tag{3.3}$$

where p_T is the transverse momentum of the constituent, $\Delta R_{ij} \equiv \sqrt{(\eta_i - \eta_j)^2 + (\phi_i - \phi_j)^2}$ and R_0 is a chosen parameter that approximately determines the jet in the $\eta - \phi$ plane. The anti-k_T and k_T algorithm differ only in the choice for the exponent k. For k_T, $k = +1$ and for anti-k_T $k = -1$.

With a chosen distance metric and set of input constituents, the algorithm iteratively proceeds as follows:

- find the smallest d_{ij} and d_{iB}
- if $d_{ij} < d_{iB}$, replace i and j by a new constituent formed by the 4-vector sum of i and j
- if $d_{ij} > d_{iB}$, declare i a jet and remove from the list of constituents

Figure 3.2 shows the results of clustering the same set of constituents with each of these algorithms. The difference between the two can be roughly explained by observing that k_T clusters the lower p_{T} constituents first, while anti-k_T clusters the higher p_{T} constituents first. Since anti-k_T takes the highest p_{T} constituents first, the jet axis stabilizes after the first few combination and results in circular jets. Circular jets have better defined acceptance, are easier to calibrate, and have more straightforward corrections for pileup. These advantages of the anti-k_T algorithm motivates its adoption as the ATLAS default and its use in this thesis.

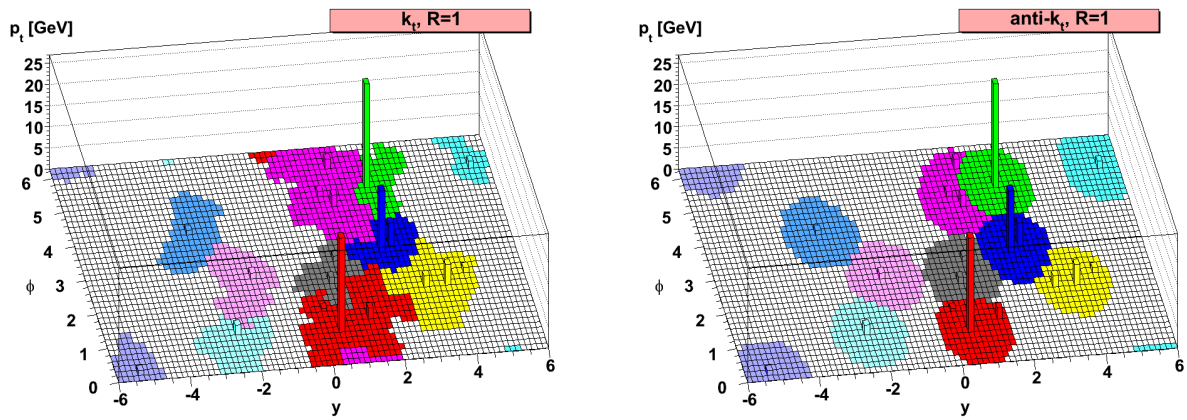

Figure 3.2: The input constituents clustered both the k_T(left) and the anti-k_T(right) algorithms [35].

Chapter 4

The ATLAS detector and the LHC

4.1 The Large Hadron Collider

The Large Hadron Collider (LHC)‘[37] is the largest and most powerful particle collider that has ever been built. Construction of the LHC involved a collaboration of more than 10,000 scientist from more than 100 countries and was completed in 2008, after a decade of work. The cost of the machine alone is about 5 billion USD (3 billion Euro). The main goal of the LHC is to investigate unsolved questions in our current understanding of particle physics, such as the details of the Higgs mechanism, the existence of new particles from SUSY or extra dimensions and the source of dark matter and dark energy.

The European Organization for Nuclear Research (CERN) built the LHC in a tunnel underneath the border of France and Switzerland, near the city of Geneva. The LHC occupies a large tunnel 27 km in circumference that was originally constructed in the 1990s for the Large Electron Positron collider (LEP). Hadrons (either protons or ions) are accelerated and focused into two beams traveling in opposite directions around this tunnel. These beams then collide with very high energy at each of the four collision points along the ring where the paths of the two beams intersect. Each collision point is home to one of the four main LHC experiments: A Large Ion Collider Experiment (ALICE) [38], ATLAS [39], the Compact Muon Solenoid (CMS) [40], and the Large Hadron Collider beauty (LHCb) experiment [41]. ALICE is a detector that looks at collisions of lead ions to study the properties of quark-gluon plasma. ATLAS is a general-purpose detector that looks for a wide range of possible new types of physics, including the Higgs boson, SUSY, and extra dimensions. CMS is an additional general-purpose detector, designed and run independently from ATLAS, but with the same goals in mind. LHCb is a detector specially designed to study the asymmetry between matter and anti-matter in the interactions of B-particles. Figure 4.1 shows a aerial view diagram with the locations of these four experiments along the LHC ring. The location of the LHC ring in relation to the city of Geneva and the French-Swiss border is also illustrated.

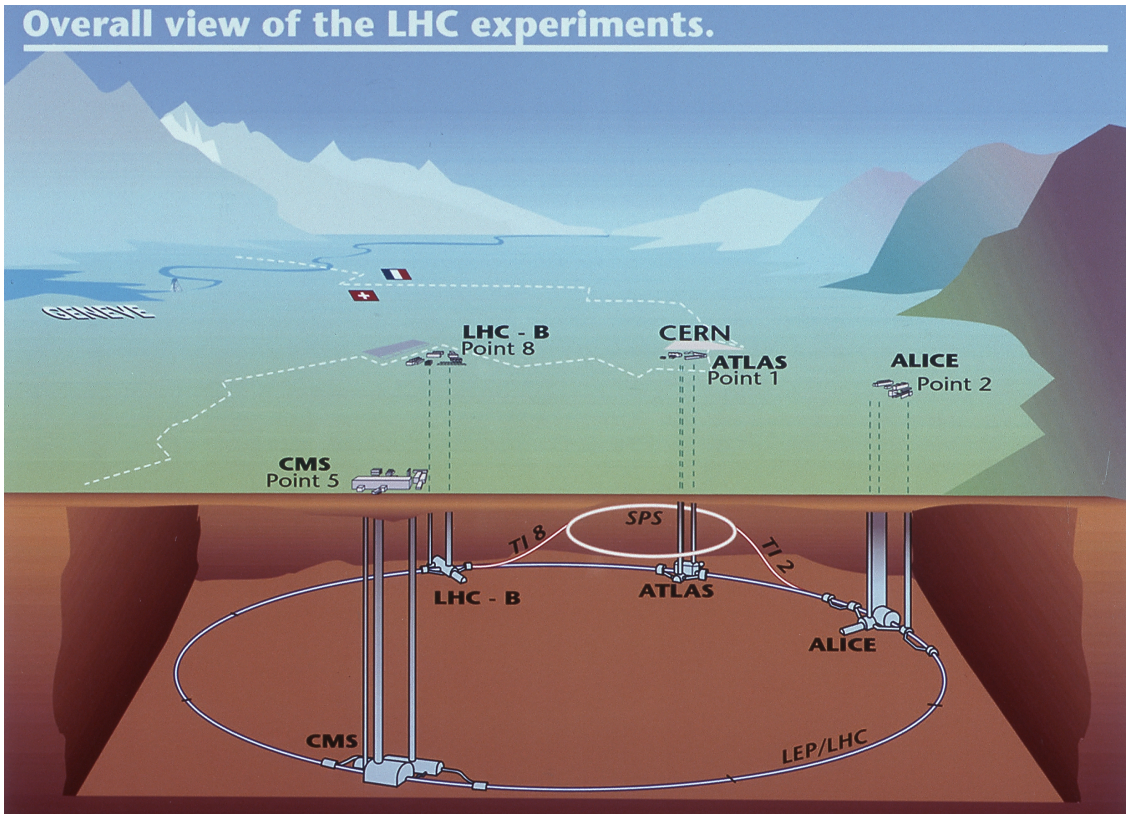

Figure 4.1: The location of the four main LHC experiments: ALICE, ATLAS, CMS and LHCb. The LHC tunnel is 27 km in circumference, situated underneath the border of France and Switzerland, near the city of Geneva, as shown [42].

4.1.1 Accelerator Complex

A succession of machines known as the *accelerator complex* accelerate particles to increasingly higher energies [43]. A diagram of the accelerator complex is shown in Figure 4.2. First, an electric field is used to strip protons from atoms in a simple bottle of hydrogen gas. Then, the first accelerator in the chain, Linac 2, accelerates protons to 50 MeV. Next, the beam is injected into the Proton Synchrotron Booster (PSB) and then the Proton Synchrotron (PS), which accelerate the protons to 1.4 GeVand 25 GeVrespectively. After that, the Super Proton Synchrotron accelerates the protons to 450 GeV. The last step in the chain is the LHC; from the SPS, protons are transferred into the two beam pipes of the LHC and accelerated in opposite direction. Filling each of the rings of the LHC takes 4 minutes and 20 seconds, and it takes another 20 minutes to accelerate each beam to its final energy of 4 TeV. The same two beams will circle for many hours.

Inside the LHC, the beams travel in opposite directions around separate rings called *beam pipes* (or beamline), which are tubes kept at ultrahigh vacuum. The beams are directed by a collection of very strong superconducting electromagnets, including 1232 dipole magnets

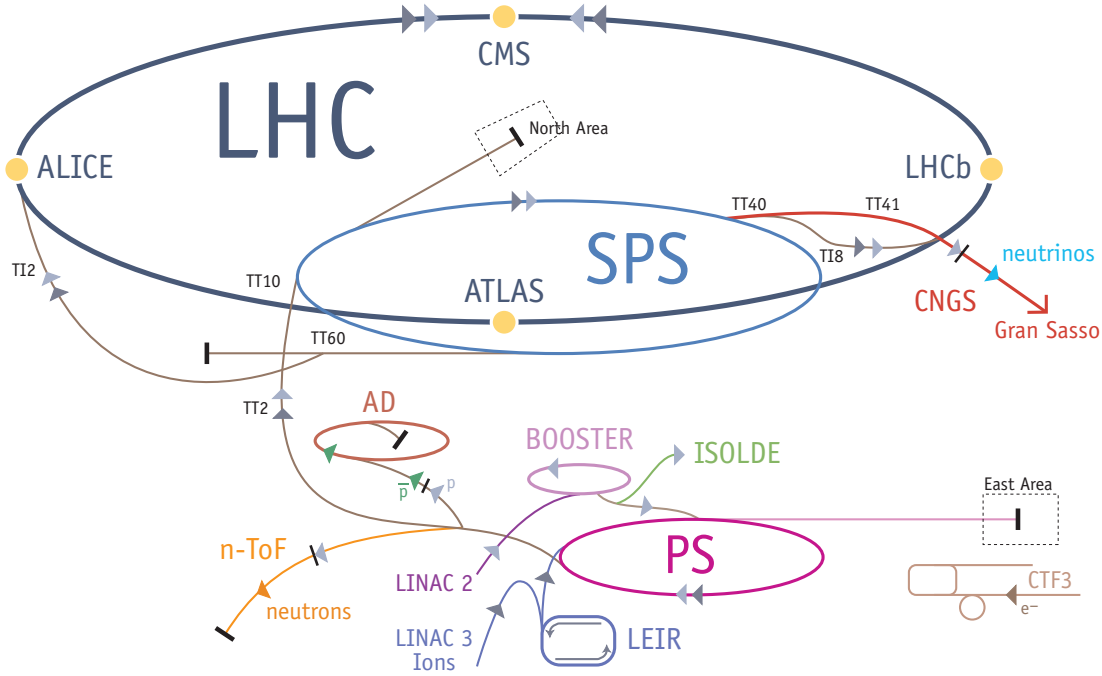

Figure 4.2: The LHC accelerator complex boosts particles to increasingly higher energies before reaching the LHC. The particle beams are accelerated successively by Linac 2, the Proton Synchrotron Booster (PSB), the Proton Synchrotron (PS), the Super Proton Synchrotron (SPS) and then finally enter the LHC rings [37].

and 392 quadrupole magnets. Superconduction requires the magnets to be cooled to -271.3 C. A distribution system of liquid helium keeps the magnets cool. The 15 meter long dipole magnets steer the beams around the ring, while the 5-7 meter long quadrupole magnets focus the beams before collision.

4.2 Beam conditions

Due to the Radio Frequency (RF) fields in the accelerating cavities, the proton beams are segmented into groups of protons called *bunches*. Each beam contains 2808 bunches, and each bunch contains 1.7×10^{11} protons. Many protons are included per bunch to maximize the probability of a proton-proton collision for a given bunch crossing. A bunch crossing occurred every 50 nanoseconds during operations in 2012.

Given two equally bunched beams, the *instantaneous luminosity* ($\mathcal{L}$) is given by [4]:

$$\mathcal{L} = f\frac{n_1 n_2}{4\pi\sigma_x\sigma_y}, \tag{4.1}$$

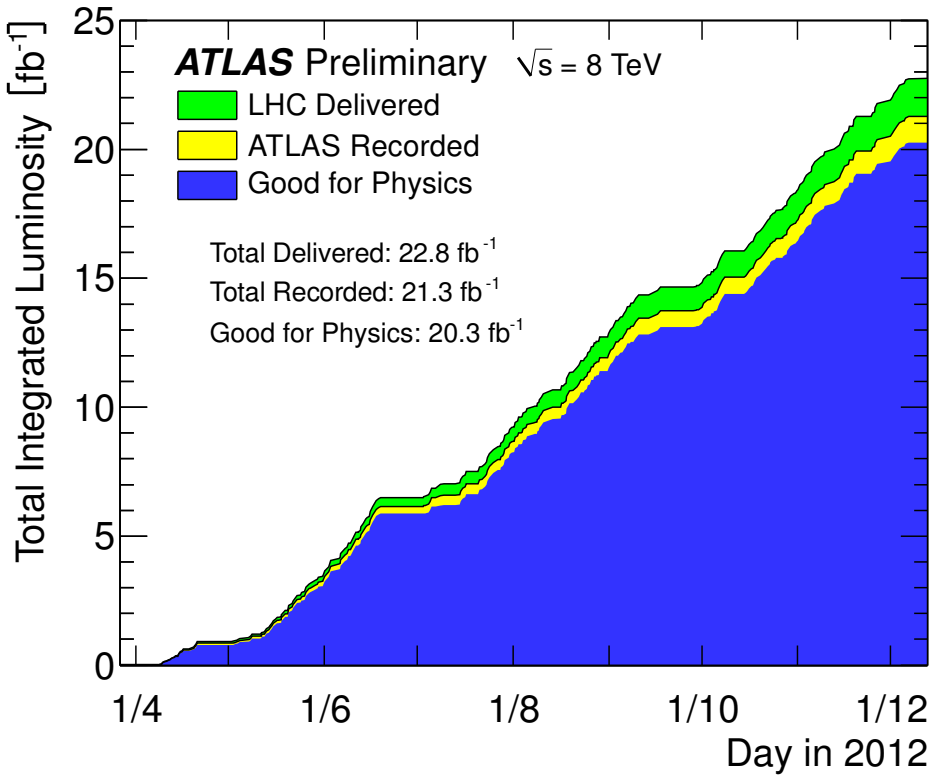

Figure 4.3: Cumulative luminosity versus time delivered to (green), recorded by ATLAS (yellow), and certified to be good quality data (blue) during stable beams and for pp collisions at 8 TeV center-of-mass energy in 2012. Luminosity can be lost due to data acquisition inefficiency or other effects.

where $f = 11\,245.5\,\mathrm{Hz}$ is the collision frequency of the LHC beams; n_1 and n_2 are the numbers of protons in each beam; and σ_x and σ_y are the RMS beam widths in the horizontal (bend) and vertical directions. The maximum instantaneous luminosity of the LHC in 2012 was 7.7×10^{33} cm^{-2} s^{-1}.

The instantaneous luminosity must be integrated over time to obtain total luminosity. The beam conditions that go into Equation 4.1 change over the duration of a run. The integral over time and varied beam conditions is called the *integrated luminosity* and can be used to relate the number of events N for a given physics process to its cross section σ:

$$N = \sigma \times \int \mathcal{L}(t)dt \tag{4.2}$$

In 2012, the total integrated luminosity of the LHC was 20.3 fb^{-1} with uncertainty of 2.8% [44]. The cumulative luminosity recorded over the course of 2012 is shown in Figure 4.3.

The beam conditions also determine the number of proton-proton interactions that occur in a single bunch crossing. When a single bunch crossing produces multiple separate

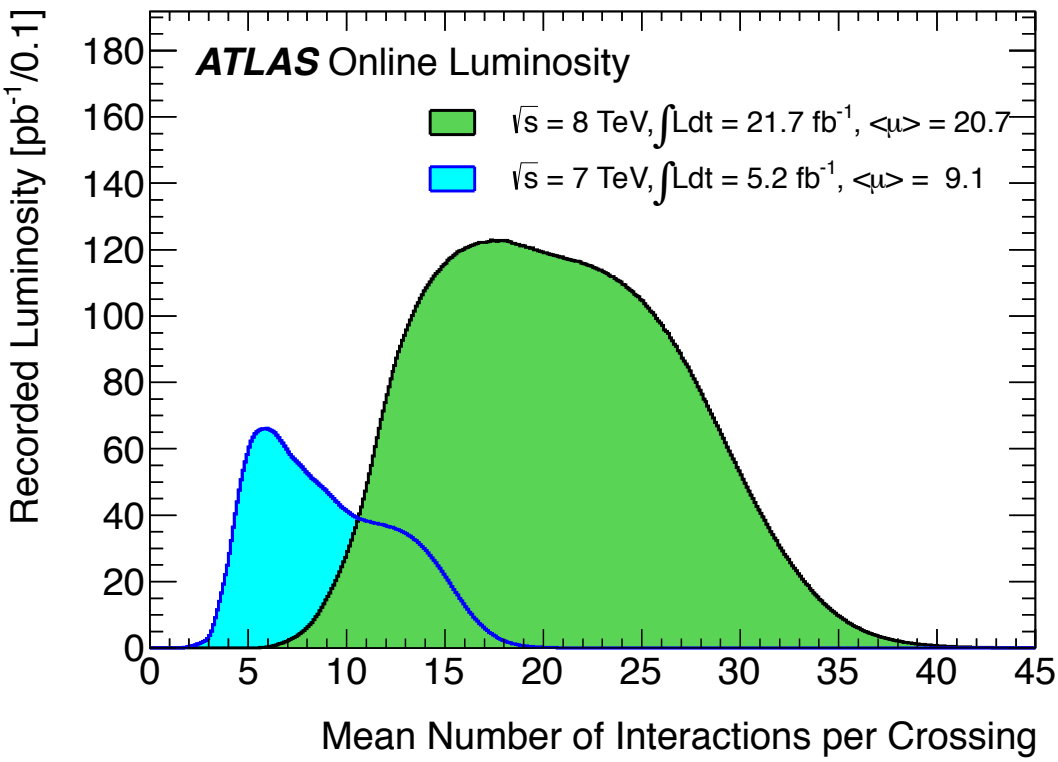

Figure 4.4: Luminosity-weight distribution of the mean number of interactions per bunch crossing. Both the full data from the 2011 and 2012 *pp* runs at the LHC are shown.

proton-proton collisions, these events are referred to as *pileup*. Pileup presents a significant challenge since it can rapidly increase the combinatoric complexity of reconstructing events and degrade the performance of the reconstruction algorithms. Figure 4.4 shows the mean number of interactions per bunch crossing for 2011 and 2012, demonstrating the substantial increase of pileup events in the latter. Reconstruction challenges were overcome by optimizing the existing reconstruction algorithms, as well as new techniques for subtracting pileup events from the physics of interest [45].

4.3 Overview of the ATLAS detector

The ATLAS detector is a general purpose detector centered over one of the four interaction points of the LHC. The detector is cylindrical in shape with a diameter of 25 meters, a length of 46 meters, and a weight of 7,000 tons; it contains around 100 million electronic channels and around 3,000 km of cables. Assembling the detector at CERN took 5 years and was completed in 2008. A schematic rendering of the ATLAS detector is shown in Figure 4.5. In order to detect a wide range of physics processes in proton-proton collisions, ATLAS must

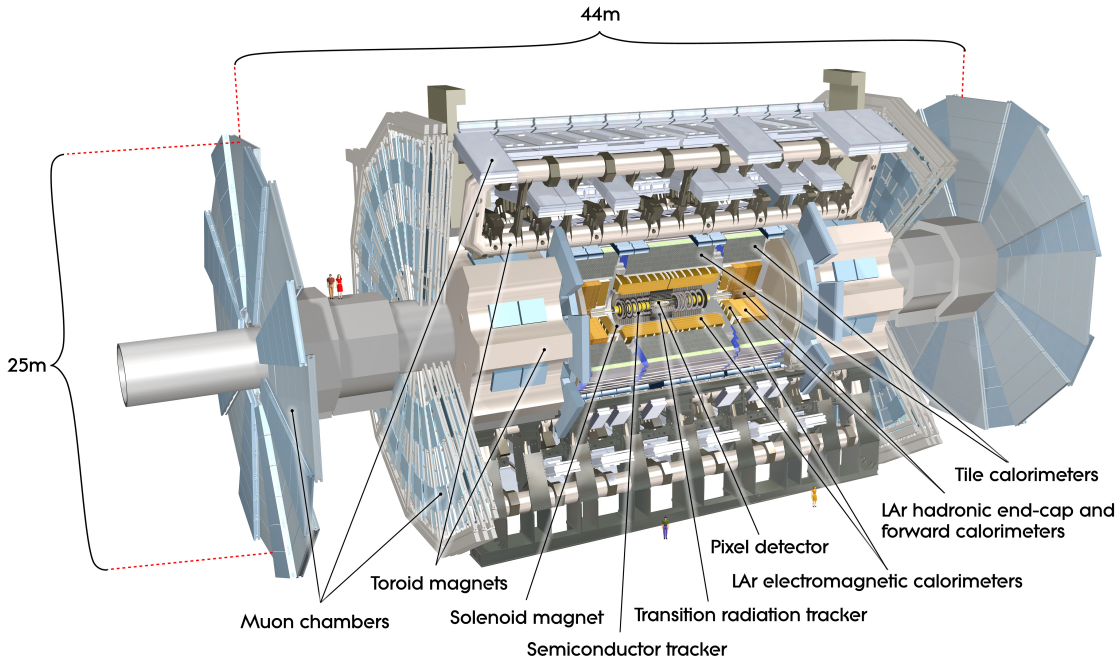

Figure 4.5: Computer generated illustration of the whole ATLAS detector detector, with various subdetectors highlighted[46].

measure the trajectory and energy of many different kinds of particles, including electrons, muons, photons, pions, kaons, protons and neutrons. Once these stable final-state particles are detected, information about the heavier, unstable particles can be inferred. This process is called *reconstruction* and is discussed in detail in Chapter 6.

ATLAS consists of specialized subdetectors designed to capture different phenomena. These subdetectors are arranged as increasingly larger concentric cylinders around the interaction point (IP) where the LHC proton beams collide. There are three main specialized sub-systems: the *inner detector* (ID), which is located just outside the beamline and uses silicon and transition radiation systems to track the trajectory of charged particles; the *calorimeters*, which are located radially outward from the ID and designed to measure the energy of particles with a shower sampling method; and the *muon system*, which is located farthest from the IP and measures muon momentum and trajectory. Details of the subdetectors are provided below. An overview of interaction of different types of particles with the subdetectors as they travel through the detector is illustrated in Figure 4.6.

ATLAS has a magnet system that bends the trajectory of charged particles as they travel through the detector. This allows the particles' momenta to be precisely calculated using the classical Lorentz force equation. The magnet system consists of a double configuration. Just outside the ID is a solenoid magnet that produces a field of approximately 2 Tesla. A large toroidal magnet within the outermost part of the detector produces a 1 to 2 Tesla field.

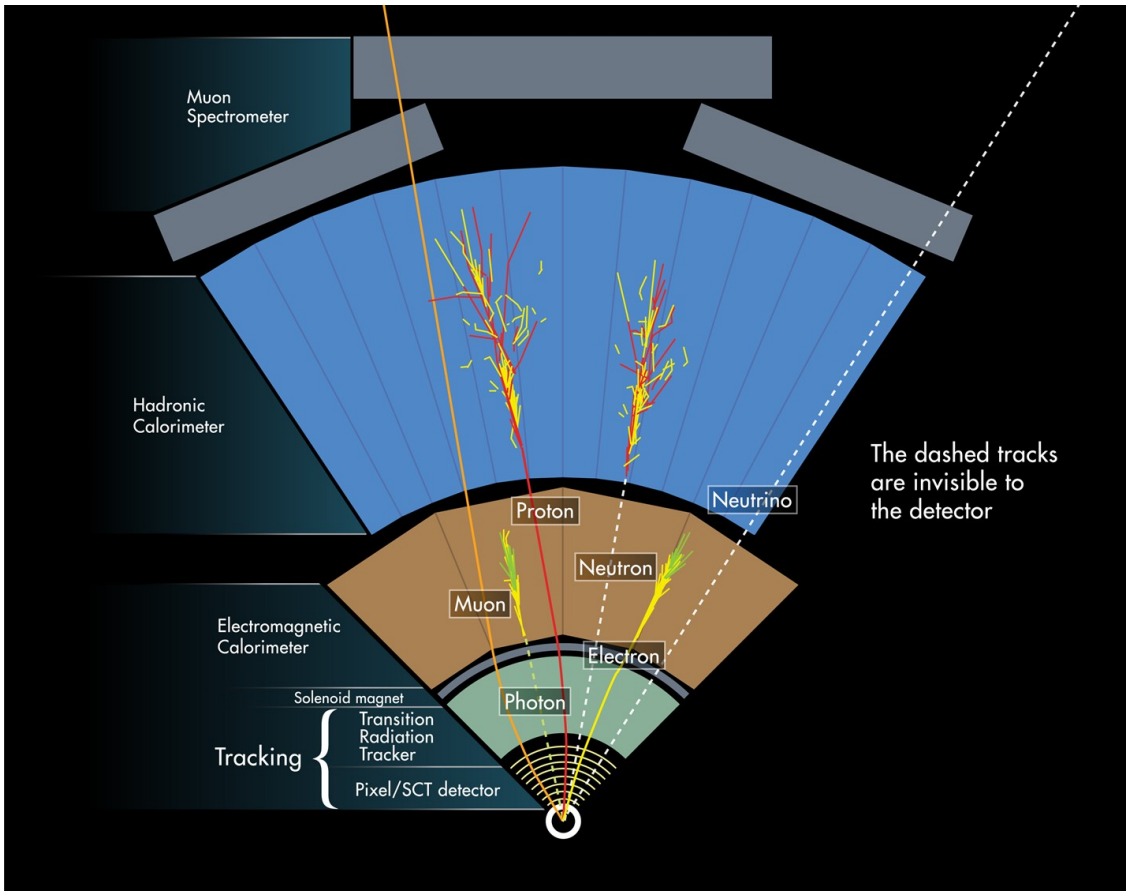

Figure 4.6: A computer-generated image representing how the ATLAS detector functions. The transverse paths of different types of particles are shown interacting with different elements of the detector[47].

4.3.1 Coordinate system

ATLAS uses a right-handed coordinate system with its origin at the IP in the center of the detector, which is illustrated in Figure 4.7. The z-axis along the beamline with the positive direction counter-clockwise around the LHC. The $x - y$ plane is defined such that the coordinate system is right-handed, with the x-axis pointing from the IP to the center of the LHC, and the y-axis pointing upwards. This plane is usually referred to as the transverse plane, since it is perpendicular to the beamline. Cylindrical coordinates, r and ϕ, are used in the transverse plane with ϕ defined as the azimuthal angle around the beamline. Instead of the polar angle from the beamline, θ, pseudorapidity is typically used and is defined as:

$$\eta = -\ln(\tan\frac{\theta}{2}) \tag{4.3}$$

The pseudorapidity is used because in the limit of a massless particle, it is invariant with respect to Lorentz boosts along the beamline. The solid angle distances ΔR can be measured

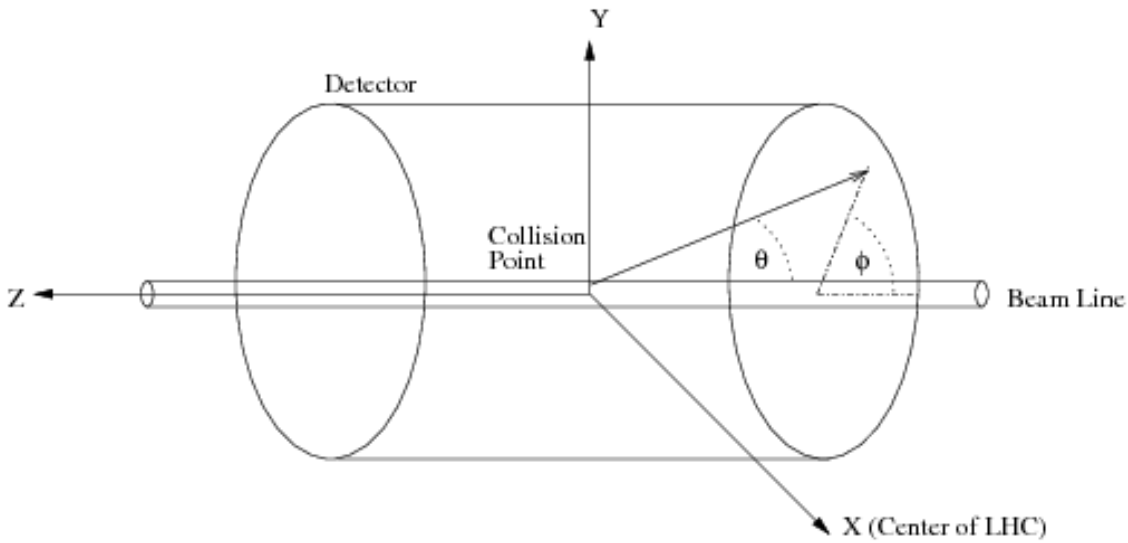

Figure 4.7: Illustration of the ATLAS coordinate system[48].

using the difference in pseudorapidity and azimuthal angle:

$$\Delta R = \sqrt{\Delta\phi^2 + \Delta\eta^2} \tag{4.4}$$

4.4 Inner detector

The ID is a series of detectors that function as a tracking system to measure the momenta and trajectory of charged particles [39]. This also allows reconstruction of the primary and secondary vertices of the collision. The innermost part of the entire detector is the pixel detector, 3 layers of silicon that accurately measure the three-dimensional spatial position of charged particles. Next is the SemiConductor Tracker (SCT), 4 layers of double-sided silicon strip modules which accurately measure tracks in the $r - \phi$ plane and are double sided to provide stereo information along the z axis. The outermost component of the ID is the Transition Radiation Tracker (TRT), straw tubes filled with Xenon gas interleaved with polymer layers which provides additional trajectory measurement and differentiate between electron and hadrons. Figure 4.8 shows a schematic outline of the entire inner detector, and Figure 4.9 illustrates a cut-away view of the inner detector barrel.

4.4.1 Pixel detector

The pixel detector is located closest to the beamline and is designed to provide fine granularity in a high radiation environment. Measuring trajectories closest to the interaction point is important for constructing the secondary vertex, necessary for the b-tagging of jets used in this analysis.

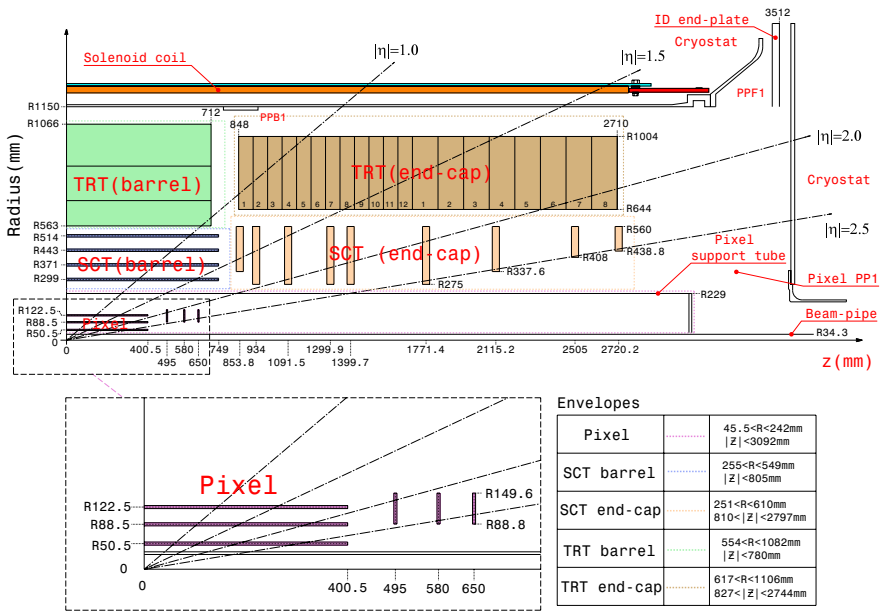

Figure 4.8: Schematic view of the Inner Detector: an $r-z$ slice of the cylindrical barrel, disc endcaps with support tubes, and the solenoid magnet. Lines of constant η are drawn [39].

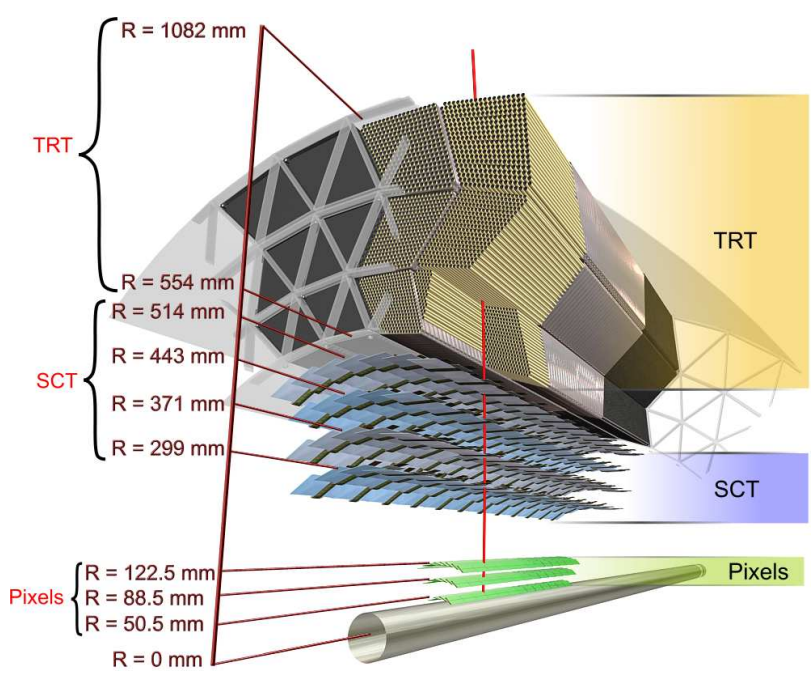

Figure 4.9: A diagram of the barrel of the Inner Detector: the three layers in the Pixels, the four layers in the SCT, and the many layers of the TRT [39].

The pixel detector has 3 barrel layers and three endcap disks on each side of the barrel. The barrel layers are located 50.5 mm, 88.5 mm and 122.5 mm radially from the interaction point. The endcaps sit at 495 mm, 580 mm and 650 mm away from the interaction point. Together, they provide coverage up to $|\eta| = 2.5$.

Each silicon pixel in these layers is a p-n junction built of n-type bulk with both p^+ and n^+ impurities. The additional n^+ implants allow the pixels to operate even after the inversion of the bulk from n-type to p-type caused by the high radiation dose. The size of each pixel is $50 \times 400\mu m^2$ with the longer side along the z direction. This allows charged particle hit resolution of approximately 115 μm in the direction of the z axis and 10μm in the direction of the transverse plane.

Pixels are bump-bonded to front-end readout chips, with a grid of 2880 pixels connected to each chip. Front-end chips are grouped into rectangular *modules* of dimension $19 \times 63\mu m^2$. Modules in the barrel layers are arranged into long structures parallel to the beamline called *staves*. Staves are tiled at 20° with respect to the radial direction and overlapped to provide full azimuthal coverage. Endcap modules are arranged into petals and then into wheels, with the sensing element perpendicular to the beam axis. These supporting structures also host power, clock, command and data lines to and from each module. Full coverage is ensured in the endcaps by alternating the placement of the sensors on the front and back of the wheel. The arrangement of the barrel and endcap layers ensures that charged particles with $|\eta| < 2.5$ will pass through at least three pixels.

4.4.2 SemiConductor Tracker

The SCT surrounds the Pixel detector and also employs silicon detector elements, using micro-strips instead of pixels. The strips are arranged in four double layers, with the pairs arranged at small angles relative to each other, to make a three-dimensional measurement. The SCT has 4 barrel layers and 2 endcaps, each with 9 disks.

The SCT is made of single-sided p-in-n sensors of thickness 285 μm with readout strips. In the rectangular barrel sensors, the readout channels are arrange with a pitch of 80 μm between them, and the trapezoidal endcap sensors have radial strips with a mean pitch of 80 μm. Modules are comprised of four sensors arranged in two layers aligned at a stereo angle of 40 mrad with respect to each other. This allows a single module to measure all three dimensions spatial position of a charged particle passing through both the front and back layers. The endcap wheels are arranged so that charged particles with $|\eta| < 2.5$ will pass through at least eight sensors. The 2112 modules in the barrel have resolution a 17 μm of in $r - \phi$ and 580 μm in z, and the 1976 endcap modules have a resolution of 17 μm in $r - \phi$ and 580 μm in r.

4.4.3 Transition Radiation Tracker

The outermost layer of the ID is the Transition Radiation Tracker (TRT). The TRT extends the tracking volume to 1106 mm and also distinguishes between electrons and pions based

on their transition radiation as they pass through. It consists of straw drift tubes 4 mm in diameter filled with a Xenon gas mixture. At the center of each tube is a 35 μm diameter anode tungsten wire held at ground potential. Charged particles ionize the gas inside the tube, then the electric field between the tube and the wire creates an ionization cascade, which can be used to infer the energy of the original particle.

The 351,000 tubes are arranged in a barrel and two endcaps. In the barrel, 73 layers of 144 cm long tubes are parallel to the beamline, with wires slit in half to allow separate measurements for positive and negative z. In the endcaps, the 160 layers of 37 cm long tubes are arranged radially. The intrinsic resolution of the TRT in the barrel is 130 μm in $r\phi$ with coverage up to $|\eta| < 2.0$. A charged particle usually passes through 30 or more tubes.

When charged particles pass through a polymer fiber mat sitting between the tubes, transition radiation may be produced. These photons from transition radiation produce an ionization cascade much higher than the signal for tracking minimum-ionizing particles. Therefore, TRT straws have two signal thresholds: a *high threshold* for transition radiation hits and a *low threshold* for tracking hits.

Transition radiation, produced when a charged particle crosses the boundary between two media of different dielectric constants, is proportional to the Lorentz γ of a particle. For an electron and charged pion of equal momentum, the electron is about 3.7 times more likely to produce transition radiation than the pion since its mass is 200 times smaller. Seven to ten high threshold hits are typical when an electron passes through the TRT.

4.5 Calorimeters

The calorimeter system stops and measures the energy of electrons, photons and jets with full coverage in ϕ and $|\eta| < 4.9$. This is done with separate electromagnetic and hadronic calorimeters, both with barrel and endcap components. A forward calorimeter provides high η measurements. ATLAS calorimeters are sampling calorimeters, which means that only part of the shower energy is observed. Absorbing material used to initiate showers is interleaved with active material for detecting the showers. The layout of the calorimeters can be seen in Figure 4.10.

4.5.1 Electromagnetic calorimeter

The EM calorimeter has alternating lead absorbers and liquid argon (LAr) active medium with kapton electrodes. The barrel component covers $|\eta| < 1.5$ and the endcap component cover $1.4 < |\eta| < 3.2$. A presampler layer covering $|\eta| < 1.8$ measures showers starting before the calorimeter.

The barrel is segmented into three layers of decreasing segmentation. The first and second layers are important for identifying shower shapes, so they are finely segmented. The first layer has a thickness of 4.3 X_0, and the second layer has a depth of 16 X_0, which usually contains the majority of the energy of the EM shower. The third layer is a shallow 2 X_0 to

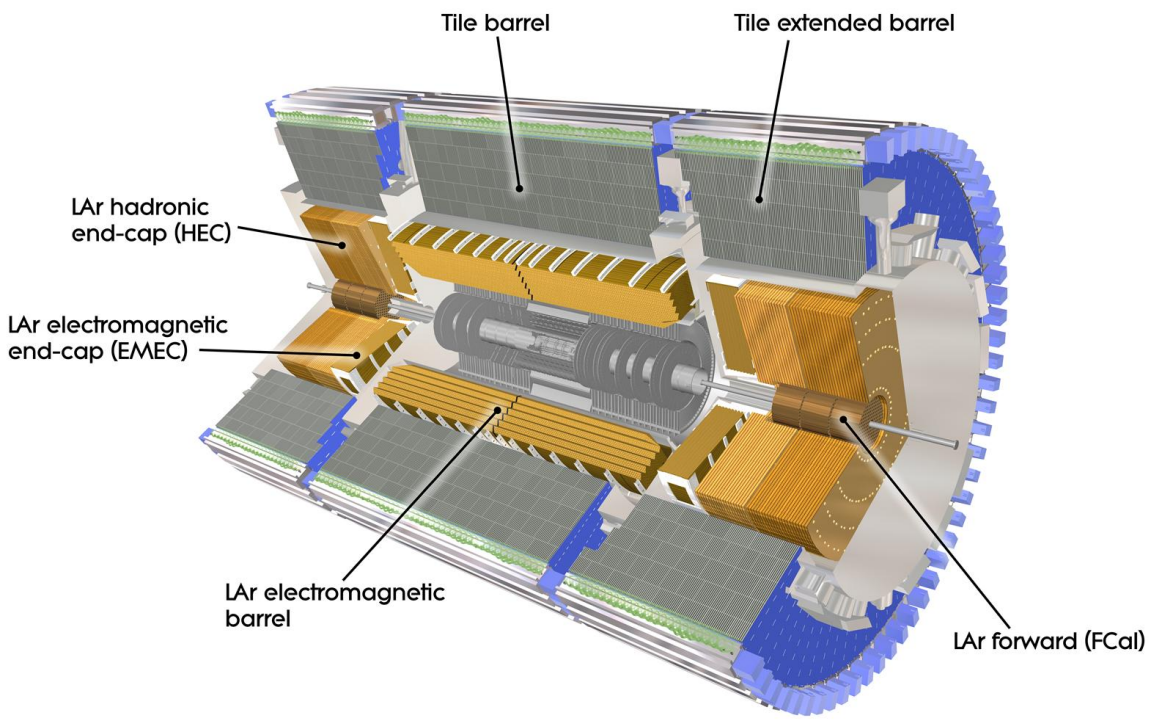

Figure 4.10: Cut-away view of the ATLAS calorimeter system [39].

capture any leftover energy after the first two layers. To provide prevent gaps in ϕ, the layers are bent into an accordion-like shape. A diagram of a barrel module is shown in Figure 4.11. The endcap of the EM calorimeter goes out to $|\eta| < 3.2$ and also has two layers, with an accordion shape oriented such that gaps in η are prevented.

4.5.2 Hadronic calorimeter

The hadronic calorimeter is divided into three components: the barrel tile calorimeter, which uses steel absorbers and scintillator tiles and covers $|\eta|$ <1.7; the Hadronic Endcap Calorimeter (HEC), which uses copper absorber and LAr active material and covers $|\eta|$¡3.2; and the forward calorimeter (FCal), which uses LAr active materials and covers $3.1 < |\eta| < 4.9$. The hadronic calorimeters are much coarser than the EM calorimeters because electrons and photons usually don't reach the radius of the hadronic calorimeters, so particle identification isn't a priority. Figure 4.12 shows a schematic of a hadronic tile module.

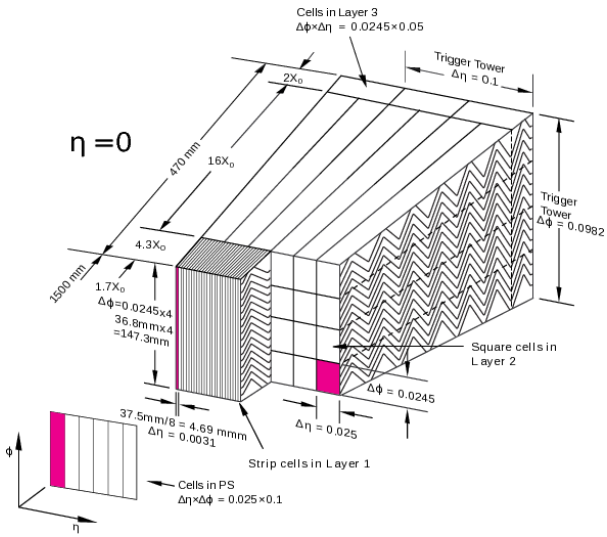

Figure 4.11: Diagram of an electromagnetic calorimeter barrel module[39].

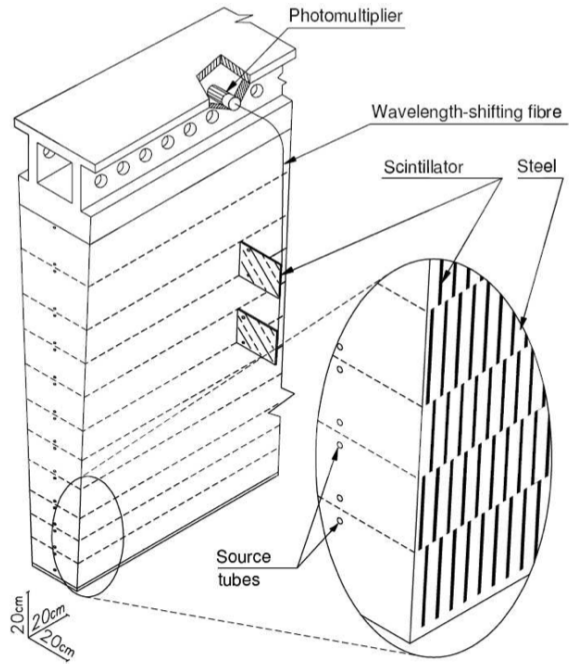

Figure 4.12: Diagram of a hadronic tile module[39].

4.5.3 Clustering

In order to identify particles, information from the shape of the calorimeter showers must be used. EM particles like photons and electrons produce narrow showers which are largely contained in the EM calorimeters. Hadrons produce broader showers and tend to travel farther into the hadronic calorimeters. Hadronic showers can also contain EM deposits from decays before the calorimeters, such as a neutral pion becoming two photons. In order to turn energy deposits in cells into clusters, information from all of the calorimeters is used as inputs to one of two principal algorithms[49]. The *sliding-window* algorithm clusters cells within fixed-sized rectangles. This algorithm is generally used for electron, photon and tau identification.

The second algorithm is the *topological* algorithm, which clusters together neighboring cells on the condition that the energy deposit in the cell is significantly more than the expected noise. This algorithm is generally used for jet and missing transverse energy reconstruction. The clusters that result from this algorithm are called *topoclusters.*

4.6 Muon System

The Muon System (MS) is the outermost subdetector, since muons are the only charged particles that can pass though the calorimeters [50]. The MS consists of a toroidal magnet

system and a charged particle tracking system. The components of the muon system, highlighted in Figure 4.13, are designed to measure the path and energy of muons, particularly high p_{T} muons which may indicate the presence of interesting physics.

The magnetic field provides the bending necessary for charge and momentum measurements and is comprised of three large air-core toroids. The toroid system has eight coils symmetrically around the beam and provides a magnetic field between 2 and 8 Tesla.

There are two types of tracking systems in the MS. The Monitored Drift Tubes (MDTs) precisely measure the track in the bending direction of the magnetic field and cover $|\eta| < 2.7$ in the outer barrel and cover $|\eta| < 2.0$ in the inner barrel. The MDTs are pressurized aluminum drift tubes filled with a mixture of argon and carbon dioxide gas, 30 mm in diameter. Each chamber has 3-8 layer of tubes and a resolution of 35 μm per chamber. The MDTs are limited to a counting rate of 150 Hz/cm^2 and thus cannot be used in the forward region of the inner layer, where high muon rates are expected. This region instead uses Cathode Strip Chambers (CSCs) for momentum measurement with better timing and spatial resolution. The CSCs cover the forward region of the inner layer, $2.0< |\eta| <2.7$. Two endcap wheels each have 16 chambers. Each chamber has 4 CSC planes. Each plane consists of two cathode strip planes sandwiching anodes wire. The arrangement of the CSCs gives resolution of 40 μm radial direction and 7 ns timing resolution.

The MS also has two types of trigger chambers: Resistive Plate Chambers (RPC) in the barrel and Thin Gap Chambers (TGC) in the endcaps. Just as with tracking, the endcap and barrel have different types of triggers due to the different rate and precision requirements. The barrel trigger system has 3 RPC layers, and the endcap trigger system has 4 TGC layers.

4.7 The trigger system

At hadron colliders, only a very small fraction of the proton-proton collisions can be feasibly recorded. The majority of events are low energy jets events that can be used for new physics searches or precision measurements like the Higgs are rarer. With bunch crossings every 50 ns, recording and reconstructing all of the collisions would take an unreasonable amount of data storage and computing power. It would also be impossible to write out events at this rate. Therefore, it is necessary to determine whether a collision will be recorded immediately after it occurs with minimal analysis.

The process quickly filtering events to record only those of physics interest is called *triggering.* Processes which take place in the trigger system are referred to as *online.* Processes which take place after triggering, such as particle reconstruction, are called *offline.*

The ATLAS trigger scheme[51] consists of three stages: Level 1 (L1), Level 2 (L2), and Event Filter (EF). All collision candidates are first run through L1, an online hardware trigger that has coarse granularity by necessity. If events pass the L1 trigger, they are then passed through the offline software triggers, collectively called the High Level Trigger (HLT) and divided into two stages: L2 and EF.

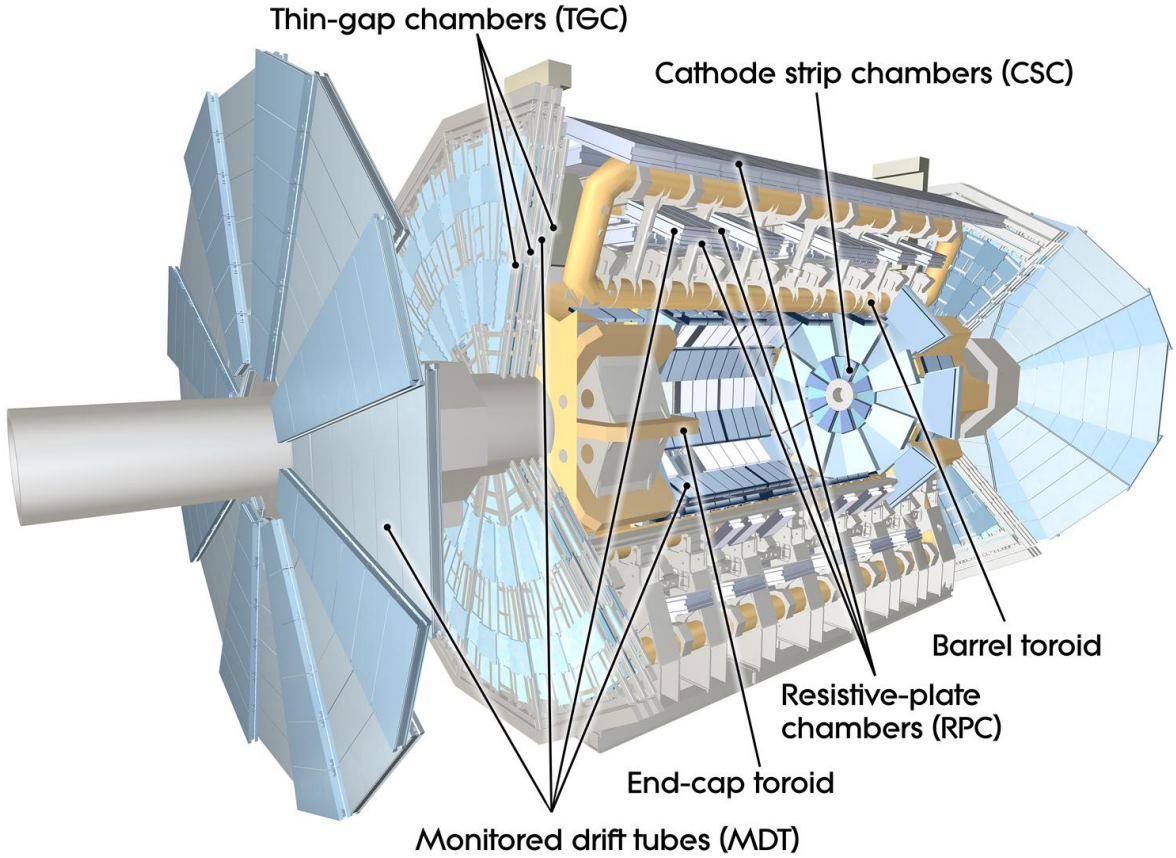

Figure 4.13: Diagram of the muon system[39].

Applying multiplicity and energy threshold requirements, L1 reduces the rate of events from 20 MHz (all pp collisions) to 75 kHz. The L1 trigger only looks at output from the calorimeters and muon system because the inner detector cannot process events at the rate required. In order to process events with the necessary speed, granularity in the calorimeter must be reduced and in the muon system, only the trigger chambers are read out. This reduction in granularity is illustrated in Figure 4.14. The maximum latency time to process at this level is 2.5 μs. The data-acquisition system must keep track of which data correspond to which bunch crossing. This presents a substantial challenge since the time for measuring a signal shape in the EM calorimeter is > 100 ns and the time of flight through the MS is > 25 ns, both longer than the time between events.

If the event passes the L1 trigger, then the L2 trigger looks at the distribution of energy deposits as Regions Of Interest (ROIs) identified by L1. The detector signals are compared to a menu of pre-programmed signatures that represent a potential physics object. For instance, a track and a cluster in the EM calorimeter might signal an electron. The L2 looks for these signatures in the ROIs by pulling information from all needed detectors.

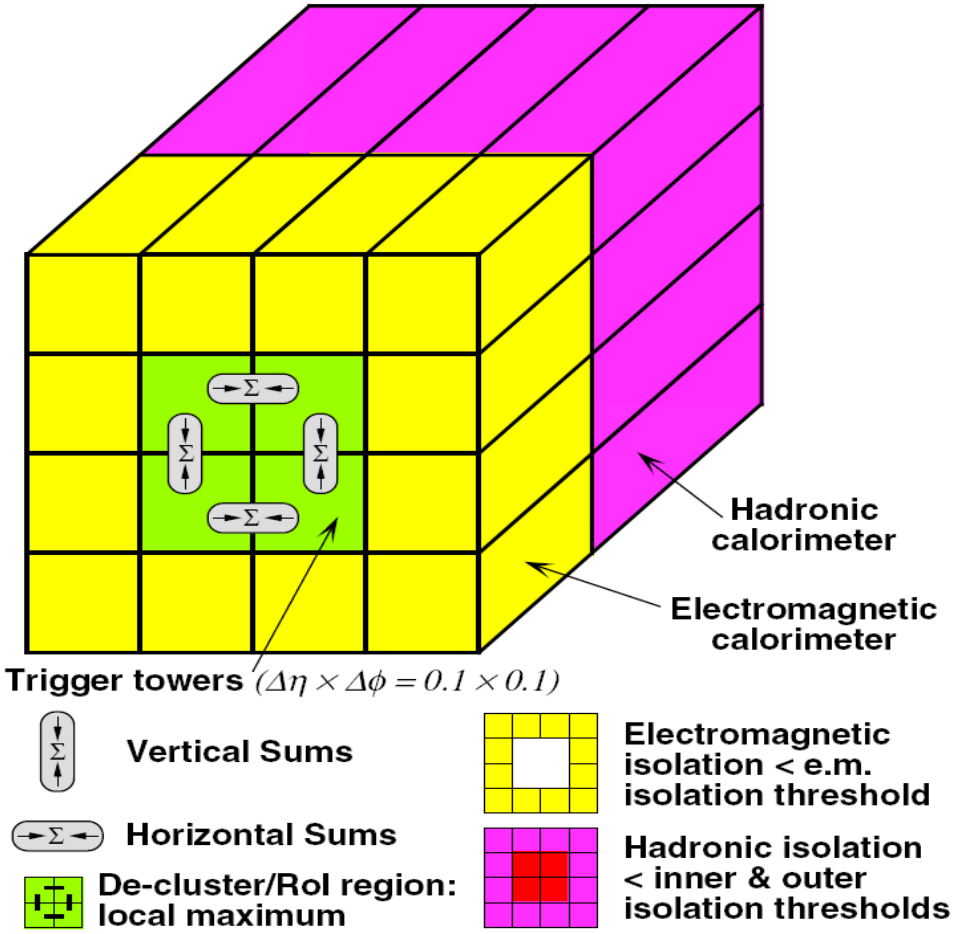

Figure 4.14: Schematic view of the calorimeter granularity available at the L1 trigger [51].

For events with signatures that pass the L2 trigger, all information for the event is read out and the standard offline reconstruction algorithm is run. The event can then be evaluated in terms of the fully reconstructed physics objects to see if particle identities and kinmatics match a menu of desired signatures. Finally, a decision about whether to record the event or not is made. This last stage of the triggering is called the Event Filter. The EF takes about 4s to process each event and can accept events at a rate up to 200 Hz.

4.7.1 Single electron trigger

The single electron trigger used for 2012 is fully described in [52]. At L1, calorimeters are split into 0.1×0.1 towers and then 2×2 clusters are used to identify e/γ leptons with the sliding window algorithm described in Section 4.5.3. Regions of 4×4 with clusters that meet isolation requirements are passed to the L2 trigger as ROIs. At L2, the position of the

cluster is identified as the energy-weighted average of the cluster. Track reconstruction is then performed and if a track can be matched to the cluster, it is considered to come from an electron, not a photon. At both L2 and EF, electron candidates are require to pass selection criteria based on the calorimeter cluster and the track, such as cuts on the lateral width of the shower and hits in the inner pixel detector.

In this analysis, the logical OR of two triggers is used to identify electrons: a 24 GeV trigger with a loose track-based isolation requirement and a 60 GeV trigger without an isolation requirement. The isolation requirement specifies that the sum of the p_{T} of tracks within a cone of ΔR=0.2 must be less than 10% the p_{T} of the electron. These trigger chains have thresholds that are maximally efficient for leptons passing offlines selections of $p_{\mathrm{T}} > 25$ GeV.

4.7.2 Single muon trigger

The single muon trigger used for 2012 is fully described in [53]. The muon trigger uses data from the RPCs in the barrel region and the TGCs in the outer region. At L1, the paths between hits in the trigger chambers are interpolated to identify muon candidates. If a hit pattern matches the requirements of the L1 trigger, the η and ϕ coordinates are passed to the L2 trigger as a ROI. At L2, the MDT and CSC information for the ROI are used to fit a higher quality track. Then, the track in the MS is combined with a track from the ID. Calorimeter data can be used to apply isolation requirements. Quality cuts are applied to the track to determine whether it passes the final trigger chain.

In this analysis, the logical OR of two triggers is used to identify muons: a 24 GeV trigger with a loose track-based isolation requirement and a 36 GeV trigger without an isolation requiment. The isolation requirement specifies that the sum of the p_{T} of tracks within a cone of ΔR=0.2 must be less than 12% the p_{T} of the muon. These trigger chains have thresholds that are maximally efficient for leptons passing offlines selections of $p_{\mathrm{T}} > 25$ GeV.

Chapter 5

Analysis strategy

Measurements of the activity of additional jets (jets not coming from the decay of top quarks) have been made by ATLAS [54, 55, 56] and CMS[57] using pp data with $\sqrt{s} = 7$ TeV. Comparison of the measured distributions with the predictions of Monte Carlo (MC) generators indicate that some state-of-the-art generators (e.g. MC@NLO) have a difficult time in reproducing the data, while for others agreement with data can be improved with appropriate choice of generator parameters. For example, in Powheg+Pythia adding a damping function that limits the resummation of higher-order effects incorportated into the Sudakov form factor improves the agreement between data and MC [55] at 7 TeV.

The range of predictions observed in standard MC generators for 8 TeV *pp* interactions is shown in Figure 5.1. The fiducial definition of these extra jets is provided in Chapter 8. Differences in rate as large as 40% are seen for jet multiplicities ≥ 5. Differences up to 20% for the leading jet and up to 40% for the subleading jet are seen at high jet transverse momentum.

This thesis presents a measurement of the multiplicity and differential cross section for additional (a.k.a. extra) jets produced in association with top quark decay products as a function of jet p_{T}. Events top quarks decaying to the the $e\mu$ final state with at least 2 b-tagged jets are used. Jets are constructed with the $R = 0.4$ anti-k_t algorithm. These additional jets are ordered in transverse momentum and labeled by *rank* i, such that $i = 1$ represents the leading (highest transverse momentum), $i = 2$ the subleading jet, *etc.*. The cross sections $\frac{1}{\sigma}\frac{d\sigma_{\mathrm{jet},i}}{dp_T}$ for $i = 1$ through $i = 4$ are measured and the multiplicity is measured for the number of jets $N_{Jets} = 1$ through $N_{Jets} = 4$ and inclusively for $N_{Jets} \geq 5$. Here σ is the fiducial production cross section for events containing a high p_{T} electron, a high p_{T} muon and two tagged b-jets, where all four objects are required to pass the fiducial selection: $p_{\mathrm{T}} > 25$ GeV and pseudorapidity $|\eta| < 2.5$, and where the additional jets in the event are required to have ${p_T}^i > 25$ GeV and $|\eta^i| < 4.5$. Thus $\int \frac{1}{\sigma}\frac{d\sigma_{\mathrm{jet},i}}{dp_T} d{p_T}^i$ gives the fraction of the accepted events that contain at least i jets.

The event selection employed here closely matches that used in the ATLAS 8 TeV cross section measurement[1]. The event rates and background estimates obtained are consistent with those obtained for that analysis and result in a sample with a greater than 99% purity

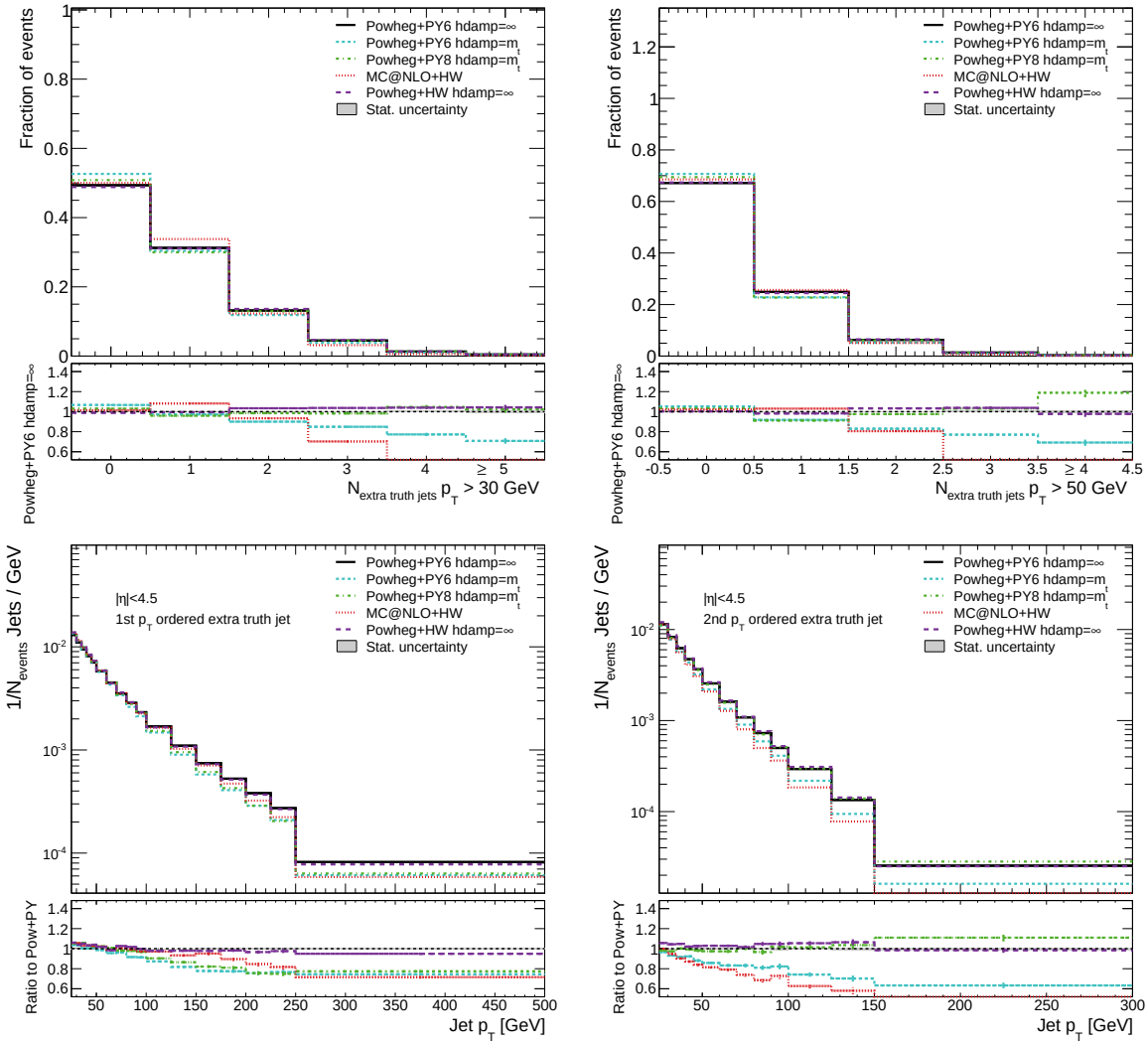

Figure 5.1: Comparison of the truth level extra jet multiplicity and p_{T} distributions in generated $t\bar{t}$ events with an opposite-sign $e\mu$ pair and at least 2 b-jets. Jets are reconstructed using the anti-k_t algorithm with the distance parameter $R = 0.4$. Each simulation is normalized by the number of events passing the truth-level selection. The ratio plots compare each generator to the predictions of the baseline POWHEG+PYTHIA sample with the hdamp parameter set to ∞.

for the dilepton plus two b-jet final state. More than 95% of the events that pass the reconstruction selection cuts also pass the truth fiducial requirements.

Rather than subtracting Wt events as background, this thesis measures the extra jets from both Wt and $t\bar{t}$ events that pass selection. This choice is motived by the following. At lowest order, the $e\mu + 2$ b-jet final state results from $t\bar{t}$ production where both the t and the $\bar{t}$ decay leptonically. Events where the leptons do not arise from W decay are suppressed by isolation and transverse momentum cuts on the leptons; they are treated as background and corrected for in the thesis. The distinction between $t\bar{t}$ and Wt final states cannot be made at NLO in QCD unless the top quark is stable. Once it decays to Wb, the same initial and final state appear in both processes, *e.g.* $gg \to W^+W^-b\bar{b}$ appears at LO and NLO via $gg \to t\bar{t} \to W^+W^-b\bar{b}$ or at NLO via $gg \to Wt\bar{b} \to W^+W^-b\bar{b}$. Quantum interference must occur and the classification into "$t\bar{t}$" and "Wt"is not possible. If restrictions are placed on the final state, this interference can be restricted and an approximate distinction made. For example, if a kinematic constraint is applied so both $W^-\bar{b}$ and W^+b have invariant mass equal to the top mass, the process is dominated by "$t\bar{t}$", if $W^-\bar{b}$ has an invariant mass far from the top quark mass "Wt" will dominate. No such kinematic constraint is applied in this thesis, so that any discussion of "$t\bar{t}$" and "Wt" contributions can only be made in simulation where samples labelled by "$t\bar{t}$" and "Wt" are used. In standard ATLAS MC samples, $\sim 3\%$ of the $e\mu + 2$ b-jet are assigned to the "Wt" process. This analysis chooses to treat this component as signal rather than background as it cannot separate them in a model independent manner. However, if a MC is used to fix the "Wt" component, then it can be subtracted from the data and comparisons with "$t\bar{t}$" MC made. The subtraction will introduce (small) additional systematic uncertainties.

Reconstructed jets not from the primary vertex are called *unmatched jets* and treated as background. Their origin can be studied using simulated samples. In the baseline MC simulation, $\sim 4\%$ of the events contain at least one reconstructed calorimeter jet that cannot be matched to a jet reconstructed from truth particles. The largest source of these unmatched jets is pileup interactions. A second source is attributable to detector effects which result in a single truth jet being reconstructed as two jets in the detector or where the separation ΔR between the reconstructed and truth jet exceeds the matching cuts. The rate of unmatched jets is determined as a function of jet rank and p_{T} and is subtracted from the reconstructed distribution before that distribution is unfolded.

The unfolding procedure used to correct the background-subtracted extra jet p_{T} distributions to the true spectra takes reconstruction efficiency and resolution effects into account. For events that pass the fiducial requirements at both the truth and the reconstruction level, a response matrix that maps between truth and reconstruction p_{T} and jet ordering is constructed using simulated data. The reconstructed spectrum is corrected for migration of jets with truth p_{T} below the 25 GeV cut but reconstructed p_{T} above it using a correction factor obtained from simulated data. Because the ordered full p_{T} distributions are corrected with a single unfolding matrix, cases where the relative rank of two reconstructed jets differs from of their associated truth jets are properly treated in the unfolding.

The unfolded jet p_{T} spectra provide unbiased measurements of the true transverse mo-

mentum distributions of the ordered jets for events passing the reconstruction-level event selection cuts. However, they do not provide an unbiased measurement of the distributions for events passing the truth fidicial selection. While most events that pass the reconstruction requirements also pass the selection cuts at truth level, the inverse is not the case. Only about 25% of the events passing the truth selection also pass reconstruction. Furthermore, the event selection efficiency depends on the kinematics of the top decays; regions of phase space where the top decay products have higher p_{T} are more likely to pass the selection criteria. The resulting bias on the unfolded distribution is corrected using bin-by-bin factors obtained from MC. These correction factors typically differ from unity by less than 10%.

The distribution obtained after applying this final correction is $\frac{1}{\sigma}\frac{d\sigma_{\mathrm{jet},i}}{dp_T}$. The multiplicity is obtained by integrating the differential p_{T} distribution separately for each jet rank.

Chapter 6

Object reconstruction

The analysis relies on the selection of electrons, muons, jets and b-tagged jets. This chapter reviews the reconstruction, definition, efficiencies and calibration of these objects in ATLAS.

6.1 Track reconstruction

Measurements from the three subdetectors of the ID are combined to make *tracks*, a description of the trajectory and momentum of each charged particle. The algorithm begins by finding track seeds in the inner silicon layers obtained by a window search algorithm. These seeds are then reconstructed into tracks with the ATLAS tracking algorithm[58].

The algorithm works first from the inside of the detector outward. Pattern recognition is used to make the pixel detector seeds into three-point track candidates. Then, a Kalman filter is used to add SCT hits radially outward. After ambiguities such as missing or shared hits are resolved, the tracks are extended into the TRT. Tracks are required to have $p_{\mathrm{T}} > 400$ MeV to be reconstructed. This cut was introduced to reduce the computation time for the pattern recognition algorithm. After this inside-out algorithm as been completed, an outside-in algorithm is run on the unused hits, to reconstruct secondary tracks left by particles not originating directly from the IP, for example kaon and lambda decay products.

Since charged particle tracks are bent by the magnetic field, the trajectory takes a helical form and can be expressed by 5 parameters:

d_0**:** the transverse impact parameter, equal to the distance of closest approach in the plane transverse to the beam of the track to the primary vertex

z_0**:** the longitudinal impact parameter, equal to the z coordinate of the point of closest approach to the primary vertex

ϕ_0**:** the azimuthal angle of the trajectory at the point of closest approach to the primary vertex

$\cos\theta$**:** the cosine of the angle the track forms with respect to the beam

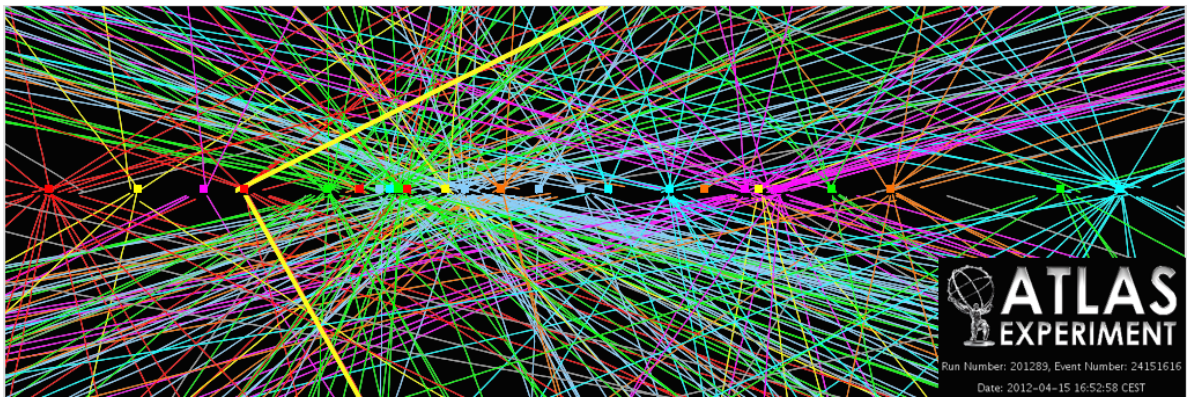

Figure 6.1: Display of a 2012 event with 25 reconstructed vertices [60].

q/p_T**:** the charge divided by the momentum in the transverse plane.

6.2 Primary vertex reconstruction

A primary vertex reconstruction algorithm determines if many tracks originate from the same pp collision[59, 58]. The vertices are reconstructed with an iterative fitting procedure. Initially, a vertex seed is created from a fit to the global maximum of the z coordinates of the tracks. Then, tracks are matched to the seed using a χ^2 algorithm. Incompatible tracks are used to seed a new vertex until all tracks are associated with a vertex.

Since several pp collisions are likely to occur for each bunch crossing, some of the tracks will be associated with secondary vertices from pileup rather than the primary vertex (PV) from the hard collision. The PV is conventionally defined as the vertex with the highest track p_{T}^2. In 2012, the average number of interactions per crossing was 20.7, as shown in Figure 4.4, so primary vertex reconstruction is essential for determining which particles came from pileup. If a track isn't associated with the PV, it is typically considered pileup. Figure 6.1 shows an event with 22 vertices, demonstrating the important of tracking and vertexing in events with high pileup.

6.3 Muons

Muons are reconstructed by combining tracks found in the muon spectrometer and inner detector. Track segments are found in each layer of the detector then combined, taking into account energy loss while crossing the calorimeters. Tracks in the ID are required to pass minimum hit requirements in the Pixel, SCT, and TRT. Muons can be reconstructed using only the MS, but in this analysis uses *combined* muons (reconstructed in both the MS and ID) to ensure high purity.

The muon reconstruction efficiency can be measured using the *tag-and-probe* method. The ID reconstruction efficiency is determined from events reconstructed with one combined muon, the *tag*, and a second muon only required to have an MS track, the *probe*. The ID reconstruction efficiency is given by the fraction of events where the MS track probe also has a track in the ID. The same method can be used to determine the efficiency of the MS reconstruction. This time, the ID segments are used as the probe and the MS+matching efficiency is given by the fraction of ID segments with a matching MS segment. The overall muon reconstruction efficiency is given by the product of these two efficiencies. To obtain the scale factors (SF), the muon reconstruction efficiency in data and MC is compared: $SF = \epsilon_{data}/\epsilon_{MC}$. These scale factors are applied to the simulation to ensure that muons are reconstructed with the same efficiency in MC as in data. For muons, the SFs are calculated in bins of p_{T} and η using $Z \to \mu\mu$ and $J/\Psi \to \mu\mu$ events [61].

The muon momentum scale and resolution of the MC must also be corrected to match data. Differences can come from mis-modeling of the detector geometry, magnetic field, or energy loss in the calorimeter. Scale factors are determined by comparing the shape of the energy distribution in $Z \to \mu\mu$ and $J/\Psi \to \mu\mu$ events. For 2012, the corrections were less than 0.1% [61].

Finally, the efficiency of the muon trigger is also estimated via the tag-and-probe method. In this analysis, the logical OR of two triggers is used to identify muons: a 24 GeV trigger with a loose track-based isolation requirement (the sum of the p_{T} of tracks within a cone of ΔR=0.2 must be less than 12% the p_{T} of the muon) and a 36 GeV trigger without an isolation requirement. For $p_{\mathrm{T}} < 100$ GeV, $Z \to \mu\mu$ events are used to estimate the trigger efficiency, while W+jets is used for p_{T} above this threshold. The muon trigger efficiency in the barrel region is derived from $Z \to \mu\mu$ events is shown in Figure 6.2.

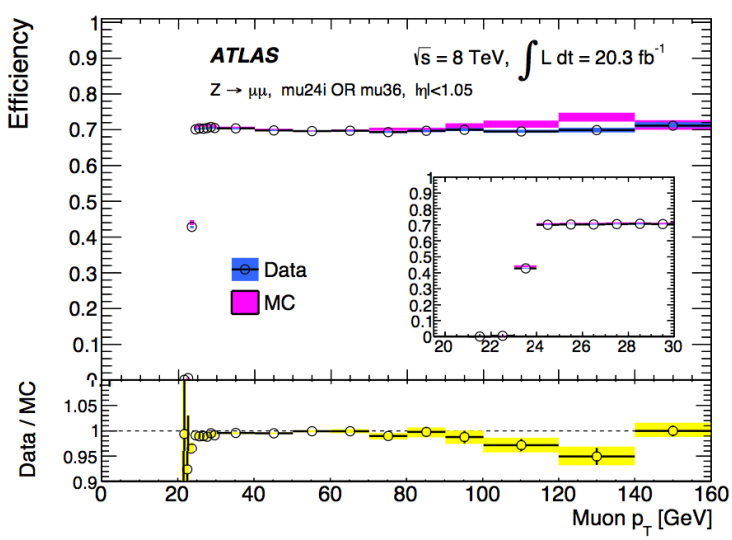

Figure 6.2: Reconstruction and identification efficiency for the muons as a function of p_{T} [62].

6.4 Electrons

The reconstruction of electrons uses information from both the EM calorimeters and tracks in the ID. First, clusters of energy are found using the sliding-window algorithm described in Chapter 4.5.3. Then, tracks reconstructed in the ID are extended into the calorimeter. Tracks and clusters are considered a match if the center of the cluster and the track are within $\Delta\eta$ <0.05 and $\Delta\phi$ <0.1. Clusters that don't match to a track are considered as candidate photons [62].

Quality requirements divide electron candidates into three categories: loose, medium and tight. In this analysis, electrons are required to match the tight requirements, such as ID hit requirements, shower shape, track quality and tighter criteria for matching tracks and clusters. The total reconstruction and identification efficiency for these tight electrons is shown in Figure 6.3. As with muon reconstruction, tag-and-probe methods determine the electron reconstruction scale factors using $Z \to ee$ events.

The electron energy scale of the MC must be corrected to match data. First, the MC simulation of electron response is used as a initial calibration of the electron energy. Then, the absolute energy scale and resolution are determined by comparing $Z \to ee$ events in data and MC. This calibration is then checked against $J/\Psi \to ee$ events.

In this analysis, the logical OR of two triggers is used to identify electrons: a 24 GeV trigger with a loose track-based isolation requirement and a 60 GeV trigger without an isolation requirement. The isolation requirement specifies that the sum of the p_{T} of tracks within a cone of ΔR=0.2 must be less than 10% the p_{T} of the electron. The trigger efficiency is evaluated with a tag-and-probe of $Z \to ee$ events, using the tight electron matched to a trigger with a lower threshold as a tag and an electron with opposite charge as a probe. This efficiency is shown in Figure 6.4.

The electron trigger efficiency is measured using tag-and-probe in $Z \to ee$ events, where the tag is a tight electron matched to a trigger with a lower threshold and the probe is an oppositely charged electron such that the ee system has invariant mass within the Z mass window of 80-100 GeV. The measured efficiency is shown in Figure 6.4.

6.5 Jets

Jet reconstruction begins with the formation of *topo-clusters* from energy deposits in the EM and hadronic calorimeter cells as described in Chapter 4.5.3. Once the clusters have been built, they are used as input to the the anti-k_t algorithm [35, 36, 63] with radius parameter $R = 0.4$. In addition to jets from calorimeter clusters, *track-jets* are also constructed from charged particle tracks for calibration purposes. The final 4-momentum of the jet is defined as the sum of the 4-momenta of its constituents.

At this stage, the jet reconstruction efficiency and its uncertainty can be measured in data using the fraction track-jets matched to calorimeter jets. The efficiency can also be calculated using a tag-and-probe method in dijet events. The reconstruction inefficiency is

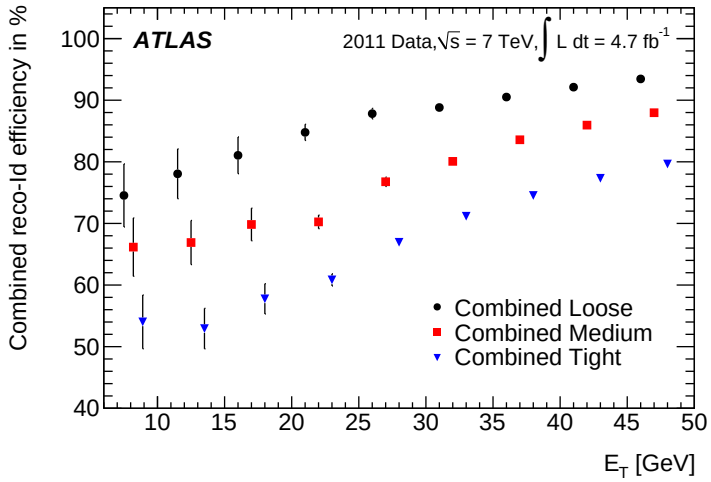

Figure 6.3: Reconstruction and identification efficiency for the electrons as a function of E_T [62].

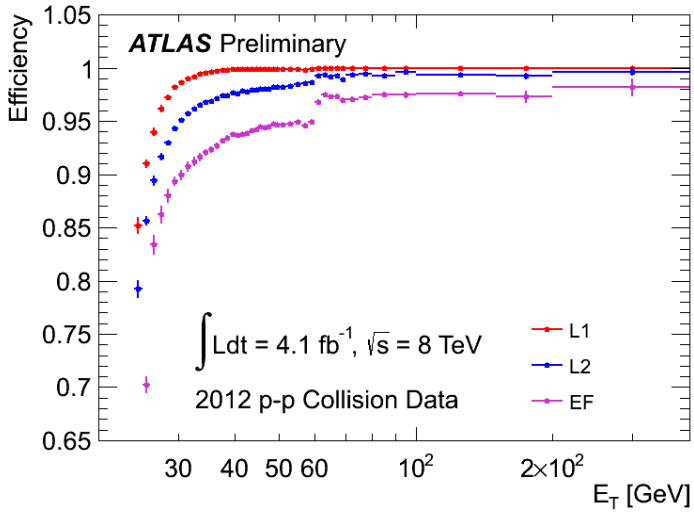

Figure 6.4: Combined efficiency of the 24 GeV and 60 GeV electron triggers. [52].

found to be very small: about 0.0002% for jets with $p_{\mathrm{T}} < 20$ GeV and negligible for jets with higher p_{T}.

The jets are first corrected for the effects of pileup using the jet area method [64]. This method corrects the p_{T} of the jet by subtracting $\rho \times A$. The quantity ρ is defined as the the energy density in the event calculated from all calibrated topo-clusters within $|\eta| \leq 2$, and the quantity A is defined as the catchment area of the jet. This correction depends both on the characteristics of the jet and the pileup in the event. Then a residual correction dependent on the instantaneous luminosity and number of reconstructed primary vertices in the event is made. This correction is primarily relevant in the forward region and is derived from simulation.

The jets are then calibrated using a function that depends on both energy and η [64]. The jet direction is corrected so that the jet originates from the primary vertex. Next, the energy scale of the jet (JES) correction is applied, which has both an MC-based and *in situ* component. The energy- and η-dependent MC-based JES scheme is derived from the ratio of the energy of a detector level jet to the matching truth level jet (jets formed using the same anti-k_t algorithm from simulated hadrons). The *in situ* correction uses data events where a jet recoils against a Z or a photon, which can be more precisely measured by the detector. However, this method can only be used for jets with $p_{\mathrm{T}} < 800$ GeV. Jets with $p_{\mathrm{T}} > 800$ GeV are calibrated with events where a high p_{T} jet recoils against a several lower p_{T} jets already calibrated by the Z or photon events. The final JES and uncertainty comes from a combination of such measurements. Figure 6.5 shows the JES uncertainty for jets in the central η region ($|\eta| < 2.5$). The jet energy resolution (JER) is studied separately via a similar process with dijet events, and the resolution in data and simulation is found to be comparable.

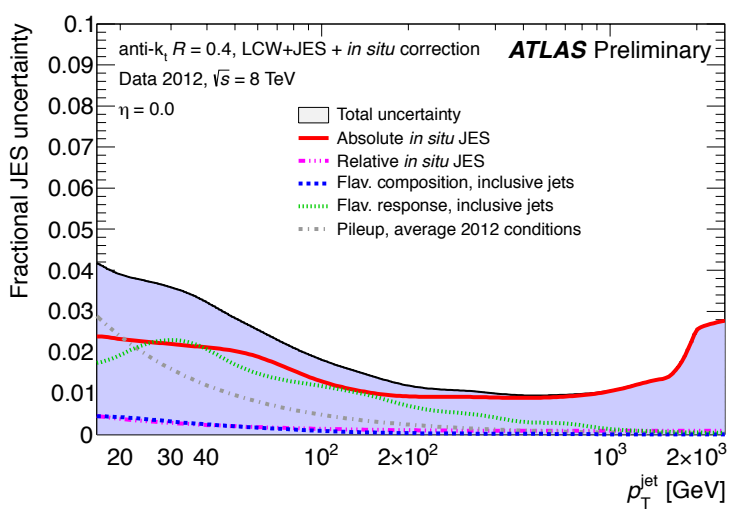

Figure 6.5: The relative Jet Energy Scale (JES) uncertainty for jets in the region [64].

6.6 b-tagged Jets

At the LHC, jets that contain b-quarks (called b-jets or b-tagged jets) can be distinguished from jets which only contain light quarks[65, 66]. The long lifetime of B-hadrons is exploited to make this distinction. Because a B-hadron will travel a relatively long path through the detector before decaying, a *secondary* vertex for this decay can be reconstructed and used to identify jets which contain a b-quark. The production of a top quark pair produces at least two b-jets (which are otherwise rare), so identifying b-jets leads to significant background reduction.

At the ATLAS detector, several algorithms are used in conjunction to identify b-jets:

IP3D is an impact parameter based algorithm that uses the tracks associated with the jet. First, tracks must pass quality cuts on the number of hits in the ID. Then, tracks are required to have $|d_0| < 1$ mm and $z_0 < 1.5$ mm in order to reject tracks from the decays of long-lived mesons, such as kaons, and photon conversion. These tracks are then associated to the jet with a jet p_{T} dependent ΔR. Then, the algorithm uses the impact parameters' significance, $d_0/\sigma(d_0)$ and $z_0/\sigma(z_0)$, to produce the likelihood for tracks to originate from a b-jet. The likelihood distribution is produced from simulation.

SV1 is an algorithm based on the secondary vertex. The tracks associated with the jet are required to pass quality cuts similar to IP3D. Next, all possible two-track vertices are considered. Vertices with masses compatible with long-lived particles like kaons or Λ have both tracks removed from the list of associated tracks. Then, all remaining two-track vertices are combined into a single vertex and the track with the worst fit is removed. This procedure is repeated until the overall χ^2 of the track errors to the vertex passes a quality threshold. Finally, a likelihood ratio technique is used to assign a b-tagging weight, using variables such as the secondary vertex mass, the number of two-track vertices, and the angle between the vertices and jet axis.

JetFitterCombNN uses the same tracks as IP3D. The algorithm attempts to find an axis and decay position of the B-hadron, including the possibility of an extra vertex due to a D-decay. A Kalman filter is used to start with the axis from the PV to the jet axis and update with addition of each track in the decay chain. The best combination of two vertices that fits the tracks is found. Then the decay length significance ($d_0/\sigma(d_0)$), the invariant mass of the tracks and the energy fraction of the tracks are combined into a neural network. The output of the neural network gives the likelihood that the jet is a light-, c-, or b-jet.

The results from these three algorithms, IP3D, SV1 and JetFitterCombNN, are combined into a single discriminant using a neural network with the MV1 b-tagger. The efficiency of these algorithms in rejecting light-jets and c-jets is shown in Figure 6.6.

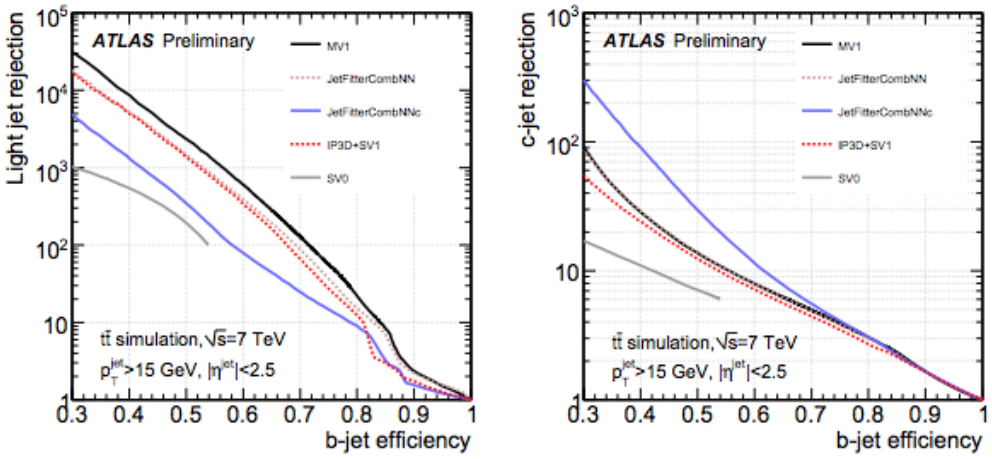

Figure 6.6: Light-jet rejection (left) and c-jet rejection (right) as a function of the b-tag efficiency for the b-tagging algorithms discussed based on simulated $t\bar{t}$ events. [66].

Chapter 7

Event selection

The following section describes the procedure used to select the events used for analysis. First, the data and simulation samples to be used are defined. Then, the fiducial definition of the physics objects used to select the events is given. Then, the criteria for selecting events is discussed. Finally, the event yields and reconstructed distributions are reviewed.

7.1 Data samples

7.1.1 Collision data

The analysis is performed on the complete 2012 pp $\sqrt{s}$ =8 TeV LHC collision dataset. Events are required to fulfill standard data quality requirements that ensure that all detector components are functioning. Events are required to pass a single electron or single muon trigger chain, with thresholds that are maximally efficient for leptons passing offline selections of $p_T > 25\,\text{GeV}$.

Events are selected from both `Egamma` and `Muons` data streams defined by the trigger chains. To avoid double counting of $e\mu$ events appearing in both streams, events passing electron triggers are only accepted from the `Egamma` stream, *i.e.* the `Muons` stream is only used for events selected *only* by muon triggers. After all these selections, the final analyzed data samples correspond to an integrated luminosity of $20.3\,\text{fb}^{-1}$ with an uncertainty of 2.8%.

7.1.2 Simulated Samples

Simulated Monte Carlo event samples are used in this analysis to evaluate the efficiency and uncertainty of signal and background. Both uncorrected and corrected data distributions are also compared to simulated samples to distiguish between physics models. .

Samples are processed either through the full ATLAS Geant4[23] based detector simulation ("FS") or through the `AtlFast2`[67] fast simulation. All samples include additional overlaid minimum bias events generated with Pythia8 [68] to simulate pileup background. The simulated samples are reweighted to reproduce the same distributions of μ, the average

number of interactions per bunch crossing, as the data. The samples are also reweighted with scale factors to reproduce the electron and muon reconstruction and trigger efficiencies, and the width of the primary vertex distribution in z, as measured in the data. Finally, scale factors are applied to account for b-tagging efficiencies.

7.1.2.1 $t\bar{t}$ samples

Several different $t\bar{t}$ generators are compared to data. The baseline $t\bar{t}$ samples are produced using Powheg [27, 28, 29, 30] interfaced to Pythia6 [22] with the Perugia 2011C tune [69], CT10 parton density functions (PDFs) [70], the hdamp parameter set to ∞ and fast simulation. This same MC tune has been processed using full simulation and the results of the two samples have been compared. The atlfast2 sample with the hdamp parameter set to ∞ is chosen as the baseline because it has signifigantly higher statistics ($\sim$ 40 times data) than either the FS or hdamp=m_t samples ($\sim$ 20 times data). Systematic uncertainties associated with the difference in the response matrices obtained from FS and atlfast are assessed in Chapter 10.

Alternative $t\bar{t}$ simulation samples are also studied. At next-to-leading-order, these include Powheg plus Pythia6 with the hdamp parameter set to m_t; Powheg plus Pythia8 with the hdamp parameter set to m_t and the A14 tune ; MC@NLO [25, 26] interfaced to Herwig [21, 71, 72] with Jimmy [73] for the underlying event modeling and with the ATLAS AUET2 [74] tune and CT10 PDFs; and Powheg plus Herwig. Alternate multi-leg leading order samples include MadGraph [75] interfaced to Pythia6 [22] with the Perugia 2011C tune [69], and CT10 parton density functions (PDFs) [70]; Alpgen [76] interfaced to Herwig and Jimmy, with the CTEQ6L1 PDFs [77]; and Alpgen interfaced to Pythia6 . To study the effects of initial and final state radiation (ISR/FSR), several samples with different radition parameters were used.

The Powheg and MC@NLO samples include all $t\bar{t}$ final states except fully-hadronic, where both W bosons decay to $q\bar{q}$ giving a negligible probability to pass the event selection. The MadGraph sample only included dileptonic final states, where both W bosons decay to leptons. Most of these MC samples contain more than ten times the data statistics.

7.1.2.2 Single top samples

Only the Wt channel of single top production contributes significantly to $e\mu+2$ b-jets events. Single top production is modeled using Powheg+Pythia with the CT10 PDFs and the Perugia P2011C tune, using the 'diagram removal' [78] generation scheme. Alternative physics models include the Powheg+Pythia sample with 'diagram subtraction' [78] and MC@NLO+ Herwig.

7.1.2.3 Background samples

Z+jets events with $Z \to \ell^-\ell^+$ and diboson production (WW, WZ and ZZ) where both bosons decay leptonically can contribute to background. Z+jets background is modeled

using ALPGEN [79] with CTEQ6L1 PDFs, interfaced to PYTHIA6 with the Perugia P2011C tune, including both samples with 0–5 additional light partons, $c\bar{c}$ plus an additional 0–3 partons, and $b\bar{b}$ plus 0–3 partons. The heavy flavor overlap procedure (HFOR) [80] is used to avoid double counting of configurations where the $c\bar{c}$ or $b\bar{b}$ pair could be produced from either the matrix element or parton shower. The simulated Z+jets events are scaled by the ratios of $Z \to ee$+2 b-jets or $Z \to \mu\mu$+2 b-jets measured in simulation and data, to account for the mismodeling of heavy-flavor jets produced with Z bosons. Ref. [1] computes this scale factor to be 1.13 ± 0.08.

Diboson production is simulated using ALPGEN+HERWIG with up to three additional partons.

7.1.3 Pileup jet samples

Modeling of pileup collisions (see Chapter 4) is studied both using the default POWHEG+PYTHIA hdamp=∞ generator as well as a data driven estimate. The data driven *overlay* sample takes pileup events from data and combines them with $t\bar{t}$ events from POWHEG+PYTHIA hdamp=∞. The difference between these two estimates is taken as a systematic uncertainty.

7.2 Object definitions

The object and event selection used in this thesis follows the generic ATLAS recommendations for 2012, with two exceptions. The first change is a loosening of the electron isolation criteria, which is possible due to the low background $e\mu$ final state. This loosened requirement is also used in Ref. [1]. The second change is to relax the η requirement on jets to $|\eta| < 4.5$.

7.2.1 Reconstructed objects

The analysis relies on the selection of electrons, muons and jets, and the tagging of jets as b-jets.

Muons: Combined muons (reconstructed in both the muon spectrometer and inner detector) are required to satisfy $p_T > 25\,\text{GeV}$ and $|\eta| < 2.5$. Muons must have

- at least one pixel hit
- at least 5 SCT hits
- fewer than 3 holes in pixel and SCT layers combined
- In the region $0.1 < |\eta| < 1.9$: $n_{TRTHits}+n_{TRTOutliers} > 5$ and $\frac{n_{TRTHits}}{n_{TRTHits}+n_{TRTOutliers}} < 0.9$, where an outliter is a TRT straw with a signal but not crossed by the nearby track.

The impact parameter in the longitudinal direction with respect to the primary vertex is required to satisfy $z_0 < 2\,\mathrm{mm}$. To reduce the background from muons from heavy flavor decays inside jets, muons are required to be separated by $\Delta R > 0.4$ from the nearest jet. Muons are required to satisfy mini-isolation requirement $I^{\ell}_{mini} < 0.05$, where the mini-isolation variable is the ratio of the sum of p_T of tracks in a variable-sized cone of radius $\Delta R = 10\,\mathrm{G}eV/p_T(\mu)$ to the p_T of the muon $p_T(\mu)$ [81].

Electrons: Electrons are selected using the offline `tight++` identification within the fiducial region $p_T > 25\,\mathrm{GeV}$ and $|\eta| < 2.47$, excluding the calorimeter transition region $1.37 < |\eta| < 1.52$. The impact parameter in the longitudinal direction with respect to the primary vertex is required to satisfy $z_0 < 2\,\mathrm{mm}$. In addition to the calorimeter isolation requirements implicit in `tight++`, the calorimeter energy in a cone of radius $\Delta R < 0.2$ around the electron (excluding the deposit from the electron itself) is required to be less than $6\,\mathrm{GeV}$, and the sum of p_T of tracks in a cone of radius $\Delta R < 0.3$ (excluding the electron track) is required to be less than 6 GeV. Further kinematic-dependent cuts are applied to these two isolation variables, corresponding to a 98 % efficiency on true prompt electrons.

Overlap removal: To prevent double-counting of electron energy deposits as jets, jets within $\Delta R < 0.2$ of a reconstructed electron are removed. If the nearest jet surviving the above cut is within $\Delta R < 0.4$ of the electron, the electron is discarded, to ensure it is cleanly separated from nearby jet activity. Electrons sharing a track with a muon are excluded by removing electrons with a muon within $\Delta\phi < 0.005$ and $\Delta\theta < 0.005$.

Jets: Jets are reconstructed using the anti-k_t algorithm [35, 36, 63] with radius parameter $R = 0.4$, starting from topological clusters. These are calibrated using the local cluster weighting (LCW) method, and corrected for the effects of pileup using the jet area method and a residual correction dependent on the instantaneous luminosity and number of reconstructed primary vertices in the event. Jets are calibrated using an energy- and η-dependent simulation-based calibration scheme, with in-situ corrections based on data [82]. Jets are accepted within the fiducial region $p_T > 25\,\mathrm{GeV}$ and $|\eta| < 4.5$. To reduce the contribution from jets associated with pileup jets with $p_T < 50\,\mathrm{GeV}$ are required to satisfy $|\mathrm{JVF}| > 0.5$, where JVF is the ratio of the sum of the p_T of tracks associated to the jet which are also associated to the primary vertex, to the sum of p_T of all tracks associated to the jet. Jets with no associated tracks or with $|\eta| > 2.4$ at the edge of the tracker acceptance are assigned $\mathrm{JVF} = -1$ by convention and thus always accepted. Reconstructed jets within $\Delta R < 0.2$ of a selected electron are removed.

***b*-tagging:** Jets within the central region ($|\eta| < 2.5$) are b-tagged using the MV1 algorithm [65, 66], which outputs a multivariate discriminant w with values between zero and one. Light-quark and gluon jets tend to have values close to zero, and b-flavored jets close to one, with charm jets somewhere in between. Jets are defined as being b-tagged if the

MV1 weight w is larger than a cut value 0.7892, which corresponds to the b-tagging working point having approximately 70% b-tagging efficiency for b-jets in $t\bar{t}$ events, although the exact efficiency varies significantly with p_T. The b-tagging calibration used is the default in `TopRootCore`, which is based on the system8 muon and jet calibration method [83].

Events reconstructed with exactly one e and μ with opposite sign and at least 2-b jets as defined above pass the reconstruction-level fiducial selection. In the case of Monte Carlo, selected events are reweighted to reproduce the same distributions of μ, the average number of interactions per bunch crossing, as in the data. The samples are also reweighted with scale factors to reproduce the electron and muon reconstruction and trigger efficiencies, and the width of the primary vertex distribution in z, as measured in the data. Finally, scale factors are applied to account for b-tagging efficiencies.

7.2.2 Truth objects

In addition to fiducial definitions for reconstructed from detector output, fiducial definitions for the "true" particles generated by the MC simulation must be made. The cuts applied to truth objects attempt to replicate the above fiducial selections for the reconstructed objects as closely as possible.

Leptons: Stable electrons and muons are required not to come from a hadron in the Monte Carlo truth particle record, either directly or through a tau decay. This ensures that the lepton is from an electroweak decay without requiring a direct W-boson match. The four momenta of the bare leptons are then 'dressed' by adding the four momenta of all stable photons within ΔR=0.1 with status code 1 and not originating from Geant4. The dressed leptons are required to have $p_{\mathrm{T}} > 25$ GeV and $|\eta| < 2.5$.

Jets: Truth jets are clustered using the anti-k_t algorithm with radius parameter $R = 0.4$, starting from all stable particles, except for selected leptons (e, μ, ν) and the photons used to dress the leptons. Truth jets are required to have $p_{\mathrm{T}} > 10$ GeV, $|\eta| < 4.5$. Though only jets with $p_{\mathrm{T}} > 25$ GeV are considered in the final result, lowering the p_{T} requirement for truth jets allows matching across the fiducial boundary. This is discussed in more detail in Chapter 8.

b-tagging: B hadrons with $p_{\mathrm{T}} > 5$ GeV are associated with jets through ghost matching [84]. Truth b-tagged jets have $p_{\mathrm{T}} > 25$ GeV, $|\eta| < 2.5$ and at least one ghost associated B-hadron with $p_T^{\mathrm{B}} > 5$ GeV.

Overlap removal: Truth objects are subject to the same overlap removal criteria as reconstructed objects, after dressing and jet reclustering. The closest jet within $\Delta R < 0.2$ of an electron is excluded from consideration. After such jets are removed, muons and electrons with $\Delta R < 0.4$ of a jet are excluded. Electrons overlapping with muons are removed if $\Delta\phi_{e\mu} < 0.005$ and $\Delta\theta_{e\mu} < 0.005$.

Events with exactly one e and μ with opposite sign and at least 2-b jets as defined above pass the fiducial truth selection.

7.2.3 Truth matching

In order to correct reconstructed objects back to truth level, a prescription must be adopted to match reconstructed and truth objects. A geometric ΔR algorithm matches reconstructed objects to truth objects satisfying the fiducial requirements above. These definitions are relevant for background unmatched extra jets, as well as various truth studies.

Leptons: Each truth e (μ) is matched to the closest reconstructed e (μ) within $\Delta R < 0.02$.

Jets: Truth jets are geometrically matched to the closest reconstructed jet within $\Delta R_{\text{recojet,truthjet}} < 0.4$. If a reconstructed jet is not matched to a truth jet, it is assumed to be either from pileup or matching inefficiency and is treated as background as discussed in Chapter 8.2.

In selecting $e\mu$+2 b-jet events, b-jets are matched to truth jets before extra jets are matched to truth jets. Thus, if both an extra jet and a b-jet satisfy $\Delta R_{\text{recojet,truthjet}} < 0.4$, the b-jet is matched to the truth jet and the extra jet is unmatched. If two b-jets or two extra jets are reconstructed within $\Delta R_{\text{recojet,truthjet}} < 0.4$ of a single truth jet, the reconstructed jet with smaller $\Delta R_{\text{recojet,truthjet}}$ is matched to the truth jet and the other reconstructed jet is unmatched.

Because of limited p_{T} resolution, the reconstructed p_{T} of a jet can vary significantly from its truth p_{T}. The p_{T} threshold for truth jets is lowered to 10 GeV, so that jets reconstructed with $p_{\text{T}} > 25$ GeV can match truth jets that fail the fiducial p_{T} cut.

Parton matching: For some studies, the truth jets from top are identified via a parton matching procedure. Each jet is matched to the highest energy parton[1] with $p_{\text{T}} > 5$ GeV within $\Delta R = 0.4$. If this parton is a decay product of the top, then the jet is considered a 'top jet.'

7.3 Event selection

The process of selecting $e\mu + 2$ b-jets events proceeds as follows. First, events are selected from simulation and data by vetoing a small number of events failing cleaning cuts defined below. Then events are required to have exactly one electron and one muon with opposite charges. Finally, events with at least two b-tagged jets are selected. In events with more than two b-tagged jets, the two b-jets with the highest MV1 are considered the b-jets used to select the event and the remaining b-jet(s) are considered extra jets. The selection requirements are identical to those in the 2012 $t\bar{t}$ cross-section analysis [1], with the exception of requiring *at least* two b-tagged jets instead of *exactly* two.

[1] Quarks (u,d,s,c,b), gluons, photons and pdgId = 0 particles.

7.3.1 Cleaning cuts

Events are required to have at least one reconstructed primary vertex with at least five associated tracks. Events containing any jets with $p_T > 20$ GeV and positive energy that fail the 'Bad Loose Minus' (also known as 'Looser') jet quality cuts [85] are removed ('jet cleaning'). To remove events containing cosmic rays, events with two muons passing the muon selection requirements given above, each having an impact parameter with respect to the primary vertex $d_0 > 0.5\,\mathrm{mm}$ and separated in azimuthal angle ϕ by $\Delta\phi > 3.1\,\mathrm{rad}$, are vetoed.

A muon undergoing catastrophic bremsstrahlung/energy loss in the calorimeter can leave a large energy deposit, causing it to be reconstructed as both an electron and a muon, and potentially giving rise to a fake $e\mu$ event. Such background is reduced by vetoing $e\mu$ events if the electron and muon are separated by $\Delta\phi < 0.005$ and $\Delta\theta < 0.005$, where ϕ and θ are the azimuthal and polar angles of the selected leptons (muon bremsstrahlung cut).

7.3.2 Event yields

The numbers of events with exactly one e and one μ before and after the b-jet requirement are given in Table 7.1. Simulation predictions are categorized into contributions from $t\bar{t}$, Wt single top, Z+jets and dibosons.

After the selection of $e\mu$ opposite-sign pairs, the biggest contribution (60%) is from $t\bar{t}$ events with the second largest from Z+jets (21.8%). The $e\mu$ event rates agree to better than 3% with those from other ongoing 2012 top analyses as documented in `TopEventChallenge`[86]. The events with at least 2 b-jets are heavily dominated by $t\bar{t}$ events, with a small $\sim 3\%$ contribution from single top. Z+jets and dibosons make up less than 0.1% of events passing the final selection, and are thus neglected in this analysis.

The number of selected events in simulation and data agree to within better than 3%, demonstrating that the Monte Carlo reproduces the data quite well. Table 7.2 compares the number of selected events from the baseline $t\bar{t}$ simulation to those from other $t\bar{t}$ generators. The two PowHeg+Pythia simulations and MC@NLO+ Herwig all agree with each other to within 2%. The MadGraph+Pythia simulation gives about 10% more events. The last column in Table 7.2 gives the scale factor used to normalize each $t\bar{t}$ generator to the number of events in data (including the single top contribution).

7.3.3 Reconstructed distributions

In Figures 7.1 and 7.2, the properties of reconstructed lepton and b-jets in $e\mu$+2 b-jet events are compared in simulation and data. The negligible contributions from Z+jets and dibosons are not shown. Simulation is normalized to the number of events in data using the scale factors in Table 7.2 in order to study the shape differences and remove uncertainties from the $t\bar{t}$ cross section. In Figures 7.1 and 7.2, the statistical uncertainity on the data is shown

as a gray band on the ratio plot and statistical uncertainties on the simulation are shown as error bars on the ratio. Systematic uncertainities are not shown.

Figure 7.1 shows the p_{T} and η distributions of the leptons. Figure 7.2 shows the p_{T} and η distributions of the 2 b-jets used to select the events.

Overall, the b-jets and the leptons are well modeled by simulation. PowHeg+Pythia hdamp=∞ agrees well, motivating its suitability as a baseline simulation.[2] These observations are consistent with those in Ref. [87].

MC Component	$e\mu$	(%)	$\geq$ 2-b jets	(%)
$t\bar{t}$	40542.1	59.4	11946.5	97.1
Single top	3955.8	5.8	356.3	2.9
Z+jets	15117.4	22.1	4.5	0.0
Dibosons	8585.7	12.6	1.7	0.0
MC Total	68201.0	100.0	12309	100.0
Data	69575		12332	

Table 7.1: Number of events with opposite sign $e\mu$ and at least 2 b-jets in the data compared to that from Monte Carlo, broken down into contributions from $t\bar{t}$, Wt single top, Z+jets and dibosons. Only central values are shown here; systematic uncertainties are discussed in Chapter 10.

Generator	$N_{t\bar{t}}$	$N_{\mathrm{data}}/(N_{\mathrm{single\ top}} + N_{t\bar{t}})$
PowHeg+Pythiahdamp=∞ (base)	11946.5	1.0024
PowHeg+PythiaP2011C hdamp=m_t	12095.8	0.9904
MC@NLO+ Herwig	12208.3	0.9815
MadGraph+Pythia	356.33	0.9194
PowHeg+Herwig	11856.6	1.0097
PowHeg+Pythia8	12115.6	0.9888

Table 7.2: Number of events with an opposite sign $e\mu$ and at least 2 b-jets for different $t\bar{t}$ generators. The last column gives scale factor to normalize the sum of the $t\bar{t}$ simulatation and single top yields ($N_{\mathrm{single\ top}} = 361.4$) to the data yield (12332).

[2]The baseline sample is primarily chosen for high statistics

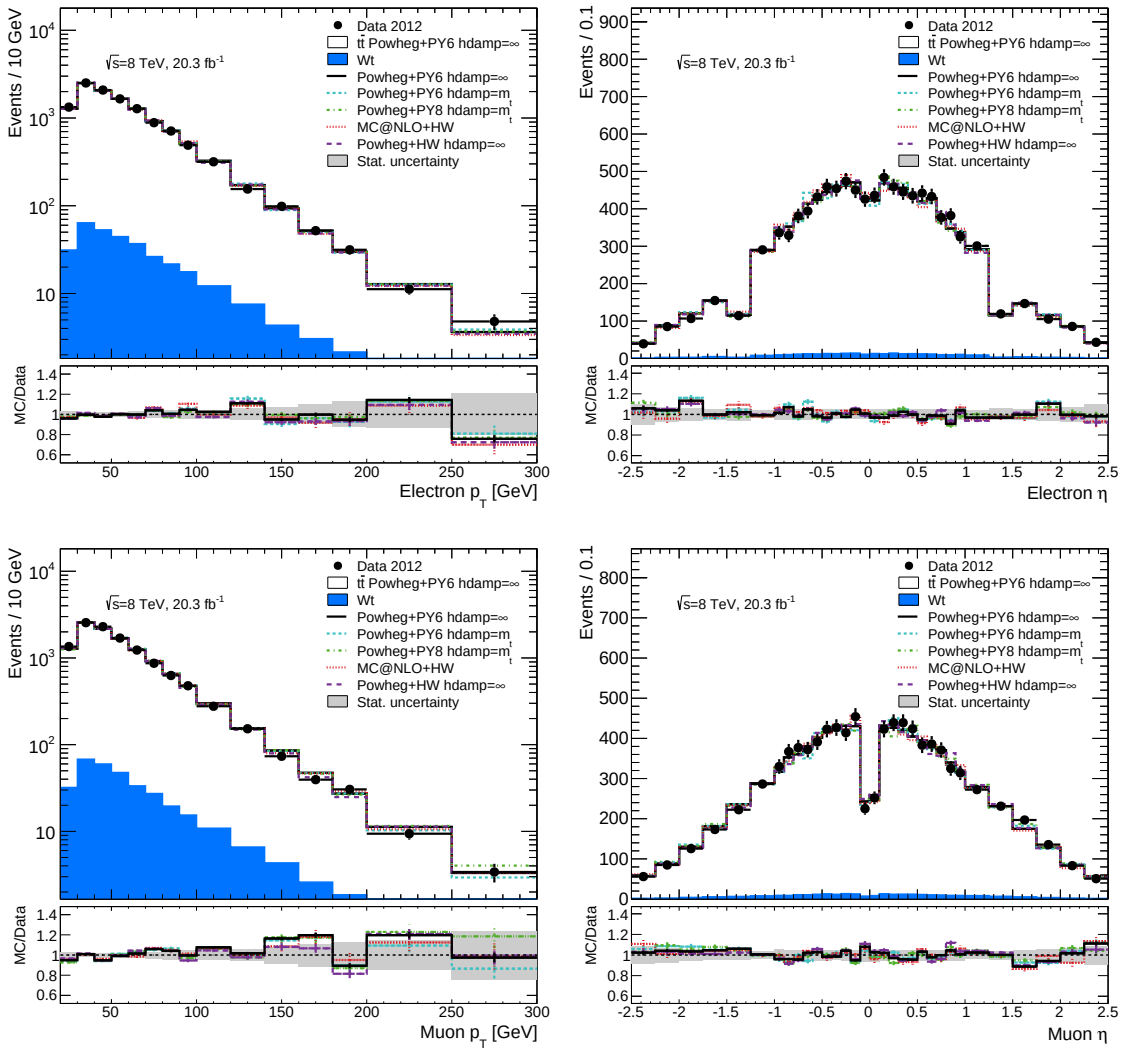

Figure 7.1: Distributions of the transverse momentum and η of the electron and muon in events with an opposite sign $e\mu$ pair and at least 2 b-jets in data and simulation. The distributions in data are compared to simulation normalized to data yields (see scale factors in Table 7.2). The ratio of different MC samples to data is shown with error bars corresponding to the MC statistical uncertainty and a shaded band corresponding to the data statistical uncertainty.

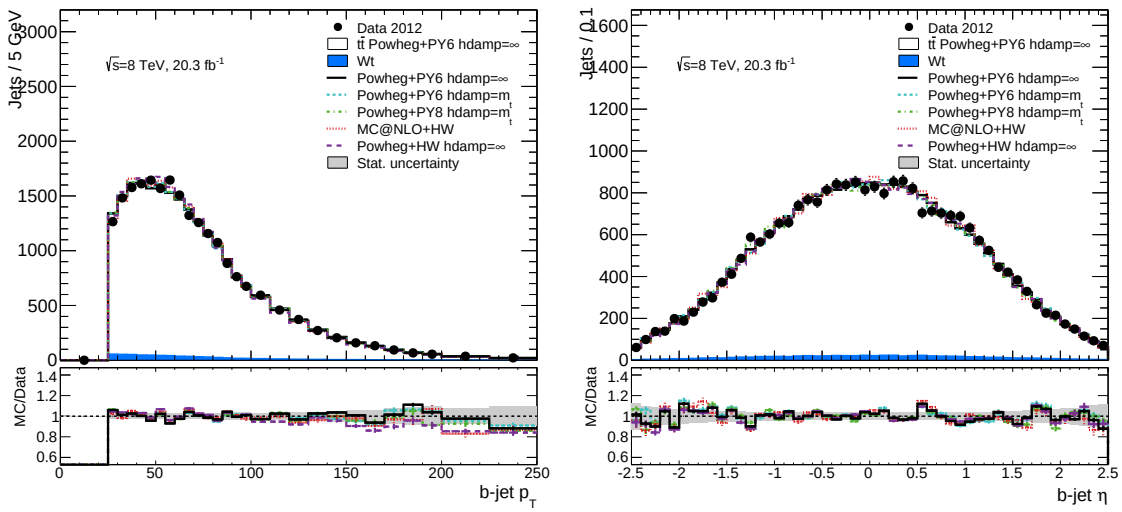

Figure 7.2: Distributions of the transverse momentum and η of the b-jets in events with an opposite sign $e\mu$ pair and at least 2 b-jets in the 2012 data. The distributions in data are compared to simulation, normalized to the same number of events as in the data (see scale factors in Table 7.2).. In events where more than two b-jets are reconstructed, the two highest p_{T} b-jets are selected and the remaining b-jet is classified as an extra jet (see Chapter 8). The ratio of different MC samples to data are shown with error bars corresponding to the MC statistical uncertainty and a shaded band corresponding to the data statistical uncertainty. Systematic uncertainties are not shown.

Chapter 8

Reconstruction of extra jets

The goal of this analysis is to study additional jets in events that pass the selection criteria described in Chapter 7. Jets in selected events are divided into two categories: the two b-jets used for event selection and any additional 'extra' jets. In simulated data, this categorization is done independently for truth jets and reconstructed jets. The b-jets are required to have $|\eta| < 2.5$. Extra jets are required to have $|\eta| < 4.5$. The final measurement of the extra jets will be corrected to the fiducial region $p_T^{jet} > 25$ GeV.

8.1 Matching criteria

As described in Chapter 7.2.3, a geometric algorithm matches reconstructed jets to truth jets. The b-jets are matched before the extra jets and no two reconstructed jets are allowed to match to the same truth jet. Though required to have reconstructed $p_{\mathrm{T}} > 25$ GeV, reconstructed jets are matched to truth jets with $p_{\mathrm{T}} > 10$ GeV. This procedure allows the unfolding to account for migration over the selection boundary.

In the $\sim 2\%$ of events with more than two reconstructed b-jets, the two reconstructed jets with the highest MV1 weights are classified as the selected b-jets and the remaining jets are treated as extra jets. In the events that contain more than two reconstructed b-jets, this prescription selects b-jets that are matched to the top decay products with 74% accuracy. In contrast, choosing the two highest p_{T} b-jets in these same events selects b-jets from the top decay 68% of the time. In simulated events with exactly 2 reconstructed b-jets, 96% of selected b-jets descend from the top quark; the remainder are consistent with mistagged [88] non b-jets. Such misclassification of b-jets is accounted for in the correction procedure described in Chapter 9.

8.2 Background contributions to extra jets

In the baseline MC sample, approximately 4% of the events contain an *unmatched* jet (see Chapter 7.2.3). The RooUnfold package used to unfold the data does not properly handle p_{T}-

dependent background subtraction. Therefore, the unfolding response matrix is constructed using only matched jets. Unmatched jets are defined to be background and are subtracted from the data before unfolding. Unmatched jets can result from two sources:

Pileup : Jets coming from additional proton-proton collisions within the same bunch crossing.

False : Jets observed in the reconstruction that arise from detector effects or jets resulting from reconstruction pathologies such as a when a single truth jet is split into two reconstructed jets or when the $\eta - \phi$ positions of the truth and reconstructed jets differ by more than the matching distance of 0.4.

The procedures used to estimate the rate of these two types of backgrounds are outlined below.

8.2.1 Pileup jets

The ATLAS simulation describes the effect of pileup on hard-scatter jets well [89]. However, the multiplicity of pileup jets has not been fully validated, especially in the region $2.4 < |\eta| < 4.5$. Ideally, the pileup rate could be estimated using the ATLAS pileup overlay simulation framework. In this framework, zero bias events from data are combined with simulated hits for the hard scattering event and the digitization and reconstruction are performed on the combined sample. However, no sample with sufficiently high statistics presently exists.

A higher statistics alternative to the overlay sample can be constructed using a hybrid technique. This hybrid technique takes as its input files from the baseline simulation and from the ZeroBiasOverlay data steam [1]. Unmatched jets are removed from the baseline simulation and the matched jets are combined with reconstructed jets from the zero bias data.

To properly estimate the pileup rate, the input ZeroBiasOverlay data must be luminosity-weighted to match the data. This weighting is done as follows. First, the run number and luminosity block number for all events passing the $e\mu$ + 2 b-jets data event selection is tabulated. Second, data from the ZeroBiasOverlay stream is skimmed to keep only those run and luminosity block pairs present in the selected data. Third, $t\bar{t}$ MC events are analysed. The e,μ, b-jets, and truth-matched additional jets are kept and the unmatched additional jets are deleted. For each MC event, a ZeroBiasOverlay data event is randomly selected from the skimmed data. The distribution of these ZeroBias events is forced to sample the list of run and luminosity block numbers to match the distribution for the $e\mu + 2$ b-jets data. The reconstructed jets in the selected ZeroBiasOverlay event are added to the $t\bar{t}$ MC event record. An overlap removal procedure removes zero bias jets that overlap hard scatter jets. If a zero

[1] Real data events collected with a zero-bias trigger that selects purely random events. The events from this stream can be combined or "overlaid" on a generated process to simulate pileup. See Ref. [90] for more information.

bias jet overlaps a lepton, then the event is removed from the sample. This hybrid sample provides the baseline estimate of the pileup contribution to the extra jet distributions.

The dependence of the extra jet rate on the average number of interactions per bunch crossing (μ) in the signal sample is used to validate this estimate. Figure 8.2 shows an example of this procedure for (a) central and (b) forward jets for the lowest jet p_{T} bin used in this analysis. The figure shows the mean number of jets in events passing the baseline selection as a function of μ and the pileup contribution estimated from the ZeroBiasOverlay stream. Before pileup subtraction, the number of jets depends on μ, with a larger dependence observed in the forward η region where the JVF cut can not be used. After subtraction of the pileup using the estimate from the ZeroBiasOveray stream, this μ dependence is eliminated. For this p_{T} bin, the estimated number of pileup extra jets per event is 0.005 (0.016) in the central(forward) region. The pileup rate decreases with jet p_{T} and is estimated to be below 0.002 for jets with $p_{\mathrm{T}} > 50$ GeV. Systematic uncertainties on this pileup estimate are discussed in Chapter 10.3.

8.2.2 False jets

Reconstruction pathologies are studied using simulated data. Because the simulation event record does not contain truth information for pileup, it is not straightforward to determine what fraction of the unmatched jets derive from pileup and what fraction are the result of other detector effects. The simplest way to study the rate of false jets would be to study them in a sample simulated without pileup, but no such $t\bar{t}$ sample exists.

The rate of false jets is estimated by studying the ΔR between extra jets. While the $\eta - \phi$ position of pileup jets is uncorrelated with the position of truth jets, false jets from reconstruction pathologies should be preferentially close to truth jets (since they are derived from particles in these truth jets). Figure 8.3 shows the distance between each reconstructed jet and the nearest additional reconstructed jet in the event ($\Delta R_{\text{reco jet, reco jet}}$) in simulation and in data for jets of rank=1-4. The data is in good agreement with the simulation. The contribution of unmatched jets at low $\Delta R_{\text{reco jet, reco jet}}$ is evident in the figure; this false jet component is needed in order to reproduce the shape observed in the data.

Figure 8.4 shows the distance between each reconstructed jet and the nearest truth jet ($\Delta R_{\text{reco jet, truth jet}}$) for jets of rank=1-4. The presence of unmatched jets with $\Delta R_{\text{reco jet, truth jet}} < 0.4$ results from the requirement that each truth jet can only be matched to a single reconstructed jet, as described in Chapter 7.2.3. Because the matching requires $\Delta R_{\text{reco jet, truth jet}} < 0.4$, all jets above this threshold are unmatched. The probability that a second (and hence, unmatched) jet is reconstructed with $\Delta R_{\text{reco jet, truth jet}} < 0.4$ is ~ 0.0068. This number represents a lower bound on the false jet rate.

The false jet rate can be estimated in another way. Figure 8.5 shows the number of unmatched jets per event in the baseline simulation as a function of μ. These unmatched jets include both the pileup and false jet contributions, with pileup dominating at high μ and false jets at low μ. The rate of false jets can be determined by fitting this distribution to a first order polynomial. The intercept of this fit predicts the false jet rate, while the slope

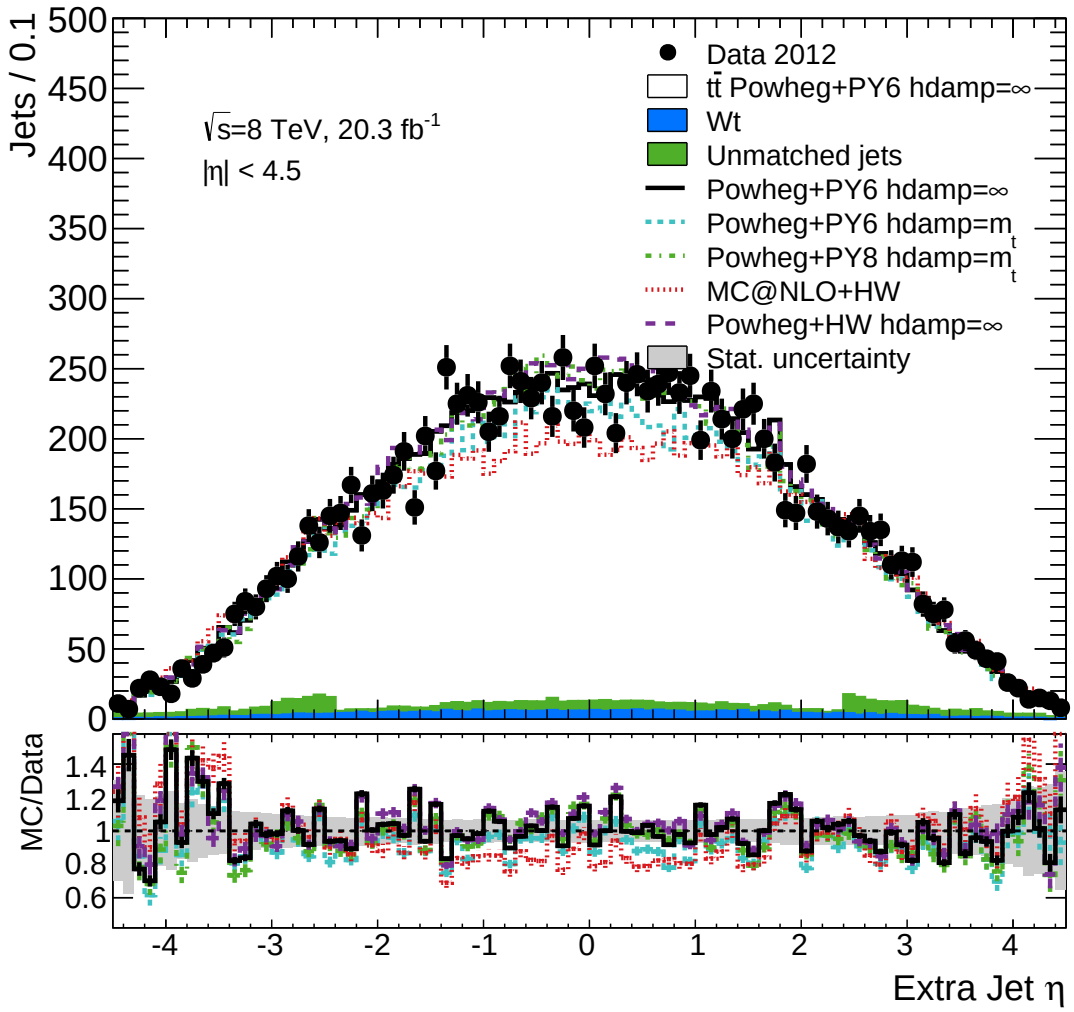

Figure 8.1: The η distribution of extra jets in simulation and data.

provides the pileup rate in the simulation. The fitted intercept is 0.0075 ± 0.0014, which is slightly higher than the estimate obtained from $\Delta R_{\text{reco jet, truth jet}}$ above, but is consistent within the statisical uncertainty on the fit. This second technique is used to obtain the baseline false jet estimate and its uncertainty.

The false jets comprise $\sim$ 20% of the total unmatched jets and have a p_{T} and rank dependence similar to pileup jets. These two contributions are combined and treated as a single background in the subtraction procedure.

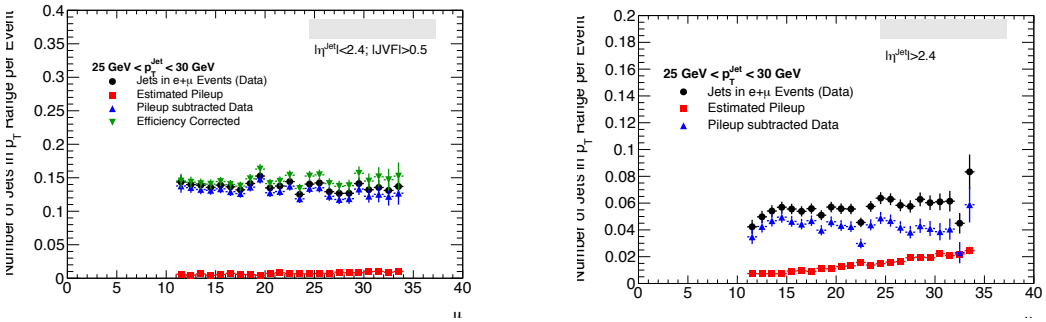

Figure 8.2: Mean number of reconstructed jets as a function of $< \mu >$ for jets in the p_T range $25 < p_T < 30$ GeV for (a) central and (b) forward jets in data events passing the e-μ selection before and after correction for pileup. Jets passing the 70% MV1 b-tagging selection are removed. The pileup rate is estimated using the ZeroBiasOverlay data stream. The blue markers show the pileup subtracted rate before correcting for the $< \mu >$-dependent efficiency of the JVF cut. The green points show the results after correction.

8.3 Reconstruction level distributions

Figures 8.6 and 8.7 compare the multiplicity and p_{T} of reconstructed extra jets in data and $t\bar{t}$ simulation, where the simulation has been normalized to the number of events in data. Statistical uncertainity on the data is shown as a gray band on the ratio plot and statistical uncertainty on the simulation is shown as error bars on the ratio. Systematic uncertainities are not shown. In data, background from pileup jets is subtracted, while in simulation, reconstructed jets are required to have a truth match. The multiplicity in the MC samples agree with that of the data, except for MC@NLO+ Herwig, which consistently underestimates the number of events with 3 or more extra jets. Figure 8.7 shows the p_{T} distributions of each extra jet, including contributions from single top events and unmatched jets. The fact that MC@NLO+ Herwig underestimates the jet multiplicity can be seen in these distributions. The jets in PowHeg+Pythia8 appear to exhibit a slightly harder spectrum than the data. All other generators agree reasonably well with the data.

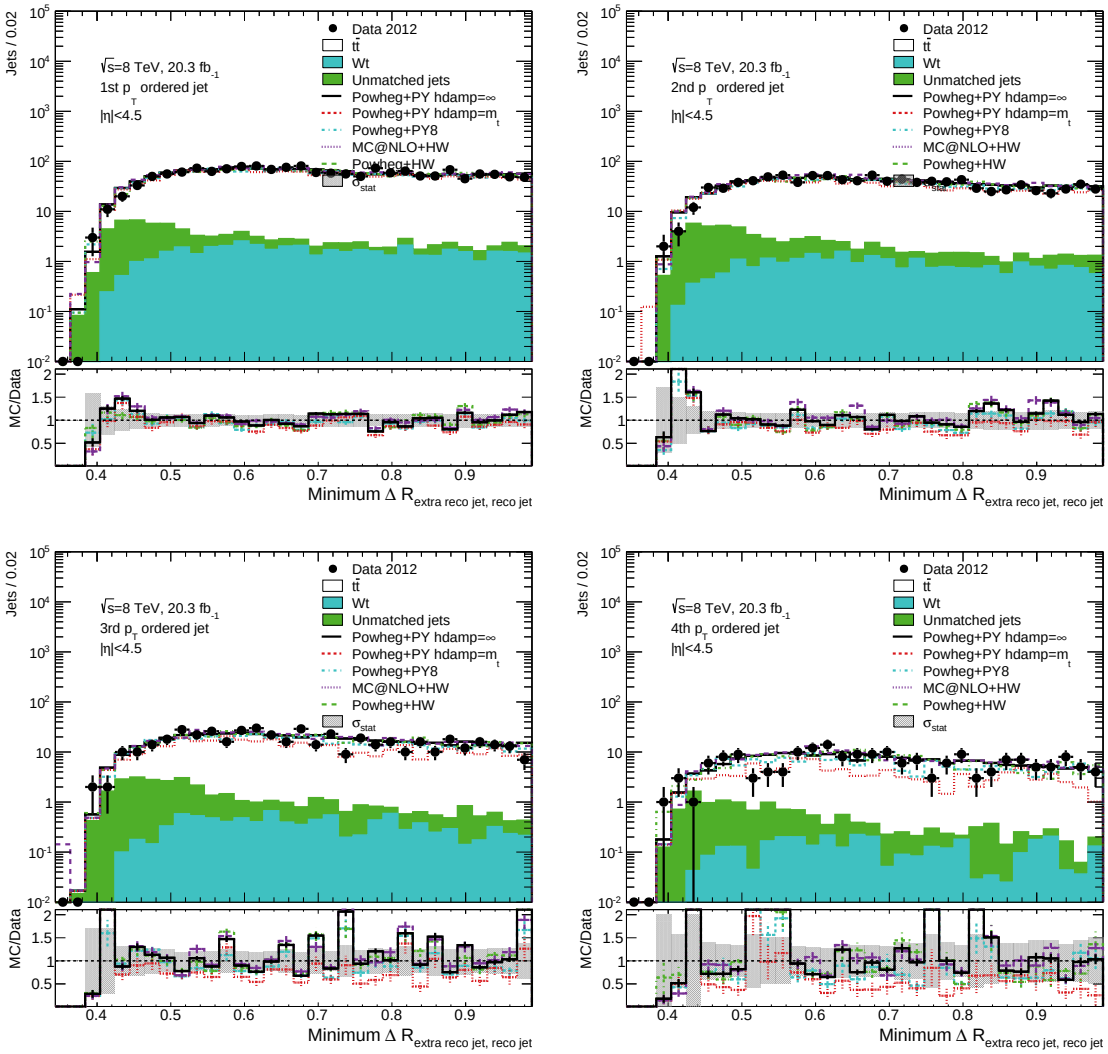

Figure 8.3: Distributions of minimum reconstructed ΔR betweeen extra jets in simulation and data for the the first, second, third and fourth extra jet.

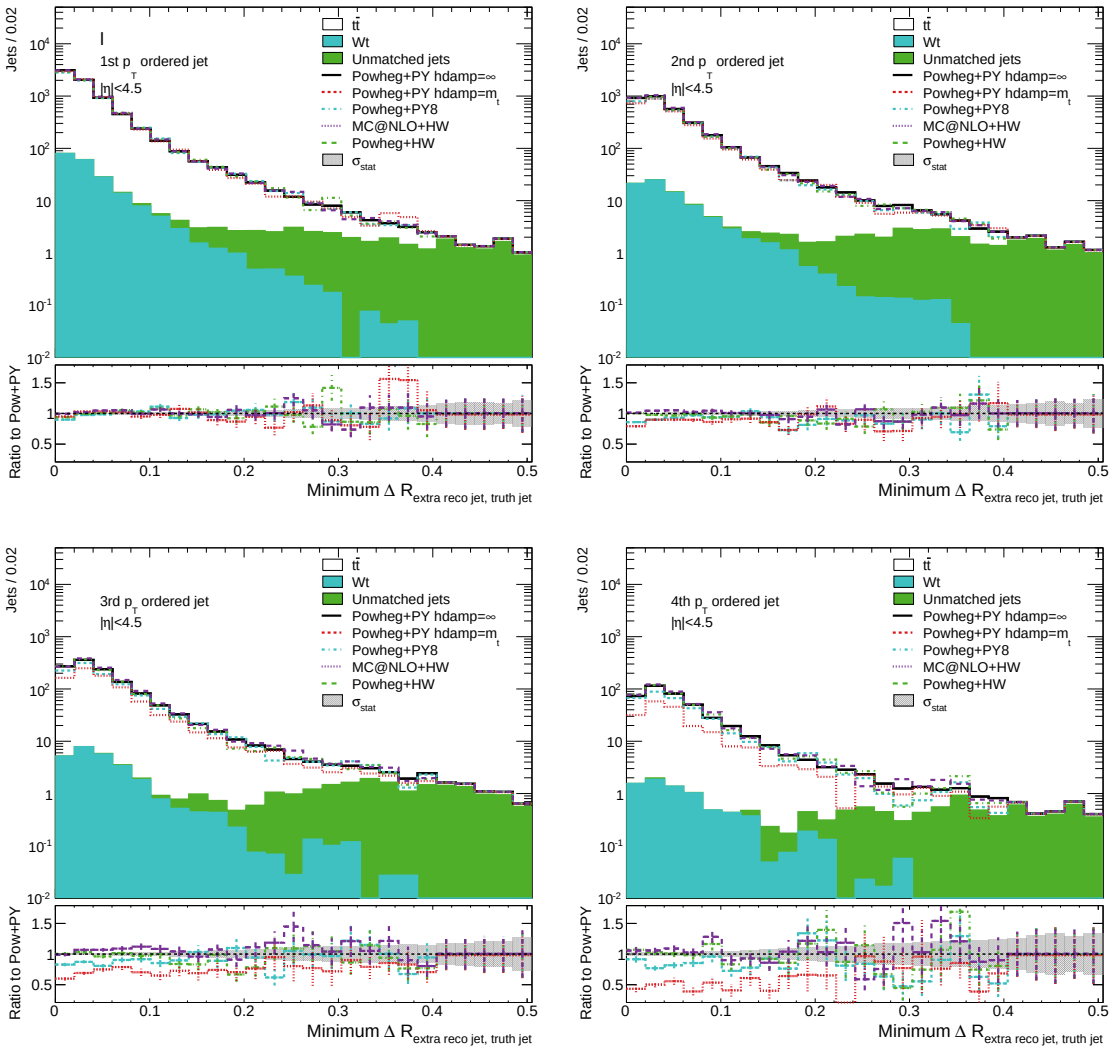

Figure 8.4: Distributions of ΔR betweeen reconstructed extra jets and the nearest truth jet for the first, second, third and fourth extra jet.

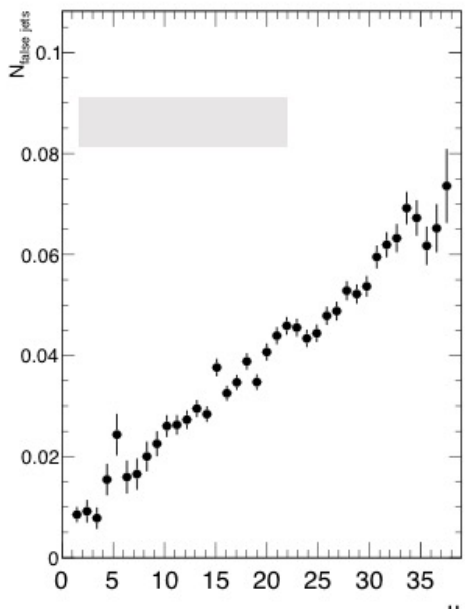

Figure 8.5: Dependence of the unmatched extra jet rate on μ for the baseline simulation.

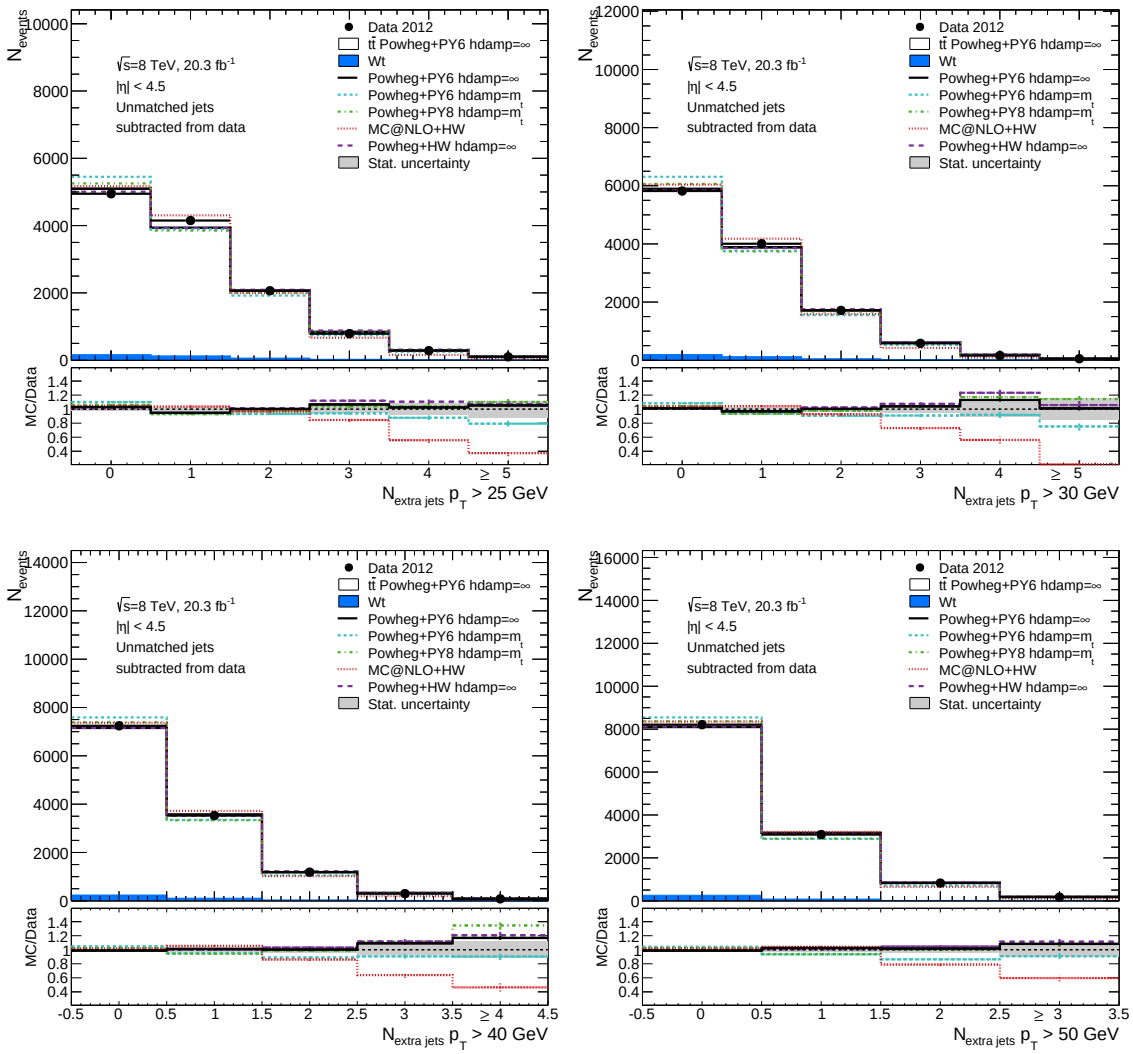

Figure 8.6: Distributions of the reconstructed extra jet multiplicity as a function of p_{T} threshold in simulation and data. The distributions in data are compared to $t\bar{t}$ simulation normalized to the same number of events as in the data. Extra jets from pileup are excluded in simulation by requiring a match to truth. Extra pileup jets are subtracted from the data. The ratio of different MC samples to data is shown with error bars corresponding to the MC statistical uncertainty and a shaded band corresponding to the data statistical uncertainty. Systematic uncertainities are not shown.

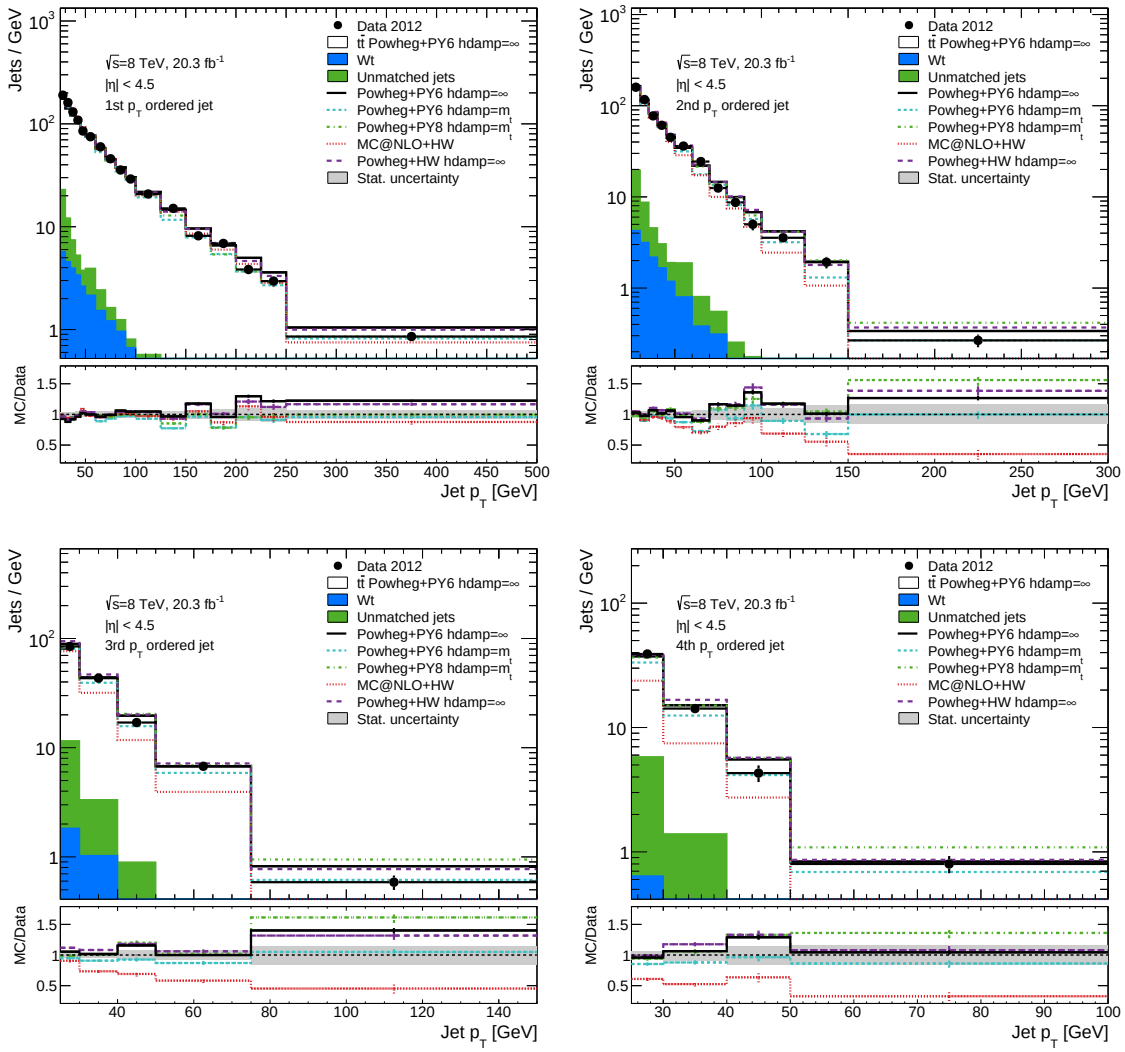

Figure 8.7: Distributions of reconstructed extra jet p_{T} in simulation and data. The distributions in data are compared to $t\bar{t}$ simulation normalized to the same number of events as in the data. Backgrounds from single top and extra pileup jets are included as background to $t\bar{t}$. The ratio of different MC samples to data is shown with error bars corresponding to the MC statistical uncertainty and a shaded band corresponding to the data statistical uncertainty. Systematic uncertainities are not shown.

Chapter 9

Correction to particle-level

9.1 Introduction to unfolding

Kinematic distributions measured by a detector contain distortions due to limited acceptance, resolution and biases. The data must be corrected for these effects in order to allow direct comparison with theoretical models or other experimental measurements. This process of correcting the detector or reconstructed level back to the generator or truth level is called *unfolding*.

Unfolding begins with building a *response* (a.k.a. migration) matrix. The response matrix is a 2-dimensional representation of how the truth value of an observable relates to the measured value, as distorted by characteristic detector effects. The response matrix is built from simulated data.

In order to go from a reconstructed distribution to a truth distribution, the response matrix must be inverted. However, some bins of the matrix may be sparsely populated, and information loss occurs from detector imperfections. Directly inverting the matrix produces unphysical bin-to-bin fluctuations, so an unfolding uses *regularization* to smooth the result and surpress these unphysical fluctuations. In this analysis, the iterative Bayesian algorithm is chosen, though the Singular Value Decomposition (SVD) technique was also considered.

9.2 Procedure

This section outlines the procedure used to unfold the reconstructed p_{T} and multiplicity of the extra jets using the software package `RooUnfold` [91].[1] This procedure corrects the background-subtracted measured spectrum to the true spectum for events that pass the fiducial requirements at both the truth and the reconstruction level. Detector effects can distort the true extra jet spectrum in several ways. Hard scattering jets can be lost due to inefficiencies in the reconstruction, resolution smearing will affect the jet p_{T}, and the rank

[1] Due to important bug fixes necessary for error propagation in this analysis, the development version of RooUnfold is used.

of two reconstructed jets can be swapped relative to the truth jets (e.g. leading truth jet reconstructed as subleading jet or vice versa). In addition, jets can migrate into and out of the fiducial region. The unfolding procedure corrects for all these effects.

The unfolding is performed on a distribution where the integral of the input distribution is the number of measured jets in the sample and the integral of the output distribution is the number of true jets passing the fiducial requirements.

The full correction procedure is given by the equation:

$$\frac{1}{\sigma}\frac{d\sigma_{\text{jet},i}}{dp_T} = \frac{1}{N_{\text{events}}}\sum_j f^i \left(\mathbf{M}^{-1}\right)^{\text{true, i}}_{\text{reco},j} g^j \left(\mathscr{N}^j_{\text{reco}} - \mathscr{N}^j_{\text{bkgnd}}\right) \ . \tag{9.1}$$

$\mathscr{N}^j_{\text{reco}}$ gives the raw distribution measured from data. The estimated extra jet background, $\mathscr{N}^j_{\text{bkgd}}$ is subtracted from this raw distribution. A 'feed-in' factor g^j corrects for migration across the fiducial boundary (cases where the reconstructed jet has $p_{\text{T}} > 25$ GeV but the truth jet has $p_{\text{T}} > 25$ GeV). The migration matrix $\mathbf{M}^{\text{true, i}}_{\text{reco, j}}$ relates the number of jets in truth bin i to the number in reconstructed bin j. The correction factor f^i removes the bias in the extra jet spectrum introduced by the event selection. Finally, the number of jets is normalized to the number of $e\mu + 2$ b-jets events passing the fiducial requirements (N_{events}) to obtain the final distribution.

This section is organized as follows. First, the scheme for binning jets in both p_{T} and rank is discussed. Second, the method for the unfolding is outlined. Third, the correction factor for event selection is discussed.

9.2.1 Binning

In order to account for the migration effects described above in a single procedure, jets are binned according to both their p_{T} value and rank. For each jet rank, variable sized p_{T} bins are chosen to satisfy two criteria. First, each bin must have at least 10 entries for the data. Second, each bin should show bias of less than 10% of the statistical uncertainty in the closure test discussed in Chapter 9.3.1. In cases where the second criterion fails, neighboring bins are combined until the closure test passes this criterion.

The rank (R) and p_{T} of each jet in an event can be mapped to a single integer bin number $\mathscr{N}(p_{\text{T}}, R)$. The bin boudaries are given in Table 9.1. The last p_{T} bin for each rank is treated as an overflow bin.

Both the p_{T} distribution and multiplicity of the extra jets can be recovered from the distribution $\mathscr{N}(p_{\text{T}}, R)$. The p_{T} distribution of the Rth jet is obtained directly from $\mathscr{N}(p_{\text{T}}, R = k)$. The jet multiplicity can be obtained by integrating over p_{T}: the number of events with at least j jets with $p_{\text{T}} \geq p$ is given by:

$$N(\geq j) = \begin{cases} N_{\text{total}} & : j = 0 \\ \int_p^\infty \mathscr{N}(p_{\text{T}}, R = j)\mathrm{d}p_{\text{T}} & : j > 0 \end{cases} \tag{9.2}$$

Then the number of events with exactly j jets is given by:

$$N(j) = N(\geq j) - N(\geq j+1) \tag{9.3}$$

and the total number of events with exactly 0 jets is $N(0) = N_{total} - N(\geq 1)$, where N_{total} is the total number of events.

Table 9.1: Binning for unfolding of extra jets. Jets are binned simultaneously in both rank (p_{T} order) and p_{T}. For each jet rank, variable sized p_{T} bins are chosen so that at least 10 data events fall in each bin. The first bin in p_{T} for each rank is treated as underflow bins. These bins are not reported as part of the measurement.

Jet rank	Bin number	Jet p_{T} (GeV)
1	1	$25-30$
1	2	$30-35$
1	3	$35-40$
1	4	$40-45$
1	5	$45-50$
1	6	$50-60$
1	7	$60-70$
1	8	$70-80$
1	9	$80-90$
1	10	$90-100$
1	11	$100-125$
1	12	$125-150$
1	13	$150-175$
1	14	$175-200$
1	15	$200-225$
1	16	$225-250$
1	17	> 250
2	18	$25-30$
2	19	$30-35$
2	20	$35-40$
2	21	$40-45$
2	22	$45-50$
2	23	$50-60$
2	24	$60-70$
2	25	$70-80$
2	26	$80-90$
2	27	$90-100$
2	28	$100-125$
2	29	$125-150$
2	30	> 150

Continued on next page

Table 9.1 –*Continued from previous page*

Jet rank	Bin number	Jet p_{T} (GeV)
3	31	$25-30$
3	32	$30-40$
3	33	$40-50$
3	34	$50-75$
3	35	>75
4	36	$25-30$
4	37	$30-40$
4	38	$40-50$
4	39	>50
5	40	$25-30$
5	41	>30

9.2.2 Unfolding procedure

The unfolding algorithm corrects the number of jets reconstructed in each bin $\mathscr{N}^i_{\mathrm{reco}}(p_{\mathrm{T}}, R)$ for detector effects to obtain the unfolded $\mathscr{N}^i_{\mathrm{unf}}(p_{\mathrm{T}}, R)$ according to:

$$\mathscr{N}^i_{\mathrm{unf}} = \sum_j \left(\mathbf{M}^{-1}\right)^{\mathrm{true},i}_{\mathrm{reco},j} g^j \left(\mathscr{N}^j_{\mathrm{reco}} - \mathscr{N}^j_{\mathrm{bkgd}}\right) \tag{9.4}$$

The procedure begins with the raw $\mathscr{N}^j_{\mathrm{reco}}$ distribution measured from data.

First, the estimated extra jet background, $\mathscr{N}^j_{\mathrm{bkgd}}$ is subtracted. This background is estimated from data and further discussed in Chapter 8.2. Sources of background include jets from pileup and cases where detector effects result in a single truth jet being split into two jets in the reconstruction. In simulation, background removal is done by requiring a match to a truth jet.

Next, a factor g corrects for migration across the fiducial boundary in reconstruction (cases where the reconstructed jet has $p_{\mathrm{T}} > 25$ GeV but the truth jet has $p_{\mathrm{T}} > 25$ GeV). For each bin j, g^j gives the fraction of reconstructed jets matched to truth jets inside the fiducial boundary (> 25 GeV):

$$g^j \equiv \frac{\mathscr{N}^j_{\text{reco match >25 GeV}}}{\mathscr{N}^j_{\text{all reco}}}$$

Figure 9.1 shows this factor estimated for several NLO $t\bar{t}$ generators. The baseline PowHeg+Pythia hdamp=∞ is used to correct the data.

The response matrix $\mathbf{M}^{\mathrm{true,\,i}}_{\mathrm{reco,\,j}}$ gives the number of jets reconstructed with bin number j; bin number i is obtained from true p_{T} and rank. The matrix is filled from simulated events that pass *both* reconstructed and truth selection requirements. Figure 9.2 provides

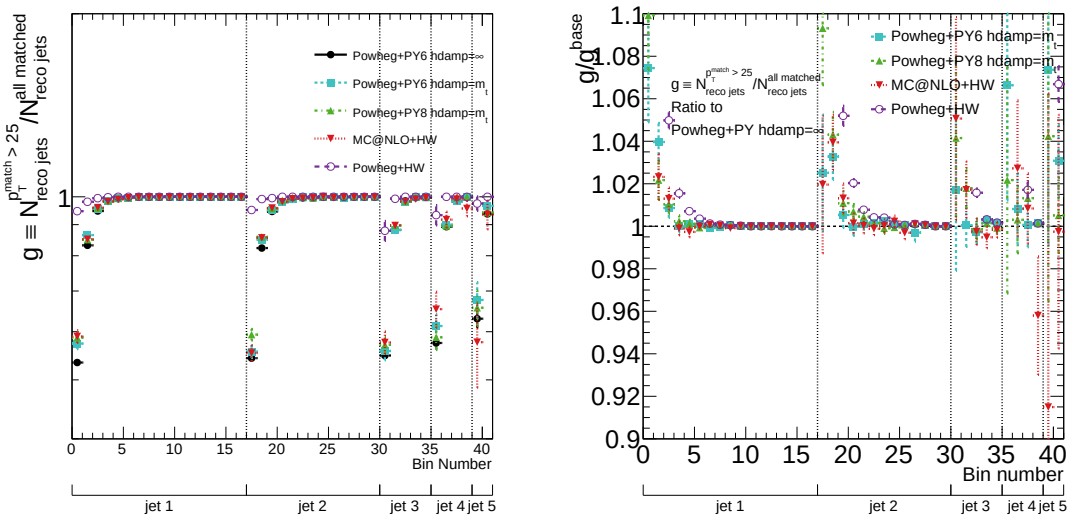

Figure 9.1: Fraction of reconstructed extra jets with truth matches inside the fiducial region (a) and ratio of alternate generators to the baseline (b). This factor is used to correct the data for p_{T} smearing across the fiducial boundary.

a graphical representation of $\mathbf{M}^{\mathrm{true},i}_{\mathrm{reco,\,j}}$. The matrix is largely diagonal, showing that jets are most likely to be constructed with the correct p_{T} and rank. However, there are significant numbers of truth subleading jets reconstructed as leading jets (for example $\mathbf{M}[1, 18; 19, 32]$), and truth leading jets reconstructed as subleading jets (for example $\mathbf{M}[19, 32; 1, 18]$). This type of migration motivates the simultaneous binning via both rank and p_{T}.

In RooUnfold, detector inefficiencies (cases where a true object is not reconstructed) are entered into the response matrix. These "misses" are shown in Figure 9.2(b) and are accounted for in the unfolding.

The response matrix is inverted using iterative Bayesian unfolding [92], which reduces fluctuations from instabilities in the inversion process. The number of iterations has been set to 2. Details on the procedure used to determine the optimal number of iterations are described in Appendix A.3.

9.2.3 Bias in extra jet distributions due to event selection requirements

The unfolding procedure described above returns unbiased extra jet distributions for events passing *both* the truth and reconstruction selection. This subsample of events has different kinematics from events passing the truth only selection. Therefore, the extra jet distributions obtained from the unfolding are biased with respect to the truth selection. In addition, a secondary contribution to the bias results from events where one of the two reconstructed b-jets is in fact a mistag. Both of these biases are corrected using a single bin-by-bin correction

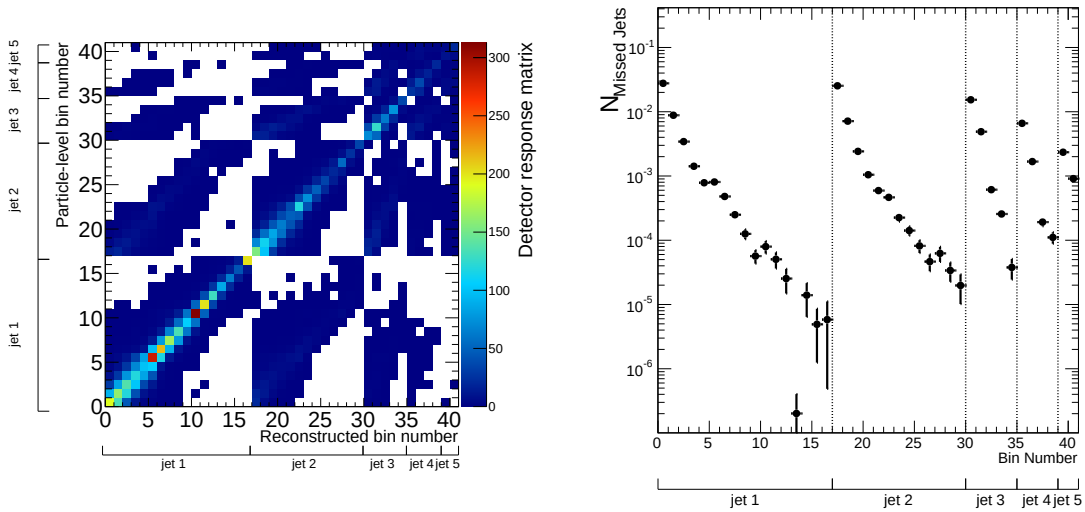

Figure 9.2: Migration matrix between the truth and reconstructed number of extra jets in each bin (a) and distribution of 'missed' truth jets not matched to reco jets (b). Jets are binned according to both p_{T} value and rank. The matrix is filled from events passing both reconstructed and truth $e\mu$+2-b jet events in the baseline $t\bar{t}$ simulation. 'Missed' jets are handled by the RooUnfold framework.

factor that is applied after the unfolding.

To understand the contributions to this correction, events that fall outside the combined truth and reconstructed fiducial region are classified and their kinematic distributions are studied. These studies use the PowHeg+Pythia hdamp=∞ $t\bar{t}$ baseline simulation. Table 9.2 gives the number of events passing the fiducial selection for different combinations of reconstruction and truth selection. Events passing both reconstructed and truth selection are properly handled by the unfolding and used to fill the migration matrix, but events that pass one set of selection criteria and not the other require additional corrections. The subsections below provide additional information on each failure category.

9.2.3.1 Reconstructed events that fail truth event selection

Table 9.3 shows that 95.85% of reconstructed $e\mu$+2 b-jet $t\bar{t}$ events also pass the truth selection and 4.15% of these are *misclassifed* events that fail. This table breaks these events into 5 categories:

1. Lepton fiducial: truth e or μ fails the fiducial p_T or η cuts, while reconstructed e or μ passes.

2. Lepton jet overlap:dressed truth e or μ overlaps with a truth jet, while reconstructed e or μ does not overlap with a reconstructed jet.

3. Lepton non-prompt: truth e or μ leptons result from the decay of a hadron or are other background (such as conversions).
4. b-jet fiducial: truth b-jet fails the fiducial p_T or η cuts.
5. b-jet other: truth jet not matched to B hadron, meaning that the reconstructed b-jet was mistagged. This category also includes a small number of cases where the two reconstructed b-jets are matched to a single truth jet or one of the two reconstructed b-jets does match any truth jet.

Figure 9.3 shows the electron p_{T}, b-jet p_{T}, b-jet MV1 weight, and extra jet multiplicity for events in the above categories. Events failing the truth lepton or b-jet fiducial cuts arise mainly from resolution smearing of the p_{T}. These produce a softer spectrum for the reconstructed lepton p_{T} in Figure 9.3(a) and reconstructed b-jet p_{T} in Figure 9.3(b). Misclassified events with overlap between a lepton and a jet show a harder reconstructed lepton p_{T} spectrum and higher extra jet multiplicity, suggesting that a jet has been reconstructed from a lepton. Events with non-prompt leptons show similar properties. Finally, in the 'b-jet other' category, the MV1 of the reconstructed b-jet is much lower than other types of events, suggesting that a light jet has been mistagged as a b-jet. The $\sim 1\%$ rate in this category is consistent with the mistag estimate for b-jets given in Ref. [88].

9.2.3.2 Truth events that fail reconstructed event selection

Due to detector inefficiencies, the majority of events passing the truth selection fail the reconstruction selection (*missed events*). Table 9.4 shows the events that pass truth selection broken into categories based on which objects were correctly reconstructed. The largest contributions come from failure to reconstruct the electron or the second b-jet in the event. A large fraction of these come from migrations across the fiducial boundary due to p_{T} smearing.

Figure 9.4 shows the truth b-jet p_{T}, extra jet multiplicity, leading extra jet p_{T} and subleading extra jet p_{T} by category. The b-jet p_{T} is much softer for events that are not reconstructed. The extra jets in these events are softer as well.

The differences in the extra jet distributions for these events can be explained by studying the relationship between the b-jet p_{T} and the number and kinematics of the extra jets. Figure 9.5 shows the extra jet multiplicity and p_{T} in truth events in bins of b-jet p_{T}. Softer b-jets correspond to events with softer and fewer extra jets. This effect is likely the result of the dependence of the b-jet p_{T} on p_T^{top}.

In summary, events that fail the reconstruction requirements on the b-jets have a lower extra jet multiplicity and softer jets than those that fall in other categories.

9.2.3.3 Event selection correction factors

To correct for the effects discussed above, bin-by-bin correction factors f^i are applied to the unfolded distribution as shown in Equation 9.1. These factors are derived by comparing unfolded simulated events that pass the reconstruction selection (with no particle level

Category	N_{events}
Reco	11997.1
Truth	43496.9
Reco AND truth	11499.0
Reco AND NOT truth	498.2
NOT Reco AND truth	31877.7

Table 9.2: Number of events passing different combinations of truth and reconstructed selection requirements.

Category	N_{events}	(%)
Lepton fiducial	67.5	0.56
Lepton jet overlap	50.6	0.42
Lepton non-prompt	10.9	0.09
b-jet fiducial	245.8	2.05
b-jet other	123.4	1.03
Total misclassified	498.2	4.15
Passes reco and truth selection	11499.0	95.85
Total reco events	11997.1	100.00

Table 9.3: Number of selected reconstructed events that fail truth selection categorized by reason they have failed. The selections are applied sequentially in the order listed in the table.

Category	N_{events}	(%)
No e	13472.3	31.06
No μ	3743.0	8.63
same-sign $e\mu$	161.1	0.37
0 b-jets	2986.0	6.88
1 b-jet	11515.3	26.55
Missed total	31877.7	73.49
Passes reco and truth selection	11499.0	26.51
Total truth events	43376.7	100.00

Table 9.4: Number of truth events that fail reconstruction selection categorized by reason they have failed. The selections are applied sequentially in the order listed in the table.

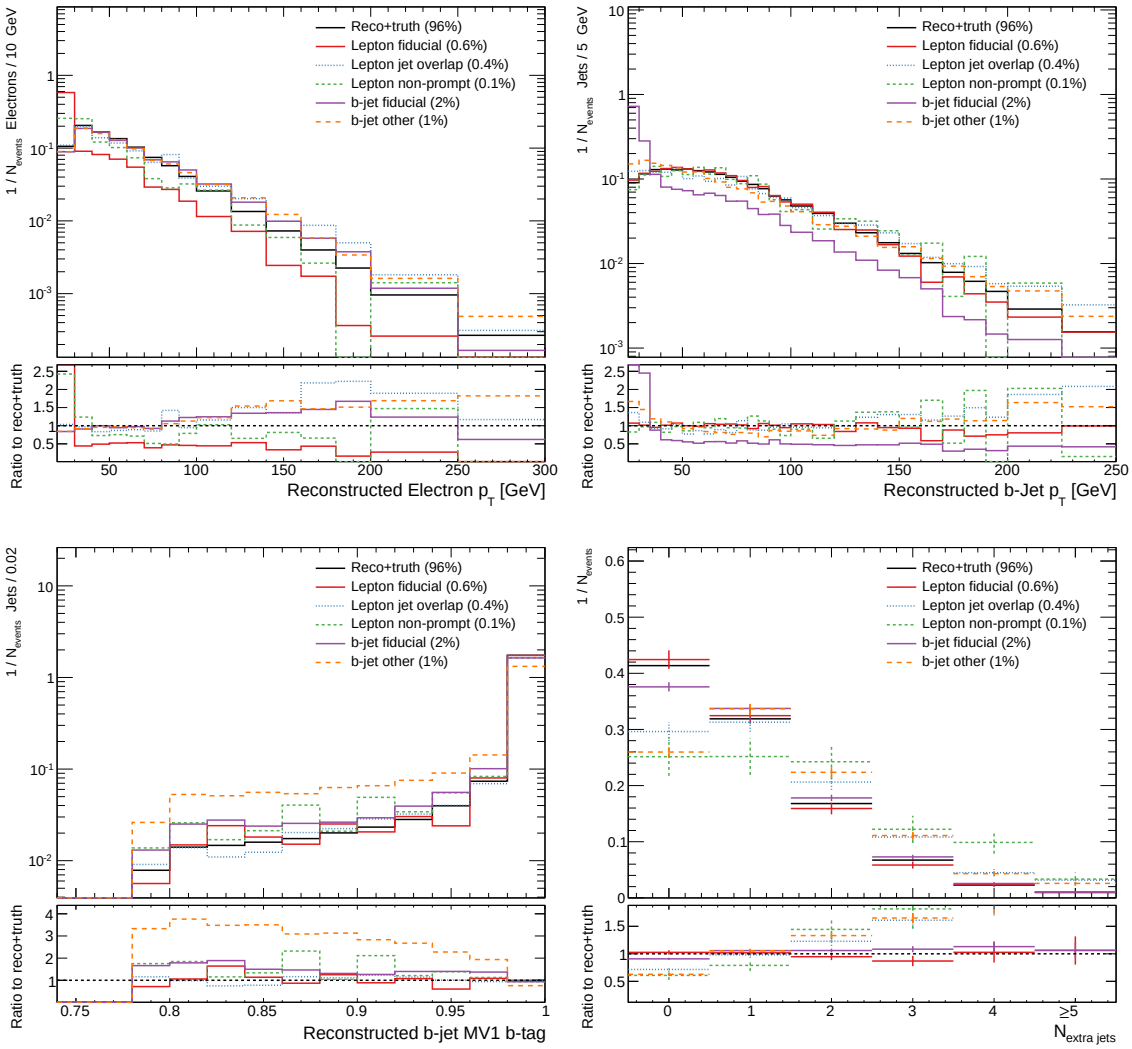

Figure 9.3: Distributions of the (a) e p_{T}, (b) b-jet p_{T}, (c) b-jet MV1 weight and (d) extra jet multiplicity. Each distribution is normalized by the number of events falling in that category. Events were simulated with POWHEG+PYTHIA hdamp=∞ $t\bar{t}$.

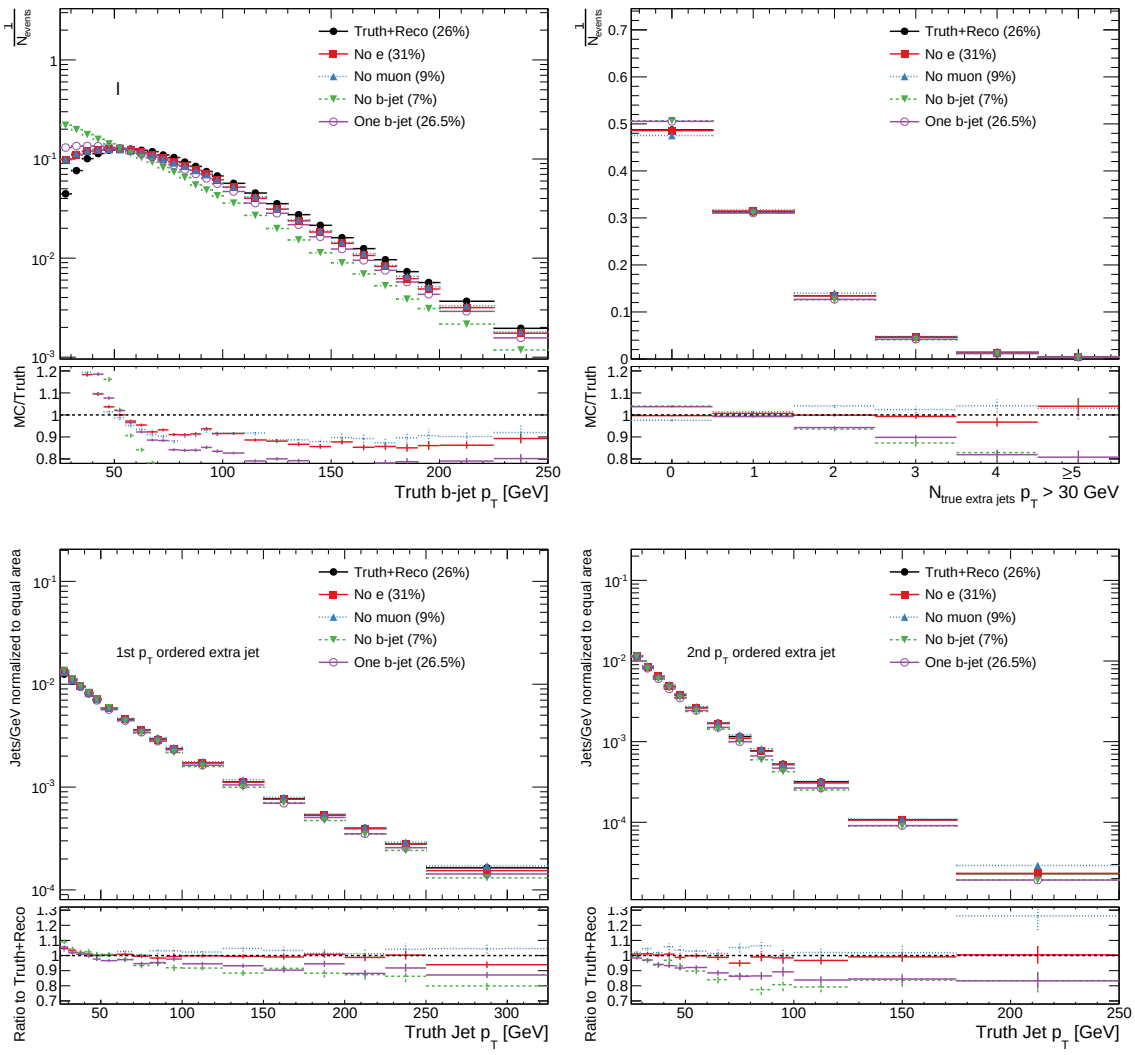

Figure 9.4: Distributions of the truth (a) $b-$jet p_{T}, (b) extra jet multiplicity, (c) leading extra jet p_{T} and (d) subleading extra jet p_{T}. Each distribution is normalized by the number of events falling in that category. Events were simulated with POWHEG+PYTHIA hdamp=∞ $t\bar{t}$ and required to pass the fiducial truth $e\mu$+2 b-jet selection.

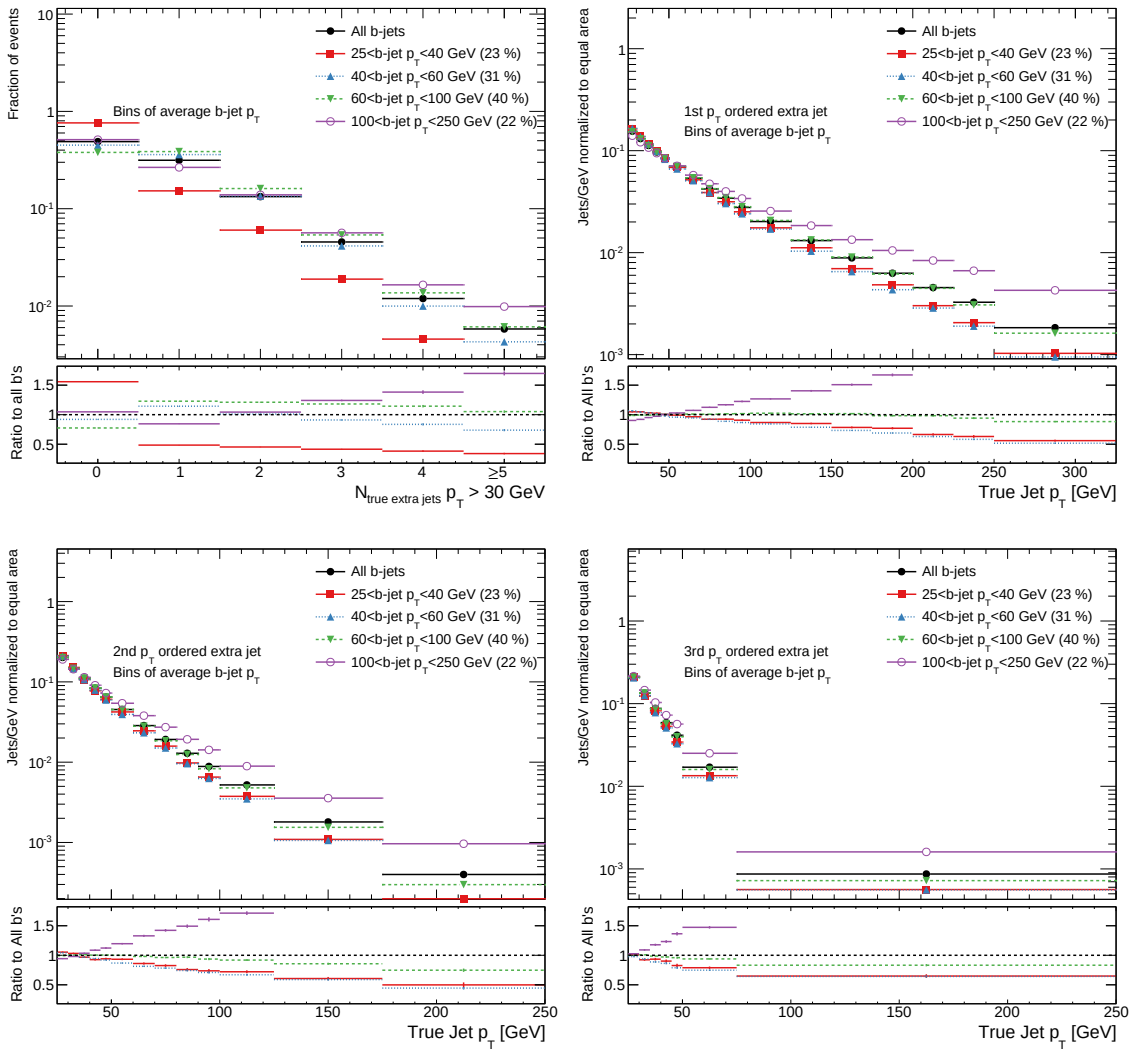

Figure 9.5: Distributions of the truth (a) extra jet multiplicity, (b) leading extra jet p_{T}, (c) subleading extra jet p_{T} and (d) subsubleading extra jet p_{T} in bins of the average of the p_{T} of the two truth b-jets used to select the event. Each distribution is normalized by the number of events falling in that bin. Events were simulated with POWHEG+PYTHIA hdamp=∞ $t\bar{t}$ and required to pass the fiducial truth $e\mu$+2 b-jet selection.

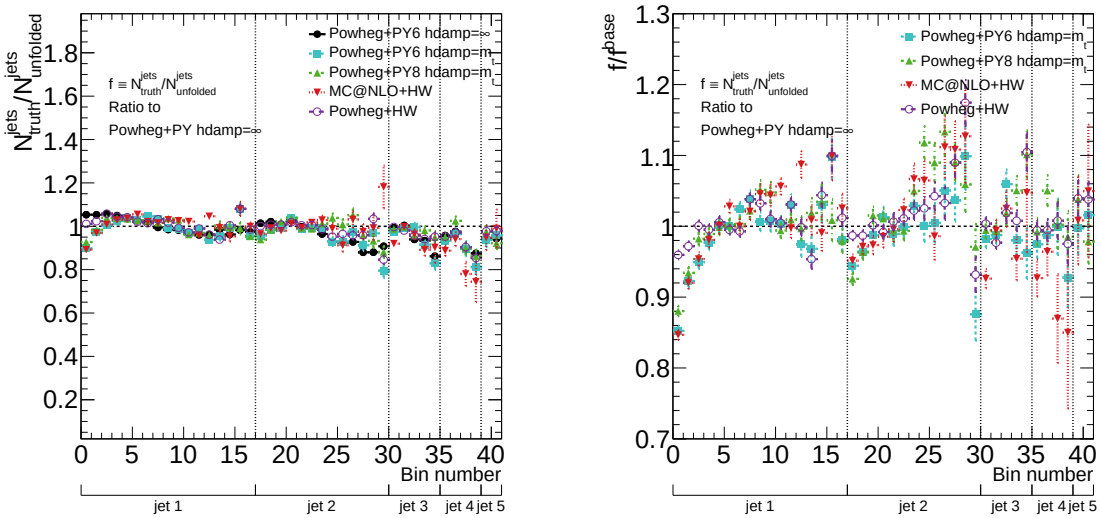

Figure 9.6: (a) Ratio of unfolded extra jets to truth extra jets different $t\bar{t}$ generators (including a 2.9% contribution from single top). (b) Fractional difference of the correction factorfrom baseline for different generators. Extra jets in events passing reconstructed and truth selection for each generator are added to single top and used to fill a response matrix. Then each generator is unfolded against itself, using all selected reconstructed events. Extra jet truth distributions are made without any reconstruction requirements. Finally, the unfolded distribution is divided by the truth distribution to obtain a correction factor for each bin.

event selection) to particle level truth distributions where no reconstruction requirements are applied. Each bin's correction factor is given by:

$$f^i \equiv \frac{\mathscr{N}^i_{\text{true}}}{\mathscr{N}^i_{\text{unf}}} \tag{9.5}$$

The simulated data used for this study includes $t\bar{t}$ and single top events with their relative contributions determined from their NLO cross sections. $\mathscr{N}^i_{\text{true}}$ and $\mathscr{N}^i_{\text{unf}}$ are normalized by number of events passing $e\mu + 2$ b-jets selection at the reconstructed and particle level, respectively. Since the final measurement given by Equation 9.1 is normalized by the number of events in data, the correction factor f^i corrects only for the bias in the extra jet spectrum, not the efficiency in number of events. Figure 9.6 shows the correction factors obtained using different choices of generator for the $t\bar{t}$ component. The final correction factors used for data are taken from the baseline POWHEG+PYTHIA hdamp=∞ sample. Systematic uncertainties associated with generator dependence of this factor are discussed in Chapter 10.4.

9.3 Validation

`RooUnfold` allows propagation of the full covariance matrix of the measured distribution through the unfolding. The package returns a covariance matrix, which is used to determine the uncertainties on the unfolded spectrum. The covariance matrix X on the unfolded distribution is calculated via pseudoexperiments. The diagonal elements of this covariance matrix give the uncertainties on the bins of p_{T} and rank.

The agreement between an unfolded spectrum and truth distribution can be estimated using a χ^2 test (including correlations among bins):

$$\chi^2 = (\mathscr{N}_{\mathrm{unf}} - \mathscr{N}_{\mathrm{true}})^T X^{-1} (\mathscr{N}_{\mathrm{unf}} - \mathscr{N}_{\mathrm{true}}) \tag{9.6}$$

The inverse covariance matrix, X^{-1}, is determined using Singular Value Decomposition (SVD) with `SciPy` [93].

This χ^2 is used validate the unfolding procedure with different MC generators in Chapter 9.3.1-9.3.2, as well as to assess the agreement of generators with the fully corrected data in Chapter 11.

9.3.1 Closure test

The closure test validates the unfolding procedure using simulation. The stability of unfolding can depend on the statistical power of the input data. To ensure that the closure test appropriately accounts for this effect, the test is performed using pseudoexperiments with the same statistical power as the data.

In the closure test, the baseline $t\bar{t}$ +3% Wt simulation is used to fill the migration matrix and one thousand pseudoexperiments are performed using randomly chosen subsamples of events. Each pseudoexperiment is chosen so the number of events is equal to that of data. The extra jet distribution from each pseudoexperiment is then unfolded. Each unfolded distribution is compared to the truth distribution obtained from the full sample of events used to train the migration matrix.

The bias $B^i = \mathscr{N}^i_{\mathrm{truth}} - \mathscr{N}^i_{\mathrm{unfold}}$ and pull $P^i = (\mathscr{N}^i_{\mathrm{truth}} - \mathscr{N}^i_{\mathrm{unfold}})/\sigma_{\mathrm{unfold}}$ distributions are measured for each bin i. Figure 9.7 shows the mean pull and its uncertainty in bins of p_{T} for jets of rank 1 through 5. The shaded bands indicate the width of the pull distribution, obtained from a Gaussian fit. The pull distributions for each bin are shown in Appendix A.2.1. The mean pull is close to zero and has a width close to unity. This demonstrates that the unfolding procedure has no significant bias and that the statistical uncertaintainties on the unfolded distribution are properly estimated. Additional test of the unfolding are provided in Appendix A.2.

In addition to the pull and bias, the average χ^2 between the unfolded pseudoexperiments and the true distribution is computed using Equation 9.6. The χ^2 obtained in the closure test is 42 for 41 degrees, indicating that the inverse covariance matrix returned from RooUnfold appropriately estimates the correlated uncertainties.

9.3.2 Stress test

'Stress' tests assess the effect of the input p_{T} spectrum on the unfolding algorithm by unfolding pseudoexperiments produced from alternate $t\bar{t}$ $\tilde{\mathrm{M}}$C generators (described in Chapter 7.1.2.1) using the response matrix and correction factors obtained from the baseline.

To study the stability of the unfolding with respect to changes in the input jet p_{T} and multiplicity spectra, pseudoexperiments are constructed by reweighting the truth jet spectrum in the baseline MC sample. The weight for each bin is given by the ratio of the alternative generator to the baseline[2]. This procedure isolates the uncertainty associated with the choice of spectrum from other generator-independent sources of instability (e.g. JES), which are accounted for separately.

Stress tests have been performed using the following samples: PowHeg+Pythia, PowHeg+Herwig, MadGraph+Pythia, MC@NLO+ Herwig, PowHeg+Pythia8, PowHeg+Pythia hdamp=m_t, RadHi MadGraph+Pythia and RadLo MadGraph+Pythia. Each of the alternate $t\bar{t}$ samples are unfolded with 1000 pseudoexperiments against a migration matrix filled from the baseline $t\bar{t}$ simulation. In both the migration matrix and the samples, a 3% constribution from single top is included. Correction factors (f and g in Equation 9.1) are also taken from the baseline.

The pull distributions for the alternate generators unfolded against the baseline are provided in Appendix A.3, including studies of number of iterations.

Figure 9.8 shows the fractional bias obtained for the stress test for four representative alternative generators. Though bin-to-bin fluctuations around zero are visible, these fluctuations fall largely within the one sigma error contour. For MC@NLO+ Herwig, the disagreements become large for jets of rank 3 and higher. The jet multiplicity in MC@NLO+ Herwig at reconstruction level is signifigantly lower than the data. For MadGraph+Pythia deviations above the one sigma level are observed for low jet p_{T}. The MadGraph+Pythia is signifigantly steeper than that of PowHeg+Pythia hdamp=∞. This will affect the size of the feed-in correction g_i. The differences with respect to MadGraph+Pythia are included in the systematic uncertainties described in Chapter 10.4.

[2]An alternative reweighting procedure where the ratios were fit to a smooth function was also studied. Changes with respect to the procedure described here were small

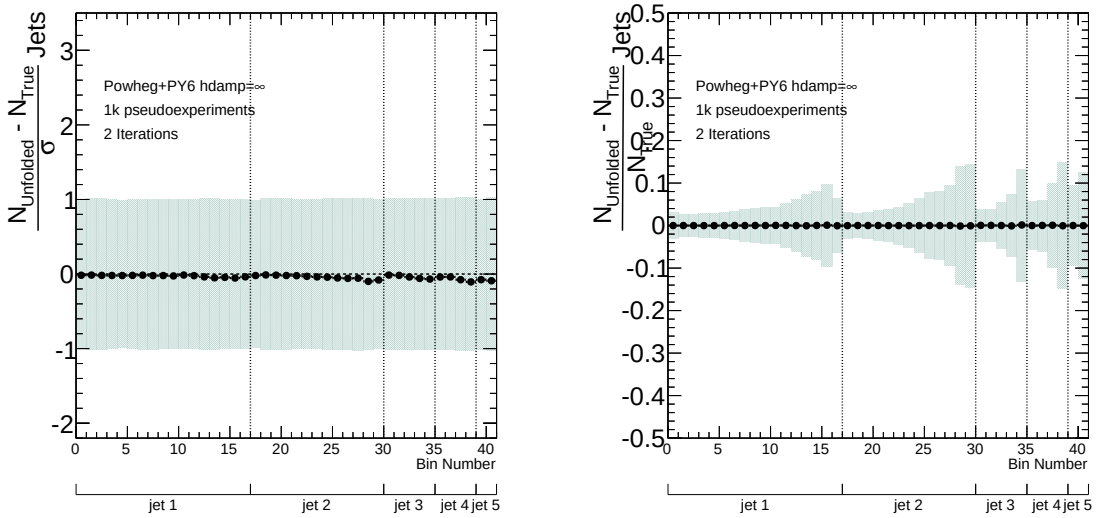

Figure 9.7: (a) Pull distribution and (b) fractional bias for the extra jets from the baseline $t\bar{t}$ simulation unfolded against a matrix filled with the baseline $t\bar{t}$ simulation with all correction factors. The Bayesian unfolding method with 2 iterations is used. One thousand pseudoexperiments, each the size of the events in data, are randomly selected from the sample and unfolded. Each bin of the pull distribution over the pseudoexperiments is fit with a gaussian. The black points show the fitted mean of each bin. A fitted mean of zero shows the unfolding is not signifigantly biased. The blue band shows the fitted σ of each bin. A fitted σ of one shows the unfolding correctly estimates the errors.

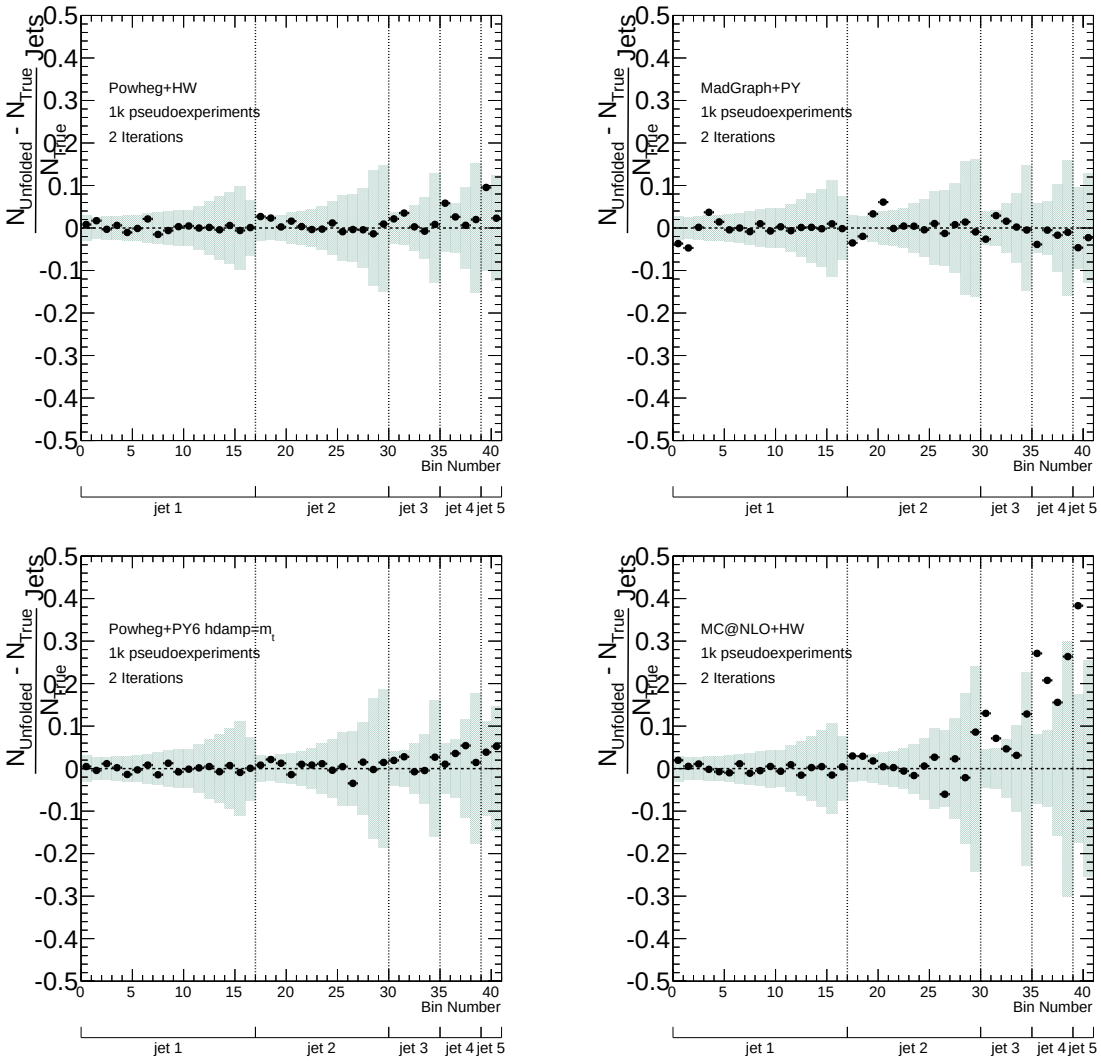

Figure 9.8: Fractional bias distributions for pseudoexperiments from alternative generators unfolded against a matrix filled with the baseline simulation. The truth spectrum of the baseline sample is reweighted to match jet p_{T} and multiplicity spectra of (a) PowHeg+Herwig(b) MadGraph+Pythia,
(c) PowHeg+Pythia hdamp=m_t, and (d) MC@NLO+ Herwig simulation. One thousand pseudoexperiments, each the size of the events in data, are constructed for each generator and unfolded. The Bayesian unfolding method with 2 iterations is used. Each bin of the distribution over the pseudoexperiments is fit with a gaussian. The black points show the fitted mean of each bin and the blue band shows the fitted sigma.

Chapter 10

Sources of uncertainty

The evaluation of systematic uncertainties in this analysis follows the standard ATLAS Top group recommendations.

Each systematic uncertainty is evaluated at the 1σ level. The shift is first evaluated at the reconstructed level and then propagated into the unfolding. The result is compared to the spectrum unfolded without a systematic shift. Except where otherwise indicated, individual systematic uncertainties are assumed to be uncorrelated.

The final χ^2 conclusions in this analysis rely not just on the bin errors of the final distribution, but on the full covariance matrix. The covariance matrices for systematics are evaluated in one of two ways. Some uncertainties depend on the difference between two discrete spectra (e.g. one generator unfolded against another), and the covariance is taken as the outer product of the systematic uncertainty for each bin. For nuisance parameters such as JES, the full covariance matrix can be computed using pseudoexperiments where the relevant parameter is varied according to a Gaussian probability distribution. The details of these two procedures are given below.

10.1 Detector modeling

Detector modeling uncertainties are evaluated using the baseline $t\bar{t}$ simulation by varying the default scale factors within their systematic uncertainties. Jet-related uncertainties, primarily the jet energy scale, are the biggest source of detector modeling uncertainity. Uncertainities due to lepton isolation, reconstruction, identification and trigger efficiencies have been evaluated, but found to be negligible.

10.1.1 Nuisance parameters

Jet energy scale uncertainties are evaluated according to the procedure outlined in Reference [64]. Each of the 23 *nuisance parameters* (independent sources of uncertainty) is independently varied. The jet energy resolution (JER) uncertainty is derived from measure-

ments of the jet response in data and found to agree well with simulation. Jet energy is smeared using a function that depends on p_{T} and η. Because this procedure only allows for an increase in resolution, the resulting uncertainty is symmetrized. The uncertainty on the jet finding efficiency is evaluated by randomly dropping jets in the nominal simulation and reanalyzing the resulting data. The resulting difference is then symmetrized.

The b-tagging scale factor and uncertainty for b-tagging efficiency and mistag is also evaluated using results discussed in Reference [94]. The modeling of the electron and muon trigger and identification efficiencies, energy scales and resolutions were studied using $Z \to ee/\mu\mu$, $J/\psi \to ee/\mu\mu$ and $W \to e\nu$ events in data and simulation, using the techniques described in References [95, 96, 97].

10.1.2 Computation of uncertainty

The impact of these systematic uncertainties on reconstructed extra jets is evaluated by varying each individual scale factor and reanalyzing the simulated data using the same prescription as for the nominal. The standard ATLAS procedure for evaluating detector systematic uncertainties is to vary each nuisance parameter individually by $\pm 1\sigma$. However, this method does not allow the construction of a full covariance matrix. The procedure used here is similar to that used in Ref. [98]. A set of 1000 modified samples is constructed from the full statistics of the PowHeg+Pythia hdamp=∞ simulation. For each sample, each nuisance parameter i is varied by $\lambda_i = \mathrm{G}auss(0, \sigma_i)$, where σ_i is the nuisance parameter uncertainty. The systematic covariance matrix from these samples is then computed:

$$C_{ij} = \frac{1}{1000} \Sigma_{x=0}^{1000} \left(\mathscr{N}_x^i - \left\langle \mathscr{N}^i \right\rangle\right) \left(\mathscr{N}_x^j - \left\langle \mathscr{N}^j \right\rangle\right) \tag{10.1}$$

where $\langle \mathscr{N}^j \rangle$ is the average jets in bin j over all samples and $\mathscr{N}_x^j$ is the number of jets in bin j in a single sample x.

As a cross-check, the uncertainities obtained using this procedure are compared to those obtained using the standard ATLAS method for the most signifigant subset of nuisance parameters. Figure 10.1 shows the uncertainties from the 15 JES eigenstates on the p_{T} for jets of rank=1-4. The band shows the uncertainty obtained from the samples with gaussian variation of all nuisance parameters. The upper and lower lines shows uncertainty from the quadratic sum of the independent variations of each nuisance parameter by $\pm 1\sigma$. The distribution of samples values has fitted $\mu = 1$ and σ consistent with the $\pm 1\sigma$ method.

10.2 Single top rate

Since the single top contribution is treated as signal, a systematic uncertainty must be placed on the rate of selected single top events relative to $t\bar{t}$. To assess the uncertainty on the extra jets, the single top rate is varied relative to the baseline 2.9% computed in Table 7.1. The uncertainty for each bin due to the single top is given by the maximum difference between

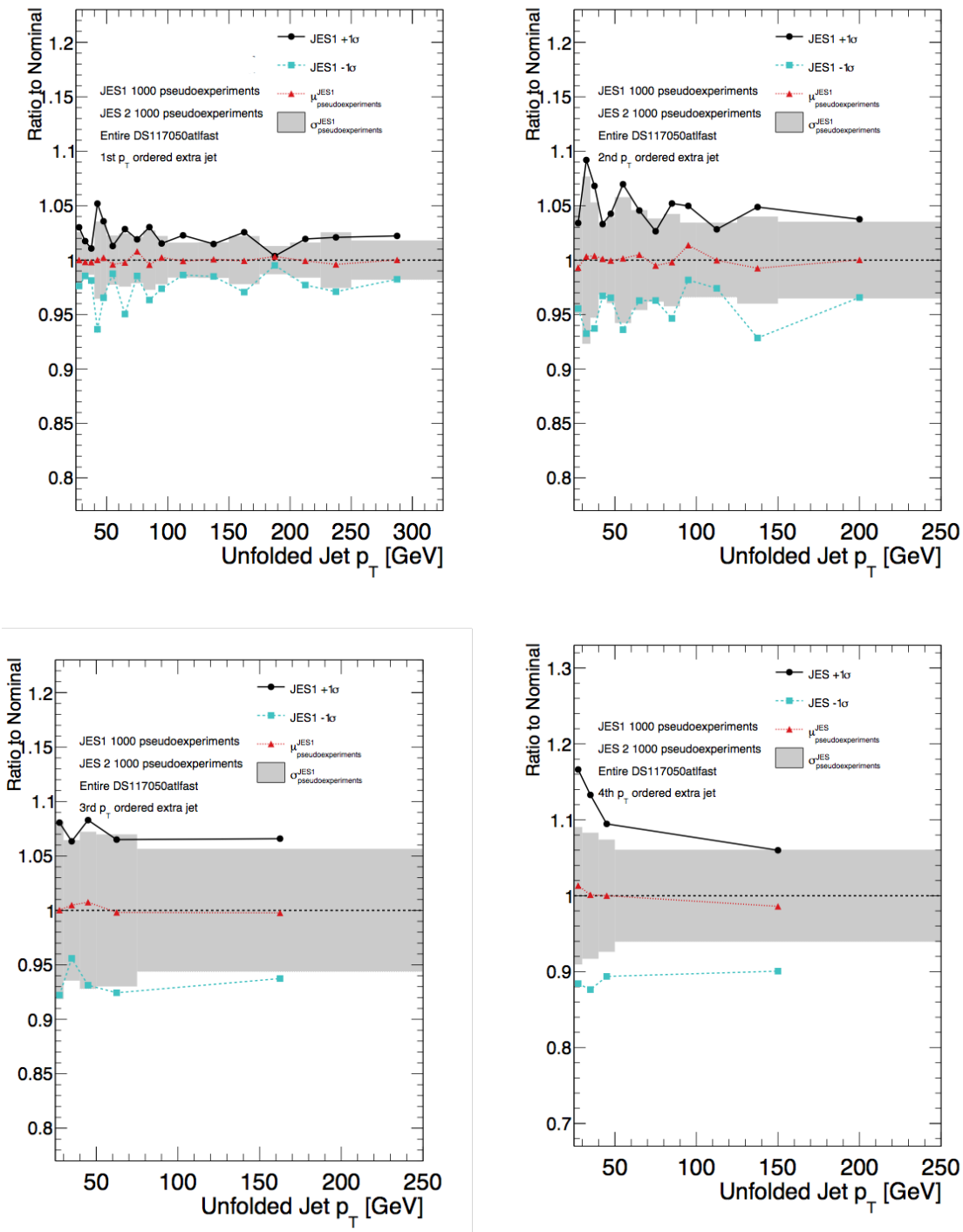

Figure 10.1: Ratio of reconstructed extra jets spectrum obtained from systematic variations of the 15 JES eigenstate nuisance parameters with respect to that obtained using the nominal parameters. The band shows the uncertainty obtained from the samples with gaussian variation of all nuisance parameters. The upper and lower lines shows uncertainty from the quadratic sum of the independent variations of each nuisance parameter by $\pm 1\sigma$. The distribution of samples values has fitted $\mu = 1$ and σ consistent with the $\pm 1\sigma$ method.

the baseline 2.9% single top and 0% or 5.8% single top. The results of this study can be found in Appendix A.6.

$$\sigma_{ij} \equiv \left\langle \max|\mathscr{N}^i_{5.8\%} - \mathscr{N}^i_{2.9\%}|, \mathscr{N}^i_{0\%} - \mathscr{N}^i_{2.9\%}|\right\rangle \left\langle \max|\mathscr{N}^j_{5.8\%} - \mathscr{N}^j_{2.9\%}|, \mathscr{N}^j_{0\%} - \mathscr{N}^j_{2.9\%}|\right\rangle$$

10.3 Pileup and false jet background

Before unfolding, unmatched jets are subtracted from the measured data distribution. The uncertainty on the modeling of these jets is estimated by taking the difference between the pileup and false jets rates obtained in Chapter 8.2 with the rate obtained from the baseline PowHeg+Pythia hdamp=∞ simulation. The unmatched extra jets obtained using these two methods are shown in Figure 10.4. The two distributions agree well at low p_{T} but differ slightly at higher p_{T}. This systematic uncertainty is small compared to the statistical uncertainty of the samples.

$$\sigma_{ij} \equiv \left\langle \mathscr{N}^i_{\text{falsePowHeg+Pythia}} - \mathscr{N}^i_{\text{ZeroBias false}}\right\rangle \left\langle \mathscr{N}^j_{\text{falsePowHeg+Pythia}} - \mathscr{N}^j_{\text{ZeroBias false}}\right\rangle$$

10.4 Input extra jet spectrum

Uncertainty due to the modeling of the input $t\bar{t}$ spectrum for the unfolding is taken from stress tests constructed using the method described in Chapter 9.3.2.

Following the prescription outlined by the Top group (see twiki Ref. [99]), the following input generator samples and unfolding procedures are used to evaluate different components of modeling uncertainty:

NLO generator: MadGraph+Pythia are unfolded using a response matrix and correction factors obtained from PowHeg+Pythia hdamp=∞. MadGraph+Pythia is used rather than MC@NLO+ Herwigbecause MC@NLO+ Herwig is inconsistent with the reconstructed distributions.

Shower: PowHeg+Herwig are unfolded using a response matrix and correction factors obtained from PowHeg+Pythia hdamp=∞.

Radiation: MadGraph+Pythia q^2 up and down are unfolded using a response matrix and correction factors obtained from nominal radiation MadGraph+Pythia.

In all cases, the unfolded result is compared to the truth for the input generator. For each component, the uncertainty is expressed as a covariance matrix obtained from the outer product of the biases:

$$\sigma_{ij} \equiv \left\langle \mathscr{N}^i_{\text{unf}} - \mathscr{N}^i_{\text{truth}}\right\rangle \left\langle \mathscr{N}^j_{\text{unf}} - \mathscr{N}^j_{\text{truth}}\right\rangle \tag{10.2}$$

The radiation uncertainty is taken from the average bias for MadGraph+Pythia q^2 up and down.

10.5 Statistical uncertainty on migration matrix

As shown in the Figure 9.2(a), the migration matrix has some elements far from the diagonal with very few entries. To account for the uncertainty introduced by the migration matrix statistics, pseudoexperiments are unfolded varying the response matrix while keeping the input spectrum constant. The migration matrix, input spectrum and correction factors are all taken from the baseline PowHeg+Pythia hdamp=∞ sample. The contribution to the covariance matrix from this componenet is evaluated according to Equation 10.1.

10.6 PDF modeling uncertainty

Uncertainty in the modeling of the parton distribution function (PDF) can affect modeling of the extra jets. Following the prescription given in Ref. [100], events are reweighted according to the x and Q^2 of the corresponding PDF variation. PDF variations are taken from the MC@NLO+ Herwig sample is used with 52 variations for the CT10 PDF, 40 variations for the MSTW PDF, and 100 variations for the NNPDF [1].

Each variation is unfolded with the nominal MC@NLO+ Herwig migration matrix. For each bin, the average bias of the variations with respect to the input spectrum is computed. The outer product of these biases is used to compute the covariance for the PDF uncertainty:

$$\sigma_{ij} \equiv \left\langle \mathcal{N}^i_{\text{unf}} - \mathcal{N}^i_{\text{truth}} \right\rangle \left\langle \mathcal{N}^j_{\text{unf}} - \mathcal{N}^j_{\text{truth}} \right\rangle$$

10.7 Combined uncertainty

A covariance matrix associated with the statistical uncertainty of the input data spectrum is returned from `RooUnfold`. The covariance matrix due to all sources of uncertainty described above is then added to the `RooUnfold` matrix to obtain the final uncertainty on the corrected data. Figure 10.6 shows (a) the statistical covariance matrix and (b) total covariance matrix for the unfolded data. The diagonal elements of total matrix are used to obtain uncertainties on unfolded data in bins of p_{T} and rank. The entire matrix is used to assess the agreement between data and generators.

Figure 10.5 shows the sum of uncertainties from all sources, broken into categories as follows.

Data Statistics: Statistical uncertainty on the data is returned from `RooUnfold`

$t\bar{t}$ modeling: NLO generator, radiation, and parton shower uncertainties(Chapter 10.4)

MC Stats: Migration matrix statistics uncertainties (Chapter 10.5)

[1] Though MC@NLO+ Herwig shows poor agreement with data, it is the only sample for which x and Q are properly recorded in ATLAS simulation

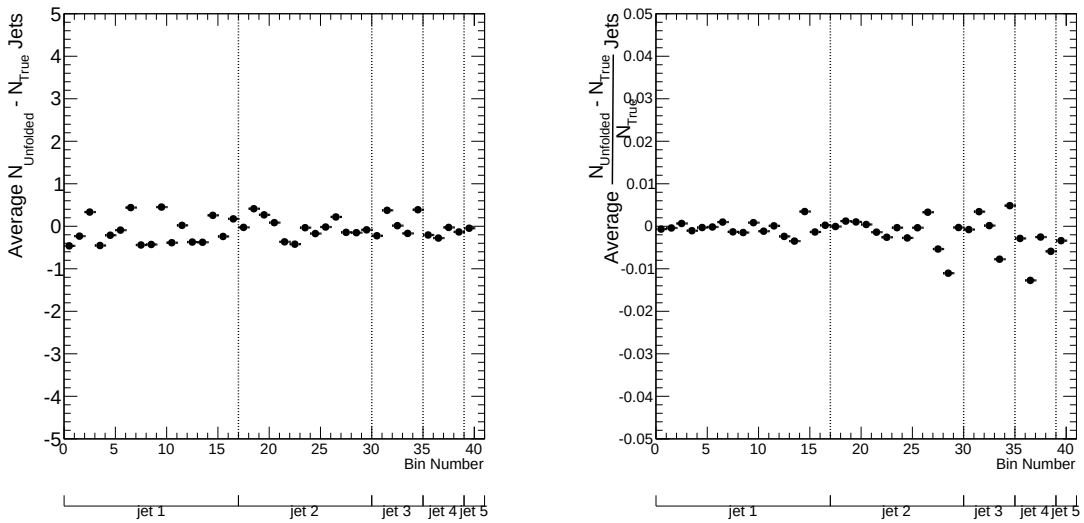

Figure 10.2: (a) bias and (b) fractional bias distributions PDF variations of MC@NLO+ HERWIGunfolded with the nominal MC@NLO+ HERWIGmigration matrix. Each bin of the distribution over the pseudoexperiments is fit with a gaussian. The outer product of the bias is used to compute the uncertainty due to the PDF.

PDF: PDF variations, determined from MC@NLO+ HERWIG(Chapter 10.6)

JVF/Unmatched Jets: Uncertainties from JVF nuisance parameters (Chapter 10.1.1) and false jet modeling (Chapter 10.3)

JES: Jet energy scale nuisance parameters (Chapter 10.1.1)

JER/JEFF: Jet energy resolution and jet finding efficiency nuisance parameters (Chapter 10.1.1)

Other detector: Lepton and b-tag nuisance parameters not in the JES, JER/JEFF or pileup category.

Backgrounds: Single top rate uncertainty Wt (Chapter10.2)

In most bins, statistical uncertainty dominates. At low jet p_{T}, JES is the largest source of uncertainty. Modeling is the largest source of uncertainty at high jet p_{T}.

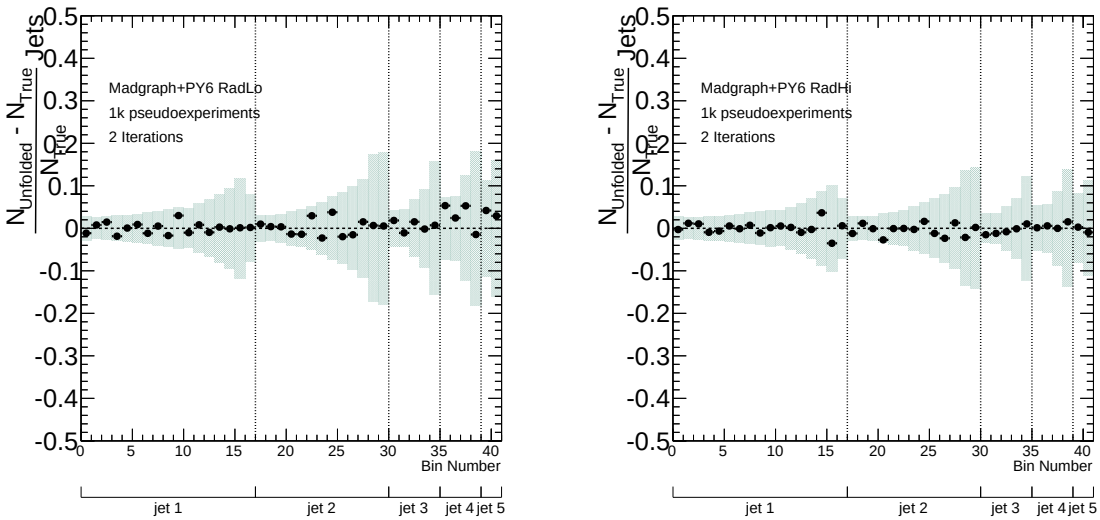

Figure 10.3: Fractional bias distributions for pseudoexperiments from MadGraph+Pythia radiation samples unfolded against a matrix filled with nominal MadGraph+Pythia. The truth spectrum of the baseline sample is reweighted to match jet p_{T} and multiplicity spectra of (a) MadGraph+Pythia RadLo (b) MadGraph+Pythia RadHi simulation. One thousand pseudoexperiments, each the size of the events in data, are constructed for each generator and unfolded. The Bayesian unfolding method with 2 iterations is used. Each bin of the distribution over the pseudoexperiments is fit with a gaussian. The black points show the fitted mean of each bin and the blue band shows the fitted sigma.

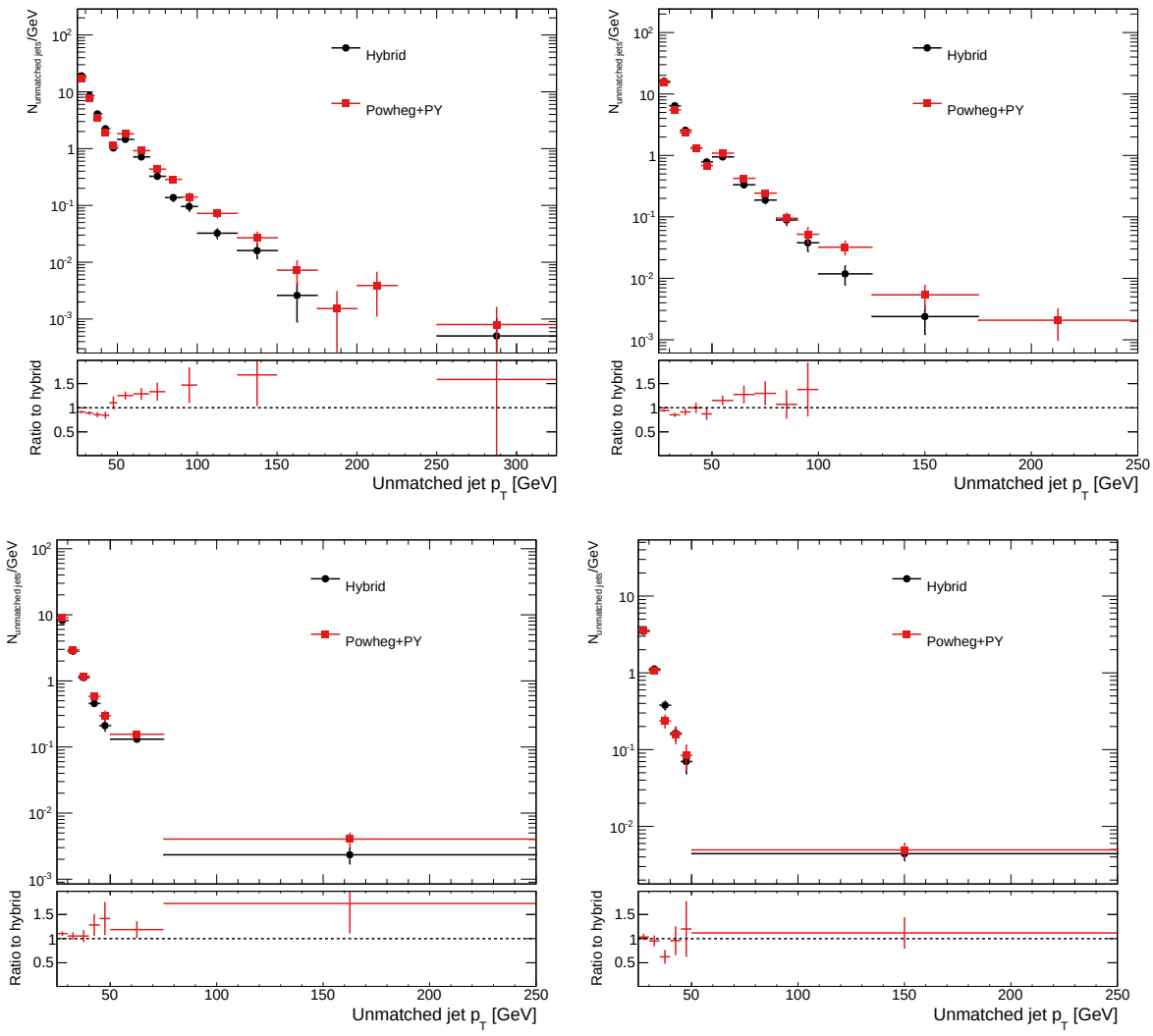

Figure 10.4: Unmatched jets in the baseline $t\bar{t}$ simulation and the hybrid sample. The difference between the two is used to estimate the uncertainty.

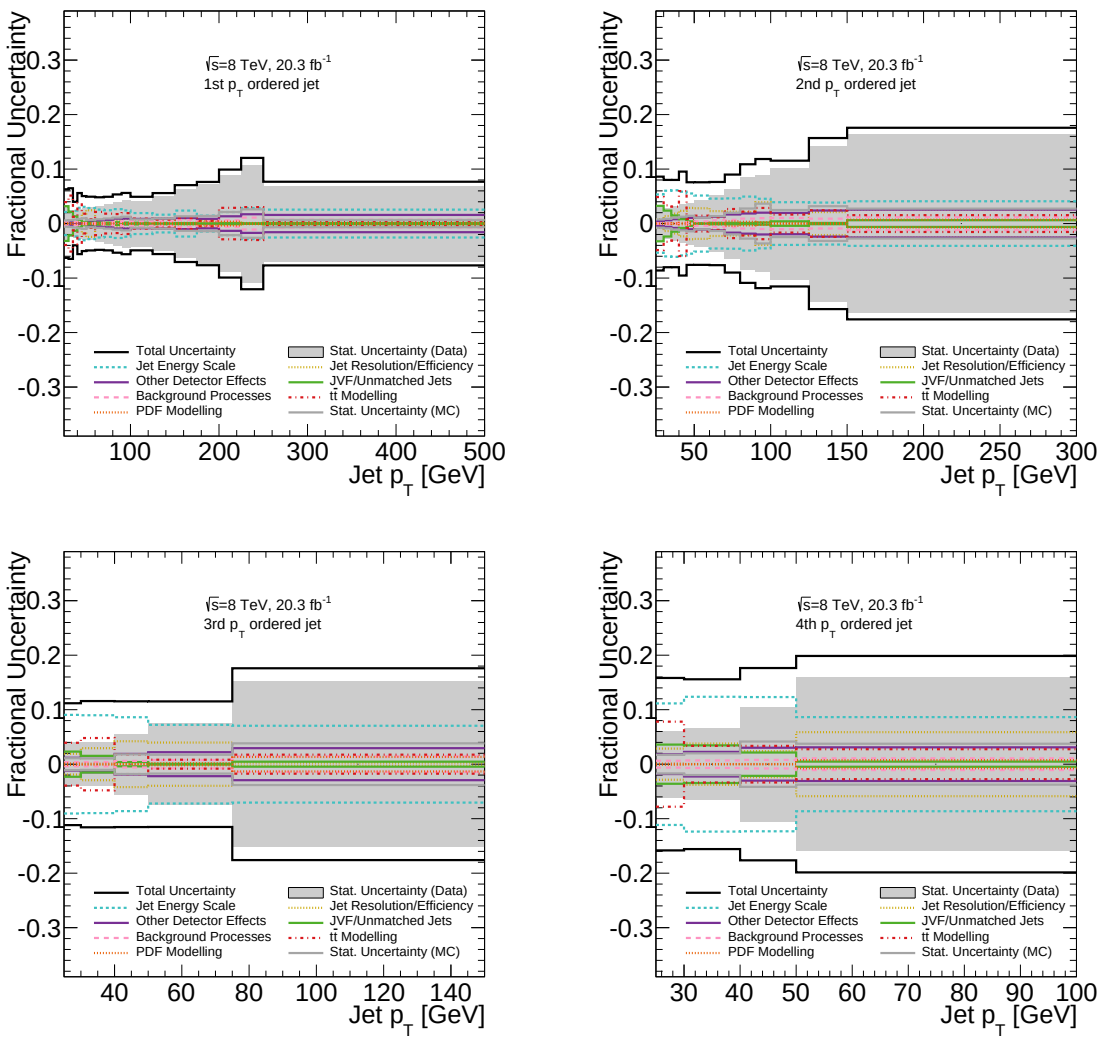

Figure 10.5: Sum of systematic uncertainties due to detector modeling. The ratio of the simulated extra jets reconstructed with each systematic variation is taken with respect to the nominal. The band shows the data statistical uncertainty for reference.

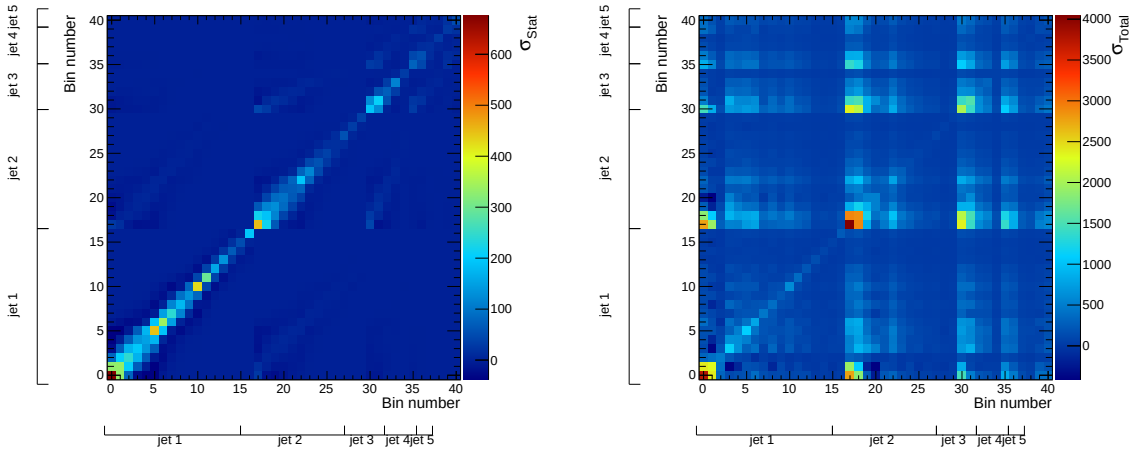

Figure 10.6: (a) The covariance matrix associated with the statistical uncertainty of the input spectrum returned from `RooUnfold`. (b) The covariance matrix from all sources of uncertainty, obtained by adding the covariance matrices from all sources of systematic uncertainty to (a). This matrix is used to determine the χ^2 agreement between generators and the fully corrected data.

Chapter 11

Results

This chapter presents the final, fully corrected results of the analysis described in the previous chapters. Fully corrected distributions are present, then the corrected data is compared to different MC generators using a χ^2 test. Finally, the results of this χ^2 test are discussed.

11.1 Fully corrected distributions

Figure 11.1 shows the normalized differential cross-section $\frac{1}{\sigma}\frac{d\sigma_{\mathrm{jet},i}}{dp_T}$ for jets of rank 1-4 and compares the data to four next-to-leading order generators. Figure 11.2 provides the multiplicity of extra jets measured. All of the generators provide a reasonable description of the leading jet. Correct modeling of the leading jet is perhaps unsurprising since NLO calculations can include one additional jet in the hard scattering calculation. Differences among the generators become larger with increasing jet rank since the generators predict significantly different rates of additional jet production. The generators also predict some differences in the shapes of the jet p_{T} spectra. The MC@NLO+ Herwig generator predicts the lowest rate of additional jet production and underestimates the number of events with at least 4 jets by 40%. The level of agreement between the remaining generators and the data can only be assessed using a more rigorous statistical test and is discussed below.

The same fully corrected data are compared to multi-leg leading order generators in Figure 11.3. In all cases, the renormalization and factorization scales are set to the defaults provided by the code authors. Alpgen used with Pythia or Herwig does a reasonable job of reproducing the data, while MadGraph+Pythia provides a less accurate description.

For lowest order generators, the predicted cross section can depend strongly on the choice of scale. Figure 11.4 shows the effects of such scale variation for the generators under consideration. In all cases the solid (dashed) line shows the predicted rate with the scale is halved (doubled). The measurement provides a smaller uncertainty on the cross section than the scale variations in the lowest order calculation would allow.

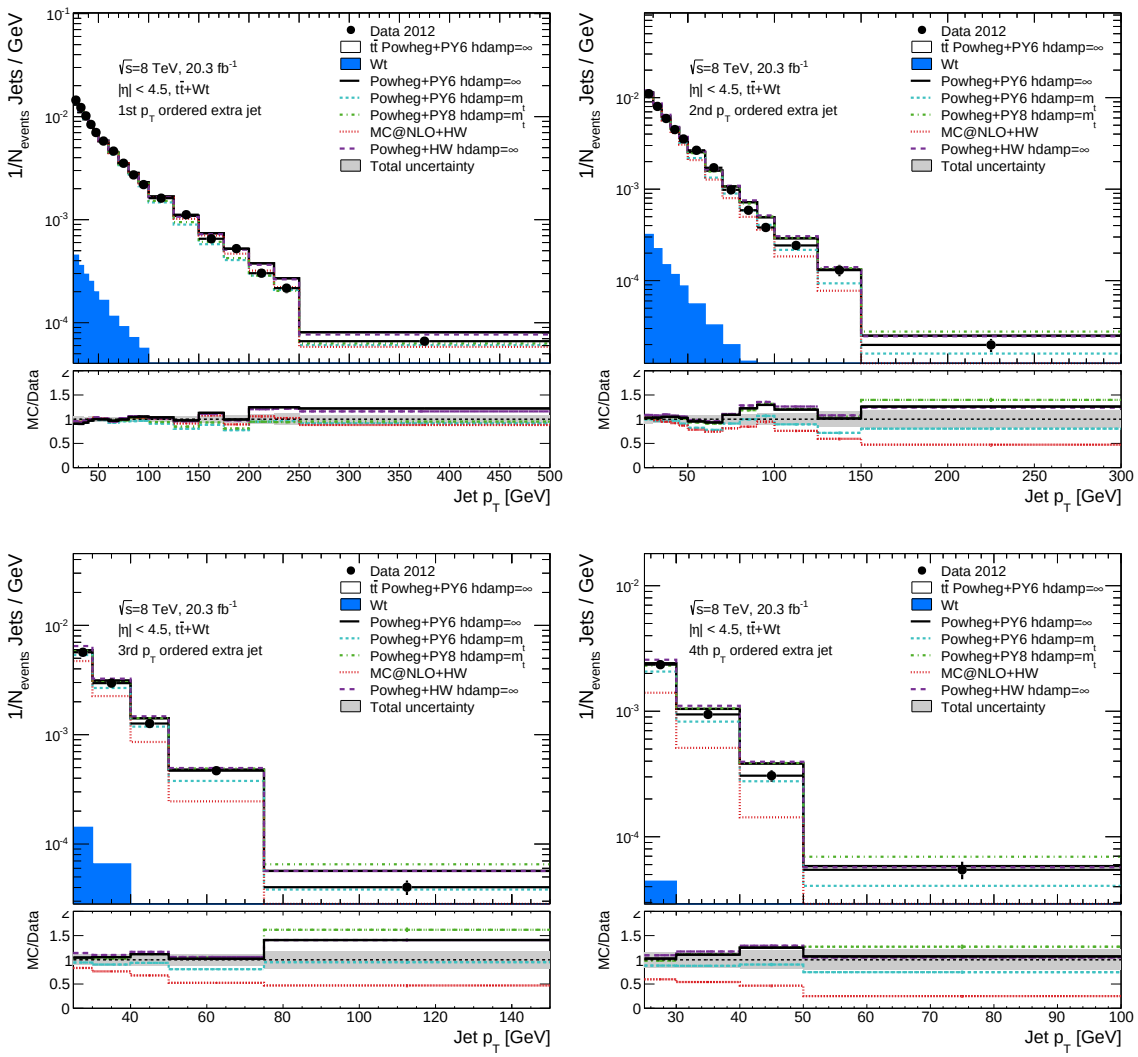

Figure 11.1: Distributions of the unfolded p_{T} of extra jets in data and simulation. Each sample is unfolded against a response matrix filled with baseline $t\bar{t}$ +single top simulation. The gray band on the ratio shows the sum of statistical and systematic uncertainties.

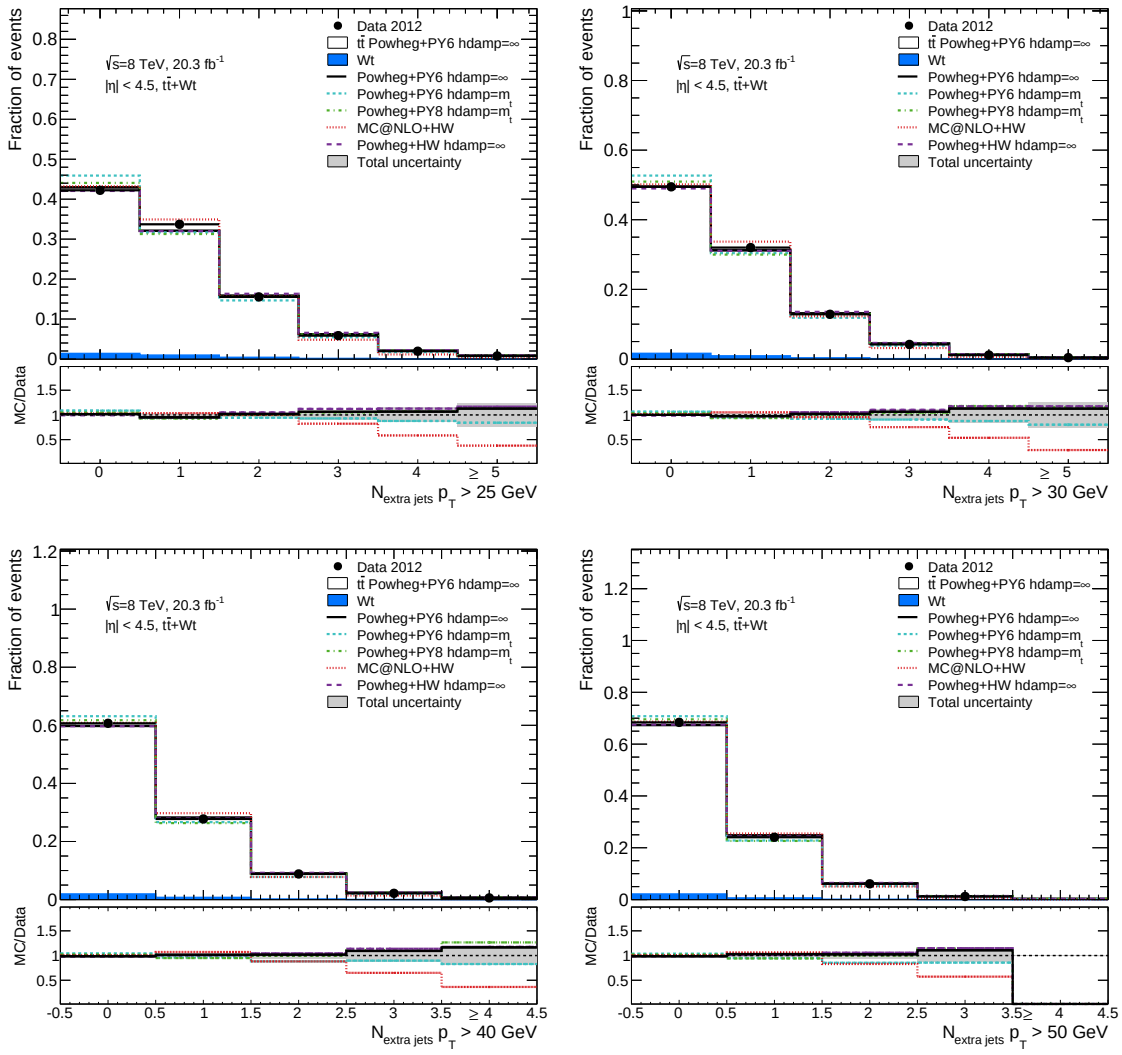

Figure 11.2: Distributions of the number of unfolded extra jets with p_{T} ¿ (a) 25, (b) 30, (c) 40 and (d) 50 GeV in data and simulation. Each sample is unfolded against a response matrix filled with baseline $t\bar{t}$ +single top simulation. The gray band on the ratio shows the sum of statistical and systematic uncertainties.

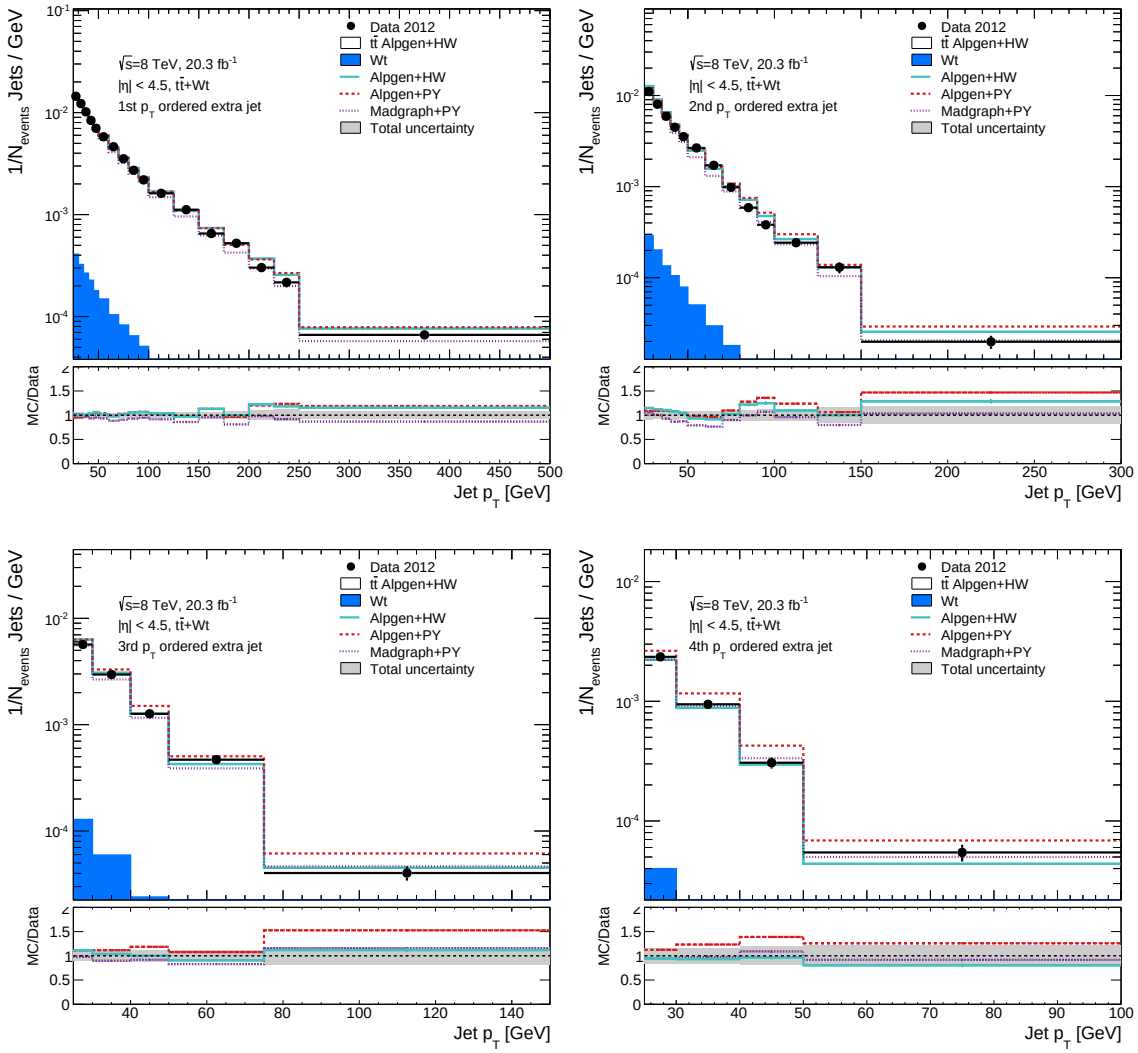

Figure 11.3: Distributions of the unfolded p_{T} of extra jets in data and simulation. Each sample is unfolded against a response matrix filled with baseline $t\bar{t}$ +single top simulation. The gray band on the ratio shows the sum of statistical and systematic uncertainties.

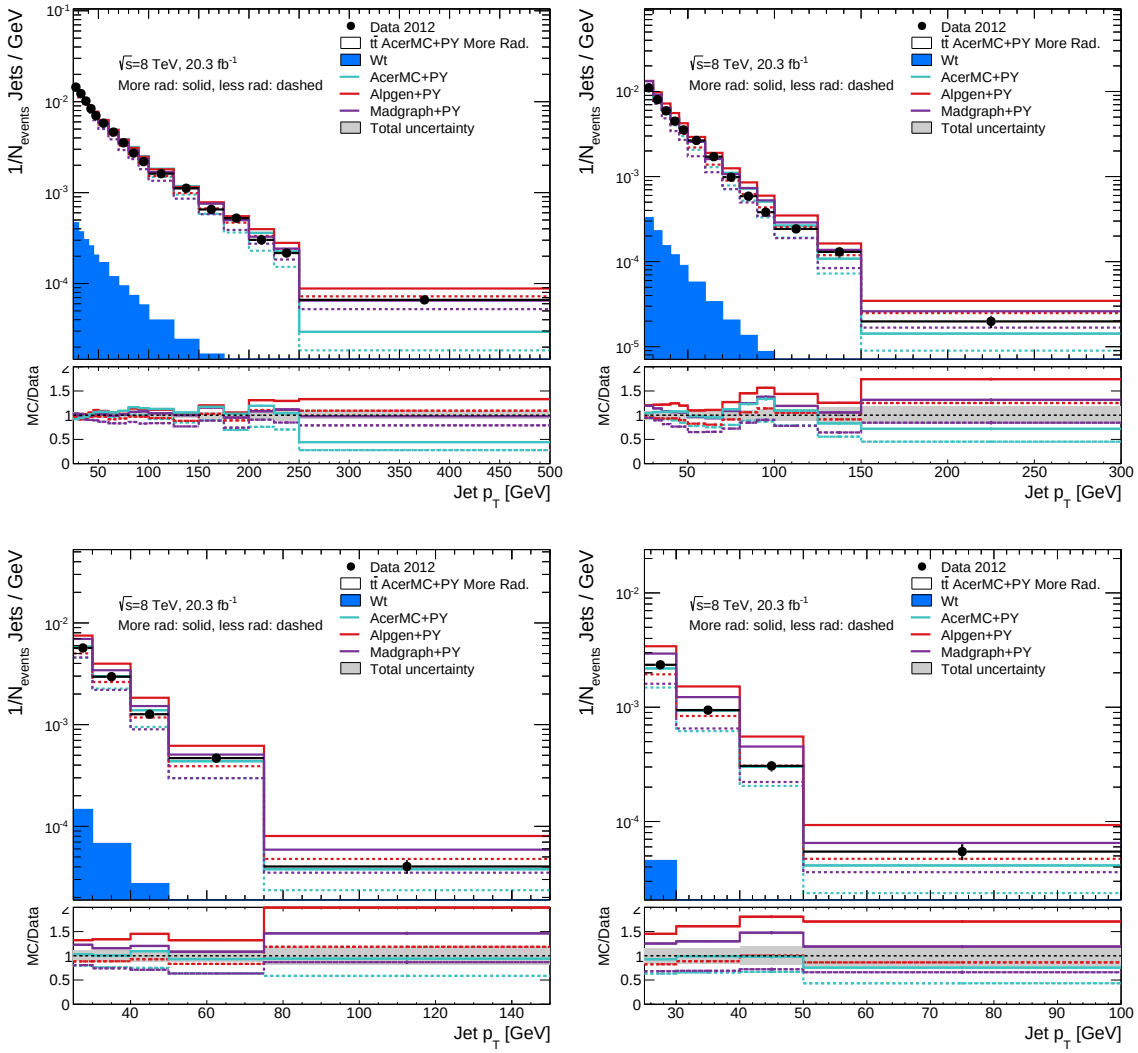

Figure 11.4: Distributions of the unfolded p_{T} of extra jets in data and simulation. Each sample is unfolded against a response matrix filled with baseline $t\bar{t}$ +single top simulation. The gray band on the ratio shows the sum of statistical and systematic uncertainties.

Generator	χ^2_{stat}	p-value	$\chi^2_{\text{stat+sys}}$	p-value
PowHeg+Pythia hdamp=∞	103.06	2.9628×10^{-7}	53.59	8.9931×10^{-2}
PowHeg+Pythia hdamp=m_t	129.84	3.6708×10^{-11}	43.77	3.5480×10^{-1}
PowHeg+Pythia8	162.67	2.0444×10^{-16}	61.72	1.9762×10^{-2}
MC@NLO+ Herwig	301.51	2.1411×10^{-41}	103.58	2.5140×10^{-7}
PowHeg+Herwig	246.22	4.3310×10^{-31}	55.95	5.9838×10^{-2}
Alpgen+Herwig	162.34	2.3213×10^{-16}	74.80	9.8529×10^{-4}
Alpgen+Pythia	147.24	6.7828×10^{-14}	50.71	1.4222×10^{-1}
MadGraph+Pythia	167.50	3.2078×10^{-17}	53.01	9.9021×10^{-2}
AcerMC+PythiaRadHi	185.62	2.6851×10^{-20}	116.39	3.8078×10^{-9}
AcerMC+PythiaRadLo	401.24	1.2019×10^{-60}	95.75	2.8533×10^{-6}
Alpgen+PythiaRadHi	709.83	7.6068×10^{-123}	104.70	1.7642×10^{-7}
Alpgen+PythiaRadLo	124.23	2.6195×10^{-10}	45.51	2.8983×10^{-1}
MadGraph+Pythiaq^2 down	187.13	1.4771×10^{-20}	55.47	6.5133×10^{-2}
MadGraph+Pythiaq^2 up	506.35	1.6412×10^{-81}	95.84	2.7788×10^{-6}

Table 11.1: χ^2 between extra jet p_{T} spectra in fully corrected data and different generators. The first column represents the agreement including only (diagonal) statistical uncertainties. The second column also includes the covariance due to systematic uncertainties (primarily JES).

11.2 χ^2 comparisons and discussion

Because the systematic and unfolding uncertainties have large correlations between bins, calculating the χ^2 from the full covariance matrix is necesarry to assess the agreement between the data and generators. Table 11.1 presents the χ^2 obtained by comparing the extra jet p_{T} and rank distributions in the data and each generator. The χ^2 is calculated using only the statistical uncertainty, as well as the sum of systematic and statistcal uncertainties. The structure of χ^2 can be be visualized as a matrix of its addends $(N^i_{mc}-N^i_{data})\sigma^{-1}_{ij}(N^j_{mc}-N^j_{data})^j$. This matrix is shown for PowHeg+Pythia hdamp=∞, PowHeg+Pythia hdamp=m_t, MadGraph+Pythia, and PowHeg+Pythia8 in Figure 11.5.

Among NLO generators, PowHeg+Pythia hdamp=m_t and PowHeg+Pythia hdamp=∞ agree the best with the data. PowHeg+Herwig and PowHeg+Pythia8 are slightly disfavored, and MC@NLO+ Herwig is excluded. For multi-leg LO generators, Alpgen+Pythia agrees well with data, while MadGraph+Pythia and Alpgen+Herwig are slightly disfavored. The less radiation systematic variation of MadGraph+Pythia agree best with data, suggesting that the scale used in baseline ATLAS tunes may predict too much radiation in this analysis' fidicual region. AcerMC+Pythia does not reproduce the data well, regardless of scale.

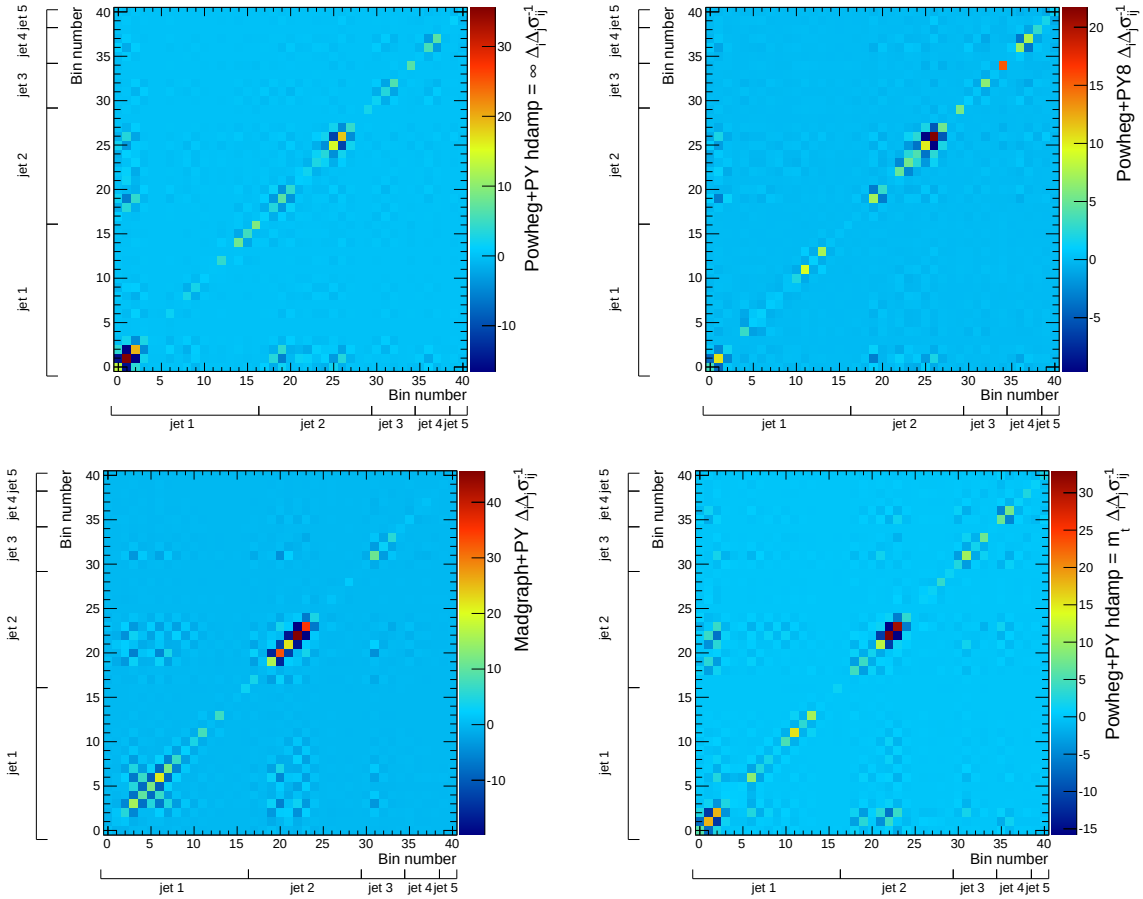

Figure 11.5: Visual representation of the χ^2 distributions for (a) PowHeg+Pythia hdamp=∞ (b) PowHeg+Pythia8 (c) MadGraph+Pythia and
(d) PowHeg+Pythia hdamp=m_t. Each element ij of the matrix is given by $M_{ij} = (N^i_{mc} - N^i_{data})\sigma^{-1}_{ij}(N^j_{mc} - N^j_{data})^j$ where N^i_{mc} is the number of jets predicted in bin i, N^i_{data} is the number of jets in bin i in data, and σ^{-1} is the inverse of the covariance matrix.

Chapter 12

Conclusions

The extra jets produced in association with top quark pairs in $e\mu$ events with at least 2 b-jets from 2012 data collected with the ATLAS detector have been fully corrected back to particle-level. Among next-to-leading order generators, PowHeg+Pythia hdamp=m_t provides the best description of the data while PowHeg+Pythia hdamp=∞ PowHeg+Pythia8 and PowHeg+Herwig are slightly disfavored. Comparisons with generators show that MC@NLO+ Herwigproduces extra jets in poor agreement with those in data. Among leading-order multi-leg generators, MadGraph and Alpgen interfaced with Pythia agree reasonably well with data, while Alpgen+Herwig does not. Comparing data to leading-order generators with scale variations shows that MadGraph and Alpgen interfaced with Pythia reproduce data with a lower scale parameter. Both scale variations of AcerMC interfaced with Pythia do not agree with data. The results presented here can be used in conjunction with other top production mesurement to further tune the parameters associated with parton shower Monte Carlo generators.

Appendix A

Extra jets

A.1 Truth distributions

A.1.1 Kinematic distributions for b- and extra jets at truth level

This appendix provides truth level distributions for b-jets and extra jets in the $t\bar{t}$ and Wt events. Predictions obtained with Powheg+Pythia hdamp=∞, MC@NLO+Herwig, Powheg+Pythia hdamp=m_{top} and MadGraph+Pythia are presented.

A.1.2 Jet distributions for $t\bar{t}$ events

Figure A.1 shows the p_{T} and η distributions for b-jets and for extra jets obtained using different $t\bar{t}$ event generators. The b-jet p_{T} and η distributions obtained with different generators agree to within a few per cent. MC@NLO has a broader η distributon for extra jets than the other generators. Figure A.2 presents the extra jet multiplicity distributions for the generators, with several choices for the minimum jet p_{T}. Differences among the generators as large as 40% are seen for extra jet multiplicities ≥ 5. The extra jet p_{T} spectra for jets of rank 1 through rank 5 are shown in Figure A.3. Differences up to 20% for the leading jet and up to 40% for higher rank jets are seen at high jet transverse momentum.

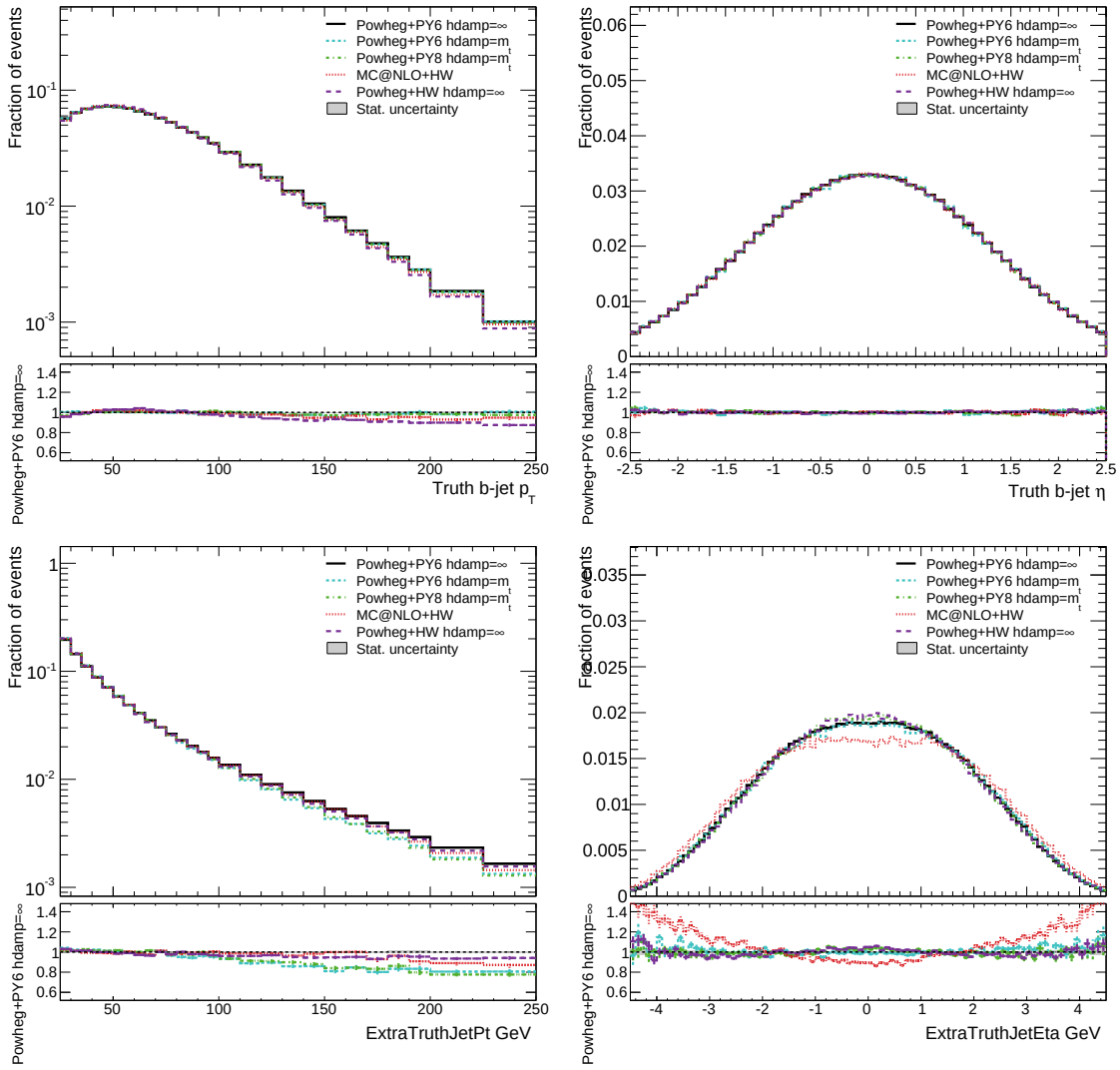

Figure A.1: Distributions of the truth b-jet (a) p_{T}, (b) b-jet η, (c) extra jet p_{T}, and (d) extra jet η in $t\bar{t}$ simulation.Several alternate physics models are compared to the baseline, each normalized by the number of selected truth events.

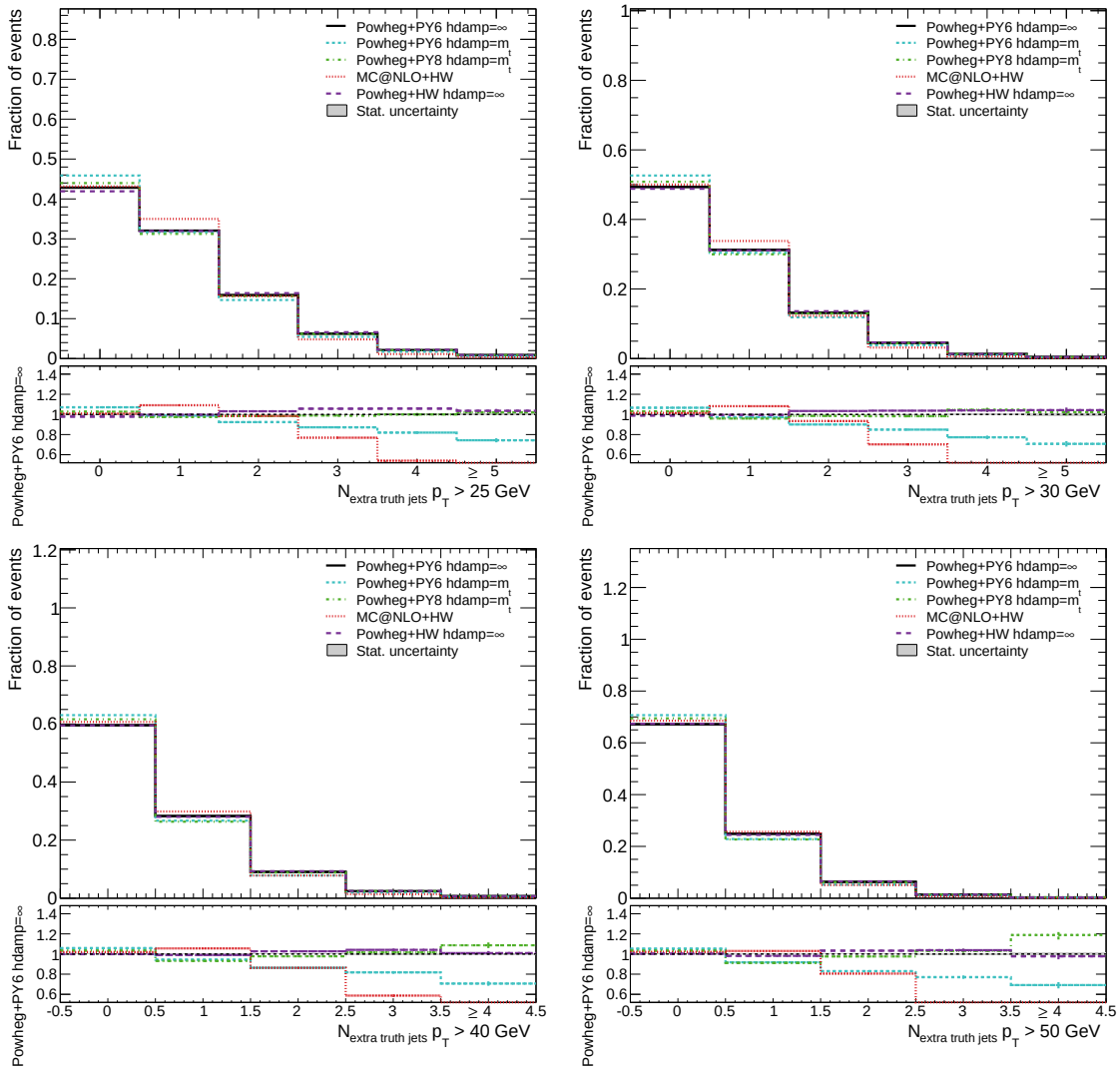

Figure A.2: Distributions of the number of extra truth jets with $p_{\mathrm{T}} >$ (a) 25, (b) 30, (c) 40 and (d) 50 GeVin $t\bar{t}$ simulation. Several alternate physics models are compared to the baseline, each normalized by the number of selected truth events.

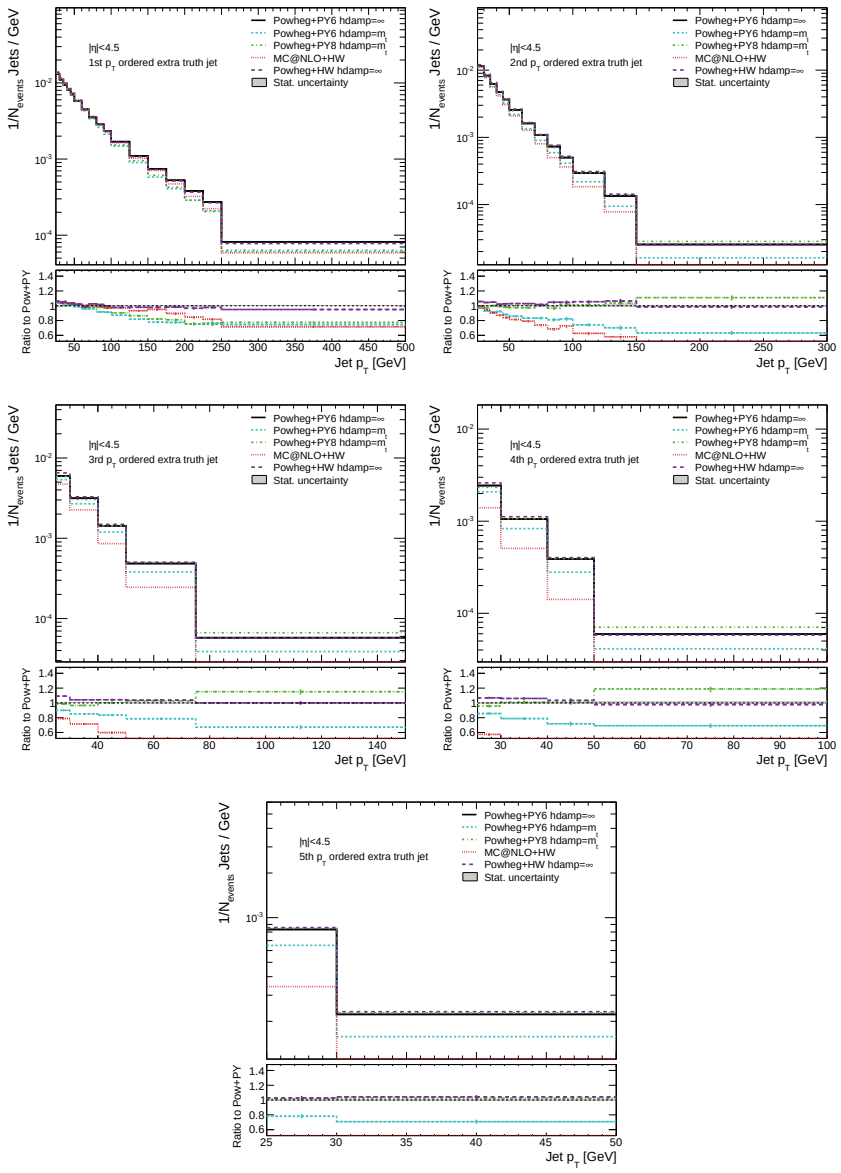

Figure A.3: Distributions of the extra truth jet p_{T} in $t\bar{t}$ simulation for jet ranks 1-5 (a-e). Several alternate physics models are compared to the baseline, each normalized by the number of selected truth events.

A.2 Unfolding validation

A.2.1 Closure test

This appendix presents the results of the closure tests used to validate the unfolding procedures. One hunded pseudoexperiments are constructed, each the weighted number of events equal to the number of $e\mu + 2$ b-jets events observed in the data, by varying the number of jets in the baseline $t\bar{t}$ +Wt simulation sample. Each pseudoexperiment is unfolded and the bias ($N_{unfolded} - N_{true}$) and pull ($(N_{unfolded} - N_{true})/\sigma_{unfolded}$) are calculated. For each bin in p_{T} and rank, the bias and pull distributions are fit to Gaussians.

p_{T} for jets of rank 1 through rank 5. The shaded band indicates the fitted sigma. There is no evidence of statistically significant bias in the unfolding.

Figures A.4 through A.6 show the pull distributions for each bin, together with parameters of Gaussian fits to these distributions. A summary of these results are also shown in Figure 9.7.

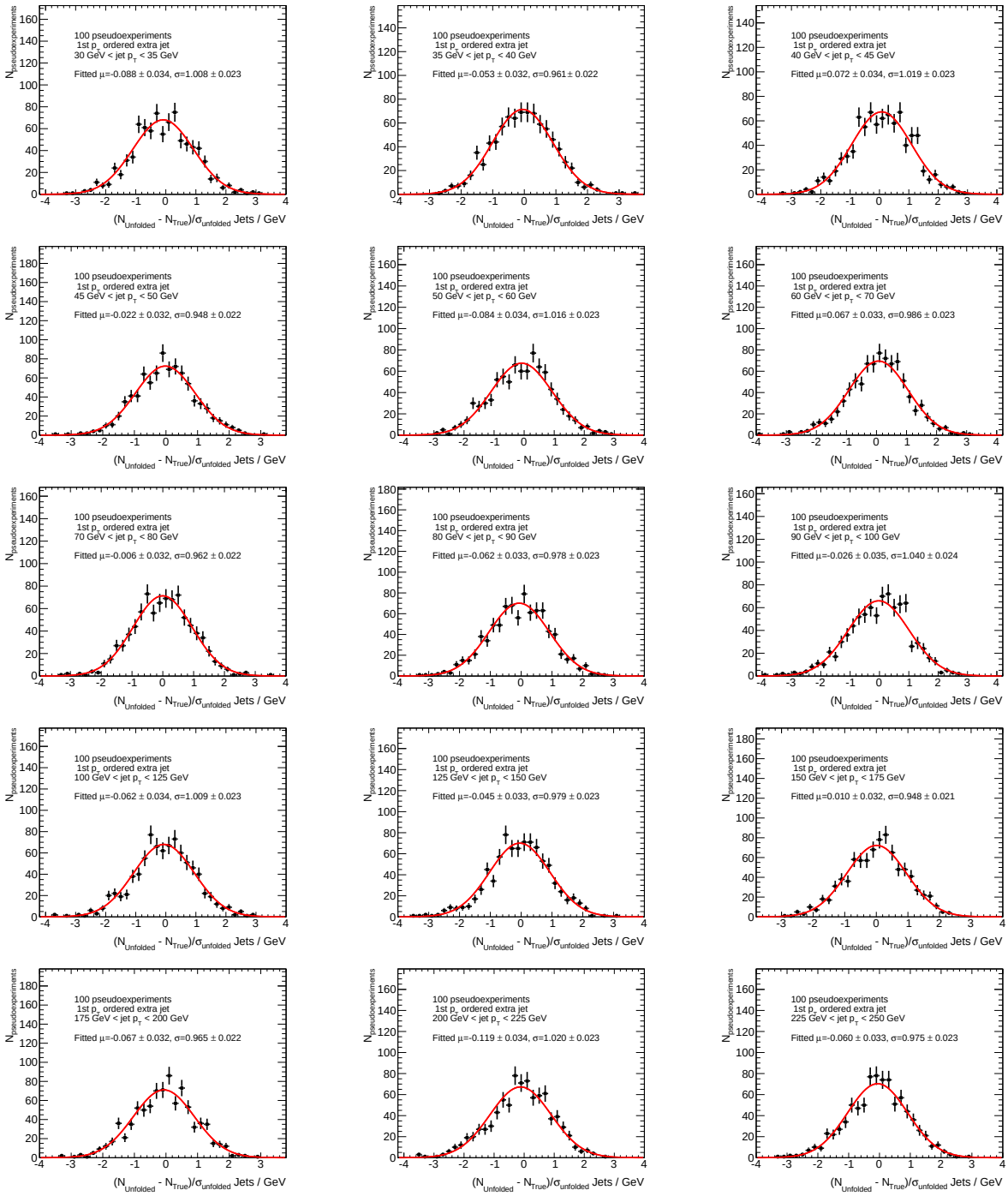

Figure A.4: Pull distributions for the extra jets from the baseline $t\bar{t}$ +Wt simulation unfolded against a matrix filled with the baseline $t\bar{t}$ +Wt simulation . The Bayesian unfolding method 4 iterations is used. One thousand pseudoexperiments, each the size of the events in data, are randomly selected from the sample and unfolded. A Gaussian is fit to the distributions of biases over the pseudoexperiments

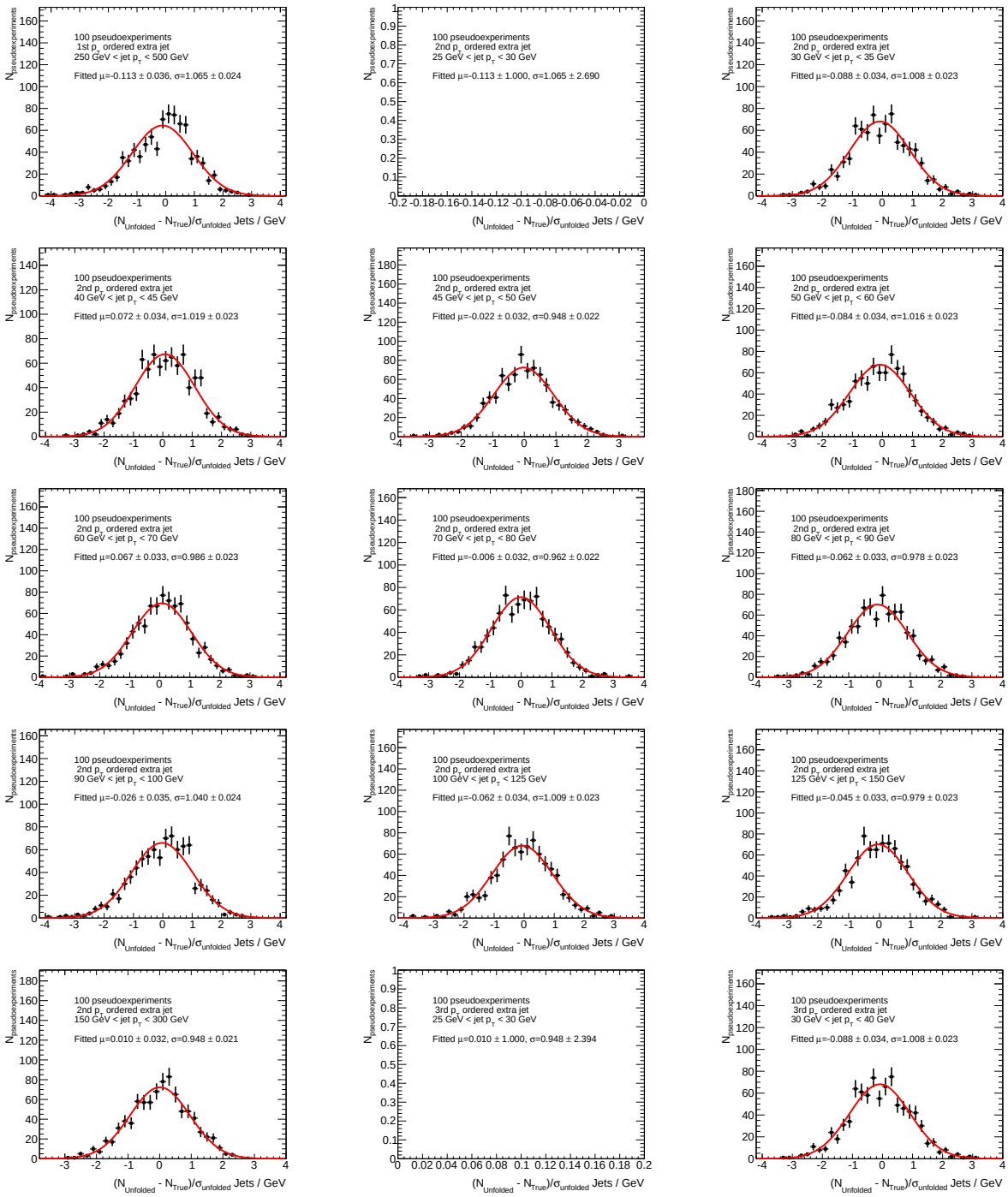

Figure A.5: Pull distributions for the extra jets from the baseline $t\bar{t}$ +Wt simulation unfolded against a matrix filled with the baseline $t\bar{t}$ +Wt simulation . The Bayesian unfolding method 4 iterations is used. One thousand pseudoexperiments, each the size of the events in data, are randomly selected from the sample and unfolded. A Gaussian is fit to the distributions of biases over the pseudoexperiments.

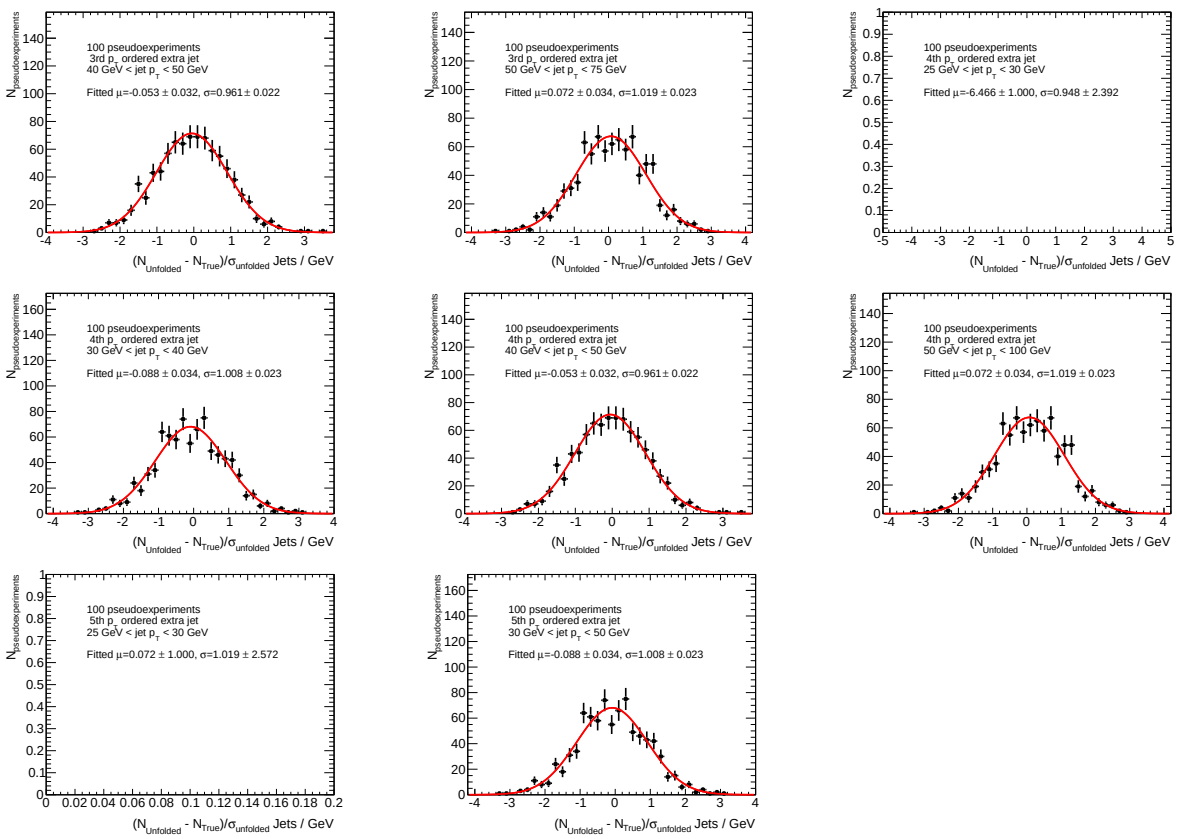

Figure A.6: Pull distributions for the extra jets from the baseline $t\bar{t}$ +Wt simulation unfolded against a matrix filled with the baseline $t\bar{t}$ +Wt simulation . The Bayesian unfolding method 4 iterations is used. One thousand pseudoexperiments, each the size of the events in data, are randomly selected from the sample and unfolded. A Gaussian is fit to the distributions of biases over the pseudoexperiments

A.3 Optimization of number of iterations for unfolding

The optimization of the number of iterations for the Bayesian unfolding is done by studying the performance of the unfolding in stress tests. The response matrix is taken from the baseline ttbar sample(PowHeg+Pythia hdamp=∞ + 3% Wt). The input reconstructed distribution are obtained from each of NLO alternate ttbar generators discussed in Chapter 7.1.2.1. The same 3% Wt contribution is included for each generator.

One thousand pseudoexperiments are constructed from each generator as in Chapter 9.3.2. These pseudoexperiments are then unfolded, varying the number of iterations from one to nine. A number of metrics are studied to understand the behavior of the unfolding.

Mean bias: The bias is calculated as $N_{\text{unfolded}} - N_{\text{true}}$ averaged one thousand pseudoexperiments.

Figures A.7-A.11 show the mean and σ of the bias for each of the 41 bins, obtained from a Gaussian fit over all one thousand pseudoexperiments for one through four iterations. Figures A.12-A.16 show the fractional bias, taken as the ratio of the bias spectrum to the truth. As the number of iterations is increased, the σ of the bias increases.

To understand whether the mean of the bias improves with the number of iterations, the bias averaged over all 41 bins is calculated in Table A.1 for N_{iter} 1-9. Bin-by-bin unfolding is also included for comparison. Bin-by-bin unfolding produces an mean bias of ~300 jets. For Bayesian unfolding, the bias varies from <1 up to ~6 jets depending on generator. This represents a fractional bias of 0.3-2% of the total number of jets.In all cases, the bias depends only weakly on N_{iter}, but tends to increase with increasing N_{iter}.

Mean bias^2: The bias squared is calculated as

$$\frac{1}{N_{\text{bins}}} \sum_{j=1}^{N_{\text{bins}}} \left(\frac{1}{N_{\text{pseudo}}} \sum_{i=1}^{N_{\text{pseudo}}} N^i_{\text{unfolded}} - N^i_{\text{true}} \right)^2_j$$

Table A.2 provides the mean bias^2 for bin-by-bin unfolding and Bayesian unfolding with N_{iter}=1-9. The bin-by-bin unfolding has a mean bias^2 of $\sim 10 \times 10^6$ jet^2. Depending on the generator, the mean bias^2 for one iteration varies from ~20 to ~80 jets^2. In all cases, the bias^2 increases with N_{iter}. For most generators, the mean bias^2 roughly stabilizes for $N_{\text{iter}} > 4$.

Mean returned error: The mean returned error is defined as

$$\frac{1}{N_{\text{bins}}} \sum_{j=1}^{N_{\text{bins}}} \frac{1}{N_{\text{pseudo}}} \sum_{i=1}^{N_{\text{pseudo}}} \sigma_{\text{ret}}{}^i_j$$

where $\sigma_{\text{ret}}{}_j^i$ is the uncertainty by `RooUnfold` for bin j and pseudoexperiment i. These mean returned errors are shown in Table A.3 for Bayesian unfolding with N_{iter}=1-9. For one iteration, the mean error is $\sim$ 8 jets for all generators. In all cases, the error increases with N_{iter}.

Pull: The pull is calculated as $(N_{\text{unfolded}} - N_{\text{true}})/\sigma$, where σ is the bin error returned by `RooUnfold`. Figures A.17-A.21 show the mean and σ of the pull for each of the 41 bins, obtained from a Gaussian fit over all One thousand pseudoexperiments for one through four iterations. The scatter in the means of the pull shows the same behavior as that of the bias. For N_{iter}=1, the returned error does not properly represent the spread seen among the pseudoexperiments. For $N_{\text{iter}} \geq 2$, the width of the pull is close to 1 for all generators and all bins.

χ^2: All of the metrics listed are insensitive to bin-to-bin correlations. To understand whether the unfolding is properly handling such correlations, the unfolded and fully corrected distributions for each generator are compared to that generator's truth distribution using the full chisq calculation in Equation9.6. Table A.3 and Figure A.3 show the χ^2 for varying number of iterations.

For the baseline generator, the chisq is properly normalized, giving $\sim$43 for 41 degrees of freedom, independent of N_{iter}. For the alternative generators, with $N_{\text{iter}} = 1$, the chisq vary from $\sim$140-$\sim$260. As N_{iter} increases, the chisq decreases, roughly stabilizing for $N_{\text{iter}} \geq 6$. This decrease in chisq is largely due to the increase in size of the uncertainty rather than improvement in the unfolding itself, as seen from the above metrics.

The metrics above do not point to a single optimal choice of N_{iter}. The bias and the bias^2 increase slowly with N_{iter}. The error uniformly increases with increasing N_{iter}. The pulls indicate that for $N_{\text{iter}} = 1$, the unfolding does not return properly normalized uncertainties. The chisq metric favors a $N_{\text{iter}} = 4 - 6$. Because $N_{\text{iter}} = 2$ provides properly normalized uncertainties (as shown by the pull) and small values for the bias and bias^2, this is chosen as the optimal number of iterations. Because the chisq returned for alternate generators is not properly normalized, a systematic uncertainty must be assigned. The procedure for assigning this uncertainty is described in Section 10.4.

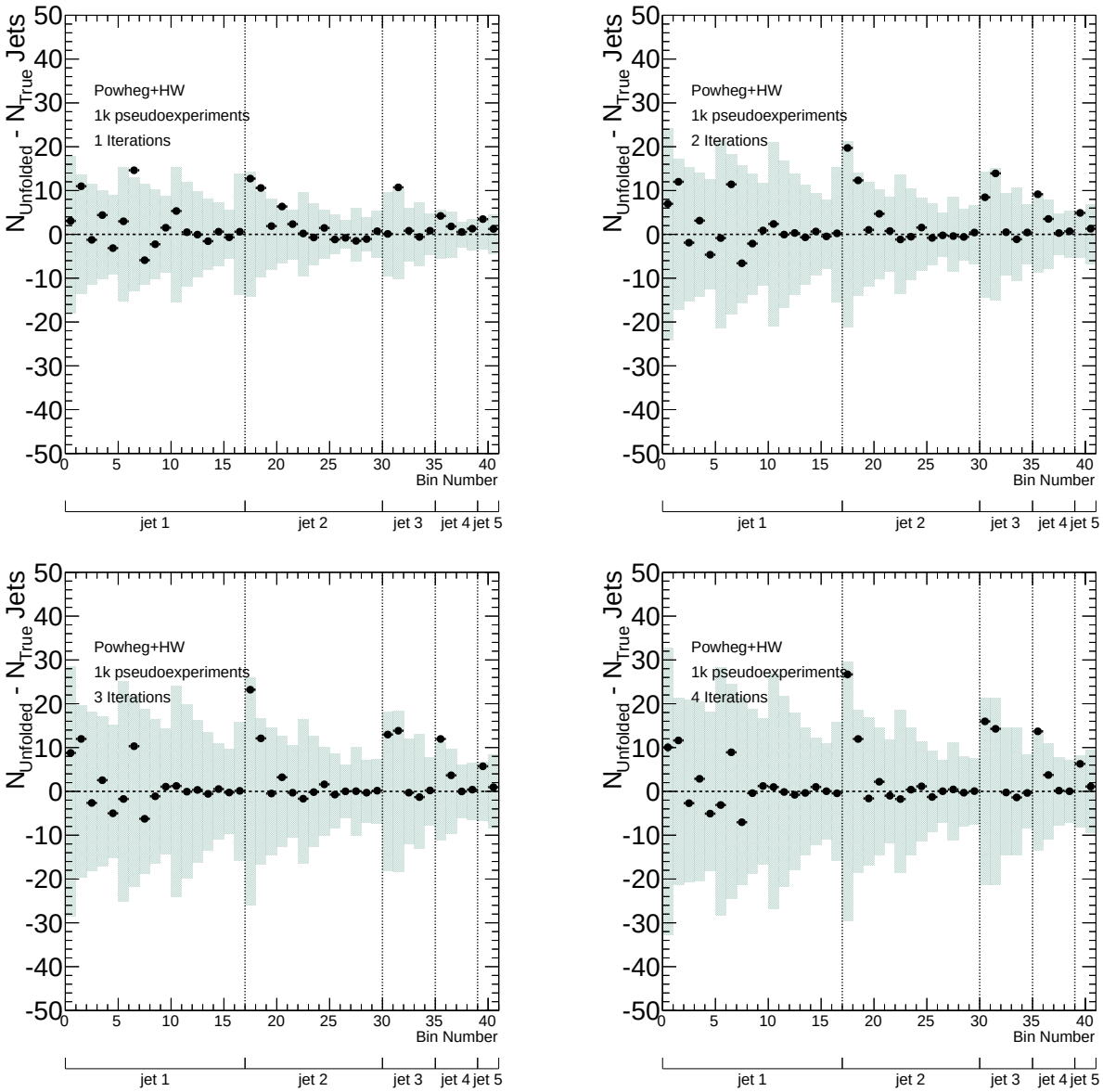

Figure A.7: Bias distribution for pseudoexperiments constructed from PowHeg+Herwig simulation unfolded against a matrix filled with the baseline simulation. One thousand pseudoexperiments, each the size of the events in data, are selected from the sample and unfolded. The Bayesian unfolding method with various numbers of iterations is used. Each bin of the distribution over the pseudoexperiments is fit with a gaussian. The black points show the fitted mean of each bin and the blue band shows the fitted sigma.

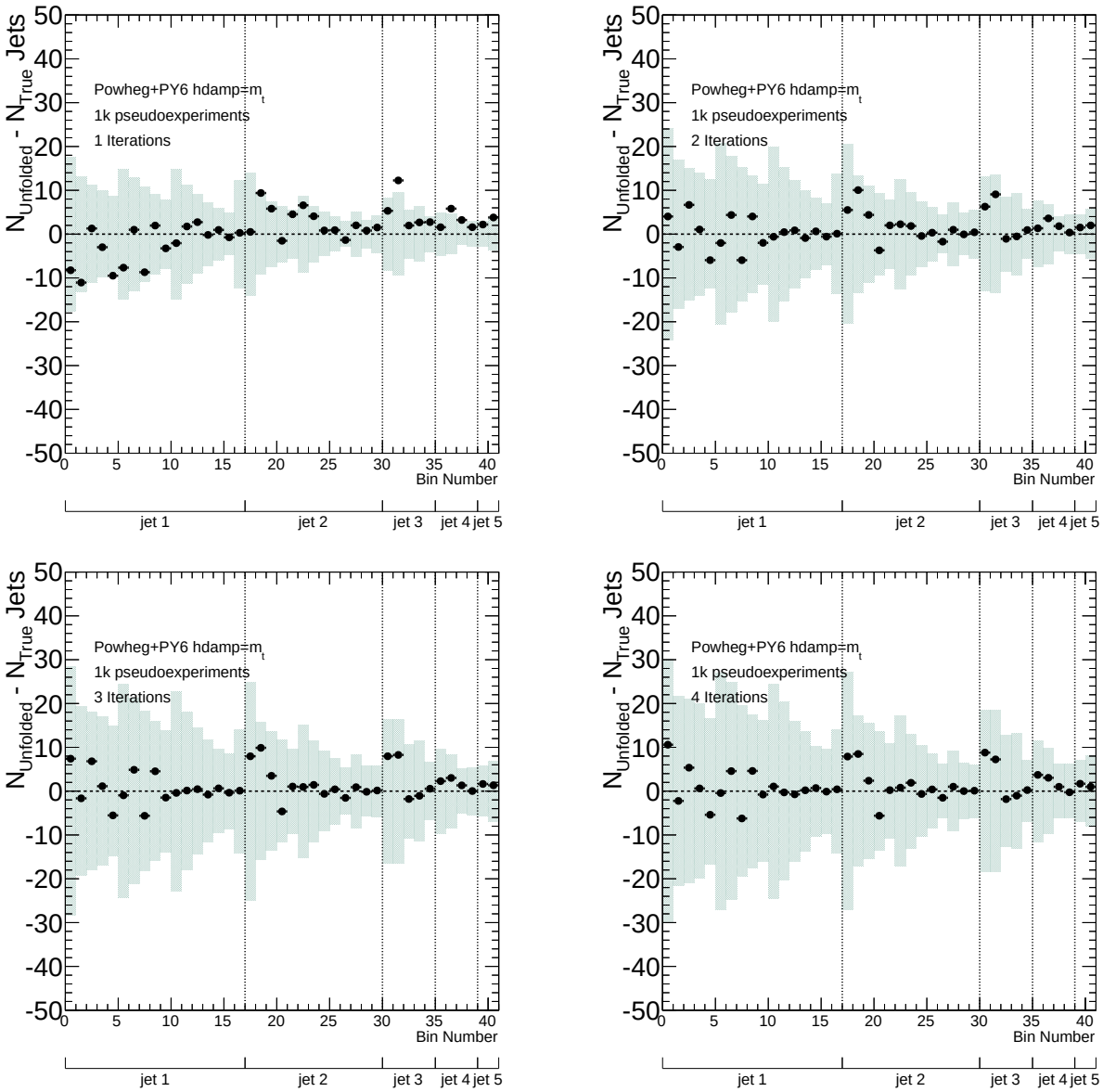

Figure A.8: Bias distribution for pseudoexperiments constructed from POWHEG+PYTHIA hdamp=m_t simulation unfolded against a matrix filled with the baseline simulation. One thousand pseudoexperiments, each the size of the events in data, are selected from the sample and unfolded. The Bayesian unfolding method with various numbers of iterations is used. Each bin of the distribution over the pseudoexperiments is fit with a gaussian. The black points show the fitted mean of each bin and the blue band shows the fitted sigma.

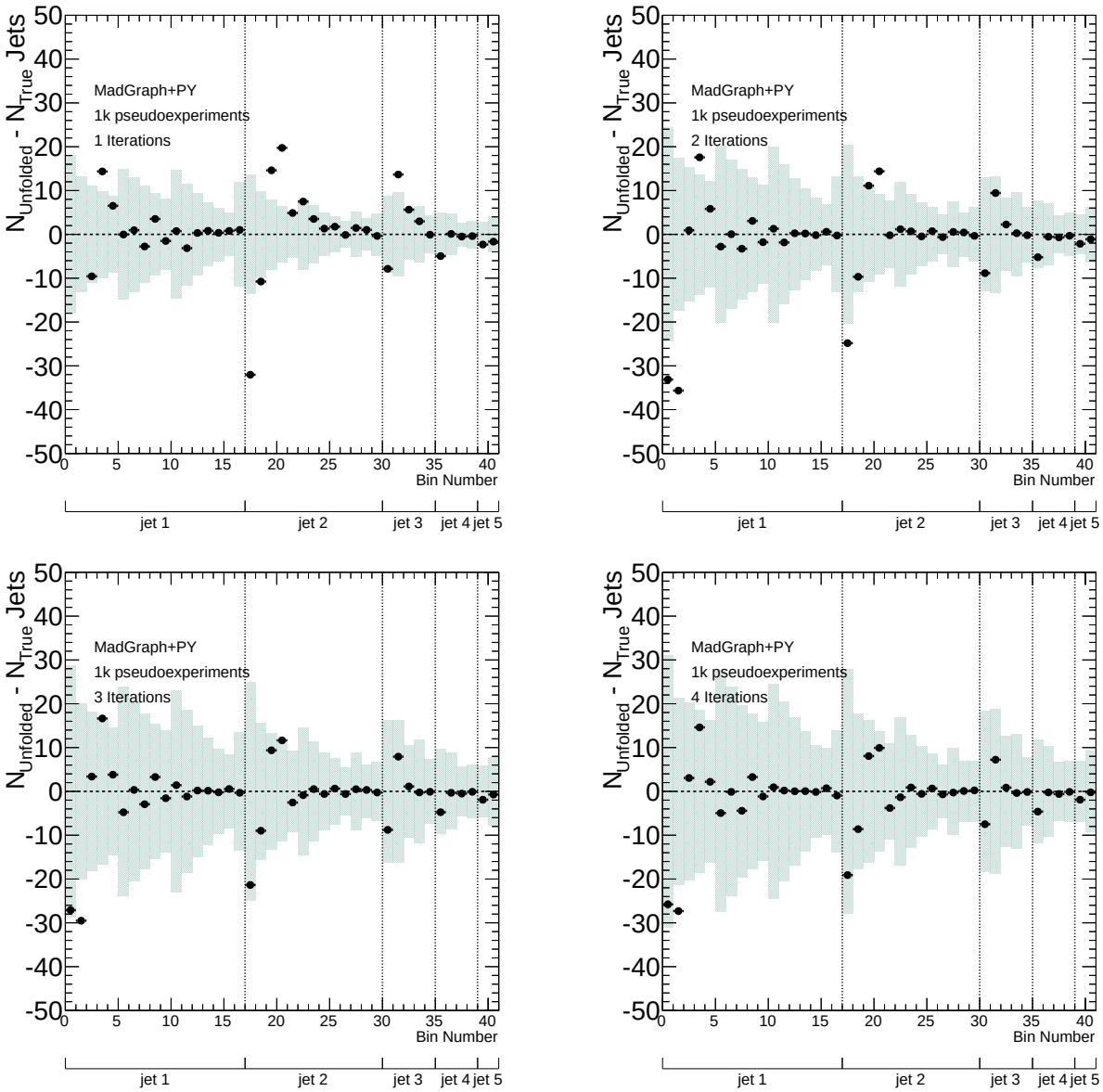

Figure A.9: Bias distribution for pseudoexperiments constructed from MadGraph+Pythia simulation unfolded against a matrix filled with the baseline simulation. One thousand pseudoexperiments, each the size of the events in data, are selected from the sample and unfolded. The Bayesian unfolding method with various numbers of iterations is used. Each bin of the distribution over the pseudoexperiments is fit with a gaussian. The black points show the fitted mean of each bin and the blue band shows the fitted sigma.

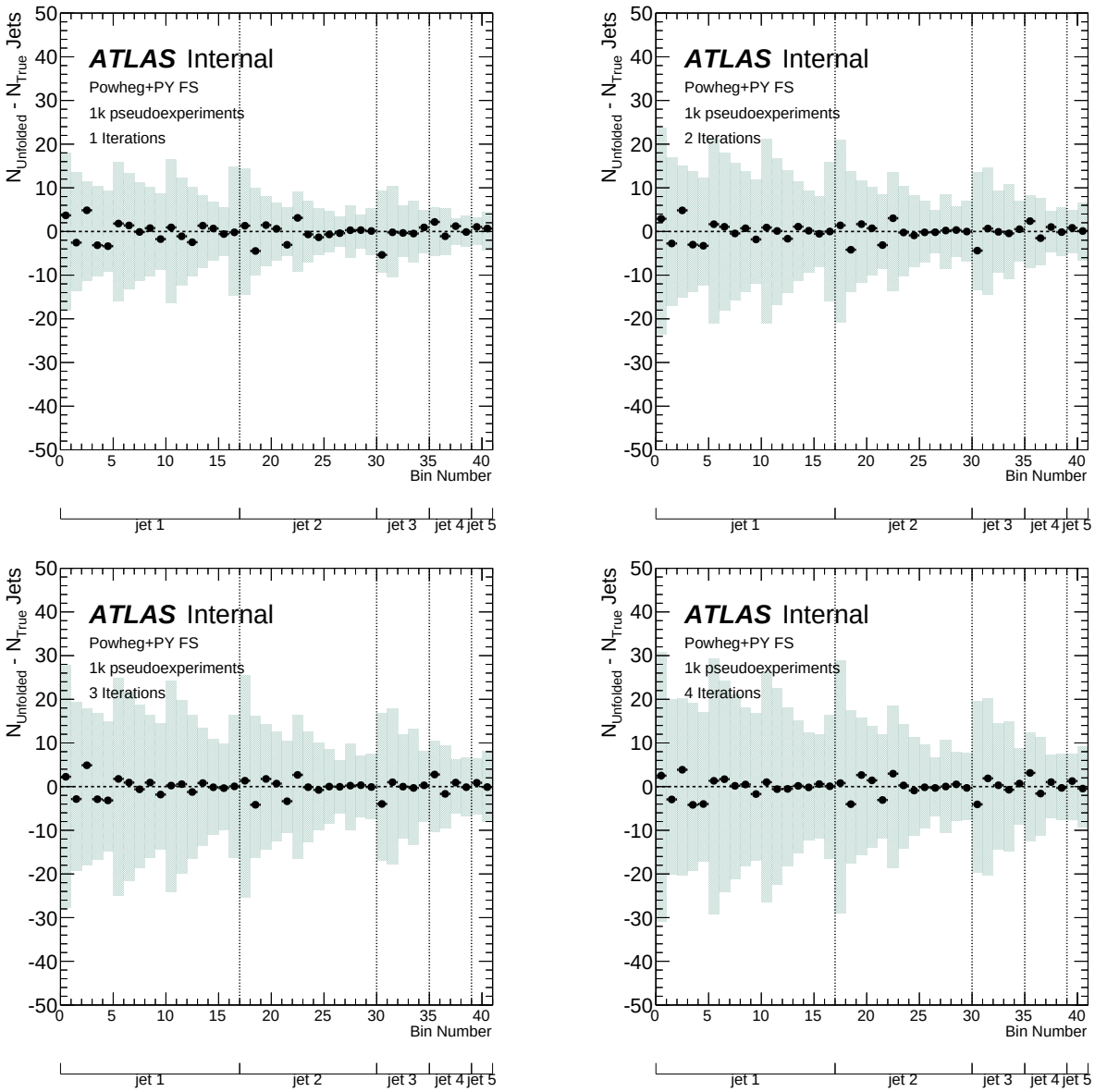

Figure A.10: Bias distribution for pseudoexperiments constructed from PowHeg+Pythia hdamp=∞ fullsim simulation unfolded against a matrix filled with the baseline simulation. One thousand pseudoexperiments, each the size of the events in data, are selected from the sample and unfolded. The Bayesian unfolding method with various numbers of iterations is used. Each bin of the distribution over the pseudoexperiments is fit with a gaussian. The black points show the fitted mean of each bin and the blue band shows the fitted sigma.

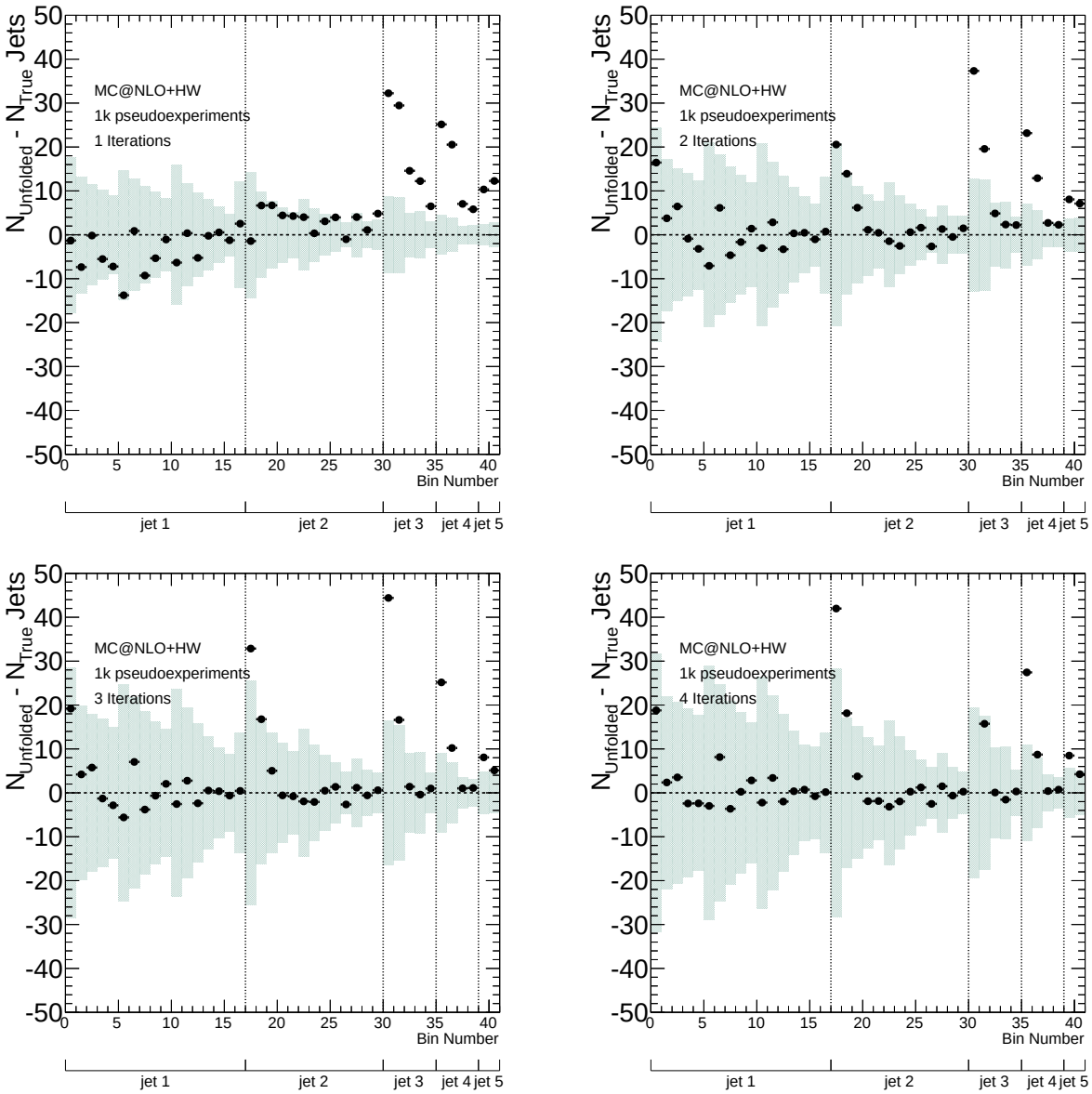

Figure A.11: Bias distribution for pseudoexperiments constructed from MC@NLO+ Herwig simulation unfolded against a matrix filled with the baseline simulation. One thousand pseudoexperiments, each the size of the events in data, are selected from the sample and unfolded. The Bayesian unfolding method with various numbers of iterations is used. Each bin of the distribution over the pseudoexperiments is fit with a gaussian. The black points show the fitted mean of each bin and the blue band shows the fitted sigma.

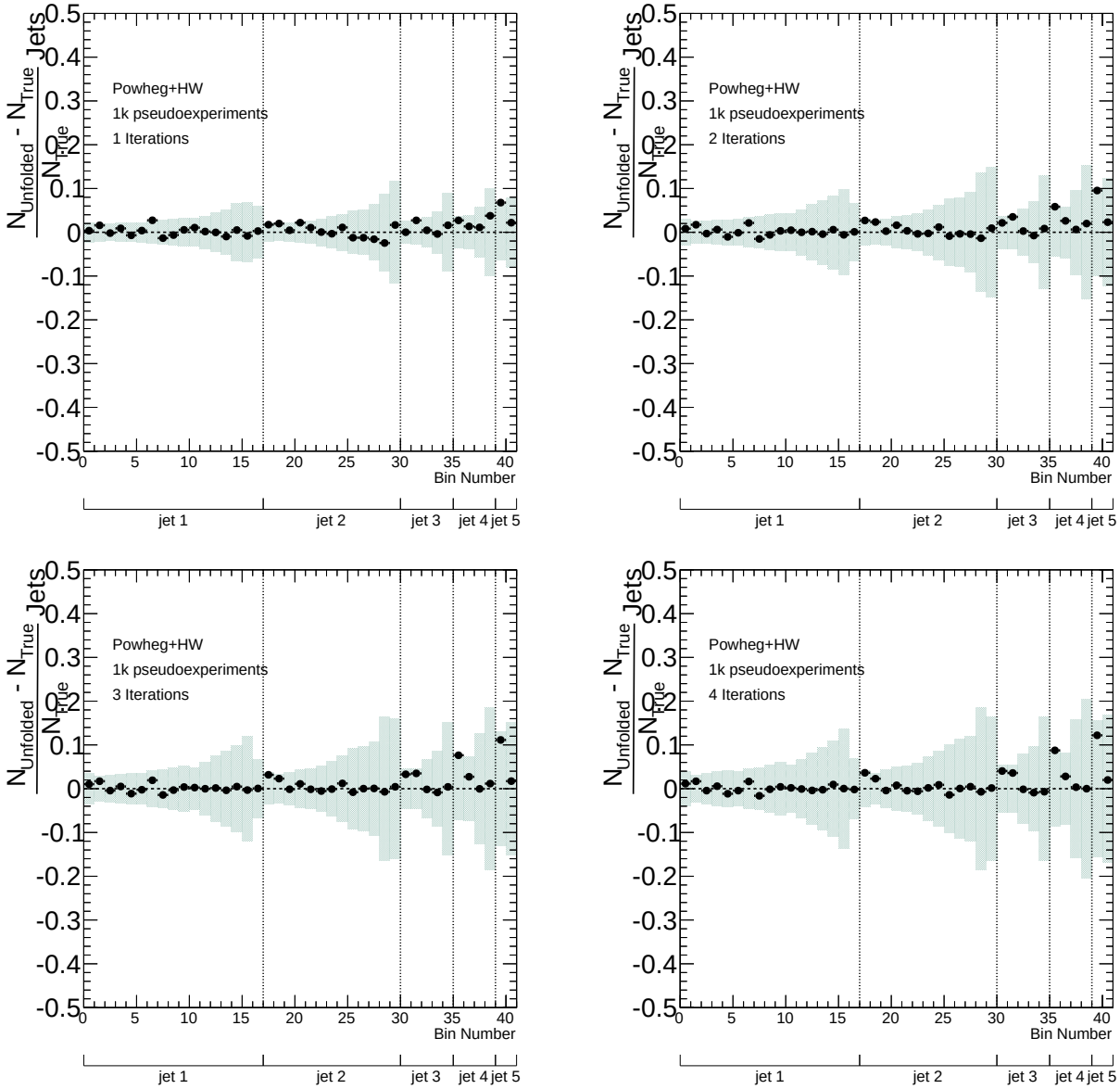

Figure A.12: Fractional bias distribution for pseudoexperiments constructed from PowHeg+Herwig simulation unfolded against a matrix filled with the baseline simulation. One thousand pseudoexperiments, each the size of the events in data, are selected from the sample and unfolded. The Bayesian unfolding method with various numbers of iterations is used. Each bin of the distribution over the pseudoexperiments is fit with a gaussian. The black points show the fitted mean of each bin and the blue band shows the fitted sigma.

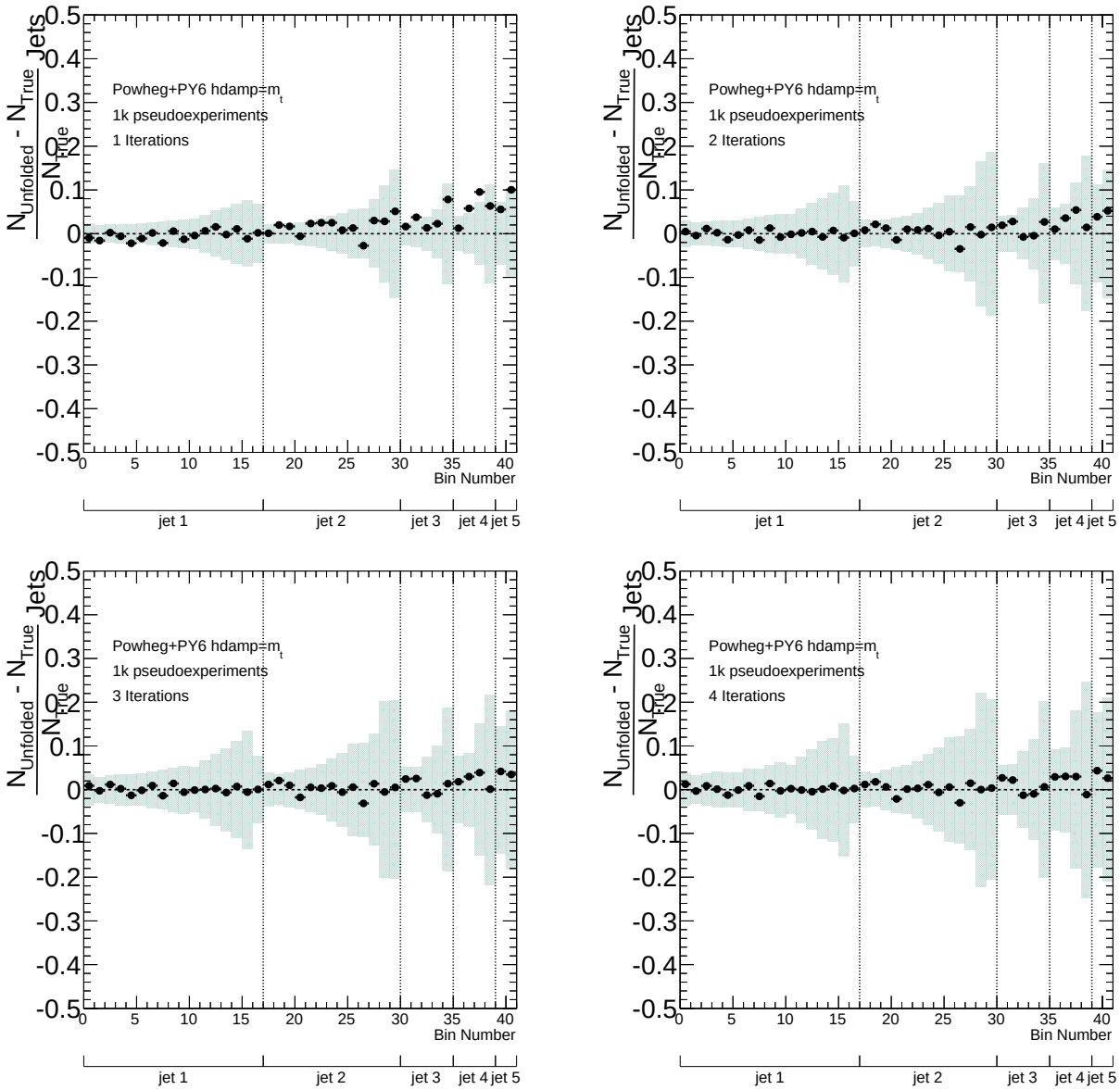

Figure A.13: Fractional bias distribution for pseudoexperiments constructed from PowHeg+Pythia hdamp=m_t simulation unfolded against a matrix filled with the baseline simulation. One thousand pseudoexperiments, each the size of the events in data, are selected from the sample and unfolded. The Bayesian unfolding method with various numbers of iterations is used. Each bin of the distribution over the pseudoexperiments is fit with a gaussian. The black points show the fitted mean of each bin and the blue band shows the fitted sigma.

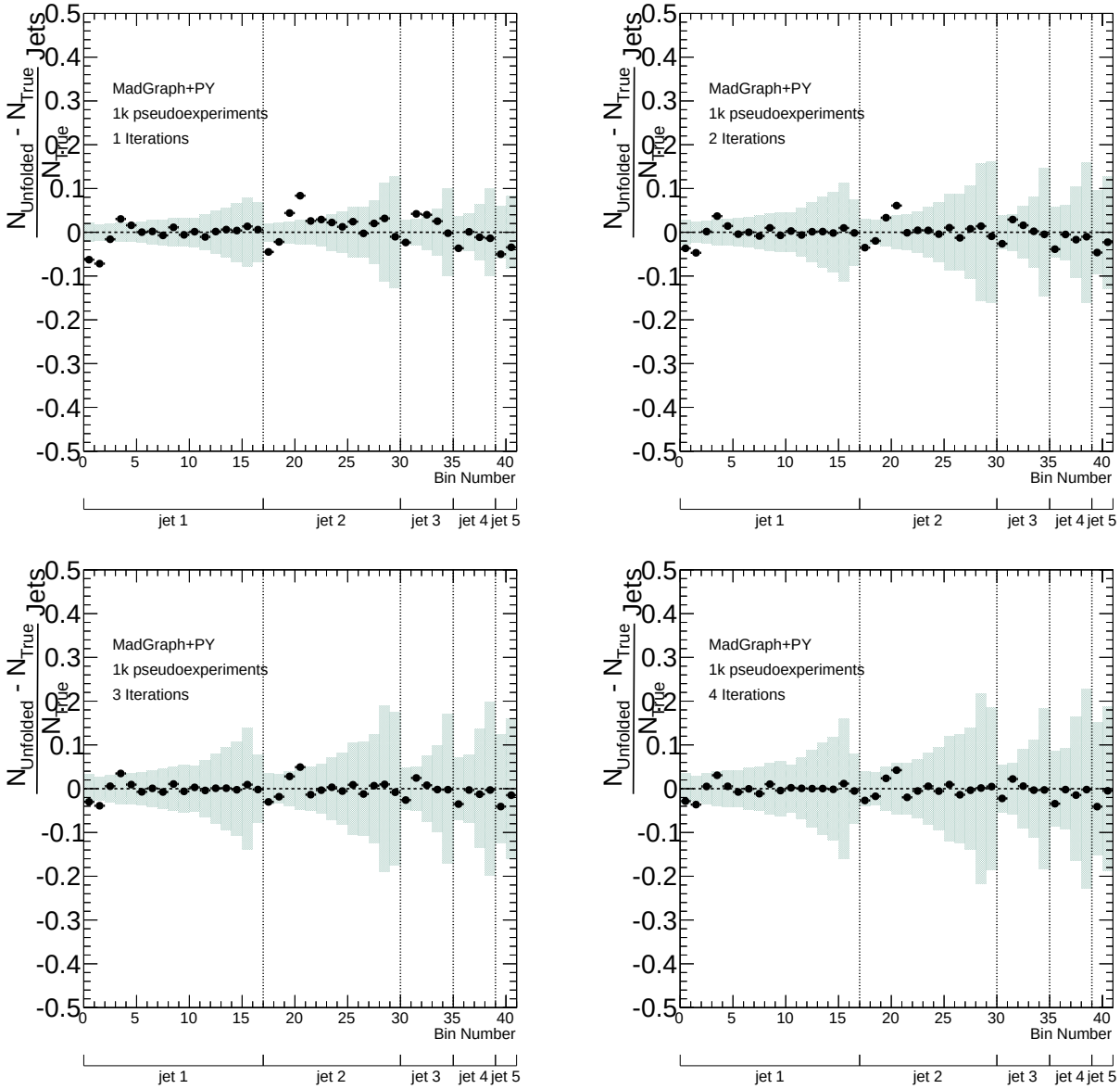

Figure A.14: Fractional bias distribution for pseudoexperiments constructed from MadGraph+Pythia simulation unfolded against a matrix filled with the baseline simulation. One thousand pseudoexperiments, each the size of the events in data, are selected from the sample and unfolded. The Bayesian unfolding method with various numbers of iterations is used. Each bin of the distribution over the pseudoexperiments is fit with a gaussian. The black points show the fitted mean of each bin and the blue band shows the fitted sigma.

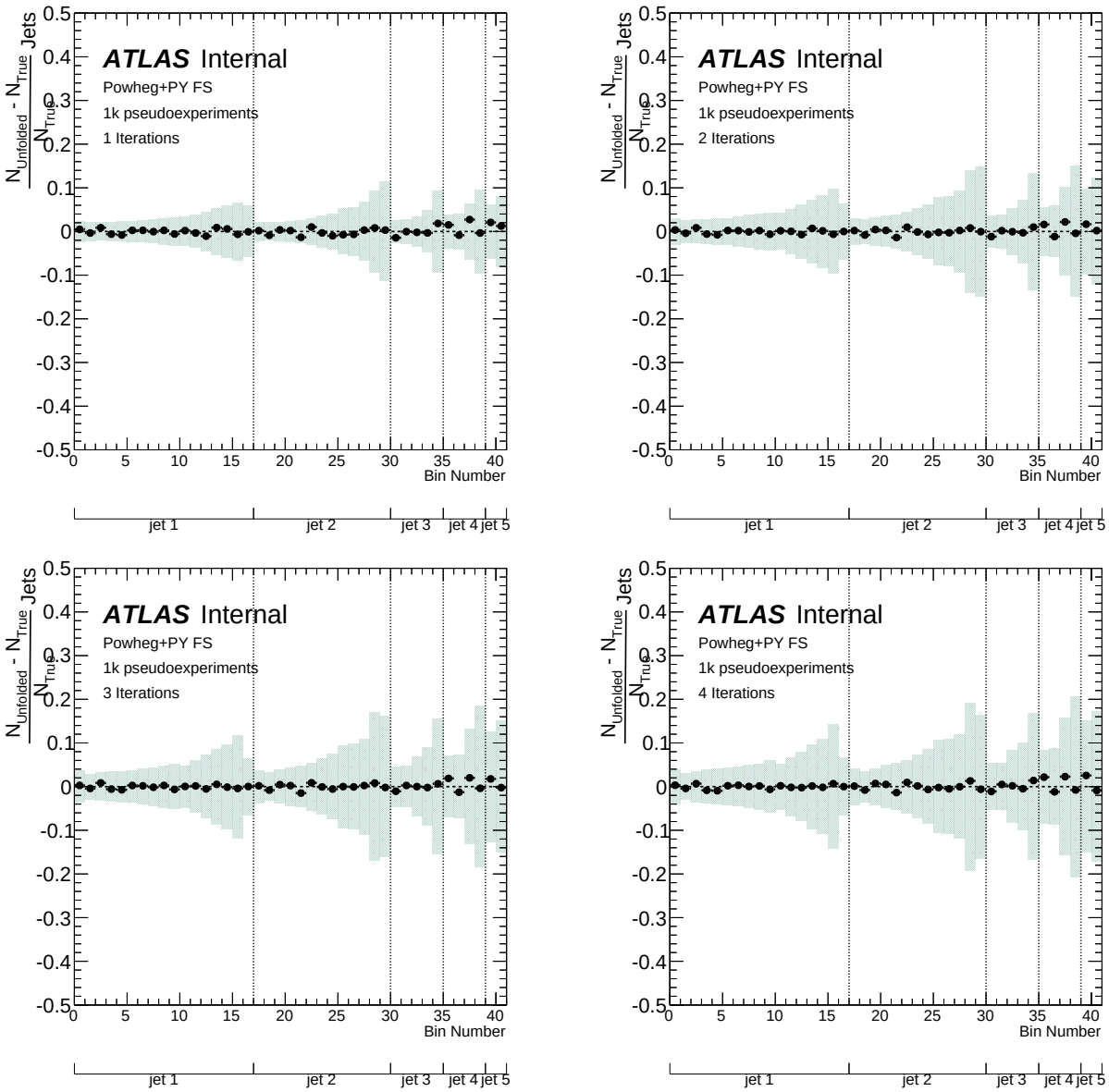

Figure A.15: Fractional bias distribution for pseudoexperiments constructed from PowHeg+Pythia hdamp=∞ fullsim simulation unfolded against a matrix filled with the baseline simulation. One thousand pseudoexperiments, each the size of the events in data, are selected from the sample and unfolded. The Bayesian unfolding method with various numbers of iterations is used. Each bin of the distribution over the pseudoexperiments is fit with a gaussian. The black points show the fitted mean of each bin and the blue band shows the fitted sigma.

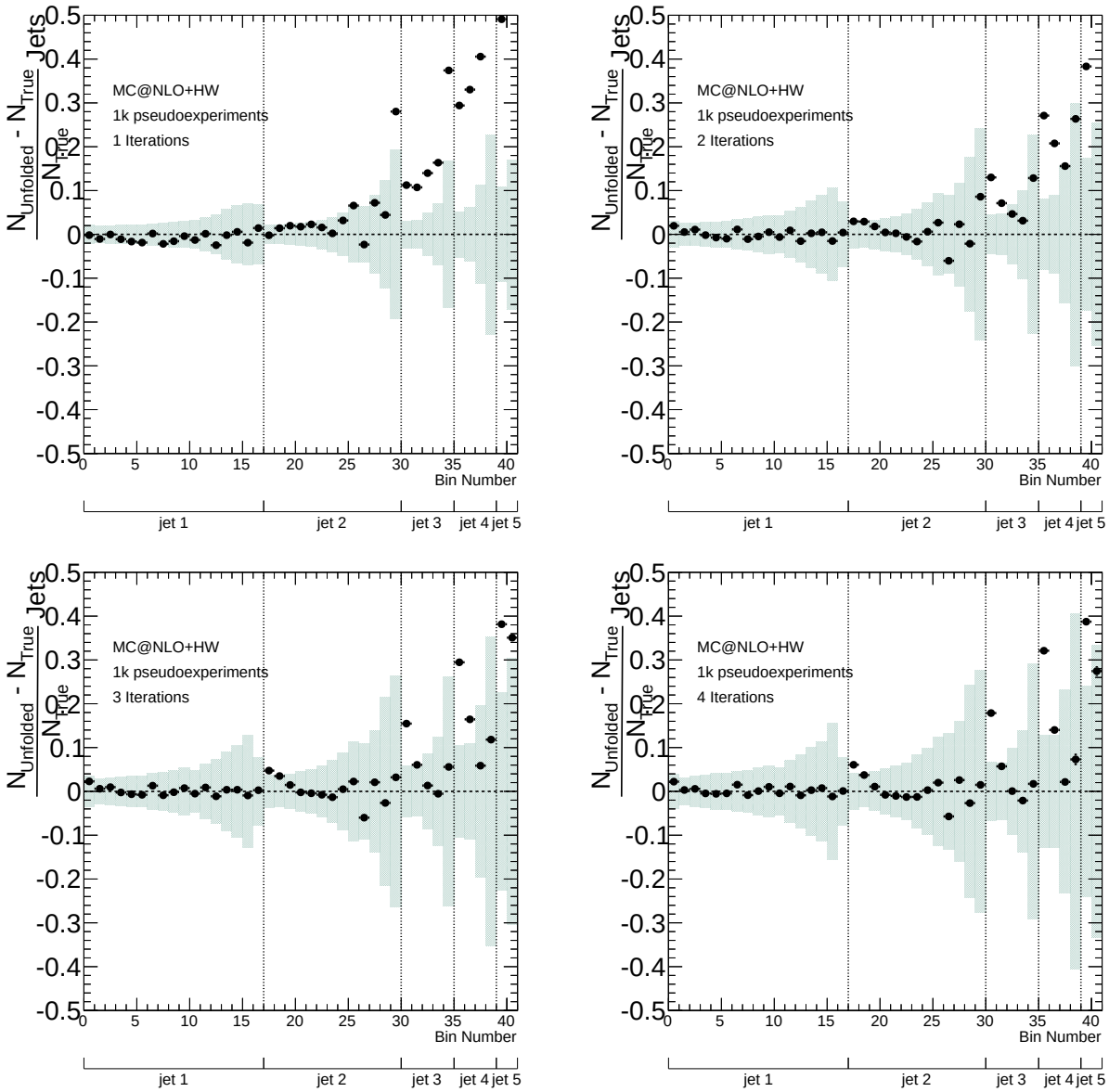

Figure A.16: Fractional bias distribution for pseudoexperiments constructed from MC@NLO+ Herwig simulation unfolded against a matrix filled with the baseline simulation. One thousand pseudoexperiments, each the size of the events in data, are selected from the sample and unfolded. The Bayesian unfolding method with various numbers of iterations is used. Each bin of the distribution over the pseudoexperiments is fit with a gaussian. The black points show the fitted mean of each bin and the blue band shows the fitted sigma.

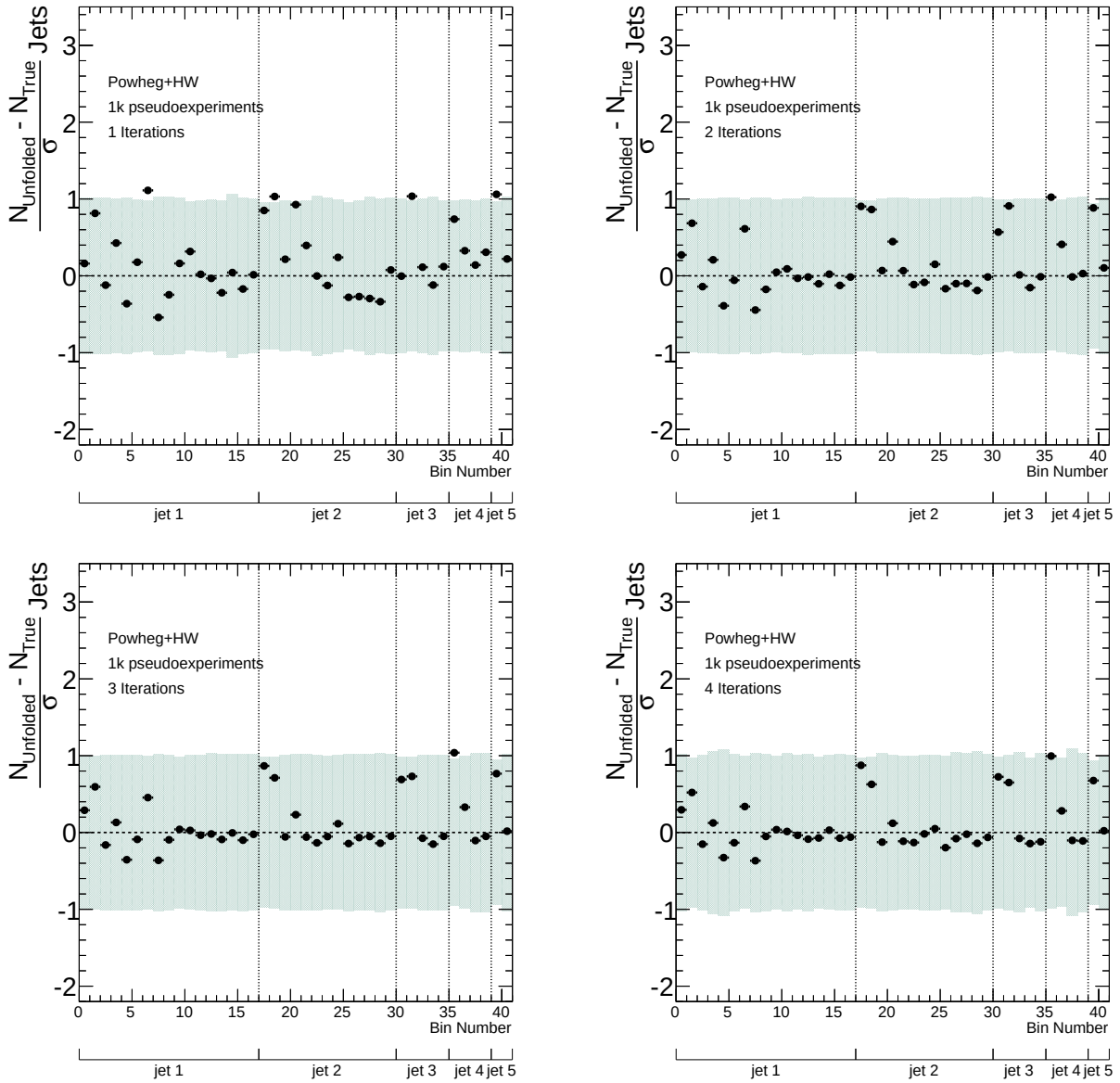

Figure A.17: Pull distribution for pseudoexperiments constructed from PowHeg+Herwig simulation unfolded against a matrix filled with the baseline simulation. One thousand pseudoexperiments, each the size of the events in data, are selected from the sample and unfolded. The Bayesian unfolding method with various numbers of iterations is used. Each bin of the distribution over the pseudoexperiments is fit with a gaussian. The black points show the fitted mean of each bin and the blue band shows the fitted sigma.

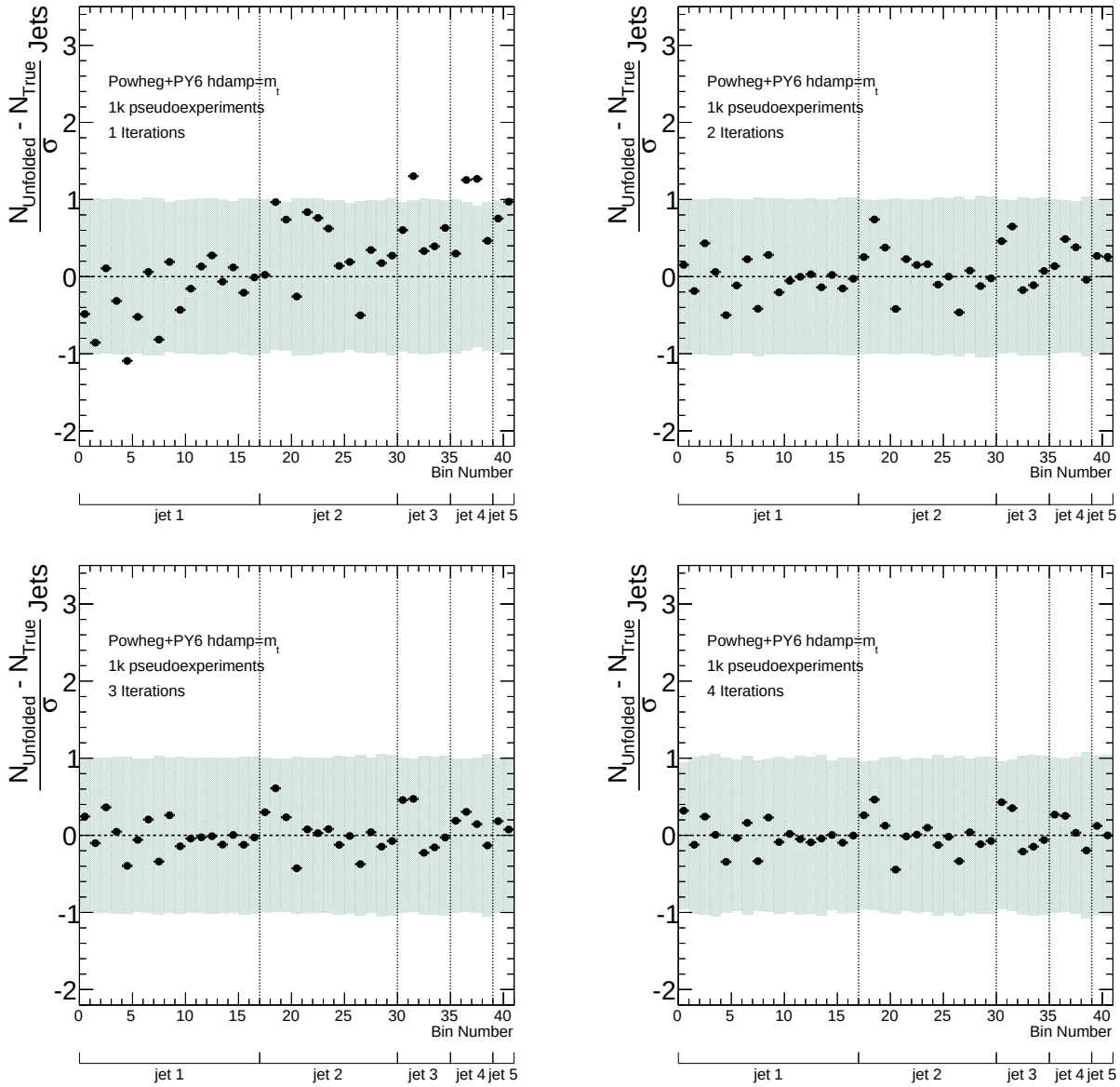

Figure A.18: Pull distribution for pseudoexperiments constructed from POWHEG+PYTHIA hdamp=m_t simulation unfolded against a matrix filled with the baseline simulation. One thousand pseudoexperiments, each the size of the events in data, are selected from the sample and unfolded. The Bayesian unfolding method with various numbers of iterations is used. Each bin of the distribution over the pseudoexperiments is fit with a gaussian. The black points show the fitted mean of each bin and the blue band shows the fitted sigma.

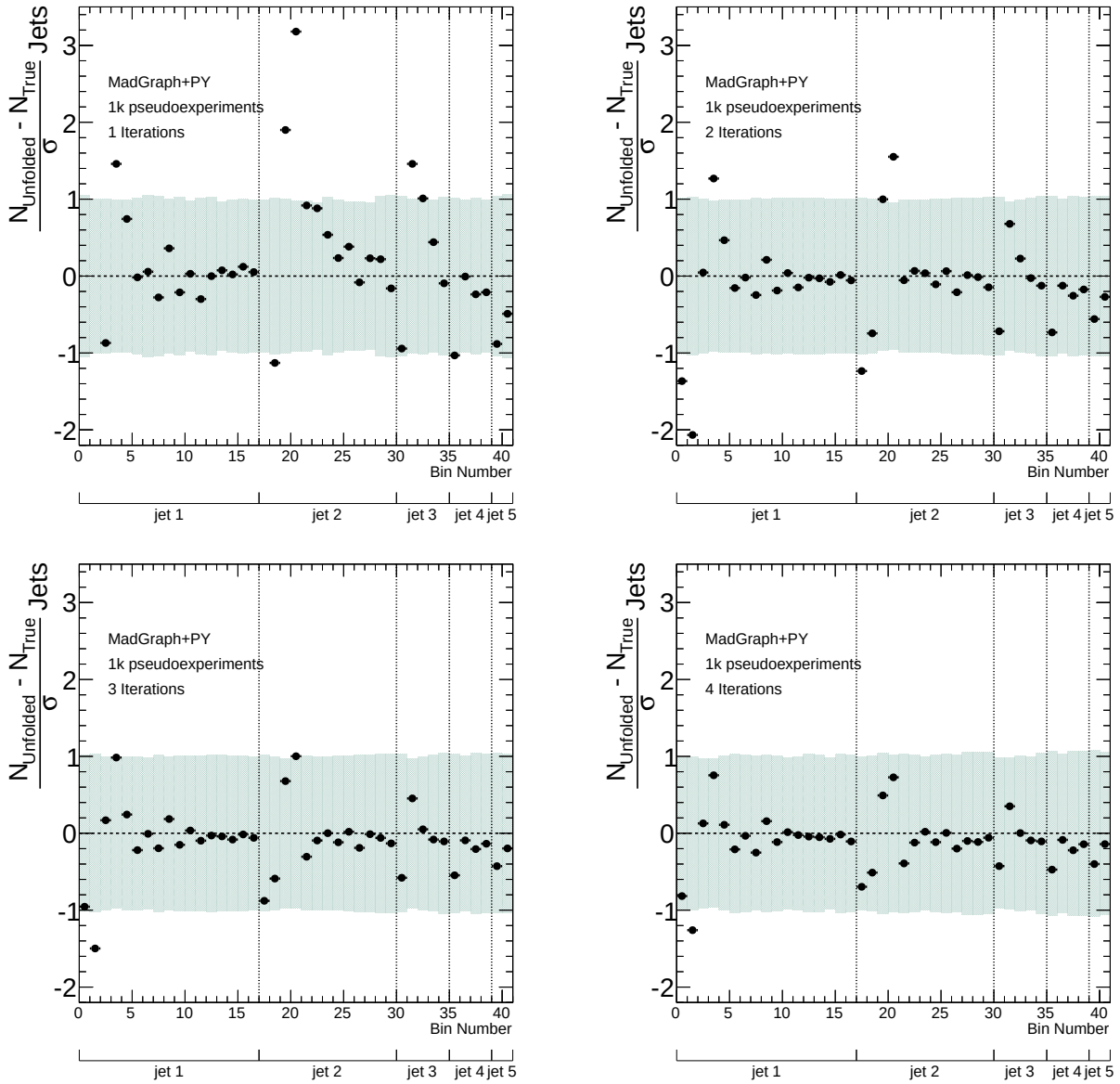

Figure A.19: Pull distribution for pseudoexperiments constructed from PowHeg+Pythia8 simulation unfolded against a matrix filled with the baseline simulation. One thousand pseudoexperiments, each the size of the events in data, are selected from the sample and unfolded. The Bayesian unfolding method with various numbers of iterations is used. Each bin of the distribution over the pseudoexperiments is fit with a gaussian. The black points show the fitted mean of each bin and the blue band shows the fitted sigma.

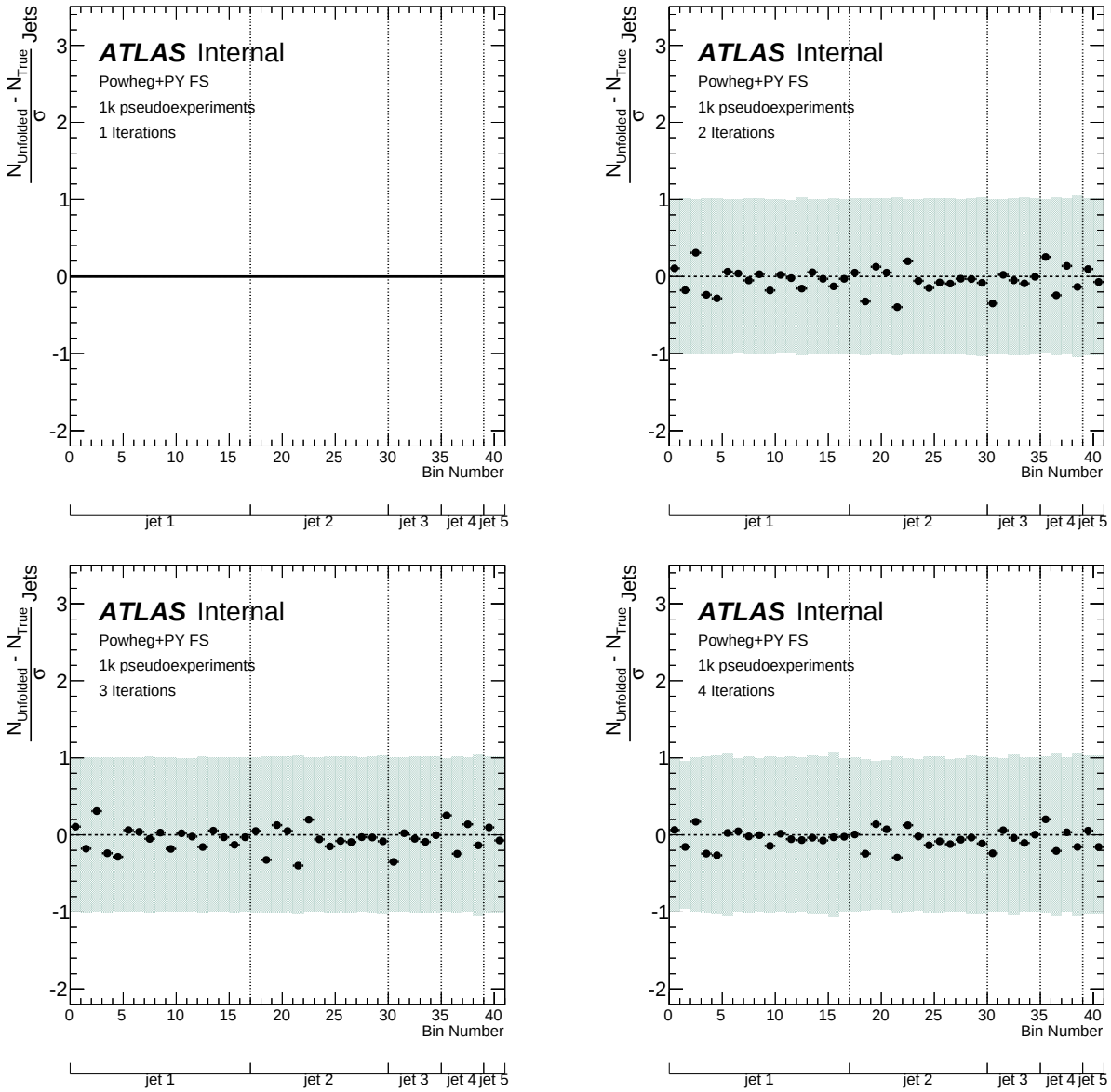

Figure A.20: Pull distribution for pseudoexperiments constructed from PowHeg+Pythia hdamp=∞ fullsim simulation unfolded against a matrix filled with the baseline simulation. One thousand pseudoexperiments, each the size of the events in data, are selected from the sample and unfolded. The Bayesian unfolding method with various numbers of iterations is used. Each bin of the distribution over the pseudoexperiments is fit with a gaussian. The black points show the fitted mean of each bin and the blue band shows the fitted sigma.

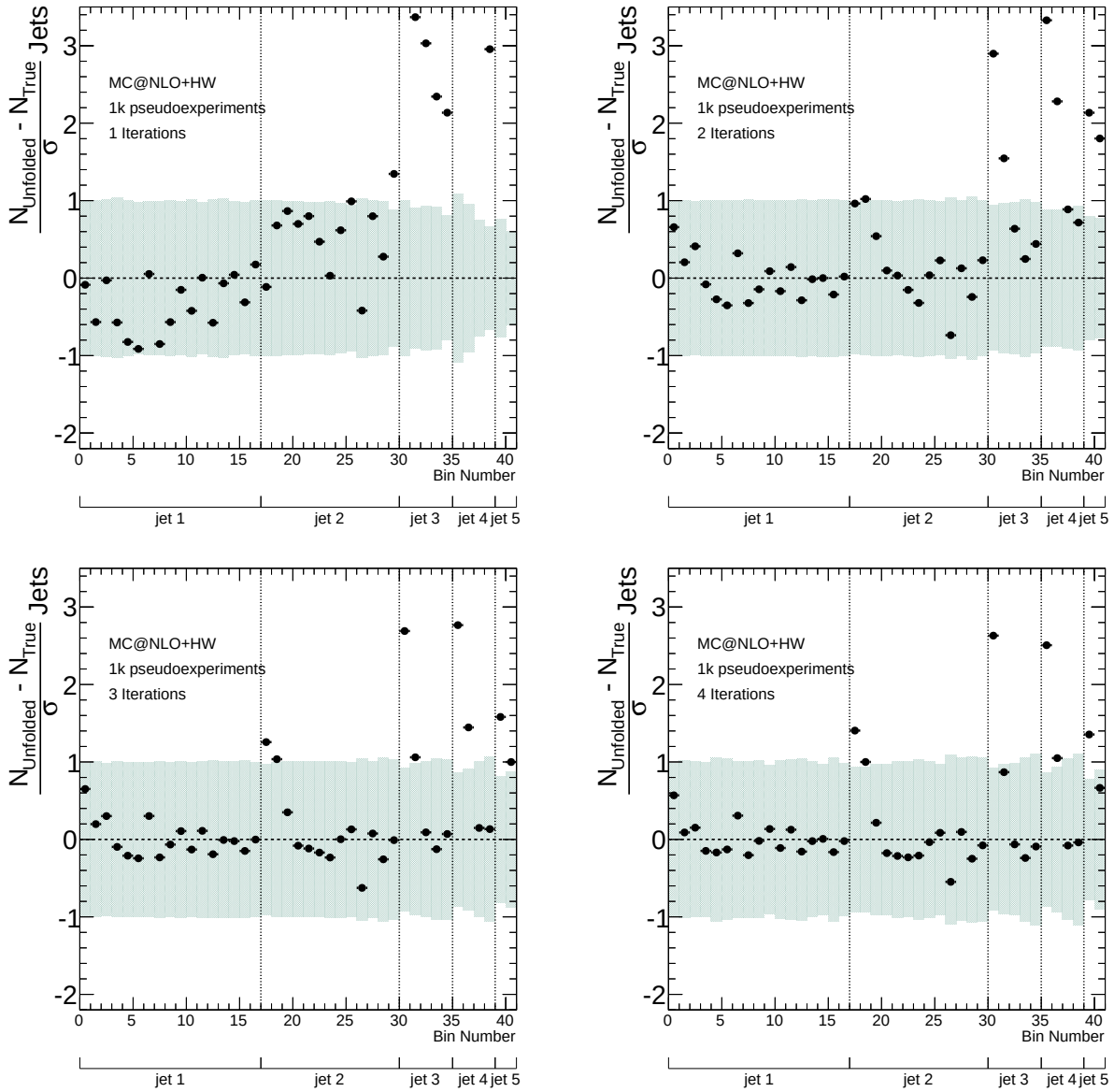

Figure A.21: Bias distribution for pseudoexperiments constructed from MC@NLO+ HERWIG simulation unfolded against a matrix filled with the baseline simulation. One thousand pseudoexperiments, each the size of the events in data, are selected from the sample and unfolded. The Bayesian unfolding method with various numbers of iterations is used. Each bin of the distribution over the pseudoexperiments is fit with a gaussian. The black points show the fitted mean of each bin and the blue band shows the fitted sigma.

Method	110404	117046	105860	105200	110872	117050	110875	110878
Bin-by-bin	-8.0×10^{2}	-5.3×10^{2}	-5.0×10^{2}	-3.8×10^{2}	-6.1×10^{2}	-2.3×10^{2}	-5.4×10^{2}	-4.8×10^{2}
1	1.0	-2.2×10^{-1}	2.2	4.0	-1.8	1.2×10^{-1}	-1.3	-2.3
2	1.2	-8.8×10^{-2}	2.4	4.4	-1.5	4.2×10^{-2}	-1.3	-2.4
3	1.3	-1.1×10^{-1}	2.6	4.7	-1.4	4.6×10^{-2}	-1.3	-2.4
4	1.3	-1.1×10^{-1}	2.5	4.7	-1.3	1.2×10^{-1}	-1.3	-2.5
5	1.3	-1.1×10^{-1}	2.5	4.8	-1.3	1.3×10^{-1}	-1.3	-2.5
6	1.4	-7.2×10^{-2}	2.7	5.0	-1.3	9.8×10^{-5}	-1.3	-2.5
7	1.4	-7.5×10^{-2}	2.8	5.1	-1.3	3.4×10^{-3}	-1.3	-2.5
8	1.5	-2.0×10^{-1}	2.7	5.1	-1.2	1.4×10^{-1}	-1.2	-2.7
9	1.5	-2.0×10^{-1}	2.8	5.2	-1.2	1.5×10^{-1}	-1.2	-2.7

Table A.1: Comparison of the average bias per bin for stress tests with several different ttbar generators and unfolding methods. All samples are atlfast. For each generator, the measured jets from one thousand pseudoexperiments are unfolded against the baseline PowHeg+Pythia hdamp=∞ atlfast response matrix and compared to the input truth spectrum.

Iterations	110404	117046	105860	105200	110872	117050	110875	110878
Bin-by-bin	4.0×10^{6}	2.6×10^{6}	1.9×10^{6}	1.0×10^{6}	2.6×10^{6}	2.0×10^{5}	2.2×10^{6}	2.4×10^{6}
1	2.2×10^{1}	2.0×10^{1}	2.3×10^{1}	1.1×10^{2}	2.0×10^{2}	7.1×10^{-1}	1.7×10^{2}	3.2×10^{2}
2	1.4×10^{1}	9.1	3.7×10^{1}	9.9×10^{1}	8.7×10^{1}	3.8×10^{-1}	1.5×10^{2}	2.9×10^{2}
3	1.6×10^{1}	7.0	4.6×10^{1}	1.3×10^{2}	6.1×10^{1}	4.2×10^{-1}	1.5×10^{2}	2.8×10^{2}
4	1.7×10^{1}	6.7	5.1×10^{1}	1.6×10^{2}	5.3×10^{1}	6.0×10^{-1}	1.5×10^{2}	2.8×10^{2}
5	1.8×10^{1}	6.3	5.6×10^{1}	1.8×10^{2}	4.8×10^{1}	7.0×10^{-1}	1.4×10^{2}	2.8×10^{2}
6	2.1×10^{1}	5.6	6.6×10^{1}	2.0×10^{2}	4.7×10^{1}	1.1	1.4×10^{2}	2.7×10^{2}
7	2.2×10^{1}	5.5	7.0×10^{1}	2.2×10^{2}	4.6×10^{1}	1.2	1.4×10^{2}	2.6×10^{2}
8	2.2×10^{1}	5.4	6.7×10^{1}	2.4×10^{2}	3.8×10^{1}	1.4	1.4×10^{2}	2.7×10^{2}
9	2.3×10^{1}	5.3	7.1×10^{1}	2.5×10^{2}	3.7×10^{1}	1.6	1.4×10^{2}	2.7×10^{2}

Table A.2: Comparison of the average bias squared per bin for stress tests with several different ttbar generators and unfolding methods. All samples are atlfast. For each generator, the measured jets from one thousand pseudoexperiments are unfolded against the baseline PowHeg+Pythia hdamp=∞ atlfast response matrix and compared to the input truth spectrum.

Method	110404	117046	105860	105200	110872	117050	110875	110878
1	8.1	8.5	8.7	8.0	8.1	8.6	7.6	8.7
2	1.1×10^1	1.2×10^1	1.2×10^1	1.1×10^1	1.1×10^1	1.2×10^1	1.1×10^1	1.2×10^1
3	1.4×10^1	1.4×10^1	1.5×10^1	1.3×10^1	1.4×10^1	1.5×10^1	1.3×10^1	1.5×10^1
4	1.5×10^1	1.6×10^1	1.7×10^1	1.5×10^1	1.5×10^1	1.6×10^1	1.4×10^1	1.7×10^1
5	1.7×10^1	1.8×10^1	1.8×10^1	1.6×10^1	1.7×10^1	1.8×10^1	1.6×10^1	1.8×10^1
6	1.8×10^1	1.9×10^1	2.0×10^1	1.8×10^1	1.8×10^1	1.9×10^1	1.7×10^1	2.0×10^1
7	1.9×10^1	2.0×10^1	2.1×10^1	1.9×10^1	1.9×10^1	2.0×10^1	1.8×10^1	2.1×10^1
8	2.0×10^1	2.1×10^1	2.2×10^1	2.0×10^1	2.0×10^1	2.1×10^1	1.9×10^1	2.2×10^1
9	2.1×10^1	2.2×10^1	2.3×10^1	2.1×10^1	2.1×10^1	2.2×10^1	2.0×10^1	2.3×10^1

Table A.3: Comparison of the average returned bin error for stress tests with several different ttbar generators and unfolding methods. All samples are atlfast. For each generator, the measured jets from one thousand pseudoexperiments are unfolded against the baseline PowHeg+Pythia hdamp=∞ atlfast response matrix and compared to the input truth spectrum.

Method	110404	117046	105860	105200	110872	117050	110875	110878
1	162.20	348.55	463.69	241.11	440.84	67.66	502.50	476.26
2	72.40	118.68	156.97	97.56	147.88	48.41	484.10	179.55
3	56.05	76.47	94.68	75.87	90.89	44.91	306.33	113.96
4	49.86	61.21	72.91	68.48	71.84	43.44	199.33	91.37
5	47.48	54.45	63.00	66.06	62.27	42.96	148.26	80.78
6	46.70	51.33	58.18	65.62	56.25	42.83	119.98	74.81
7	46.00	49.18	54.97	65.24	53.14	42.71	103.28	71.36
8	45.49	48.04	52.77	66.20	51.17	42.76	92.02	69.23
9	45.23	47.12	51.38	66.55	49.81	42.75	84.55	67.70

Table A.4: The χ^2 of extra jets from the each $t\bar{t}$ simulation unfolded against a matrix filled with the same baseline $t\bar{t}$ simulation (PowHeg+Pythia hdamp=∞). All samples are atlfast. The same 3% contribution from Wt is included in both the migration matrix and the unfolding. The Bayesian unfolding method is used with iterations ranging from 1 to 10. One thousand pseudoexperiments, each the size of the events in data, are randomly selected from the sample and unfolded. The $\chi^2$is calculated according to Equation 9.6. The χ^2 in compares the fully corrected reco jets to truth jets in truth events.

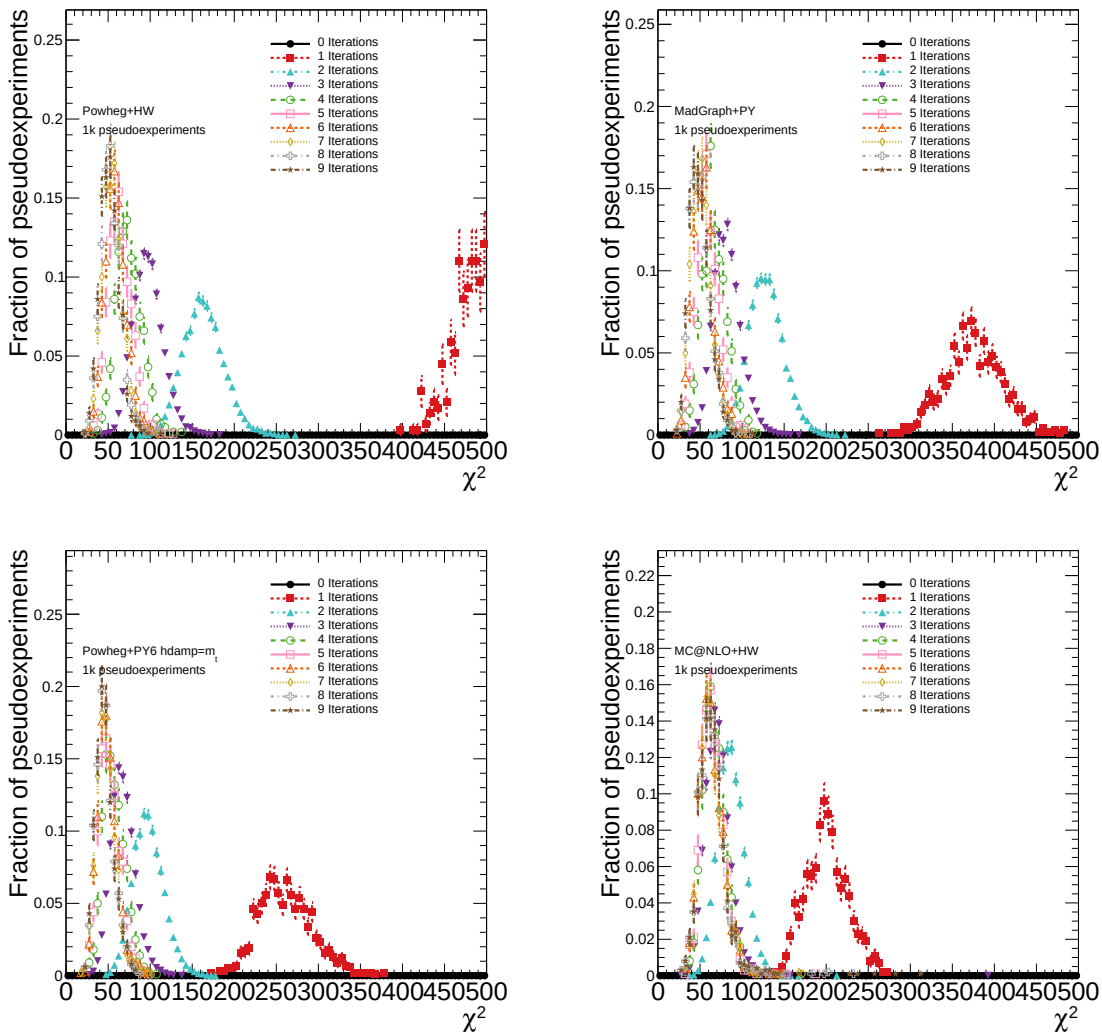

Figure A.22: The χ^2 of extra jets from the each $t\bar{t}$ simulation unfolded against a matrix filled with the same baseline $t\bar{t}$ simulation (PowHeg+Pythia hdamp=∞). All samples are atlfast. The same 3% contribution from Wt is included in both the migration matrix and the unfolding. The Bayesian unfolding method is used with iterations ranging from 1 to 10. One thousand pseudoexperiments, each the size of the events in data, are randomly selected from the sample and unfolded. The $\chi^2$is calculated according to Equation 9.6. The χ^2 in compares the fully corrected reco jets to truth jets in truth events.

A.4 Detector level systematics

A.4.1 Event counts for nuisance parameters

Table A.5: Number of selected events for various detector-modeling nuisance parameters. Events are siumlated with POWHEG+PYTHIA$t\bar{t}$ hdamp= ∞ simulation and compared to the nominal number, including scale factor event weights.

Parameter	N_{events}	ΔN (%)
Nominal	11997.2	0
JESMIX1DOWN	11987.8	-0.078
JESMIX1UP	12006.2	0.075
JESMIX2DOWN	12010.5	0.111
JESMIX2UP	11983.2	-0.116
JESMODE1DOWN	11916.7	-0.671
JESMODE1UP	12074.5	0.644
JESMODE2DOWN	11999.5	0.02
JESMODE2UP	11994.5	-0.023
JESMODE3DOWN	11991.9	-0.044
JESMODE3UP	12002.8	0.047
JESMODE4DOWN	11996.7	-0.004
JESMODE4UP	11997.3	0.001
JESDET1DOWN	11993.1	-0.034
JESDET1UP	12001.1	0.033
JESDET2DOWN	11991.5	-0.048
JESDET2UP	12003.5	0.053
JESDET3DOWN	11996.4	-0.006
JESDET3UP	11997.9	0.006
JESSTAT1DOWN	11964	-0.276
JESSTAT1UP	12029.4	0.268
JESSTAT2DOWN	11999.8	0.022
JESSTAT2UP	11994.4	-0.023
JESSTAT3DOWN	11997.2	0
JESSTAT3UP	11997.1	-0.001
JESFCOMPDOWN	12014.1	0.141
JESFCOMPUP	11979.2	-0.15
JESFRESDOWN	11985.2	-0.1
JESFRESUP	12008.3	0.092
JESFWDDOWN	11981.6	-0.13
JESFWDSDOWN	11975.9	-0.178
JESFWDSUP	12017.8	0.172

Continued on next page

Table A.5 –*Continued from previous page*

Parameter	N_{events}	ΔN (%)
JESFWDUP	12011.1	0.116
JESPMUDOWN	12001.8	0.038
JESPMUUP	11992.6	-0.038
JESPTDOWN	11997.7	0.005
JESPTUP	11996.7	-0.004
JESPUNCHDOWN	11997.2	0
JESPUNCHUP	11997.2	0
JESPVDOWN	12009	0.098
JESPVUP	11984.5	-0.105
JESRHODOWN	11937.4	-0.498
JESRHOUP	12056.5	0.494
JESSNGLDOWN	11997.2	0
JESSNGLUP	11997.2	0
JESPMUDOWN	12001.9	0.039
JESPMUUP	11992.7	-0.038
JESPVDOWN	12009	0.099
JESPVUP	11984.6	-0.105
EERDOWN	12003.2	0.05
EERUP	11989.9	-0.061
EESDOWN	11944.8	-0.436
EESUP	12040.1	0.357
JEFF	11994.6	-0.022
JER	11870.9	-1.053
JVFDOWN	12017.7	0.171
JVFUP	11971.5	-0.214
MUSCALEDOWN	11994.3	-0.024
MUSCALEUP	12000.1	0.024
BTAGSFDOWN	10215.1	-14.855
BTAGSFUP	13918.6	16.016
CTAGSFDOWN	11990.8	-0.053
CTAGSFUP	12003.7	0.054
EL_ID_SFDOWN	11707.2	-2.417
EL_ID_SFUP	12287.2	2.417
EL_RECO_SFDOWN	11970.6	-0.222
EL_RECO_SFUP	12023.9	0.223
EL_TRIG_SFDOWN	11977	-0.168
EL_TRIG_SFUP	12017.5	0.169
JVFSFDOWN	11997.3	0.001
JVFSFUP	11997.3	0.001

Continued on next page

Table A.5 –*Continued from previous page*

Parameter	N_{events}	ΔN (%)
LEP_RECO_SFDOWN	11942.1	-0.459
LEP_RECO_SFUP	12052.5	0.461
LEP_TRIG_SFDOWN	11975.2	-0.183
LEP_TRIG_SFUP	12019.3	0.184
MISTAGSFDOWN	11975.3	-0.182
MISTAGSFUP	12019.2	0.184
MU_ID_SFDOWN	11937.2	-0.5
MU_ID_SFUP	12057.3	0.501
MU_RECO_SFDOWN	11968.6	-0.238
MU_RECO_SFUP	12025.9	0.239
MU_TRIG_SFDOWN	11990.6	-0.055
MU_TRIG_SFUP	12003.8	0.055

A.5 Truth matching correction

Table A.6 provides the bin-by-bin correction factors applied to the unfolded extra jet distribution. The number of extra jets per bin is compared in unfolding and truth in baseline PowHeg+Pythia$t\bar{t}$ hdamp= ∞ (DS 117050). The response matrix was filled with events passing both reconstructed and truth selection. For 100 pseudoexperiments, $N_{data}^{events} = 12176$ events were selected from $t\bar{t}$ simulation events passing reconstructed selection, with no truth requirement. The reconstructed extra jets, excluding pileup, in each pseudoexperiment were then unfolded using Bayes with 4 iterations. The average of 100 unfoldings is given by $N_{unfolded}^{jets}$. N_{truth}^{jets} gives the number of extra jets at truth level without any reconstruction requirements, normalized to N_{data}^{events}.

Table A.6: Bin-by-bin correction factors applied to the unfolded extra jet p_{T} distribution .

Bin number	$N_{truth}^{jets}/N_{unf}^{jets}$
1	1.0686 ± 0.0029
2	1.0593 ± 0.0031
3	1.0583 ± 0.0033
4	1.0500 ± 0.0036
5	1.0334 ± 0.0038
6	1.0228 ± 0.0029
7	1.0111 ± 0.0033
8	0.9915 ± 0.0036
9	0.9708 ± 0.0040
10	0.9615 ± 0.0044
11	0.9365 ± 0.0032
12	0.9196 ± 0.0039
13	0.9228 ± 0.0047
14	0.9331 ± 0.0057
15	0.9117 ± 0.0066
16	0.9241 ± 0.0079
17	0.8971 ± 0.0044
18	1.0209 ± 0.0029
19	1.0253 ± 0.0035
20	1.0027 ± 0.0039
21	1.0143 ± 0.0045
22	0.9854 ± 0.0050
23	0.9772 ± 0.0042
24	0.9419 ± 0.0051
25	0.8961 ± 0.0060
26	0.8929 ± 0.0073

Continued on next page

Table A.6 –*Continued from previous page*

Bin number	$N^{jets}_{truth}/N^{jets}_{unfolded}$
27	0.8964 ± 0.0088
28	0.8325 ± 0.0068
29	0.8363 ± 0.0101
30	0.8372 ± 0.0096
31	0.9920 ± 0.0040
32	0.9919 ± 0.0039
33	0.9141 ± 0.0053
34	0.9070 ± 0.0057
35	0.8150 ± 0.0087
36	0.9500 ± 0.0059
37	0.9581 ± 0.0064
38	0.8586 ± 0.0096
39	0.8435 ± 0.0107
40	0.9226 ± 0.0099
41	0.9021 ± 0.0094

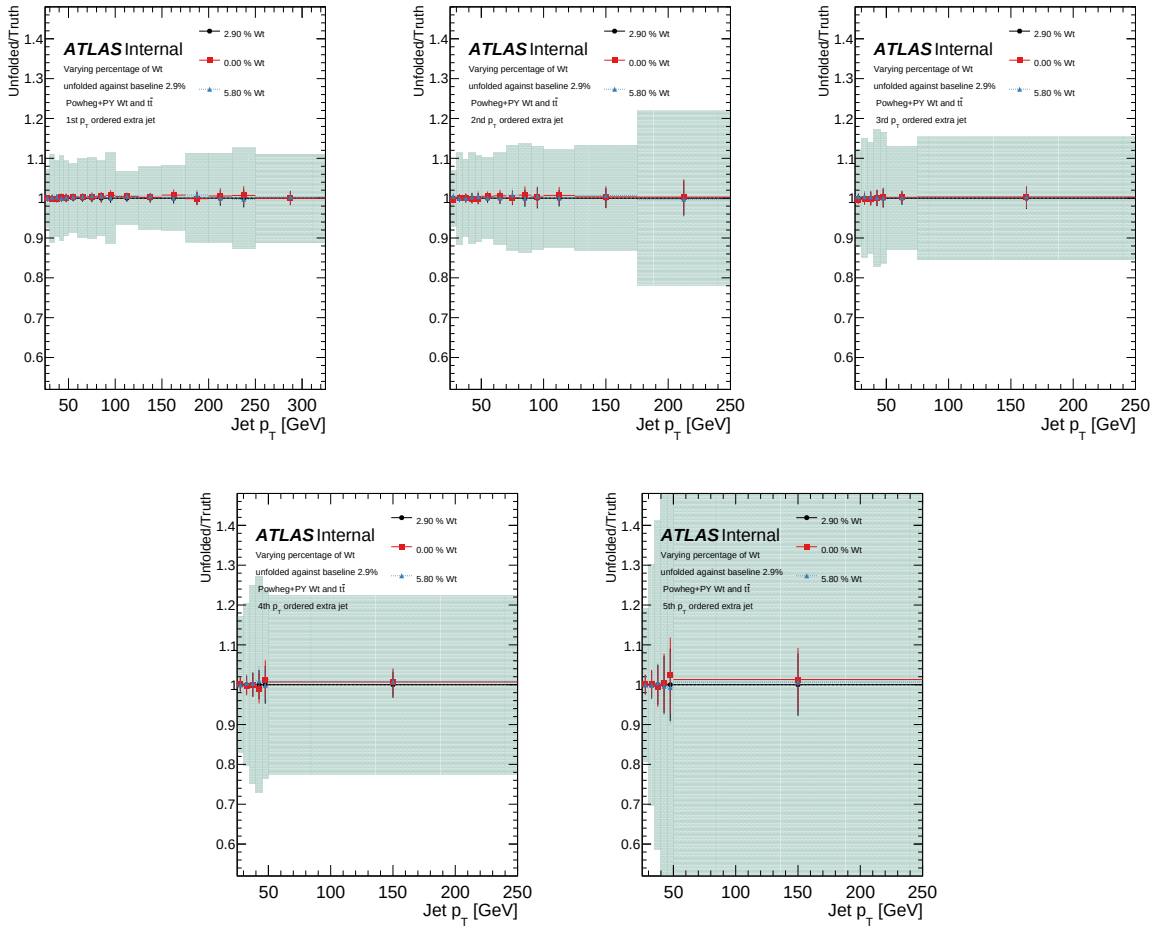

Figure A.23: The systematic uncertainty on the unfolded spectrum due uncertainties in the Wt atio of N^{unfolded} over N^{true} jets per GeVfor events from $t\bar{t}$ +single top simulation. The response matrix is filled with the 97.1% $t\bar{t}$ events and nominal 2.9% single top events. The rate of single top is then varied and unfolded against the nominal matrix.

A.6 Single top rate

Because the Wt process produces events with a different extra jet spectrum from $t\bar{t}$ uncertainties on the Wt rate can be a source of systematic uncertainty on the unfolding. This uncertainty is studied using the baseline unfolding procedure but varying the Wt contribution to the input spectrum between 0% anf 5%. The results of this study are presented in Figure A.23. The resulting systematic uncertainy is at the sub-percent level.

A.7 Estimated double parton scattering as a function of minimum jet $p_{\mathbf{T}}$

Generic expression for double parton scattering (DPS) in proton-proton scattering [101]:

$$\sigma^{DPS}_{(pp\to ab)} = \frac{m}{2}\frac{\sigma^{SPS}_{(pp\to a)} \cdot \sigma^{SPS}_{(pp\to b)}}{\sigma_{(eff,pp)}} \tag{A.1}$$

where $m = 2$ if a and b are distinguishable, $m = 1$ if not.

Fit $\sigma_{eff} = 15$ mb from $W(\to l\nu) + 2$ jets[102]:

Divide out signal cross section to get P that DPS occurs with another process b[102]:

$$P_{t\bar{t}|dijet} = \sigma dijet/\sigma_{eff} \tag{A.2}$$

From $t\bar{t}$ cross-section measurement[1]: $\sigma t\bar{t} = 242.1 \pm 1.7 \pm 5.5 \pm 7.5 \pm 4.2$ pb at $\sqrt{s} = 8$ TeV, so we have uncertainty $\sim 8\%$. Let's assume that we need

$$P_{t\bar{t}|dijet} = \sigma dijet/\sigma_{eff} \approx 1\% \tag{A.3}$$

Use Pythia to generate 5000 events for inclusive dijets at $\sqrt{s} = 8$ TeV. From log file, $\sigma dijet, total = 5.379 \times 10^6$ nb.

$$P_{t\bar{t}|dijet} = \frac{N_{p_T^{jet}<p_T^{max}}}{N_{total}} \cdot 5.379 \times 10^6 nb/15mb \tag{A.4}$$

$$0.01 = 0.3586\frac{N_{p_T^{jet}<p_T^{max}}}{N_{total}} \tag{A.5}$$

$$.02786 = \frac{N_{p_T^{jet}<p_T^{max}}}{N_{total}} = \frac{N_{p_T^{jet}<29.5GeV}}{N_{total}} \tag{A.6}$$

where $\frac{N_{p_T^{jet}<p_T^{max}}}{N_{total}}$ is calculated from the generated sample.

Appendix B

Generator studies

The following Appendix studies Monte Carlo generator predictions for bottom and charm hadrons in the decays of top quarks and the fragmentation of high p_T jets. These results have also been published as an ATLAS public note [103].

B.1 Introduction

Final states that include heavy flavor (bottom and charm) hadrons are important for the study of many processes at the Large Hadron Collider (LHC). Examples of such processes include top quark pair ($t\bar{t}$) production, Higgs production (with decay to a bottom quark pair) and searches for signals from physics beyond the Standard Model (SM). To fully exploit the large data samples that will be collected during Run II at the LHC, a reduction in current systematic uncertainties associated with the modeling of heavy flavor hadron production and decay will be needed. Although data-driven methods are likely to play a major part in the effort to reduce these uncertainties, improvementsin the Monte Carlo (MC) models used to determine reconstruction efficiencies will also be necessary.

An overview of the physics of general purpose MC event generators can be found in reviews such as References [104] and [105]. Simulation of QCD processes using these generators involves four separate stages. First, the short distance cross section for the process of interest is calculated from the hard-scattering matrix elements obtained using a fixed-order perturbative QCD calculation. Second, perturbative contributions from initial- and final-state parton showers are included. These stages together provide a descripiton of the kinematic properties of quarks, gluons and leptons. Third, soft hadronic phenomena are treated using QCD-inspired models. In this step, the quarks and gluons are transformed into colorless objects using a hadronization model which includes the effects of fragmentation and soft gluon radiation. The most common hadronization models are the string model (used by Pythia6 [106] and Pythia8 [107]) and the cluster model (used by Herwig [108] and Herwig++ [109]). For hadronic initial states, the underlying event and effects from multiple parton interactions are incorporated at this stage. The generators all include adjustable

phenomenological parameters that are determined by comparing MC predictions to experimental data. Differences in the treatment of the soft physics and in the values chosen for the adjustable parameters can lead to substantial variations in the kinematic properties of the particles produced (see, for example, the results compiled in Reference [110]). Fourth, hadron and τ decays proceed according to particle tables that have been adapted from experimental data.

This note presents a study of heavy flavor hadron production and decay properties for four MC generators (Pythia8, PYTHIA6, Herwig++ and HERWIG) extensively used to model pp interactions at the LHC. Two benchmark physics processes are used for these comparisons: $t\bar{t}$ production, in which a b-quark is produced in each top decay and a c-quark is produced in approximately 1/3 of the W decays [1] and high transverse momentum (p_{T}) jet production, in which the generators produce b- and c-quarks via both the matrix element calculation and the parton shower. In addition, ancillary $e^+e^- \to b\bar{b}$ and $e^+e^- \to c\bar{c}$ samples are generated using shower parameterizations consistent with those used for LHC tunes. These samples are used to check the consistency of the fragmentation functions with data for the processes in which the fragmentation functions were originally measured.

The note is organized as follows. Section B.2 provides information on the configuration of the MC generators used for these studies. Section B.3 presents the bottom and charm hadron production fractions obtained with these generators and compares them to world averages of experimental data. These production fractions are sensitive to the adjustable parameters of the hadronization model. Section B.4 provides a detailed study of the modeling of heavy quark fragmentation. The MC generators all rely on the assumption that non-perturbative fragmentation functions are universal (aside from the QCD scaling violations). Section B.5 compares decay properties of heavy flavor hadrons in each of the four generators to world average experimental data. In addition, these results are compared to those obtained with the EvtGen [32] decay package, which implements detailed models of flavor decay and uses branching fraction measurements compiled in Reference [111]. Section B.6 provides a brief summary of the results presented here.

B.2 Monte Carlo Samples

The versions of the four generators studied here are PYTHIA 6.427, Pythia 8.175, HERWIG 6.520 with JIMMY 4.31 [112] for the underlying event and Herwig++ 2.6.3a. All pp samples have been generated with a center-of-mass energy of $\sqrt{s} = 8$ TeV.

Two physics processes are studied:

- Top-pair production ($t\bar{t}$) is calculated using POWHEG [113, 114, 115, 116] r2330 and the CT10 [117] parton distribution functions (PDFs). At keast one of the W bosons in the $t\bar{t}$ event is required to decay leptonically. The output of POWHEG are files in

[1] Although bottom and charm hadrons can also be produced in the parton shower, the rate for such production is small when compared to that produced in the top decays.

Les Houches Event (LHE) format, which contain the top-pair decay products (leptons and quarks). The same POWHEG LHE files are then passed to each of the four generators for parton shower, hadronization and underlying-event modeling. The generator tunes used are Perugia 2011C [118] (PYTHIA6), AU2(CT10) [119] (Pythia8) [2], AUET2(CT10) [120] (JIMMY) and UE-EE-4-LO** [121] (Herwig++). In PYTHIA6 and Pythia8, heavy quark fragmentation uses the Lund symmetric model with the Bowler modification [122]. In HERWIG and Herwig++, heavy quarks are fragmented using the cluster model.

- High p_{T} jet samples are generated using the matrix element calculations provided by each generator. The generator tunes and fragmentation models used are the same as those used for the $t\bar{t}$ samples. Events are required to have at least one jet with p_{T} between 500 GeV and 1 TeV.

For both processes, jets are reconstructed from stable particles [3] using the infrared- and collinear-safe anti-k_t algorithm [123] with radius parameter $R = 0.4$ using the FastJet package [124]. In the case of $t\bar{t}$ samples, leptons from the W decay are excluded from the jet recontruction.

For the fragmentation studies in Section B.4, e^+e^- samples are generated. Unless otherwise stated, these samples are generated with initial state QED radiation enabled. Comparisons with LEP and SLC data use $e^+e^- \to b\bar{b}$ samples generated at $\sqrt{s} = 91.2$ GeV. In addition, $e^+e^- \to b\bar{b}$ samples generated at $\sqrt{s} = 200$ GeV with initial state QED disabled for comparison to the $\sqrt{s} = 91.2$ GeV samples. Comparisons with Belle and CLEO data are studied using $e^+e^- \to c\bar{c}$ samples with $\sqrt{s} = 10.53$ GeV.

For studies of bottom and charm hadron decay properties, EvtGen 2.0 [32] is used. Decay products of all heavy flavor hadrons are removed from the event record and the four-momenta of the heavy flavor hadrons are passed to EvtGen, which redecays these hadrons; these new decay products are added to the event record. In some cases, modifications to the EvtGen default decay table have been made. These changes are discussed in Section B.5.

B.3 Heavy Flavor Hadron Production Fractions

The relative rates for production of different heavy flavor species depend on each generator's choice of hadronization model and the values of the tunable parameters of that model. These production fractions have been studied for weakly decaying bottom and charm hadrons in both the $t\bar{t}$ and the high p_{T} jet samples. Results for the $t\bar{t}$ are shown here; the difference between production fractions in the two processes is less than 0.006.

[2] While the default release of Pythia 8.175 uses the tau lifetimes specified in the POWHEG LHE files, a patch was applied to overrule the incorrect lifetimes written out in the POWHEG event record. This patch has since become part of Pythia 8.175.

[3] Stable particles are defined as those with a mean lifetime, $c\tau_0$, < 10 mm.

Species	Pythia8	PYTHIA6	Herwig++	HERWIG	World Average[111]
B^+	43.2	42.1	40.9	39.1	40.2 ± 0.7
B^0	43.2	42.2	40.9	39.1	40.2 ± 0.7
B_s^0	8.4	8.2	9.5	10.1	10.4 ± 0.6
Baryons	5.1	7.3	8.6	11.7	9.3 ± 1.5

Table B.1: Percentage probability that a bottom quark decays to a bottom hadron of a given species for Pythia8, PYTHIA6, Herwig++, HERWIG and for the world average from Reference [111].

Figure B.1 compares the production fractions for weakly decaying bottom and charm hadrons:

$$B^0\ B^+\ B_s^0\ B_c^+\ \Lambda_b^0\ \Xi_b^-\ \Xi_b^0\ \Omega_b\ D^+\ D^0\ D_s^+\ \Lambda_c^+\ \Xi_c^+\ \Xi_c^0\ \Omega_c^0$$

and their charge conjugates for the four generators. Charm hadron production fractions include only those hadrons produced directly (not from bottom hadron decays). Although the Σ_B should not decay weakly, HERWIG erroneously decays them weakly under some conditions; these decays are shown on the plot.

Recent results from LHCb constrain the ratio of B_s production to B^0 production to be $f_s/f_d = 0.259 \pm 0.015$ [125], with no evidence of dependence on the p_{T} or η of the hadrons. However, the baryon fraction in the forward region is observed to depend significantly on the p_{T} and η of the hadron [126]. Thus, results from LHCb are of limited use in constraining baryon production at central rapidities.

The PDG [111] provides values for the bottom hadron production fractions at high energy, using results obtained from Z decays and central $p\overline{p}$ collisions, under the assumption that these fractions should be universal aside from forward, leading-particle effects in hadron collisions. Fractions obtained from the four generators are compared to the PDG values in Table B.1. All the generators are in reasonable agreement with the data, although the baryon fraction in Pythia8 is low.

For the case of charm hadrons, the experimental data have been compiled and averaged, including a careful treatment of correlated systematic uncertainties in Reference [127]. Results for the different generators are compared to these averages in Table B.2. In general, the generators overestimate the D^+ fraction. The D^0 fraction in HERWIG is significantly lower than the fraction in the data and other three generators. Charm baryon fractions are poorly constrained by the data and vary widely among the generators.

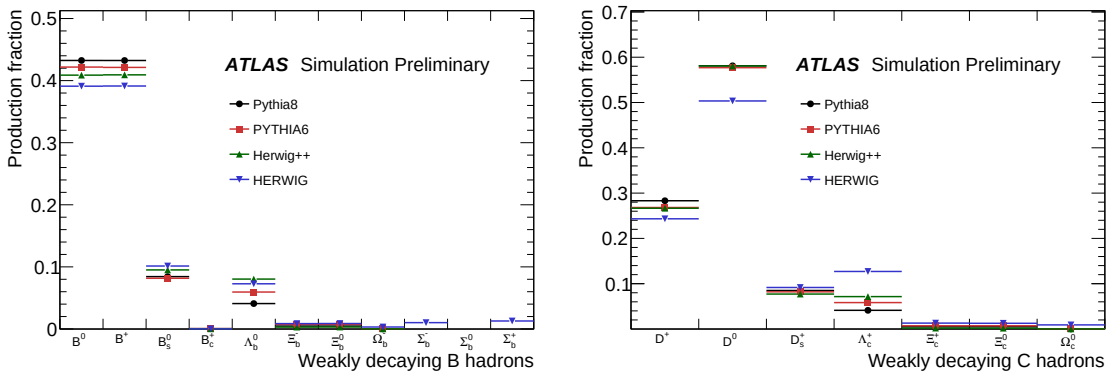

Figure B.1: Comparison of the production fractions for various weakly decaying (a) bottom and (b) charm hadrons in Pythia8, PYTHIA6, Herwig++ and HERWIG. The Σ_b should not decay weakly, but some weak decays of the Σ_b are observed in HERWIG.

Species	Pythia8	PYTHIA6	Herwig++	HERWIG	Reference [127]
D^+	28.3	26.8	26.7	24.3	22.56 ± 0.77
D^0	58.1	57.7	58.1	50.3	56.43 ± 1.51
D_s	8.5	8.2	7.7	9.2	7.97 ± 0.45
Baryons	5.1	7.2	7.6	16.2	10.8 ± 0.91

Table B.2: Percentage probability that a charm quark fragments to a charmed hadron of a given species for Pythia8, PYTHIA6, Herwig++, HERWIG and for the world average from Reference [127].

B.4 Heavy Flavor Fragmentation

The fragmentation of a b- or c-quark into a heavy flavor hadron is modeled by the generators using a non-perturbative fragmentation function $D_Q^H(z, \mu^2)$ that describes the probability that a quark of species Q will fragment into a hadron of species H carrying fraction z of the quark's momentum [111]. As with parton distribution functions, the fragmentation functions exhibit scaling violations and therefore must be evaluated at an appropriate scale μ. These fragmentation functions are assumed to be universal, aside from the scale dependence, which can be calculated perturbatively. Modeling of the fragmentation functions differs among the generators, but in all cases the parameters of the models have been tuned using data from e^+e^- collisions.

To assess the performance of the four generators, the following strategy is used. First, $e^+e^- \to b\bar{b}$ and $e^+e^- \to c\bar{c}$ samples are generated at the center-of-mass energy of the most accurate experimental measurements, using shower parametrizations consistent with those used for the LHC tunes. These samples are used to validate the modeling of the non-perturbative heavy flavor fragmentation functions. Second, the evolution of fragmentation

functions is studied by comparing these samples with $e^+e^- \to b\bar{b}$ and $e^+e^- \to c\bar{c}$ events generated at $\sqrt{s} = 200$ GeV. Third, the fragmentation is studied for each of the generators in the process $pp \to t\bar{t}$, in which the production of b- and c-jets are predominantly produced from the $t\bar{t}$ hard scatter. Finally, to study the case where heavy flavor is produced both in the hard scatter and in the parton shower, samples of high p_{T} jets are analyzed.

Data on b-quark fragmentation are available from LEP and SLC. The measurements parametrize the fragmentation function as a function of $x \equiv E/E_{\,beam}$ where E is the energy of the bottom hadron. Figure B.2 (a) compares the distribution

$$F(x) \equiv \frac{1}{N_B}\frac{dN_B}{dx}$$

for the four generators to measurements from DELPHI [128] and SLD [129] . The mean values of these distributions are given in Table B.3. To better match the experimental requirements on these measurements, events in the MC samples are required to satisfy the criteria that $|\cos\theta_{\,thrust}| < 0.7$ [4] and that the number of weakly decaying bottom hadrons (N_B) satisfy $0 < N_B < 3$. The mean value of x in the MC samples varies from 0.6782 ± 0.0005 (Herwig) to 0.7303 ± 0.0005 (Pythia8). Pythia6 and Herwig++ agree well with the data, while Pythia8 is high by $\sim 2\%$ and Herwig is low by $\sim 3\%$. These results are consistent with those presented in Reference [110].

Figure B.2 (b) shows the same distribution for the four generators at a center-of-mass energy of $\sqrt{s} = 200$ GeV. The samples are generated without initial state QED in order to isolate the effect of increased $\sqrt{s}$. As expected, the mean value of x is lower than at the Z-pole, due the evolution of the fragmentation function. The ratio of the means at the higher energy to those at the lower energy are 93.8%, 95.8%, 94.0% and 97.2% for Pythia8, Pythia6, Herwig++ and Herwig respectively.

Studies of c-quark fragmentation are available from Belle [130] and CLEO [131]. The fragmentation function is measured as a function of $x_p \equiv p/p_{\,max}$ where p is the momentum of the charm hadron and $p_{\,max}$ is the maximum momentum that is kinematically allowed. Charm hadrons are required to be directly produced; bottom hadron decay products are excluded. Figures B.3 (a) and B.3 (b) compare the four generators to the experimental measurements for D^+ and D^0 mesons respectively. Table B.4 gives the mean value of the fragmentation functions. The Pythia8 fragmentation appears to be significantly harder than the data, while other generators agree reasonably well with the data and with each other.

In e^+e^- collisions, the fragmentation function can be measured relative to the beam energy, since the momentum transfer of the hard scatter is fixed by the energy of the initial beams (aside from initial state photon radiation). However, fragmentation in hadron collisions must be parameterized with respect to the output of a jet-finding algorithm. By convention, the p_{T} of the jet containing the heavy flavor hadron is used to approximate the

[4] The thrust axis is defined as the axis $\mathbf{n}$ that maximizes the value of $\sum_i \mathbf{n}\cdot\mathbf{p}_i / \sum_i \mathbf{p}_i$, where the sum is taken over all stable particles in the event.

unknown p_{T} of the heavy flavor parton. The resulting fragmentation function $f(z)$ is defined to be

$$f(z) \equiv \frac{\vec{p}_{\,hadron} \cdot \vec{p}_{\,jet}}{p^2{}_{jet}}.$$

For this study, the $f(z)$ is measured for anti-$k_t(R = 0.4)$ jets with $|\eta^{jet}| < 2.5$. Jets are defined to be heavy flavor jets if there is a weakly decaying heavy flavor hadron with $p_{\mathrm{T}} > 5\,\mathrm{GeV}$ within $\Delta R = \sqrt{\Delta\phi^2 + \Delta\eta^2} < 0.3$ of the jet direction. For measurements of the charm fragmentation function, jets are vetoed if the charm hadron contained in the jet is a bottom hadron decay product.

For large momentum scale processes, an additional perturbative contribution (from $g \to b\bar{b}$) becomes significant. In some cases, this perturbative component is explicitly included in the matrix element calculation, while in other cases this component is treated as part of the parton shower. Such jets are included here in the definition of b- and c- jets.

Figure B.4 and Table B.5 show the bottom and charm fragmentation functions $f(z)$ for jets in the $t\bar{t}$ samples satisfying the requirement $p_T^{\mathrm{jet}} > 25$ GeV in events containing a lepton with $p_T^{lep} > 20$ GeV and $|\eta^{lep}| < 2.5$. The mean value of z varies from 0.741 (Herwig) to 0.772 (Herwig++) for b-quarks and from 0.552 (Pythia6) to 0.575 (Herwig) for c-quarks. The b-quark (c-quark) fragmentation in Herwig++ (Herwig) is noticeably harder than for the other generators.

The fragmentation function in jets is sensitive to many other aspects of the simulation. Measurements depend on the choice of jet algorithm and can be affected by the underlying event tune, as well as by the transverse shape of the generated jet. Details of the shower modeling itself, such as the suppression of QCD radiation from heavy particles (the *dead-cone* effect [132]) can also play a role. To better study the fragmentation model, these effects are probed using additional distributions for these heavy flavor jets. Figure B.5 shows the width of the b-quark and c-quark jets, where the jet width (W) is obtained from the p_{T} weighted distribution of the distance ΔR from the center of the jet:

$$W \equiv \frac{\sum_i p_{Ti}\,\Delta R_i}{\sum_i p_{Ti}}$$

and the sum is taken over all stable particles that are constituents of the jets. The mean value of the jet widths for all generators agree to within a few percent, although the distribution of widths for b-quark jets is slightly broader for Pythia8 than for the other generators and the distribution of widths for c-quarks is slightly narrower for Herwig and Herwig++ than for Pythia6 and Pythia8.

The differential jet shape $\rho(r)$ in an annulus of inner radius $r - \Delta r/2$ and outer radius $r + \Delta r/2$ from the axis [5] of a given jet is defined as

[5] The jet axis is defined to be the direction of the momentum vector of the jet from the anti-$k_t(R = 0.4)$ algorithm.

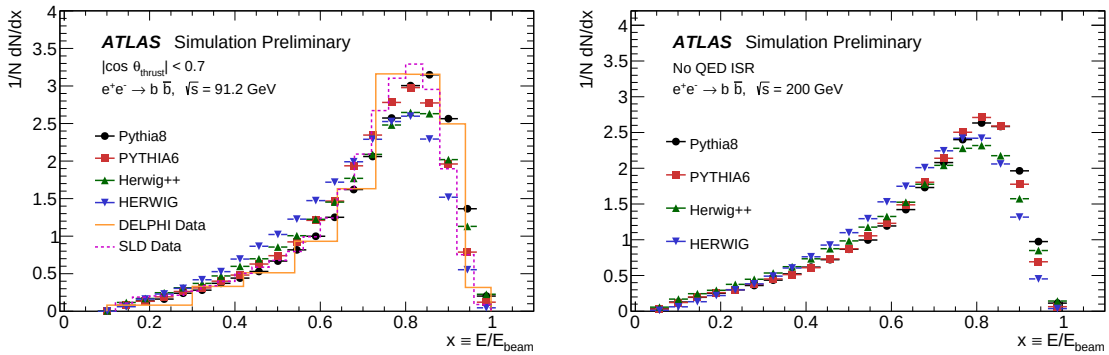

Figure B.2: The b-quark fragmentation function obtained with Pythia8, PYTHIA6, Herwig++ and HERWIG for (a) $\sqrt{s} = 91.2$ GeV and (b) $\sqrt{s} = 200$ GeV $e + e-$ collisions. DELPHI and SLD data in (a) are taken from References [128] and [129] respectively and are plotted without error bars.

E_B/E_{beam}	
Pythia8	0.7303 ± 0.0005
PYTHIA6	0.7090 ± 0.0005
Herwig++	0.7012 ± 0.0006
HERWIG	0.6782 ± 0.0005
Delphi Data	0.699 ± 0.011
SLD Data	0.709 ± 0.005

Table B.3: The mean b-quark fragmentation function obtained with Pythia8, PYTHIA6, Herwig++ and HERWIG for $\sqrt{s} = 91.2$ GeV in $e + e-$ collisions. DELPHI and SLD data in (a) are taken from References [128] and [129] respectively.

p_C/p_{max}		
	D^+	D^0
Pythia8	0.6337 ± 0.0010	0.6156 ± 0.0007
PYTHIA6	0.5918 ± 0.0022	0.5744 ± 0.0011
Herwig++	0.5611 ± 0.0016	0.5390 ± 0.0010
HERWIG	0.5981 ± 0.0016	0.5797 ± 0.0011
Belle Data	0.578 ± 0.00148	0.5703 ± 0.0020
CLEO Data	0.582 ± 0.009	0.570 ± 0.006

Table B.4: The mean c-quark fragmentation function obtained with Pythia8, PYTHIA6, Herwig++ and HERWIG for $\sqrt{s} = 10.53$ GeV for $e + e-$ collisions for (a) D^+ and (b) D^0 mesons. CLEO and Belle data are taken from References [131] and [130] respectively.

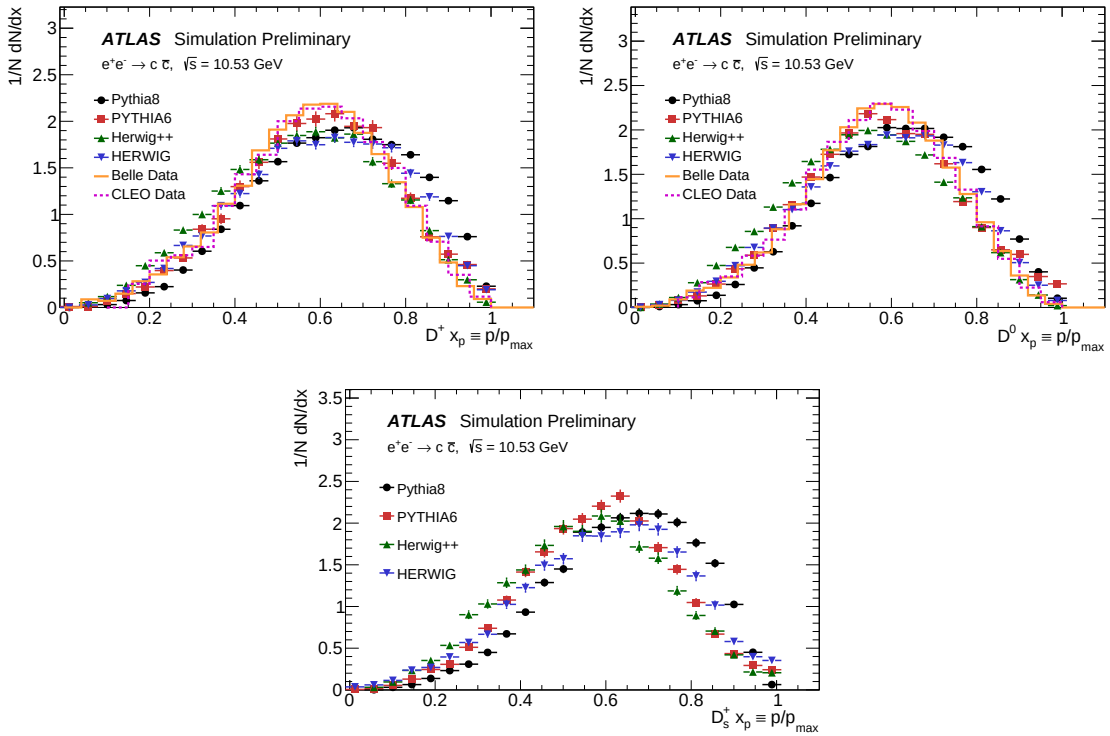

Figure B.3: The c-quark fragmentation function obtained with Pythia8, PYTHIA6, Herwig++ and HERWIG for $\sqrt{s} = 10.53$ GeV for $e+e-$ collisions for (a) D^+ and (b) D^0 mesons. CLEO and Belle data are taken from References [131] and [130] respectively and are plotted without error bars.

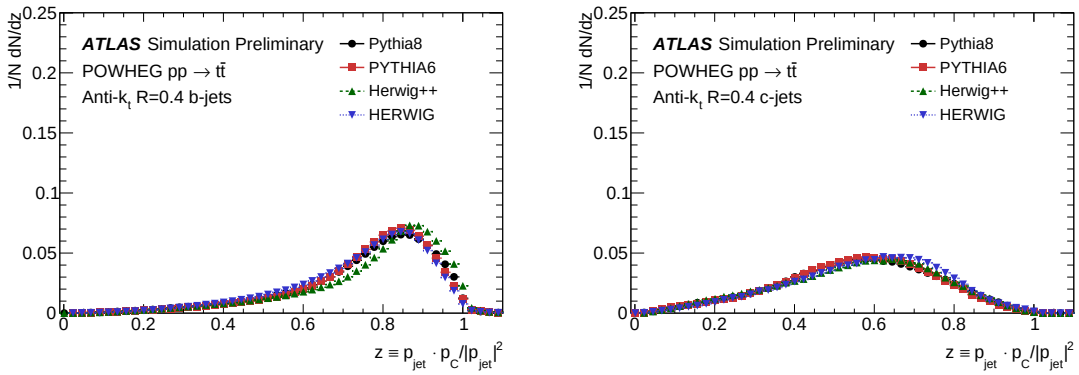

Figure B.4: The fragmentation function for for the parton shower, hadronization and underlying event modeling.

Generator	$p_{jet} \cdot p_B / p_{jet}^2$	$p_{jet} \cdot p_C / p_{jet}^2$
Pythia8	0.7529 ± 0.0001	0.5550 ± 0.0004
PYTHIA6	0.7561 ± 0.0001	0.5525 ± 0.0004
Herwig++	0.7719 ± 0.0001	0.5590 ± 0.0004
HERWIG	0.7411 ± 0.0001	0.5751 ± 0.0004

Table B.5: The mean fragmentation function for b-jets and c-jets in POWHEG $t\bar{t}$ samples where Pythia8, PYTHIA6, Herwig++ and HERWIG have been used for the parton shower, hadronization and underlying event modeling.

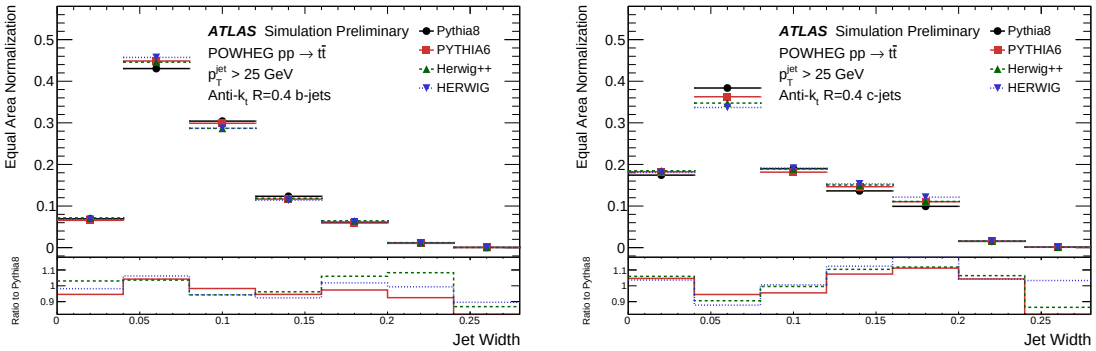

Figure B.5: The jet width for (a) b-jets and (b) c-jets in POWHEG $t\bar{t}$ samples where Pythia8, PYTHIA6, Herwig++ and HERWIG have been used for the parton shower, hadronization and underlying event modeling.

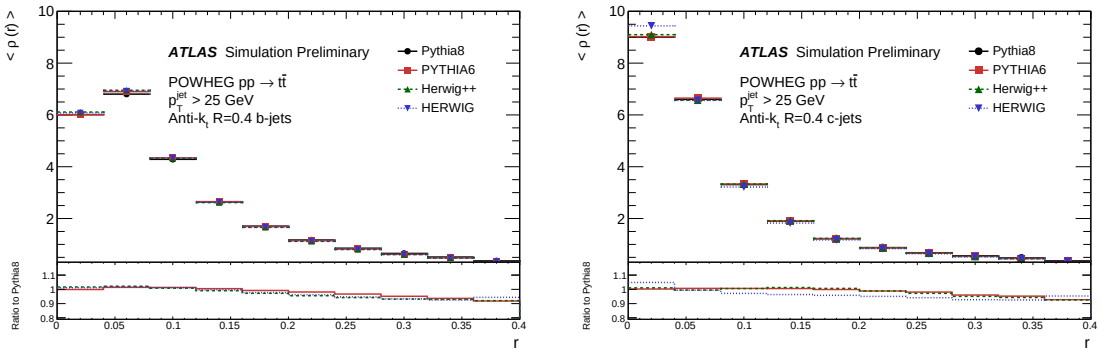

Figure B.6: The differential jet shape $\rho(r)$ distribution for (a) b-jets and (b) c-jets in POWHEG $t\bar{t}$ samples where Pythia8, PYTHIA6, Herwig++ and HERWIG have been used for the parton shower, hadronization and underlying event modeling.

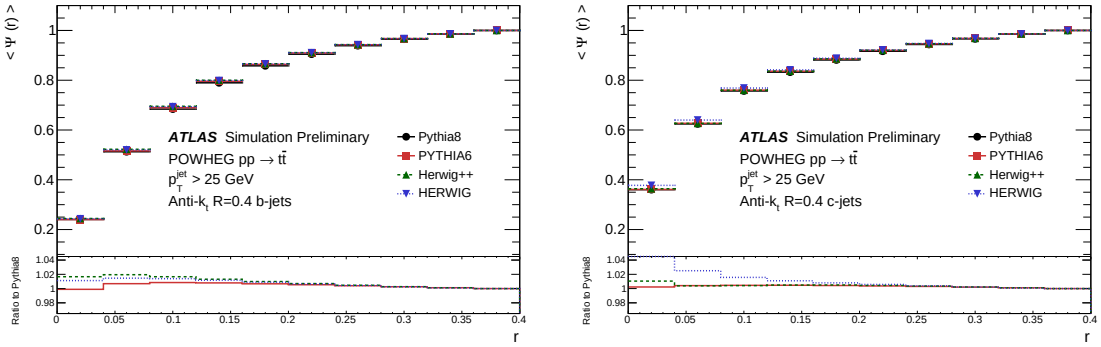

Figure B.7: The integral jet shape $\Psi(r, R = 0.4) \equiv \Sigma p_T(0, r) \sum p_T(0, R)$ distribution for (a) b-jets and (b) c-jets in POWHEG $t\bar{t}$ samples where Pythia8, PYTHIA6, Herwig++ and HERWIG have been used for the parton shower, hadronization and underlying event modeling. The legend includes the value and error of the mean of each distribution.

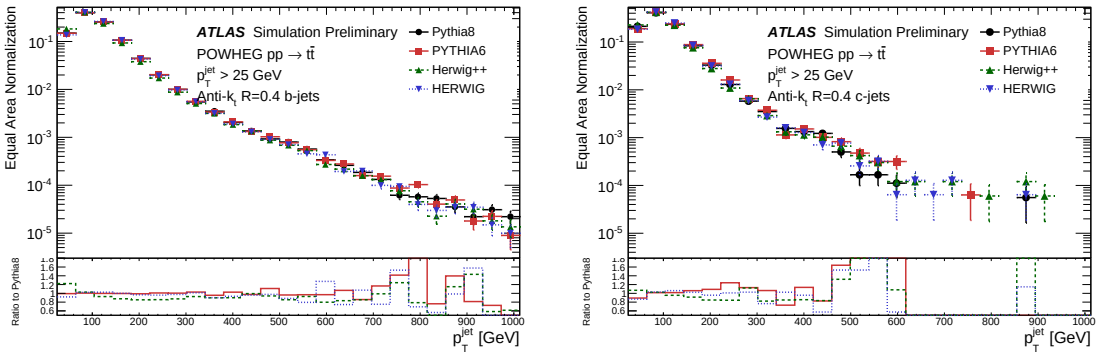

Figure B.8: The p_T^{jet} distribution for (a) b-jets and (b) c-jets in POWHEG $t\bar{t}$ samples where Pythia8, PYTHIA6, Herwig++ and HERWIG have been used for the parton shower, hadronization and underlying event modeling.

All jets

All jets		
Generator	$p_{jet} \cdot p_B / p_{jet}^2$	$p_{jet} \cdot p_C / p_{jet}^2$
Pythia8	0.3683 ± 0.0012	0.1853 ± 0.0004
PYTHIA6	0.3633 ± 0.0010	0.1841 ± 0.0004
Herwig++	0.4356 ± 0.0011	0.2442 ± 0.0005
HERWIG	0.3984 ± 0.0011	0.2614 ± 0.0006

Heavy flavor hadron jets		
Generator	$p_{jet} \cdot p_B / p_{jet}^2$	$p_{jet} \cdot p_C / p_{jet}^2$
Pythia8	0.5747 ± 0.0022	0.3790 ± 0.0018
PYTHIA6	0.5696 ± 0.0019	0.3787 ± 0.0016
Herwig++	0.6473 ± 0.0017	0.4549 ± 0.0015
HERWIG	0.5953 ± 0.0017	0.4674 ± 0.0015

Table B.6: The mean fragmentation function for (a) b-jets and c-jets in the high p_{T} jet sample and for the subset of (b) b-jets and c-jets satisfying the additional requirement that there be no other weakly decaying heavy flavor hadron with $p_{\mathrm{T}} > 5.0$ GeV within a cone $\Delta R = 1$ of the jet.

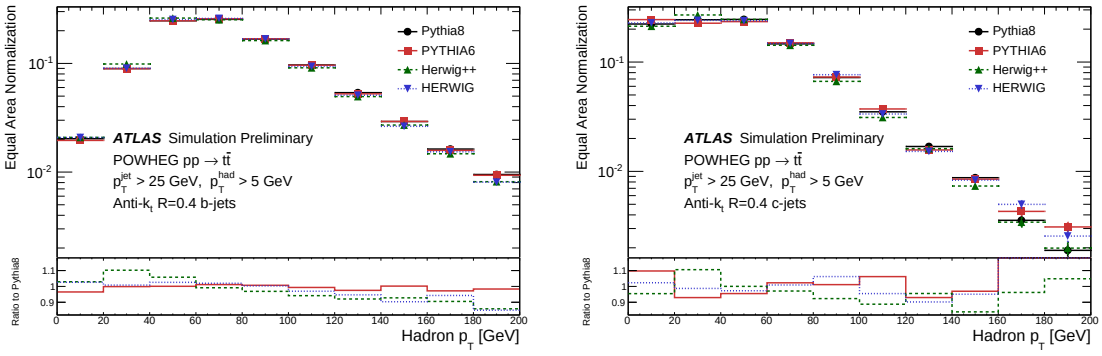

Figure B.9: The p_T^{hadron} distribution for (a) b-jets and (b) c-jets in POWHEG $t\bar{t}$ samples where Pythia8, PYTHIA6, Herwig++ and HERWIG have been used for the parton shower, hadronization and underlying event modeling.

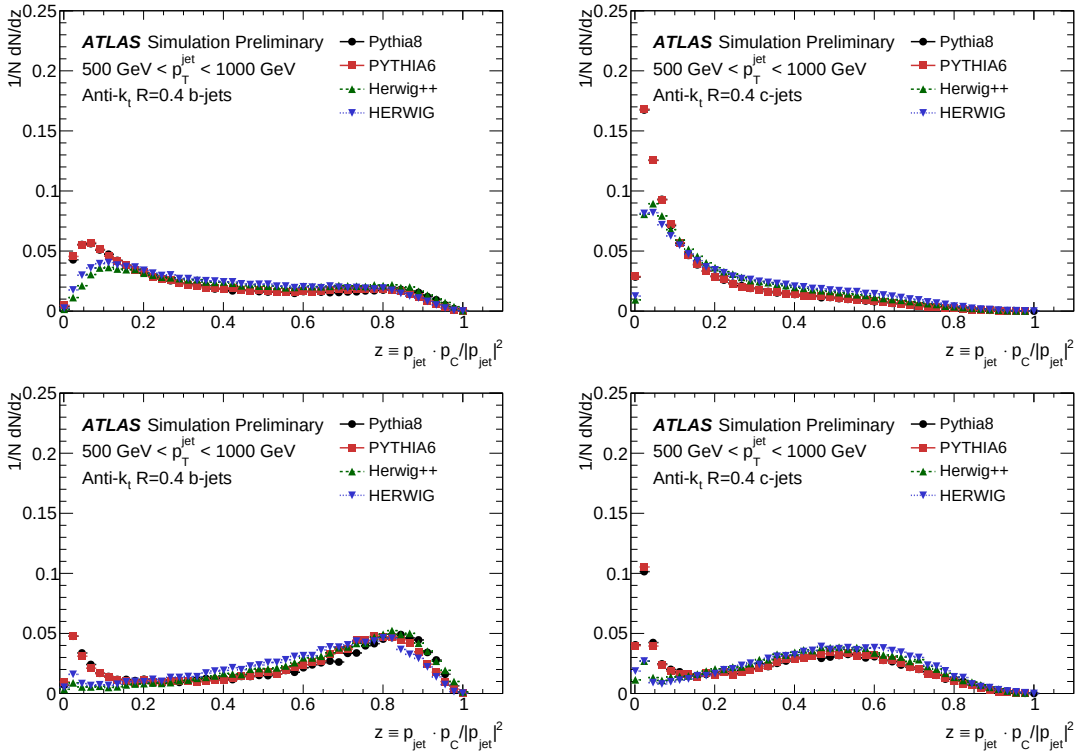

Figure B.10: The fragmentation function for (a) b-jets and (b) c-jets in the high p_{T} jet sample and for the subset of (c) b-jets and (d) c-jets containing exactly one heavy flavor hadron.

$$\rho(r) = \frac{1}{\Delta r} \frac{p_T\left(r - \Delta r/2, r + \Delta r/2\right)}{p_T\left(0, R\right)}$$

Here $\Delta r = 0.04$ is the width of the annulus, r, such that $\Delta r/2 \leq r \leq R - \Delta r/2$ is the distance to the jet axis in the $\eta - \phi$ plane and $p_T(r_1, r_2)$ is the scalar sum of the p_T of the jet constituents with radii between r_1 and r_2. Figure B.6 shows the distribution of the variable $\rho(r)$. ATLAS results for $t\bar{t}$ production at 7 TeV indicate that POWHEG with PYTHIA6 for the parton shower give good agreement with the data for this variable [133]. No experimental results are currently available at 8 TeV.

The integrated jet shape in a cone of radius $r < R$ around the jet axis is defined as the cumulative distribution for $\rho(r)$, i.e.

$$\Psi(r) \equiv \frac{p_T\left(0, r\right)}{p_T\left(0, R\right)},\ 0 \leq r \leq R$$

which satisfies $\Psi(r = R) = 1$. Figure B.7 shows the distribution of $\Psi(r)$. For each of these jet shapes, differences between the generators are small. The fact that Herwig++ (HERWIG) b-quark (c-quark) fragmentation is harder than for the other generators is not clearly explained by differences in the the W, $\rho(r)$ or $\Psi(r)$ distributions.

Figure B.8 shows the jet p_{T} distribution for b- and c-jets in the $t\bar{t}$ samples. For b-jets, the generators are in reasonable agreement, except for Herwig++, which exhibits a slightly softer spectrum. All generators agree well for c-jets. Figure B.9 shows the p_{T} distributions of the bottom and charm hadrons contained in these jets. Herwig++ produces a slightly softer p_{T} spectrum for the bottom hadrons, while HERWIG has a softer spectrum for charm hadrons.

For high p_{T} jets, the $f(z)$ distribution has two components. The fragmentation of heavy flavor created in the hard scatter produces a distribution at higher z. The production of heavy flavor in additional processes gives a component at lower z. Examples of such processes include gluon splitting, multiple parton interactions and heavy flavor production within the hadronization process. These components have been studied for jets with p_T^{jet} between 500 GeV and 1 TeV. Figures B.10 (a) and B.10 (b) show the distribution of $f(z)$ for the four generators for b- and c-jets respectively. The dominant feature in these distributions is a large peak at low z, although this peak is less pronounced for HERWIG and Herwig++ than for PYTHIA6 and Pythia8. To enhance the high z contribution from the hard scatter, the distributions are examined in Figures B.10 (c) and (d) for the subset of b- and c-jets satisfying an additional requirement that there be no other weakly decaying heavy flavor hadron with $p_T^{\mathrm{hadron}} > 5.0$ GeV within a cone $\Delta R = 1$ of the jet. While some evidence of the low z peaking still remains, the distributions for $z > 0.2$ in Figures B.10 (c) and (d) are qualitatively similar to those of Figures B.4 (a) and (b) respectively.

B.5 Heavy Flavor Hadron Decays

Heavy flavor decay properties are studied for different Monte Carlo generators. All weakly decaying bottom and charm hadrons (listed in Section B.3) were selected from inclusive $t\bar{t}$ events and their decays were then analyzed.

Pythia8, PYTHIA6, Herwig++ and HERWIG each maintain separate particle properties and particle decay tables. Therefore, the generated lifetimes, semileptonic branching fractions and charged multiplicities for heavy flavor hadrons differ among the generators. Such differences can affect the b-tagging efficiency and the mistag rate for charm hadrons passing the b-tagger in simulated data. An alternative approach is to redecay all heavy flavor hadrons using a unified decay description. This approach has been studied by using EvtGen to redecay all heavy flavor hadrons produced for each of the four generators. Results are presented here for each generator both with and without EvtGen.

EvtGen version 2.0 is used with the particle properties table provided with the EvtGen release and its standard inclusive decay table DECAY_2010.DEC. In some cases, the data in these standard tables differ from the values reported by the PDG. These differences are highlighted in the figures that follow and a proposed update to the decay table is provided.

Figure B.11 and Figure B.12 compare the lifetimes of four weakly decaying bottom (B^0, B^+, B_s^0 and Λ_b) and charm hadrons (D^0, D^+, D_s and Λ_c) respectively for the four generators and for EvtGen. Using EvtGen improves the agreement of lifetimes with the experimental averages in the PDG. The value of the B_s^0 lifetime in the default EvtGen particle properties table differs from the world average listed by the PDG.

Figure B.13 and Figure B.14 show the semileptonic branching fractions for the same bottom and charm hadrons. These figures demonstrate that the branching fractions in the default EvtGen particle properties table differ from the world averages listed by the PDG. In order to improve agreement with the PDG semileptonic branching fractions, a custom decay table was updated for ATLAS, rescaling the semileptonic modes so that the inclusive semileptonic fraction matched that in the PDG. The results from the two decays tables are shown in Figure B.13 and Figure B.14 for comparison.

Table B.7 and Figures B.15-B.16 show the charged multiplicity distributions for these bottom hadrons and charm hadrons while Table B.8 and Figures B.17-B.18 show the total (charged plus neutral) multiplicity. Here a stable particle is defined as a particle with a proper lifetime $c\tau_0 > 10$ mm so that, for example, the K_S is considered stable, but the π^0 is allxowed to decay. The multiplicities vary between generators by as much as $\sim 20\%$ for bottom hadrons and as much as $\sim 15\%$ for charm hadrons.

B.6 Summary

Studies of heavy flavor production fractions, fragmentation functions and decay properties for four MC generators are presented. Bottom production fractions vary among generators, largely due to large differences of up to 6.5% in the baryon fraction. For charm production,

Multiplicity of charged, stable decay products					
Particle	Pythia8	PYTHIA6	Herwig++	HERWIG	Pythia8+EvtGen
B^0	4.928 ± 0.006	5.336 ± 0.006	4.475 ± 0.005	4.690 ± 0.005	4.853 ± 0.004
B^+	4.754 ± 0.005	5.102 ± 0.006	4.435 ± 0.005	4.636 ± 0.005	4.750 ± 0.004
B_s^0	4.661 ± 0.012	5.136 ± 0.013	4.319 ± 0.010	4.665 ± 0.011	4.623 ± 0.008
Λ_b^0	4.976 ± 0.018	5.010 ± 0.015	4.153 ± 0.011	4.280 ± 0.012	4.957 ± 0.013
D^0	2.215 ± 0.003	2.273 ± 0.003	2.182 ± 0.003	2.263 ± 0.003	2.208 ± 0.002
D^+	1.965 ± 0.003	2.161 ± 0.004	1.920 ± 0.004	2.154 ± 0.005	1.958 ± 0.002
D_s	2.103 ± 0.007	2.410 ± 0.008	2.129 ± 0.008	2.476 ± 0.009	2.102 ± 0.005
Λ_c^+	2.222 ± 0.010	2.353 ± 0.009	2.004 ± 0.008	1.980 ± 0.006	2.193 ± 0.007

Table B.7: Mean number of charged, stable decay products for the weakly decaying bottom and charm hadrons species in Pythia8 PYTHIA6
Herwig++ HERWIG and EvtGen. A stable particle is defined as a particle with a proper lifetime $c\tau_0 > 10$ mm.

Multiplicity of stable decay products					
Particle	Pythia8	PYTHIA6	Herwig++	HERWIG	Pythia8+EvtGen
B^0	11.379 ± 0.012	11.939 ± 0.013	9.919 ± 0.011	10.339 ± 0.012	10.982 ± 0.009
B^+	11.527 ± 0.013	12.263 ± 0.014	10.283 ± 0.012	10.550 ± 0.012	11.250 ± 0.009
B_s^0	11.933 ± 0.030	12.552 ± 0.032	10.516 ± 0.024	10.706 ± 0.024	11.631 ± 0.021
Λ_b^0	11.220 ± 0.040	11.298 ± 0.034	9.376 ± 0.024	10.060 ± 0.026	10.772 ± 0.027
D^0	4.920 ± 0.006	5.002 ± 0.006	4.784 ± 0.006	4.748 ± 0.007	4.853 ± 0.004
D^+	4.344 ± 0.007	4.554 ± 0.008	4.053 ± 0.007	4.437 ± 0.009	4.265 ± 0.005
D_s	5.564 ± 0.017	5.842 ± 0.019	5.393 ± 0.019	5.548 ± 0.019	5.500 ± 0.012
Λ_c^+	5.007 ± 0.021	5.100 ± 0.019	4.219 ± 0.015	4.485 ± 0.013	4.751 ± 0.014

Table B.8: Mean number of stable decay products for the weakly decaying bottom and charm hadrons species in Pythia8 PYTHIA6
Herwig++ HERWIG and EvtGen. A stable particle is defined as a particle with a proper lifetime $c\tau_0 > 10$ mm.

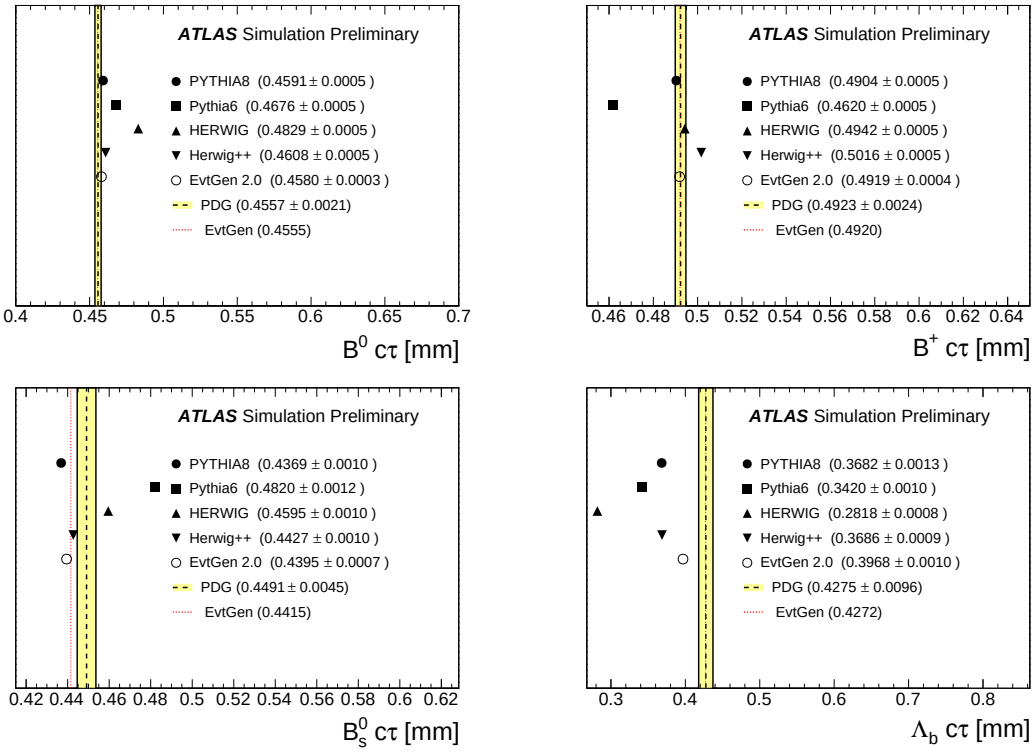

Figure B.11: Comparison of lifetimes of the weakly decaying bottom hadrons (a) B^0, (b) B^+, (c) B_s^0 and (d) Λ_b for four different generators, PYTHIA6 version 427.2, Pythia8 version 175, Herwig++ version 2.6.3 and HERWIG version 6.520.2, both with and without EvtGen. EvtGen version 2.0 is used with the particle properties table provided with EvtGen and with its standard inclusive decay table DECAY_2010.DEC. The value of the B_s^0 lifetime in this default EvtGen particle properties table differs from the world average listed by the PDG [111].

the generators overestimate the D^+ fraction. The D^0 fraction in HERWIG is significantly lower than for the other three generators; HERWIG, PYTHIA6, and Pythia8 are in good agreement with world average data. Distributions of x (x_p), the fraction of the heavy quark energy (momentum) carried by the bottom (charm) hadron have been studied using e^+e^- samples generated with the same showering parameters used in modern LHC tunes. Differences in the mean value of x generated differ by up to 5% for bottom and up to 12% for charm. Studies of $f(z)$, the fraction of the jet momentum carried by the heavy flavor hadron, from $t\bar{t}$ samples show good agreement among all the generators except for Herwig++, which has a mean value of z for bottom jets s higher by about 2%. Comparisons of $f(z)$ distributions for high transverse momentum jets indicate that the treatment of heavy flavor pair production differs between among the generators. EvtGen was found to improve agreement with PDG values for the decays of heavy flavor particles, but modifications to the standard EvtGen inclusive decay table further improve agreement with the experimental

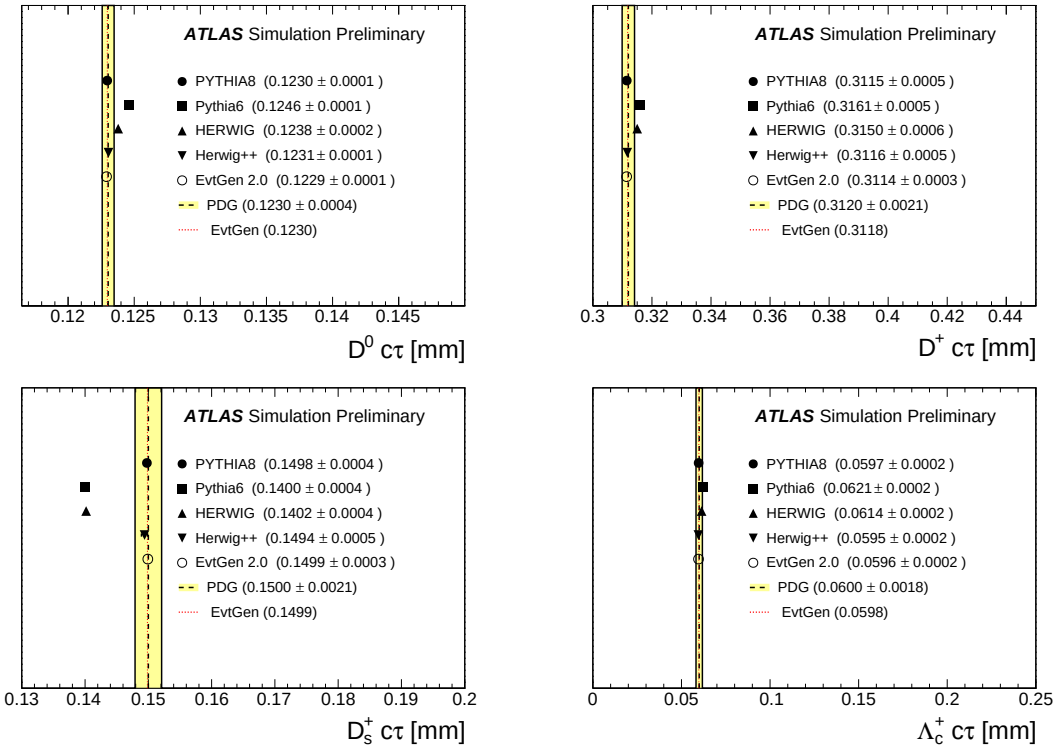

Figure B.12: Comparison of lifetimes of the weakly decaying charm hadrons (a) D^0, (b) D^+, (c) D_s and (d) Λ_c in four different generators, PYTHIA6 version 427.2, Pythia8 version 175, Herwig++ version 2.6.3 and HERWIG version 6.520.2, both with and without EvtGen. EvtGen version 2.0 is used with the particle properties table provided with EvtGen and with its standard inclusive decay table DECAY_2010.DEC.

measurements of branching fractions.

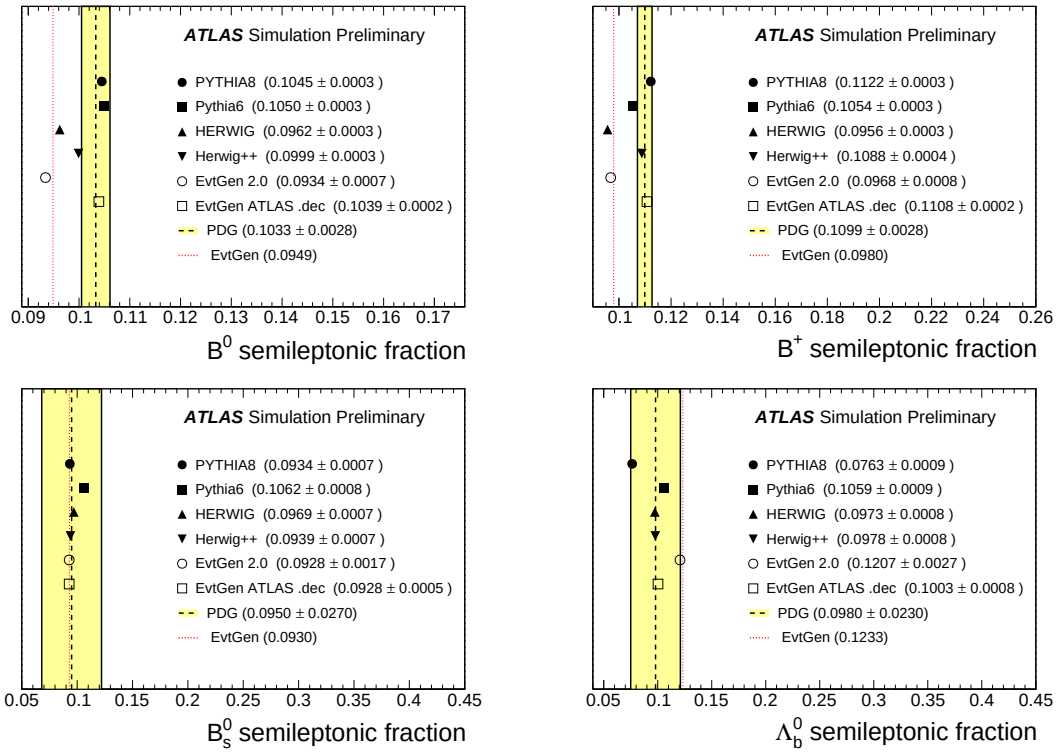

Figure B.13: Comparison of semileptonic branching fraction $B \to e^-\overline{\nu_e}X$ of the weakly decaying bottom hadrons (a) B^0, (b) B^+, (c) B_s^0 and (d) Λ_b in four different generators, PYTHIA6 version 427.2, Pythia8 version 175, Herwig++ version 2.6.3 and HERWIG version 6.520.2, both with and without EvtGen. EvtGen version 2.0 is used with the particle properties table provided with EvtGen and with its standard inclusive decay table DECAY_2010.DEC, as well as a custom decay table with developed for ATLAS with the most up to date semileptonic fractions from the PDG. Only decays where the electron is the direct decay product of the bottom hadron are included here (e.g. electrons coming from charm or τ decays are excluded). The band shown for the world average branching fractions correspond to the measured decay fraction for $B \to e\nu X_c$ listed by the PDG[111]. The values of the B^0, B^+ and Λ_b^0 semileptonic fractions in the default EvtGen particle properties table have been tuned to the observed inclusive $B \to D\ell\nu +$ anything branching fraction, which has a larger uncertainty.

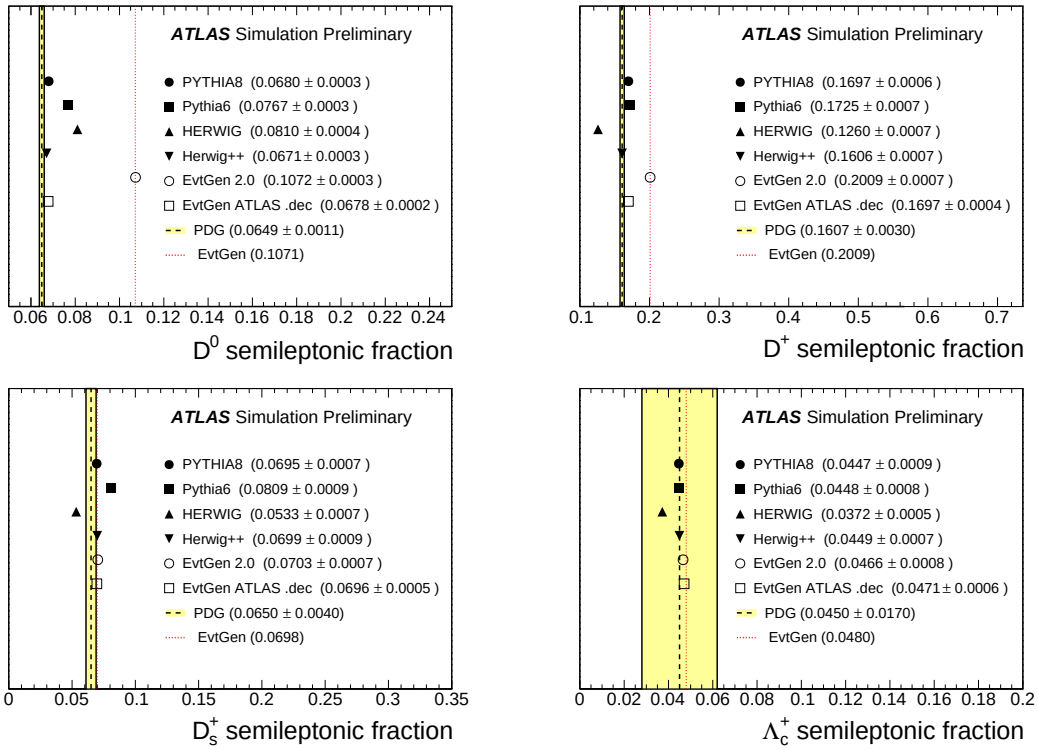

Figure B.14: Comparison of semileptonic branching fraction $D \to e^-\overline{\nu_e}X$ of the weakly decaying charm hadrons (a) D^0, (b) D^+, (c) D_s and (d) Λ_c in four different generators, PYTHIA6 version 427.2, Pythia8 version 175, Herwig++ version 2.6.3 and HERWIG version 6.520.2, both with and without EvtGen. EvtGen version 2.0 is used with the particle properties table provided with EvtGen and with its standard inclusive decay table DECAY_2010.DEC, as well as a custom decay table with developed for ATLAS with the most up to date semileptonic fractions from the PDG. Only decays where the electron is the direct decay product of the charm are included. The values of the D^0, D^+, D_s^+ and Λ_c^+ semileptonic fractions in this default EvtGen particle properties table differ from the world averages listed by the PDG [111].

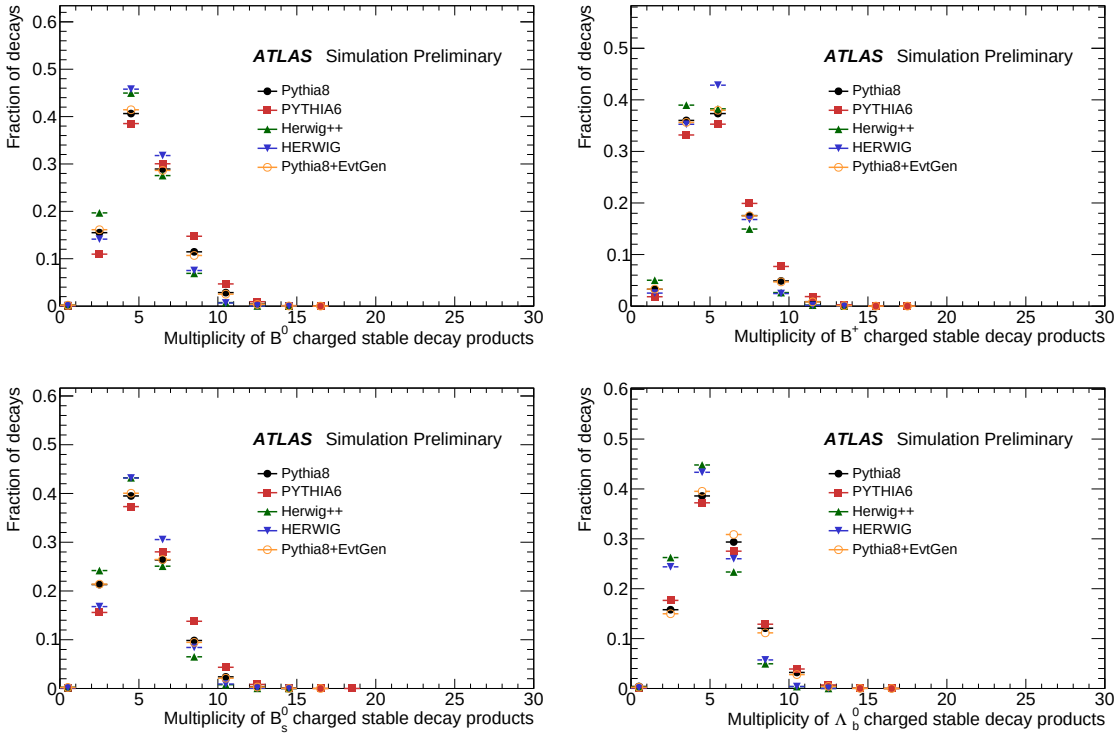

Figure B.15: Comparison of the multiplicity of charged, stable decay products for the weakly decaying bottom hadrons (a) B_0, (b) B^+, (c) B_s^0 and (d) Λ_b in Pythia8 PYTHIA6 Herwig++ HERWIG and EvtGen. A stable particle is defined as a particle with a proper lifetime $c\tau_0 > 10$ mm.

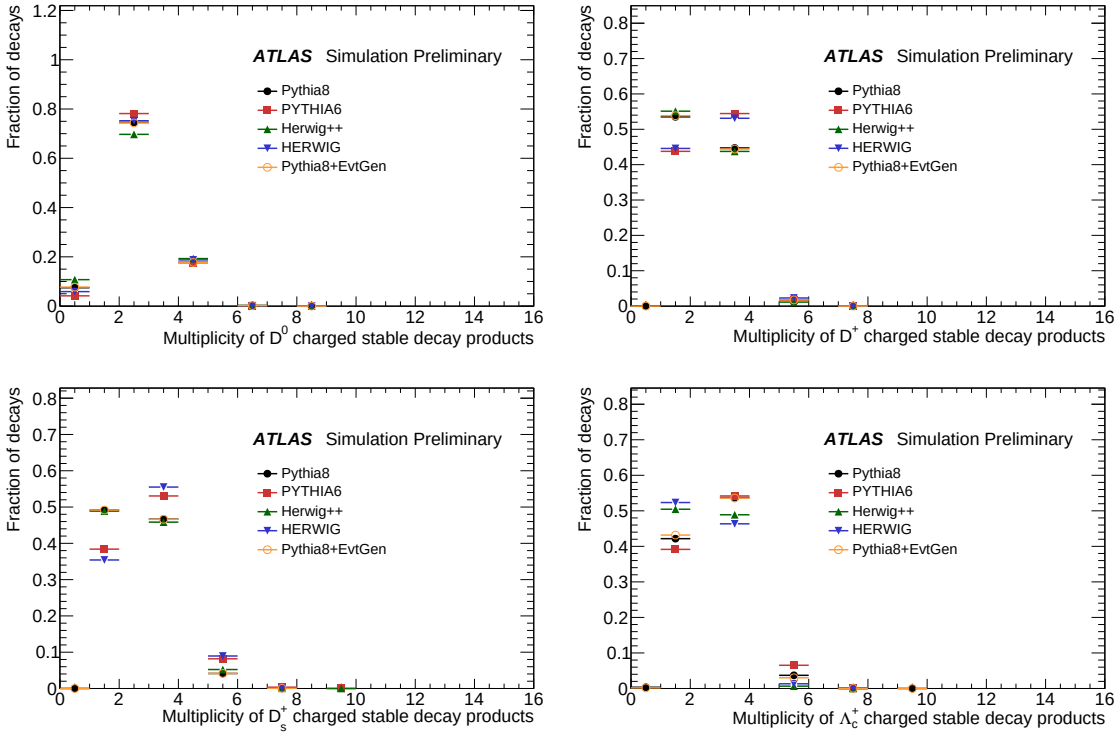

Figure B.16: Comparison of multiplicity of charged, stable decay products for the weakly decaying charm hadrons (a) D^0, (b) D^+, (c) D_s and (d) Λ_c in Pythia8 PYTHIA6 Herwig++ HERWIG and EvtGen. A stable particle is defined as a particle with a proper lifetime $c\tau_0 > 10$ mm.

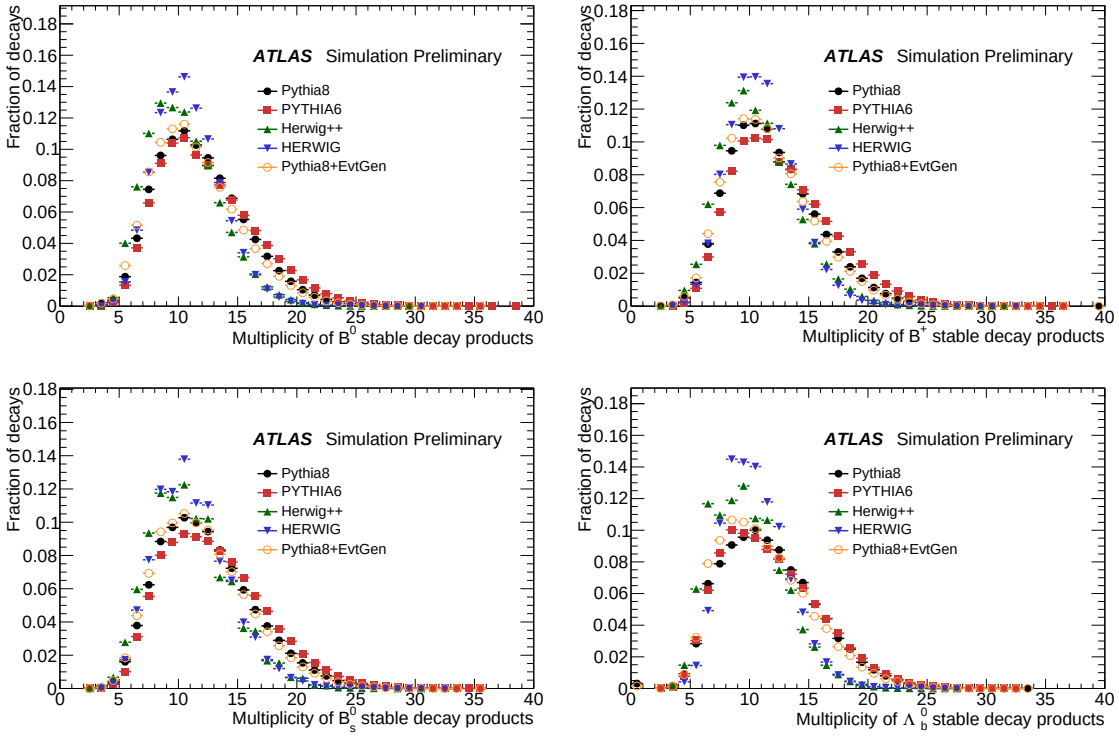

Figure B.17: Comparison of the multiplicity of stable decay products for the weakly decaying bottom hadrons (a) B^0, (b) B^+, (c) B_s^0 and (d) Λ_b in Pythia8 PYTHIA6 Herwig++ HERWIG and EvtGen. A stable particle is defined as a particle with a proper lifetime $c\tau_0 > 10$ mm.

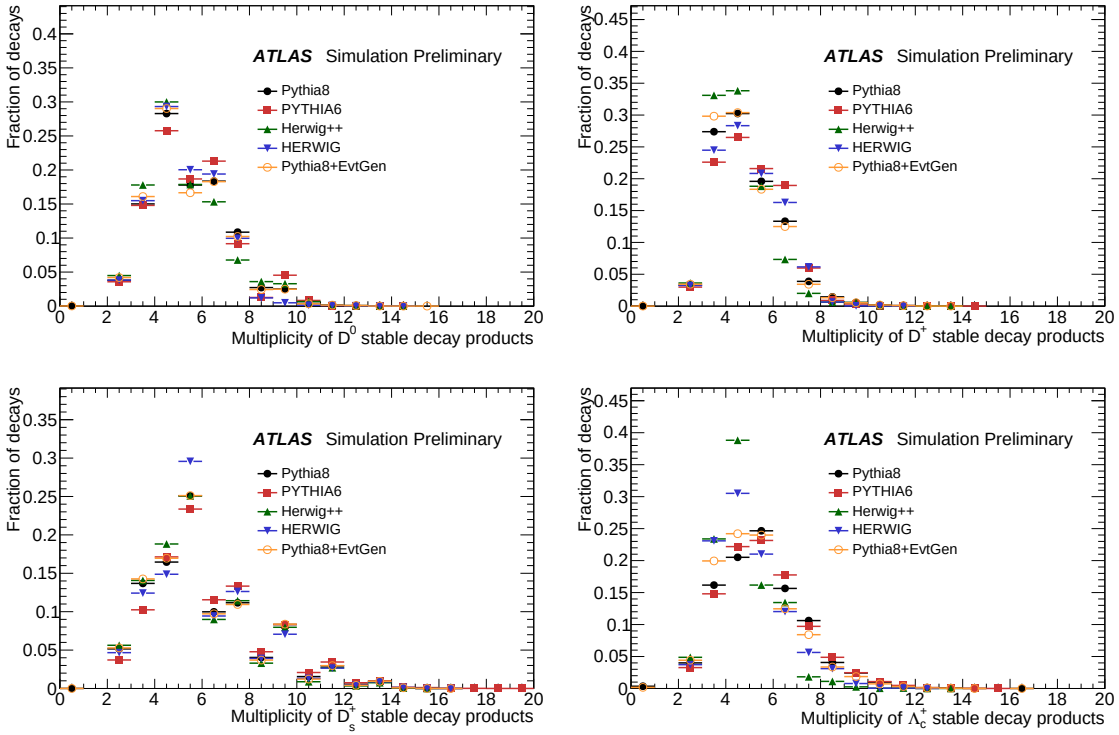

Figure B.18: Comparison of the multiplicity of stable decay products for the weakly decaying charm hadrons (a) D^0, (b) D^+, (c) D_s and (d) Λ_c in Pythia8 PYTHIA6 Herwig++ HERWIG and EvtGen. A stable particle is defined as a particle with a proper lifetime $c\tau_0 > 10$ mm.

Bibliography

[1] G. Aad *et al.*, "Measurement of the $t\bar{t}$ production cross-section using $e\mu$ events with b -tagged jets in pp collisions at $\sqrt{s} = 7$ and 8 TeV with the ATLAS detector," *Eur.Phys.J.*, vol. C74, no. 10, p. 3109, 2014.

[2] M. E. Peskin and D. V. Schroeder, *An introduction to quantum field theory.* Boulder (Colo.): Westview Press Reading (Mass.), 1995.

[3] F. Halzen and A. Martin, *Quarks and leptons: an introductory course in modern particle physics.* Wiley, 1984.

[4] K. Olive *et al.*, "Review of particle physics," *Chin.Phys.*, vol. C38, p. 090001, 2014.

[5] "First combination of Tevatron and LHC measurements of the top-quark mass," 2014.

[6] G. Aad *et al.*, "Observation of a new particle in the search for the Standard Model Higgs boson with the ATLAS detector at the LHC," *Phys. Lett.*, vol. B716, pp. 1–29, 2012.

[7] T. van Ritbergen, J. A. M. Vermaseren, and S. A. Larin, "The Four loop beta function in quantum chromodynamics," *Phys. Lett.*, vol. B400, pp. 379–384, 1997.

[8] J. M. Campbell, J. Huston, and W. Stirling, "Hard Interactions of Quarks and Gluons: A Primer for LHC Physics," *Rept.Prog.Phys.*, vol. 70, p. 89, 2007.

[9] G. Altarelli and G. Parisi, "Asymptotic Freedom in Parton Language," *Nucl. Phys.*, vol. B126, p. 298, 1977.

[10] A. D. Martin, W. J. Stirling, R. S. Thorne, and G. Watt, "Parton distributions for the LHC," *Eur. Phys. J.*, vol. C63, pp. 189–285, 2009.

[11] F. Abe *et al.*, "Observation of top quark production in $\bar{p}p$ collisions," *Phys.Rev.Lett.*, vol. 74, pp. 2626–2631, 1995.

[12] S. Abachi *et al.*, "Observation of the top quark," *Phys.Rev.Lett.*, vol. 74, pp. 2632–2637, 1995.

[13] M. Czakon, P. Fiedler, and A. Mitov, "Total Top-Quark Pair-Production Cross Section at Hadron Colliders Through $O(\frac{4}{S})$," *Phys.Rev.Lett.*, vol. 110, p. 252004, 2013.

[14] C. D. White, S. Frixione, E. Laenen, and F. Maltoni, "Isolating Wt production at the LHC," *JHEP*, vol. 11, p. 074, 2009.

[15] K. G. Chetyrkin and M. Steinhauser, "Short distance mass of a heavy quark at order α_s^3," *Phys. Rev. Lett.*, vol. 83, pp. 4001–4004, 1999.

[16] S. P. Martin, "A Supersymmetry primer," 1997. [Adv. Ser. Direct. High Energy Phys.18,1(1998)].

[17] B. Lillie, L. Randall, and L.-T. Wang, "The Bulk RS KK-gluon at the LHC," *JHEP*, vol. 0709, p. 074, 2007.

[18] "A search for $\mathbf{t\bar{t}}$ resonances using lepton plus jets events in proton-proton collisions at $\sqrt{s} = 8$ TeV with the ATLAS detector," Tech. Rep. ATLAS-CONF-2015-009, CERN, Geneva, Mar 2015.

[19] G. Aad *et al.*, "Search for top squark pair production in final states with one isolated lepton, jets, and missing transverse momentum in $\sqrt{s}$ =8 TeV *pp* collisions with the ATLAS detector," *JHEP*, vol. 1411, p. 118, 2014.

[20] S. Höche, "Developments in Sherpa and BlackHat." http://indico.cern.ch/event/296900/session/9/contribution/13/material/slides/0.pdf, 2014.

[21] G. Corcella *et al.*, "HERWIG 6.5 release note," 2002.

[22] T. Sjostrand, S. Mrenna, and P. Z. Skands, "PYTHIA 6.4 Physics and Manual," *JHEP*, vol. 0605, p. 026, 2006.

[23] GEANT4 Collaboration (S. Agostinelli et al.), "Geant4: A simulation toolkit," *Nucl. Instr. Meth.*, vol. A506, pp. 250–303, 2003.

[24] T. Sjostrand, "Monte Carlo Tools," in *Proceedings, 65th Scottish Universities Summer School in Physics: LHC Physics (SUSSP65)*, pp. 309–339, 2009.

[25] S. Frixione and B. R. Webber, "Matching NLO QCD computations and parton shower simulations," *J. High Energy Phys.*, vol. 0206, p. 29, 2002.

[26] S. Frixione *et al.*, "Single-top hadroproduction in association with a W boson," *J. High Energy Phys.*, vol. 0807, p. 029, 2008.

[27] S. Frixione, P. Nason, and C. Oleari, "Matching NLO QCD computations with parton shower simulations: the POWHEG method," *J. High Energy Phys.*, vol. 0711, p. 70, 2007.

[28] P. Nason, "A New method for combining NLO QCD with shower Monte Carlo algorithms," *J. High Energy Phys.*, vol. 0411, p. 040, 2004.

[29] S. Alioli *et al.*, "A general framework for implementing NLO calculations in shower Monte Carlo programs: the POWHEG BOX," *J. High Energy Phys.*, vol. 1006, p. 043, 2010.

[30] S. Frixione, P. Nason, and G. Ridolfi, "A Positive-weight next-to-leading-order Monte Carlo for heavy flavour hadroproduction," *J. High Energy Phys.*, vol. 0709, p. 126, 2007.

[31] S. Jadach, Z. Was, R. Decker, and J. H. Kuhn, "The tau decay library TAUOLA: Version 2.4," *Comput. Phys. Commun.*, vol. 76, pp. 361–380, 1993.

[32] D. J. Lange, "The EvtGen particle decay simulation package," *Nucl. Instrum. Meth.*, vol. A462, pp. 152–155, 2001.

[33] A. Buckley, H. Hoeth, H. Lacker, H. Schulz, and E. von Seggern, "Monte Carlo tuning and generator validation," in *Proceedings, 1st International Workshop on Multiple Partonic Interactions at the LHC (MPI08)*, pp. 267–283, 2009.

[34] R. Atkin, "Review of jet reconstruction algorithms," *J. Phys. Conf. Ser.*, vol. 645, no. 1, p. 012008, 2015.

[35] M. Cacciari, G. P. Salam, and G. Soyez, "The anti-k_t jet clustering algorithm," *J. High Energy Phys.*, vol. 0804, p. 63, 2008.

[36] M. Cacciari and G. P. Salam, "Dispelling the N^3 myth for the k_t jet-finder," *Phys. Lett.*, vol. B641, p. 57, 2006.

[37] C. Lefevre, "Lhc: The guide," 2009.

[38] "The alice experiment at the cern lhc," *Journal of Instrumentation*, vol. 3, p. S08002, 2008.

[39] "The atlas experiment at the cern large hadron collider," *Journal of Instrumentation*, vol. 3, p. S08003, 2008.

[40] "The cms experiment at the cern lhc," *Journal of Instrumentation*, vol. 3, p. S08004, 2008.

[41] "The lhcb detector at the lhc," *Journal of Instrumentation*, vol. 3, p. S08005, 2008.

[42] "Atlas photos," 2015.

[43] L. Evans and P. Bryant, "Lhc machine," *Journal of Instrumentation*, vol. 3, p. S08001, 2008.

[44] ATLAS Collaboration, "Improved luminosity determination in *pp* collisions at $\sqrt{s} = 7$ TeV using the ATLAS detector at the LHC," *Eur. Phys. J.*, vol. C73, p. 2518, 2013.

[45] G. Aad *et al.*, "Performance of pile-up mitigation techniques for jets in *pp* collisions at $\sqrt{s} = 8$ TeV using the ATLAS detector," 2015.

[46] J. Pequenao, "Computer generated image of the whole ATLAS detector." Mar 2008.

[47] "Atlas photos," 2015.

[48] M. Schott and M. Dunford, "Review of single vector boson production in pp collisions at $\sqrt{s} = 7$ TeV," *Eur. Phys. J.*, vol. C74, p. 2916, 2014.

[49] "Calorimeter clustering algorithms: Description and performance." https://cds.cern.ch/record/1099735002, 2008.

[50] "Commissioning of the atlas muon spectrometer with cosmic rays," *Eur. Phys. J.*, vol. C70, pp. 875–916, 2010. https://cds.cern.ch/record/1275998.

[51] "Level-1 trigger technical design report." http://atlas.web.cern.ch/Atlas/GROUPS/DAQTRIG/TDR/tdr.html, 1998.

[52] G. Pasztor, R. White, F. Monticelli, M. Wielers, T. Kono, F. Zhang, F. Wang, and K. Behr, "Electron trigger performance in 2012 ATLAS data," Tech. Rep. ATL-COM-DAQ-2015-091, CERN, Geneva, Jul 2015.

[53] G. Aad *et al.*, "Performance of the ATLAS muon trigger in pp collisions at $\sqrt{s} = 8$ TeV," *Eur. Phys. J.*, vol. C75, p. 120, 2015.

[54] G. Aad *et al.*, "Measurement of $t\bar{t}$ production with a veto on additional central jet activity in pp collisions at sqrt(s) = 7 TeV using the ATLAS detector," *Eur.Phys.J.*, vol. C72, p. 2043, 2012.

[55] ATLAS Collaboration, "Comparison of Monte Carlo generator predictions for gap fraction and jet multiplicity observables in top-antitop events." ATL-PHYS-PUB-2014-005.

[56] G. Aad *et al.*, "Measurement of the $t\bar{t}$ production cross-section as a function of jet multiplicity and jet transverse momentum in 7 TeV proton-proton collisions with the ATLAS detector," *JHEP*, vol. 1501, p. 020, 2015.

[57] S. Chatrchyan *et al.*, "Measurement of jet multiplicity distributions in $\mathrm{t\bar{t}}$ production in pp collisions at $\sqrt{s} = 7\,\mathrm{TeV}$," *Eur.Phys.J.*, vol. C74, no. 8, p. 3014, 2014.

[58] "Performance of the atlas inner detector track and vertex reconstruction in the high pile-up lhc environment." https://atlas.web.cern.ch/Atlas/GROUPS/PHYSICS/CONFNOTES/ATLAS-CONF-2012-042/, 2012.

[59] "Performance of primary vertex reconstruction in proton-proton collisions at $\sqrt{s}$ = 7 tev in the atlas experiment." https://atlas.web.cern.ch/Atlas/GROUPS/PHYSICS/CONFNOTES/ATLAS-CONF-2010-069/, 2010.

[60] "Stand-alone event displays." https://twiki.cern.ch/twiki/bin/view/AtlasPublic/EventDisplayStandAlone, 2015.

[61] G. Aad *et al.*, "Measurement of the muon reconstruction performance of the ATLAS detector using 2011 and 2012 LHC proton-proton collision data," 2014.

[62] G. Aad *et al.*, "Electron reconstruction and identification efficiency measurements with the ATLAS detector using the 2011 LHC proton-proton collision data," *Eur.Phys.J.*, vol. C74, p. 2941, 2014.

[63] M. Cacciari, G. P. Salam, and G. Soyez, "FastJet user manual," *Eur. Phys. J.*, vol. C72, p. 1896, 2012.

[64] ATLAS Collaboration, "Jet energy measurement and its systematic uncertainty in proton-proton collisions at $\sqrt{s} = 7$ TeV with the ATLAS detector," 2014. Submitted to *Eur.Phys.J.* C.

[65] ATLAS Collaboration, "Commissioning of the ATLAS high-performance b-tagging algorithms in the 7 TeV collision data." ATLAS-COM-2011-102.

[66] ATLAS Collaboration, "Measurement of the b-tag efficiency in a sample of jets containing muons with 5fb^{-1}of data from the ATLAS detector." ATLAS-COM-2012-043.

[67] ATLAS CollaborationThe simulation principle and performance of the atlas fast calorimeter simulation fastcalo.ATL-PHYS-PUB-2010-013, "The simulation principle and performance of the atlas fast calorimeter simulation fastcalosim," 2010.

[68] T. Sjostrand, S. Mrenna, and P. Z. Skands, "A Brief Introduction to PYTHIA 8.1," *Comput.Phys.Commun.*, vol. 178, pp. 852–867, 2008.

[69] P. Z. Skands, "Tuning Monte Carlo Generators: The Perugia Tunes," *Phys.Rev.*, vol. D82, p. 074018, 2010.

[70] H.-L. Lai, M. Guzzi, J. Huston, Z. Li, P. M. Nadolsky, *et al.*, "New parton distributions for collider physics," *Phys.Rev.*, vol. D82, p. 074024, 2010.

[71] G. Marchesini *et al.*, "HERWIG: A Monte Carlo event generator for simulating hadron emission reactions with interfering gluons," *Comput. Phys. Commun.*, vol. 67, pp. 465–508, 1992.

[72] G. Corcella *et al.*, "HERWIG 6: An Event generator for hadron emission reactions with interfering gluons (including supersymmetric processes)," *J. High Energy Phys.*, vol. 0101, p. 10, 2001.

[73] J. Butterworth, J. R. Forshaw, and M. Seymour, "Multiparton interactions in photoproduction at HERA," *Z.Phys.*, vol. C72, pp. 637–646, 1996.

[74] ATLAS Collaboration, "New ATLAS event generator tunes to 2010 data." ATLAS-PUB-2011-008.

[75] J. Alwall, M. Herquet, F. Maltoni, O. Mattelaer, and T. Stelzer, "MadGraph 5 : Going Beyond," *JHEP*, vol. 1106, p. 128, 2011.

[76] M. L. Mangano, M. Moretti, F. Piccinini, R. Pittau, and A. D. Polosa, "ALPGEN, a generator for hard multiparton processes in hadronic collisions," *JHEP*, vol. 0307, p. 001, 2003.

[77] J. Pumplin *et al.*, "New generation of parton distributions with uncertainties from global QCD analysis," *J. High Energy Phys.*, vol. 0207, p. 12, 2002.

[78] S. Frixione, E. Laenen, P. Motylinski, B. R. Webber, and C. D. White, "Single-top hadroproduction in association with a W boson," *JHEP*, vol. 0807, p. 029, 2008.

[79] M. L. Mangano, M. Moretti, F. Piccinini, R. Pittau, and A. D. Polosa, "ALPGEN, a generator for hard multiparton processes in hadronic collisions," *JHEP*, vol. 0307, p. 001, 2003.

[80] "Heavy flavour overlap removal procedure."

[81] ATLAS Collaboration, "Object selection and calibration, backgroundestimations and MC samples for top quark analyses using the full 2012 dataset." ATLAS-CONF-2013-1016.

[82] ATLAS Collaboration, "Jet energy scale and its systematic uncertainty in proton-proton collisions at $\sqrt{s} = 7\,\mathrm{TeV}$ with ATLAS 2011 data." ATLAS-COM-2013-004.

[83] ATLAS Collaboration, "Measurement of the b-tag Efficiency in a Sample of Jets Containing Muons with 5fb^{-1}Data from the ATLAS Detector." ATLAS-CONF-2012-043.

[84] M. Cacciari, G. P. Salam, and G. Soyez, "The Catchment Area of Jets," *JHEP*, vol. 0804, p. 005, 2008.

[85] ATLAS Collaboration, "Selection of jets produced in proton-protoncollisions with the ATLAS detector using 2011 data." ATLAS-CONF-2012-020.

[86] "ATLAS Top Event Challenges."

[87] R. Hawkings, "Measurement of the $t\bar{t}$ production cross-section in pp collisions at $\sqrt{s}$ =7-8 TeV using $e\mu$ events with b-tagged jets," Tech. Rep. ATL-COM-PHYS-2014-017, CERN, Geneva, Jan 2014. Requesting INT approval as corresponding paper TOPQ-2013-04 has been accepted by journal for publication.

[88] ATLAS Collaboration, "Measurement of the Mistag Rate of b-tagging algorithms with $5\,\mathrm{fb}^{-1}$ of Data collected by the ATLAS Detector." ATLAS-CONF-2012-040.

[89] ATLAS Collaboration, "Pileup subtraction and suppression for jets in ATLAS." ATLAS-CONF-2013-083.

[90] T. Martin, "Development and online operation of minimum bias triggers in atlas," *Journal of Instrumentation*, vol. 5, no. 12, p. C12051, 2010.

[91] T. Adye, "Unfolding algorithms and tests using RooUnfold," pp. 313–318, 2011.

[92] G. D'Agostini, "A Multidimensional unfolding method based on Bayes' theorem," *Nucl. Instrum. Meth.*, vol. A362, pp. 487–498, 1995.

[93] E. Jones, T. Oliphant, P. Peterson, *et al.*, "SciPy: Open source scientific tools for Python," 2001–.

[94] ATLAS Collaboration, "Performance of b-Jet Identification in the ATLAS Experiment," *submitted to JINST*, 2015.

[95] ATLAS Collaboration, "Electron reconstruction and identification efficiency measurements with the ATLAS detector using the 2011 LHC proton–proton collision data," *Eur. Phys. J. C*, vol. 74, p. 2941, 2014.

[96] ATLAS Collaboration, "Electron and photon energy calibration with the ATLAS detector using LHC Run 1 data," *Eur. Phys. J. C*, vol. 74, p. 3071, 2014.

[97] ATLAS Collaboration, "Measurement of the muon reconstruction performance of the ATLAS detector using 2011 and 2012 LHC proton–proton collision data," *Eur. Phys. J. C*, vol. 74, p. 3130, 2014.

[98] W. Bell, L. Bellagamba, C. Bernard, P. Berta, K. Bilsback, K. Black, T. Childers, R. Di Sipio, L. DellAsta, M. Franchini, C. Gabaldon, M. Yamada, J. Kanzaki, J. Kvita, R. Romano, A. Sady, J. Schovancova, F. Spano', R. Spighi, J. Sjolin, M. Talby, N. Tannoury, and I. Watson, "Measurement of top quark pair differential cross section with ATLAS in pp collisions at sqrt(s)=7 TeV: Measurement of top quark pair differential cross section with ATLAS using 5/fb of data collected in 2011 and the rel.17 version of the Atlas software ," Tech. Rep. ATL-COM-PHYS-2012-1137, CERN, Geneva, Jul 2012.

[99] "Systematics affecting Top MC for 8 TeV 2012 analyses."

[100] "TopPdfUncertainty."

[101] D. d'Enterria and A. M. Snigirev, "Double-parton scattering cross sections in proton-nucleus and nucleus-nucleus collisions at the LHC," 2014.

[102] G. Aad *et al.*, "Measurement of the production cross section of prompt J/ψ mesons in association with a $W^{\pm}$ boson in pp collisions at $\sqrt{s} = 7$ TeV with the ATLAS detector," *JHEP*, vol. 1404, p. 172, 2014.

[103] "Comparison of Monte Carlo generator predictions for bottom and charm hadrons in the decays of top quarks and the fragmentation of high pT jets," Tech. Rep. ATL-PHYS-PUB-2014-008, CERN, Geneva, Jun 2014.

[104] A. Buckley, J. Butterworth, S. Gieseke, D. Grellscheid, S. Hoche, *et al.*, "General-purpose event generators for LHC physics," *Phys.Rept.*, vol. 504, pp. 145–233, 2011.

[105] Particle Data Group, "Review of Particle Physics, Monte Carlo Event Generators," *Phys. Rev. D*, vol. 86, 2012.

[106] T. Sjostrand, S. Mrenna, and P. Z. Skands, "PYTHIA 6.4 Physics and Manual," *JHEP*, vol. 05, 2006.

[107] T. Sjostrand, S. Mrenna, and P. Z. Skands, "A Brief Introduction to PYTHIA 8.1," *Comput.Phys.Commun.*, vol. 178, 2008.

[108] G. Corcella *et al.*, "HERWIG 6.5 release note," 2002.

[109] M. Bahr *et al.*, "Herwig++ Physics and Manual," *Eur. Phys. J.*, vol. C 58, 2008.

[110] A. Karneyeu, L. Mijovic, S. Prestel, and P. Skands, "MCPLOTS: a particle physics resource based on volunteer computing," *Eur.Phys.J.*, vol. C74, 2014.

[111] Particle Data Group, "Review of Particle Physics," *Phys. Rev. D*, vol. 86, 2012.

[112] J. M. Butterworth, J. R. Forshaw, and M. H. Seymour, "Multiparton interactions in photoproduction at HERA," *Z. Phys.*, vol. C 72, 1996.

[113] P. Nason, "A new method for combining NLO QCD with shower Monte Carlo algorithms," *JHEP*, vol. 11, 2004.

[114] S. Frixione, P. Nason, and C. Oleari, "Matching NLO QCD computations with Parton Shower simulations: the POWHEG method," *JHEP*, vol. 11, 2007.

[115] S. Alioli, P. Nason, C. Oleari, and E. Re, "A general framework for implementing NLO calculations in shower Monte Carlo programs: the POWHEG BOX," *JHEP*, vol. 06, 2010.

[116] S. Alioli, P. Nason, C. Oleari, and E. Re, "NLO vector-boson production matched with shower in POWHEG," *JHEP*, vol. 07, 2008.

[117] H.-L. Lai *et al.*, "New parton distributions for collider physics," *Phys.Rev.*, vol. D82, 2010.

[118] P. Z. Skands, "Tuning Monte Carlo Generators: The Perugia Tunes," *Phys.Rev.*, vol. D82, 2010.

[119] "Summary of ATLAS Pythia 8 tunes," ATL-PHYS-PUB-2012-003 `https://cdsweb.cern.ch/record/1474107`.

[120] "New ATLAS event generator tunes to 2010 data," ATL-PHYS-PUB-2011-008 `https://cds.cern.ch/record/1345343`.

[121] M. H. Seymour and A. Siodmok, "Constraining MPI models using σ_{eff} and recent Tevatron and LHC Underlying Event data," *JHEP*, vol. 1310, 2013.

[122] M. Bowler, "e+ e- Production of Heavy Quarks in the String Model," *Z.Phys.*, vol. C11, 1981.

[123] M. Cacciari, G. P. Salam, and G. Soyez, "The Anti-k(t) jet clustering algorithm," *JHEP*, vol. 04, 2008.

[124] M. Cacciari and G. P. Salam, "Dispelling the N^3 myth for the k_t jet-finder," *Phys. Lett.*, vol. B 641, 2006.

[125] "Updated average f_s/f_d b-hadron production fraction ratio for 7 TeV pp collisions," *https://cds.cern.ch/record/1559262, LHCb-CONF-2013-011*, 2013.

[126] R. Aaij *et al.*, "Measurement of b-hadron production fractions in 7 TeV pp collisions," *Phys.Rev.*, vol. D85, p. 032008, 2012.

[127] E. Lohrmann, "A summary of charm hadron production fractions," 2011.

[128] "A study of the b-quark fragmentation function with the DELPHI detector at LEP I and an averaged distribution obtained at the Z Pole," *Eur.Phys.J.*, vol. C71, 2011.

[129] "Measurement of the b quark fragmentation function in Z0 decays," *Phys.Rev.*, vol. D65, 2002.

[130] "Charm hadrons from fragmentation and B decays in e+ e- annihilation at s**(1/2) = 10.6-GeV," *Phys.Rev.*, vol. D73, 2006.

[131] "Charm meson spectra in e^+e^- annihilation at 10.5-GeV c.m.e.," *Phys.Rev.*, vol. D70, 2004.

[132] G. Marchesini and B. Webber, "Simulation of QCD Coherence in Heavy Quark Production and Decay," *Nucl.Phys.*, vol. B330, 1990.

[133] G. Aad *et al.*, "Measurement of jet shapes in top-quark pair events at $\sqrt{s} = 7$ TeV using the ATLAS detector," *Eur.Phys.J.*, vol. C73, 2013.